The University Of Sheffield.

Improving Retention of Blowing Agent in Rigid Polyisocyanurate Foams Through the Introduction of Metal-Organic Frameworks and Nanosheets

Michael Harris

A thesis submitted in partial fulfilment of the requirements for the degree of Doctor of Philosophy

The University of Sheffield

Faculty of Science

Department of Chemistry

November 2022

Abstract

The building sector accounts for up to 40 % of the global energy consumption and up to 50 % of greenhouse gas emissions, with the energy required to keep buildings warm contributing significantly. The United Nations Environmental Programme has estimated 30 to 80 % of energy consumption for heating can be lowered through effective energy reduction technologies, primarily through the use of insulators to retain building temperatures. Insulating materials have inefficient transport of thermal energy through their structure, with polymeric foam insulators producing some of the most efficient insulating materials available. More than 50 % of heat transfer through polymeric insulators comes from the gaseous blowing agent used within the sealed bubbles, or cells, of the foam, making the blowing agent vital to the performance of the insulator. Many polymeric foam insulators suffer from loss of blowing agent over time as the gas diffuses out of the cells and can be mitigated through introduction of barrier materials in the polymer matrix, such as metal-organic frameworks and nanosheets.

Metal-organic frameworks (MOFs) are three-dimensional co-ordination networks that contain potential voids and consist of regularly ordered structures of metal ions/clusters and organic linkers. MOFs are highly programmable materials that can be tailored by their metals/linkers for specific application and have seen success in separation of gasses when combined in polymer matrixes. Metal-organic nanosheets (MONs) are a unique class of free-standing two-dimensional materials that approach monolayer thicknesses with high aspect ratios. MONs retain the highly tuneable nature of MOFs but add increased surface areas and nanoscopic dimensions which are expected to enhance the formation of tortuous paths for gas separation applications. In this thesis, both MOFs and MONs were added to rigid Polyisocyanurate (PIR) foams to create novel composites to restrict the loss of pentane-based blowing agent from the foam. Additionally, the synthesis of novel MONs and their post-synthetic modification was explored to produce tailored materials for addition to the foams.

In **Chapter 2** a robust and reliable accelerated aging method for monitoring the loss of blowing agent from rigid PIR foams was developed. This method was then tested with example layered additives MoS_2 and Graphite to determine optimum loadings of additives, and to demonstrate that the influence of gas loss by additives can be measured by the monitoring technique. Copper-based paddle-wheel MOFs and MONs were used as additives in **Chapter 3**, demonstrating the complex relationship between the surface functionality, size, and stability of MOFs/MONs on the loss of blowing agent from rigid PIR foams. The introduction of a copper aminoterephthalic acid MOF (Cu(ABDC)(DMF)) or a maleic acid functionalized uncentrifuged MON (Cu(MA-ABDC)(DMF)) demonstrated a reduced loss of blowing agent from the rigid PIR foams. **Chapter 4** expands on this work by looking at an alternative MOF; NH_2-MIL-53. This MOF was modulated and exfoliated into ultrathin MONs. The use of MOF in this system provided no reduction in blowing agent loss, but uncentrifuged MON did result in a reduction of the loss of blowing agent from the foam. **Chapter 5** described the novel synthesis of the MOF Cu(MA-ABDC)(DMF) from Cu(ABDC)(DMF) and the subsequent exfoliation of the nanosheets. The amine functionality of Cu(ABDC)(DMF) was reacted with maleic anhydride to produce alternative carboxylic acid functionality. The 31 % functionalized Cu(MA-ABDC)(DMF) MOF was exfoliated into ethanol to produce predominantly monolayer MONs, that were utilized as an additive in **Chapter 3**. Finally, **Chapter 5** described the attempted addition of polymeric chains to the surface of MONs through ring-opening polymerization techniques to produce polymer enhanced MONs.

This thesis demonstrates the use of MONs as effective barrier materials within rigid PIR foams and provides insights into the synthesis and modification of novel MONs utilized within the work. These rigid PIR foams could be utilized as a basis for the next generation of insulating materials, and the measurement techniques for loss of blowing agents can be utilized for further development of new composite rigid PIR foams.

Acknowledgements
I cannot write enough here about all the people who have helped me throughout this work, both directly and indirectly. This is just a snippet of all those who've been involved through my PhD, and I know so many more names deserved to be mentioned, but I hope everyone knows they helped me in this work and this achievement could have only been done with your support.

Primary thanks needs to be given to **Dr Jonathan Foster** and **Prof. Anthony Ryan**, who I'm sure have thoroughly enjoyed the mass amounts of editing I have put them through for this thesis. The meetings, events, injuries and putting up with my constant cynicism I'm sure was the highlight of your careers. This project has been so interesting and allowed me to develop as a researcher so significantly that I wouldn't trade the experience for anything else. Additional thanks has to go to Kingspan, and specifically **Gwyn Davis**, who has helped immensely in the direction of the project and in the understanding of the industrial world, and for delivering everything needed to make my foams.

Thank you to **Dr Seb Spain** and **Dr Hamish Yeung** for being my examiners for this work. I hope it is interesting and can generate a good discussion on how this work can be developed further for the future.

The Foster and RyMyk groups over the past 4 years have shown me immense kindness and worked to integrating me as a true member of both, thank you to all the students, PhDs, Post-Docs and more who have worked with and alongside me. **Dr Joshua Nicks, Dr Dave Ashworth, Dr Kezia Sasitharan, Dr Ram R R Prasad, Dr Justin Driver, Dr Charlotte Kiker, Freya Cleasby, Amelia Wood, Benedict Smith, Jiangtian (Andy) Tian, Sanyou (Victor) Xu, Ellen Wilson, Sophia van Mourik, Courtney Thompson, Dr Melody Obeng, Dr James Cosby, Dr Deborah Beattie, Dr Harry Wright and Prof Oleksandr (Sasha) Mykhaylyk**. I could right reams here of all the things that each person has helped me with, even small corridor conversations have made massive differences to my life during this PhD. But to highlight, Josh and Kez, I am so thankful for your insight and jokes, your oddities and inspiration, and simply keeping in touch with the strangest messages since moving to your new positions. Ben and Millie have been an amazing laugh in and out of the lab, and seeing your projects develop and understanding your work throughout our time at Sheffield has been an inspiration to me as well. I will miss working with you all, but I definitely will be keeping in touch.

A specific thank you has to go out to the soon-to-be Dr's: **George Freeman, Evelin Csyáni, Bradley Westwater, Csilla Györgi** and **Ryan Euesdan.** Doing my PhD alongside you guys has helped significantly, from bouncing around dumb ideas, to performing experiments together, to just sharing the mental load when things became a lot. You all honestly made this PhD worth it.

Thanks to all the undergraduate students I've had the privilege of having worked on my projects, **Joel Parkins, Melissa Townsend, Alana Barlow, Josie Robins and Priyanka Chohan**. Your hard work allowed me to explore around this project and helped me immensely in becoming a better supervisor. Furthermore, thank you to all the undergraduate students and **Dr Natalka Johnson** who had me as a demonstrator during your labs. The mix of nostalgia for my own labs and being able to wind everyone up on how your experiments were going has left me with lasting memories of you all.

So much of this work could not have been completed without the training and guidance of so many experts within the university. Therefore, my thanks go out to **Dr Craig Robertson, Rob Hanson, Dr Oday Hussein, Dr Khalid Doudin, Dr Simon Parker, Dr Deeba Zahoor, Heather Grievson, Dr Holly Evans, Dr Ria Mitchell, Dr Chris Hill** and **Joe Quick**. I am

now a jack-of-all trades thanks to all of you and am not finished learning to use every other piece of equipment I can get my hands on. Further thanks goes out to **Denise Richards** and **Louise Brown-Leng**, who's administrative work and putting up with my many questions on what I need to do has helped me whenever I have felt lost. Finally, a massive thank you to **Nick Smith** and **Sharon Curl**, who, whilst delivering top banter, ensured all chemicals and deliveries always got to me, even going beyond, and chasing up companies for me. Without your work, I wouldn't be able to attempt any synthesis.

A massive thank you to **Dr Robert Dawson**, who hates being called "Big Rob", and **Dr J. Grant Hill** for your contributions to my undergraduate at Sheffield and continued support through my PhD. Thank you to **Audrey Caspar** who planted the seed for me to start this PhD to begin with and keeping in touch all the way through this time. To go far enough back, thank you to **Mrs Bridges**, **Dr Fogg,** and **Mr Horton** for your inspiration during sixth form, your nudge to university study has allowed me to get this far, and I hope to keep pushing further.

To really enjoy a PhD, you have to relax as much as you work, so thank to you all my friends, **Sam Blacktop, Mike Walters, Ben Thorington-Jones, Joel Hirons, Josh Lawlor, Max Revels, Tom Fishwick, Jo Redfern, Holly Richards, Emily Ratcliffe, and Hayley Boddison** for constant amounts of parties, adventures, drinks, costumes, drama, and everything that has helped me balance my life during this PhD.

My family has also been a massive help throughout all my life, and I'm sure your support will help me continue further, thank you **Mom, Dad, Leah, and Charlie.** I hope I have done you proud.

Finally, to my fiancée **Christina Harper**, who throughout everything has supported me and challenged me to be better at all times. I probably would not have made it this far without you and the billions of memories we've made along the way. I love you so much, and I cannot wait for our wedding.

"Oh whence, I asked, and whither?

He smiled and would not say,

And looked at me and beckoned

And laughed and led the way.

And with kind looks and laughter

And nought to say beside

We two went on together,

I and my happy guide."

— A snippet from The Merry Guide, a poem by A. E. Houseman an English classical scholar and poet from Bromsgrove

Author's Declaration

This research has been performed between the months of October 2018 and November 2022, within the Department of Chemistry at the University of Sheffield, under the supervision of Dr Jonathan Foster and Prof Anthony J. Ryan.

I, the author, confirm that the Thesis is my own work. I am aware of the University's Guidance on the Use of Unfair Means (www.sheffield.ac.uk/ssid/unfair-means). This work has not been previously presented for and award at this, or any other university.

1st referee	Dr Seb Spain, The University of Sheffield
2nd referee (external)	Dr Hamish Yeung, The University of Birmingham

List of Publications

Manuscript contributions

1. Liquid exfoliation of a series of expanded layered metal-organic frameworks to form nanosheets, Joshua Nicks, **Michael S. Harris**, David J. Ashworth, George Danczuk and Jonathan A. Foster, manuscript in preparation.
2. Reactive Inkjet printing of a Metal Organic Framework enabling selective encapsulation of a dye, Jonathan A. Foster, David Alexander Gregory, Joshua Nicks, Joaquin Artigas-Amaudas, **Michael S. Harris**, Patrick Smith, manuscript in preparation.

List of Conference Presentations

Oral Presentations

1. **Michael Harris**, Jonathan A. Foster, Anthony J. Ryan, "Brushing up on 2D materials- Polymer functionalized metal-organic nanosheets (PolyMONs)" American Chemical Society (ACS) Spring Conference, San Diego, March **2022**
2. **Michael Harris**, Jonathan A. Foster, Anthony J. Ryan, "Enhancement of Rigid Polyurethane Foams with 2D Metal-Organic Nanosheets" Science Graduate Virtual Showcase, Sheffield, **2021**
   - Student choice award
3. **Michael Harris**, Jonathan A. Foster, Anthony J. Ryan, "Improving Polymer Insulation with Metal-Organic Nanosheets as Gas Barriers" Polymer CDT Summer School, Sheffield, **2021**
4. **Michael Harris**, Jonathan A. Foster, Anthony J. Ryan, "Improving Polymer Insulation with Metal-Organic Nanosheets as Gas Barriers" Polymer CDT Summer School, Sheffield, **2019**
   - Best presentation prize

Poster Presentations

1. **Michael Harris**, Jonathan A. Foster, Anthony J. Ryan, "Enhancement of Rigid Polyurethane Foams with 2D Metal-Organic Nanosheets" Science Graduate Virtual Showcase, Sheffield, **2021**
   - Student choice award

Table of Contents

Chapter 5: Functionalization of MOFs for addition to rigid PIR foams

Chapter 6: Conclusions and Outlook

Chapter 7: Experimental Methods

List of Common Abbreviations

Please note, all abbreviations are defined at first use in each chapter. Some abbreviations are only used in one chapter, and are not included in this list, which is intended to summarise terms used across multiple chapters.

2D	Two-dimensional
3D	Three-dimensional
AFM	Atomic force microscopy
ATR	Attenuated total reflectance
CCDC	Cambridge Crystallographic Data Centre
DLS	Dynamic light scattering
DMF	N,N'-dimethylformamide
DMSO	Dimethylsulfoxide
FT-IR	Fourier-transform infra-red (spectroscopy)
GC	Gas Chromatography
MDI	Methylene bis-diphenyl isocyanate
MeCN	Acetonitrile
MOF	Metal-organic framework
MON	Metal-organic framework nanosheet
NMR	Nuclear magnetic resonance (spectroscopy)
PIR	Polyisocyanurate
pMDI	Polymeric MDI
PSF	Post-synthetic Functionalisation
PU	Polyurethane
PXRD	Powder X-ray diffractometry/diffraction
SBU	Secondary building unit
SEM	Scanning electron microscopy
TGA	Thermal gravimetric analysis
UV-Vis	Ultraviolet-visible (spectroscopy)

Abbreviations of Framework Systems and Ligands:

ABDC	2-aminobenzenedicarboxylate (or BDC-NH2)
BDC	1,4-benzenedicarboxylate
Bim	Benzimidazole
BTetC	1,2,4,5-Benzenetetracarboxylic Acid
MA-ABDC	Maleic Anhydride functionalised ABDC
MIL	Matériaux de l'Institut Lavoisier (MOF)

TCPP	Tetrakis(4-carboxyphenyl)porphyrin
UiO	University of Oslo (MOF)
ZIF	Zeolitic imidazolate framework

List of Corrections

Preliminary

Page i, paragraph 3, line 9 and 10

Definitions of Cu(ABDC)(DMF) and Cu(MA-ABDC)(DMF) added.

Line spacing reduced to fit onto one page.

Page ii, paragraph 3, line 1

Name change from Prof Andrew Slark to Dr Seb Spain.

Page iv, paragraph 3, line 1

Name change from Prof Andrew Slark to Dr Seb Spain.

Page vi

Table of contents page updated to include a list of corrections and reflect any page number changes as a result.

Page xii

A list of corrections inserted.

Chapter 1

Page 2, paragraph 1, line 1 and 2

Hyphen between 40 – 50 % updated to a dash. Dashes between 25 - 40 % and 40 - 50 % updated with spaces in between.

Page 2, paragraph 1, line 3

“in 2016” added to reflect the date data was published for energy consumption in the UK.

Page 3, paragraph 2, line 2

“value” changed to “factor”.

Page 3, paragraph 2, line 3

“h°Fft^2” updated to “BTU-in/h-ft^2-°F” as quoted from reference 33 of the chapter.

Page 7, paragraph 1, line 2

“(such as polypropylene glycol [33])” added

Page 9, paragraph 3, line 8

“performance for application” changed to “retardance”.

Added “compared to polyurethanes”.

Page 9, paragraph 4, line 2

“solid” changed to “bulk”.

Page 10, figure 1.4

Diagram updated to remove inaccurate intermediate route.

Page 14, paragraph 3, line 3

"are" changed to "can be".

Page 16, paragraph 1, line 3

"methylimidazole" changed to "2-methylimidazole".

Page 16, paragraph 3, line 3

"free standing" updated to "free-standing".

Page 17, paragraph 1, line 3

Removed "an"

Page 18, paragraph 5, line 4

Sentence broken into two after "application".

Page 19, paragraph 3, line 7

"With" removed.

Page 20, paragraph 1, line 1

"preforming" changed to "performing".

Page 20, paragraph 2, line 4

"a" added.

Page 20, paragraph 3, line 2

"Important" changed to "important", duplicate "in" removed.

Page 22, paragraph 1, line 2

"A" removed.

Page 23, paragraph 3, line 1

"extend" changed to "extent".

Page 32, reference 123

Reference updated to correct formatting.

Chapter 2

Page 41, paragraph 1, line 7

"products" changed to "product's".

Page 43, figure 2.3

"cm-1" changed to "cm^{-1}"

Page 44, figure 2.4

Tick marks added.

Page 45, figure 2.5

Tick marks added.

Page 46, figure 2.6

Outline of graph removed, tick marks added.

Page 47, figure 2.7

Tick marks added.

Page 49, figure 2.8

Decimal places removed on time axes, tick marks added.

Page 51, figure 2.10

Decimal places removed on time axes, tick marks added.

Page 53, paragraph 1

Paragraph added to outline reasoning behind why no further modelling of the gas loss behaviour was attempted.

Page 53, figure 2.11

Tick marks added.

Page 55, figure 2.12

"MoS2" changed to "MoS_2", tick marks added.

Page 56, figure 2.13

Decimal places removed on time axes, tick marks added.

Page 58, paragraph 2, line 1

"was" changed to "were".

Page 60, paragraph 2, line 1

"6" changed to "7".

Page 62, figure 2.17

Tick marks added.

Page 62, table 2.1

Figure 2,18 changed to Table 2.1

Chapter 3

Page 68, paragraph 4, line 4

"Cu(BTetC)(DMF)" changed to "Cu_2(BTetC)$(DMF)_2$".

Page 68, paragraph 4, line 5

"and referred to as Cu(BTetC)(DMF) throughout the work for brevity" added.

Page 70, figure 3.1

Tick marks added.

Page 70, paragraph 1, line 6

"(figure 3.11)" added.

Page 71, figure 3.2

Tick marks added.

Page 71, paragraph 1, line 5

"(figure 3.18)" added.

Page 72, figure 3.4

Tick marks added.

Page 72, paragraph 1, line 5

"pendant" changed to "pendent".

Page 73, paragraph 1, line 2

"(figure 3.25)" added.

Page 73, figure 3.5

Tick marks added.

Page 75, figure 3.6

Tick marks added.

Page 77, paragraph 3, line 3

"to the" removed.

Page 78, paragraph 3, line 3

"outlined in figure 3.8" added. New figure 3.8 added to better describe the centrifuged vs uncentrifuged MON processing.

Page 79, paragraph 2, line 2

"(table 3.10)" added.

Page 80, figure 3.9

Renamed to figure 3.9 from 3.8, tick marks added.

Page 81, figure 3.10

Renamed to figure 3.10 from 3.9.

Page 82, table 3.1

Renamed to table 3.1 from figure 3.10.

Page 82, paragraph 1, line 4

", compared to the standard foam," added.

Page 82, paragraph 2, line 1

"Figure 3.10" changed to "Table 3.1"

Page 83, paragraph 2, line 5

"repulsive effects" changed to "poor interaction between MON and polymer".

Page 83, paragraph 4, line 5

"preformed" changed to "performed".

Page 84, paragraph 3, line 1

"figure 3.9" changed to "figure 3.10".

Page 86, paragraph 1, line 1

“6” changed to “7”.

Page 87, title 3.6.2

“Chapter 3.6.2” changed to “3.6.2”.

Page 87, table 3.2

Renamed to table 3.2 from figure 3.11.

Page 88, figure 3.11 and 3.12

Renamed to figure 3.11 from 3.12.

Renamed to figure 3.12 from 3.13, tick marks added.

Page 89, figure 3.13 and 3.14

Renamed to figure 3.13 from 3.14, tick marks added.

Renamed to figure 3.14 from 3.15, tick marks added, border removed.

Page 90, figure 3.15 and 3.16

Renamed to figure 3.15 from 3.16, tick marks added.

Renamed to figure 3.16 from 3.17.

Page 91, figure 3.17 and table 3.3

Renamed to figure 3.17 added to DLS graph, tick marks added.

Figure 3.18 renamed to table 3.3.

Page 92, figure 3.18

Renamed to figure 3.18 from 3.19.

Page 93, figure 3.15 and 3.16

Renamed to figure 3.19 from 3.20, tick marks added.

Renamed to figure 3.20 from 3.21, tick marks added.

Page 94, figure 3.21

Renamed to figure 3.21 from 3.22, tick marks added.

Page 95, figure 3.22 and 3.23

Renamed to figure 3.22 from 3.23, tick marks added.

Renamed to figure 3.23 from 3.24.

Page 96, figure 3.24 and table 3.4

Renamed to figure 3.24 added to DLS graph, tick marks added.

Figure 3.25 renamed to table 3.4.

Page 97, figure 3.25

Renamed to figure 3.25 from 3.24.

Page 98, figure 3.26 and 3.27

Renamed to figure 3.26 from 3.27, tick marks added.

Renamed to figure 3.27 from 3.28, tick marks added.

Page 99, figure 3.28 and 3.29

Renamed to figure 3.28 from 3.29, tick marks added.

Renamed to figure 3.29 from 3.30.

Page 96, figure 3.30, figure 3.31 and table 3.5

Renamed to figure 3.30 from 3.31.

Renamed to figure 3.31 added to DLS graph, tick marks added. Size reduced.

Figure 3.32 renamed to table 3.5.

Chapter 4

Page 104, figure 4.1 and caption, line 3

Tick marks added.

"NH_2-MIL-53 building unit" added.

Page 105, paragraph 2, line 2

"Al" changed to "al".

Page 106, figure 4.2

Tick marks added.

Page 109, paragraph 2, line 2 and line 5.

"the" removed, "was" added.

"spectra (figure 4.8)" added.

Page 110, figure 4.4 and 4.5

Tick marks added.

Page 111, figure 4.6

Tick marks added.

Page 113, table 4.1 and paragraph 1, line 1

Renamed figure 4.8 to table 4.1.

"Figure 4.8" changed to "Table 4.1".

Page 115, paragraph 2, line 9

Italics removed from "Grey".

Page 116, paragraph 3, line 1

"outlines" changed to "outlined".

Page 116, table 4.2

Renamed figure 4.9 to table 4.2

Page 118, figure 4.8

Renamed figure 4.10 to figure 4.8

Added "Satellite peaks present from DMSO at 2.3 and 2.7 pm." to caption.

Page 119, figure 4.9 and figure 4.10

Renamed figure 4.11 to figure 4.9. Tick marks added.

Renamed figure 4.12 to figure 4.10. Tick marks added.

Page 120, figure 4.11 and figure 4.12

Renamed figure 4.13 to figure 4.11.

Renamed figure 4.14 to figure 4.12.

Page 121, figure 3.30, figure 4.13 and table 4.3

DLS graph labelled 4.13 with caption, tick marks added.

Figure 4.15 renamed to table 4.3.

Chapter 5

Page 126, paragraph 2, line 5 and 8

"1,3-propane sultone" changed to "1,3-propansultone".

Removed "if".

Page 128, figure 5.1

Tick marks added.

Page 129, paragraph 2, line 2 and 5

"spectroscopy" inserted.

"reffered" changed to "referred".

Page 129, figure 5.2

Caption updated to "^{1}H NMR spectra of Cu(MA-ABDC)(DMF) 31 % MOF digested with CDCl3/DCl. Residual CHCl3, DMF and Maleic anhydride remain in the pores."

Image size reduced to keep caption and image on one page.

Peak labelling updated.

Page 130, figure 5.3

Tick marks added.

"form" changed to "from" in caption.

Page 131, figure 5.4

Tick marks added.

Page 133, paragraph 1, line 3, and figure 5.5

"analysis (figure 5.5)" inserted.

Tick marks added.

Page 134, figure 5.6 and table 5.1

Scatter graph updated with caption.

Tick marks added.

Figure 5.6 renamed to Table 5.1.

Page 135, figure 5.6 and table 5.1

DLS graph updated with caption.

Tick marks added.

Figure 5.7 renamed to Table 5.2.

Page 136, paragraph 1, line 1 and paragraph 4, line 4

“Whilst” removed.

“owing to” added.

Page 137, paragraph 3, line 6

“As” removed.

Page 139, paragraph 4, line 3

“Though” removed.

Page 140, paragraph 2, line 3

“are” added.

Page 146, paragraph 3, line 2

“funtional” changed to “functional”.

Page 148, figure 5.14 and 5.15

Added “Peaks 5 and 6 omitted for clarity.” to 5.14 caption.

Tick marks added to 5.15.

Page 151, figure 5.18

Tick marks added.

Page 152, paragraph 3, line 1, 7 and 8

“pre” changed to “post”.

“is” changed to “was”.

“has” changed to “had”.

Page 153, paragraph 1, line 1 and Figure 5.19

“are” changed to “were”.

Added “Peaks 5 and 6 omitted for clarity.” to 5.19 caption.

Page 155, paragraph 2, line 3

“If” removed.

Page 161, figure 5.24 and 5.25

Tick marks added.

Page 163, figure 5.26

Tick marks added.

Page 163, table 5.3

Figure 5.29 renamed to Table 5.3.

Chapter 6

Page 172, paragraph 3, line 7

"Whilst" removed.

Page 173, paragraph 3, line 7

"difficultly" changed to "difficulty".

Page 174, paragraph 1, line 1

"Modulated" changed to "modulated".

Chapter 7

No corrections.

Chapter 1

Introduction

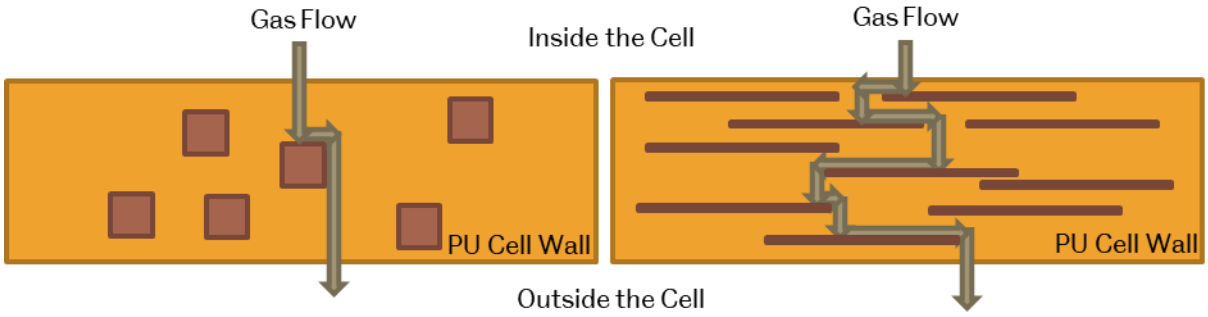

"Had to be me. Someone else might have gotten it wrong."

— Mordin Solus in Mass Effect, by Electronic Arts, an American game company

1.1 - Project Motivation

1.1.1 – Climate Change and Energy Use

The building sector accounts for approximately 25 - 40 % of total global energy consumption[1–5], and approximately 30 - 50 % of greenhouse gas emissions[5–8]. Approximately 40 - 50 % of the total energy consumed in the UK was used for heating in 2016, where domestic heating accounted for at least half that figure.[9–12] The UK has set a target to reduce overall carbon emissions by 80% by 2050.[13,14] The United Nations Environmental Programme (UNEP) has estimated that energy consumption of buildings can be reduced by 30 - 80 %[15] when utilizing technologies such as more efficient boilers[16], newly built homes requiring higher energy performance certification ratings[17], introduction of heat-pumps[18] and solar panels[19]. However, overall, they concluded that the most effective route to reducing CO_2 emissions from heating buildings is to improve insulation.

1.1.2 – Insulation

Effectively insulating a building reduces CO_2 emissions caused by heating (or cooling) the interior of a building by enabling it to remain at a habitable temperature without losing (or gaining) heat to the outdoors.[20–22] A variety of materials can be used for insulation, and largely depend on factors such as geographical location[23], price[23,24], and available space[25]. For example, buildings with extremely low construction footprints will require thin and effective insulation to provide the maximum habitable space possible, requiring highly efficient insulators to be chosen for installation. Whilst buildings based on low budget materials will utilize less efficient, but thicker insulators[22]. Finally, there is a consideration on environmental impact[22] and safety[26–28] of the materials used, but typically with the materials being incorporated into buildings for their lifetime, the reduction in CO_2 from their use outweighs the amount made in their production, and is clearly demonstrated by life cycle analysis[29]. Insulating properties rise sharply when the thickness of insulation is increased, with diminishing economic returns occurring at thicker sizes, as the cost of the materials will outweigh the savings made over the

lifetime of the insulator.[30] This indicates the need for well-designed materials for insulation, rather than very thick insulating layers, in order to achieve the best possible performance.[31] Thermal insulation performance can be described by the material's K-factor,[32] a value used to indicate the thermal conductivity of a material, with a lower value indicating a better thermal insulator.[33] The K-factor is defined as follows:

$$K = \frac{Btu}{h \times ft^2 \times \frac{°F}{in.}}$$

Where Btu is a British Thermal Unit, h is hours, ft is feet, F is Fahrenheit, and in is inches. K-factor is representative of the thermal flow in Btus per hour through a 1 inch, 1 foot square section of insulation for a difference in temperature of 1 °F [33], providing a value in BTU-in/h-ft^2-°F. The value can also be quoted and converted into SI units, $Wm^{-1}K^{-1}$, by multiplying by a factor of 1.73, where W is Watts, m is meters and K is Kelvin.[33]

Radiation, conduction, and convection[33–35] are the primary routes that heat can be transferred through insulating materials. Dependent on the make-up and environment of the material, these factors will have varying levels of contribution to a material's K-factor. Radiation will depend on the transparency and thickness of the material used[34]; conduction is dependent on many factors such as density of the material[36], with higher densities contributing more; and convection is reliant upon if any gas is contained within the insulator[37], what gas is contained[33], and the distance the gas can travel within the insulator. With these requirements in consideration, two materials typically used for insulating buildings are fibrous (*e.g.,* mineral wool), and polymeric foams (*e.g.,* polyurethane and expanded polystyrene foams)[23,25,33,37].

Fibrous insulating materials are typically produced with fibres creating mats or sheets. These mats have low K-factor (such as mineral wool at 0.035-0.045 $Wm^{-1}K^{-1}$[38]) due to their inefficient conduction through the fibre matrix and interruption of any convection of gases inside the mat. Mineral wool currently has a dominant share of the insulation market (approximately 50-

60 %) . [39,40] The production of mineral wool requires the acquisition of minerals or glasses (such as bauxite or recycled glass) that are then melted (at 1330-1450 °C)[21] and spun into fibres.[40] Though the mineral wool itself can be 100 % recycled in principle[40], it is typically considered unrecyclable as a variety of materials are classified as mineral wool, and the condition and cleanliness may vary from sample to sample. These factors make recycling harder, and the use of virgin material more common.[38] Alternative fibrous materials are available such as glass fibres or natural fibres[39], but are used less commonly.

In contrast, polymeric foam insulation can be produced in a larger variety, utilizing different polymers, and creating different forms of final products. [41] For example, polystyrene can be utilized to produce expanded polystyrene (EPS) boards from combined expanded polystyrene beads (K-factor of <0.042 $Wm^{-1}K^{-1}$)[26], or extruded polystyrene (XPS) boards (K-factor of <0.017 $Wm^{-1}K^{-1}$)[42] created from extrusion of polystyrene through a laminating sheet die. Alternatively polyurethane foam (K-factor of <0.24 $Wm^{-1}K^{-1}$)[33], polyisocyanurate foam (K-factor of <0.022 $Wm^{-1}K^{-1}$)[43] or phenolic foam (K-factor of <0.024 $Wm^{-1}K^{-1}$)[43] boards can also be utilized. Overall, the most commonly used material worldwide for polymeric insulation are polyurethanes/polyisocyanurates due to their low thermal conduction, high strength compared to weight, adhesive properties, and durability for installation. [32, 44, 45]

All these polymeric foam insulating materials utilize a polymer to create a solid matrix of bubbles (known as cells) in which a gas, or blowing agent, is contained. If a cell is fully encapsulated by polymer, it can be described as a closed cell, conversely if the cell is missing a wall or is damaged, it is open.

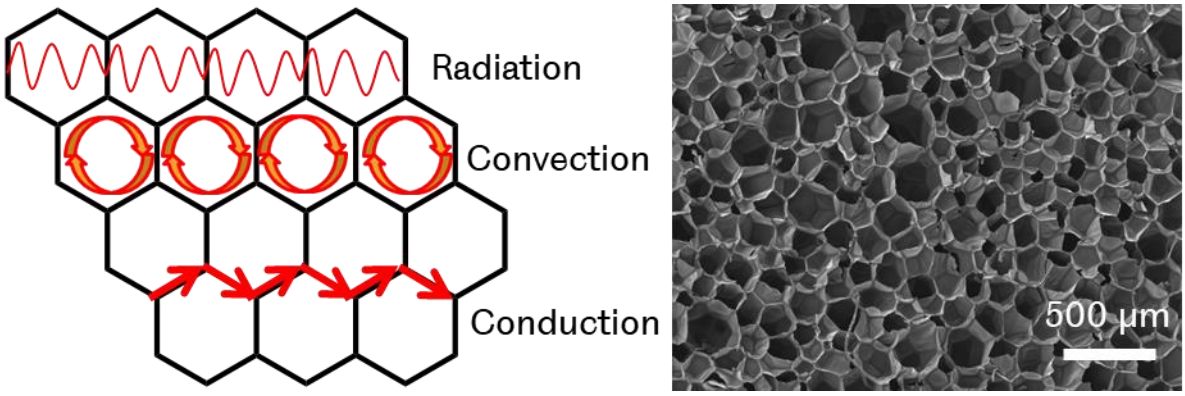

Figure 1.1 A simplified scheme showing the primary modes of heat transfer through a foam compared to an SEM image of a polyisocyanurate foam.

Figure 1.1 demonstrates the methods in which heat is transferred through foam, where typically more than 50% of the heat transfer comes directly from convection of the blowing agent, therefore having a significant impact in the K-factor of the foam insulator[30,46]. Blowing agents for polymer foams have been shown to diffuse out over time, making aging of the insulation properties a barrier to their long term efficiency.[46–49] As the air diffuses into the foam, it lowers the amount of thermal energy needed to create convection, and therefore increases the K-factor of the insulator.[32] The extent of the reduction in efficiency is dependent upon the insulation type, any gas used within the insulator, its application, and environmental factors (such as heating and humidity).[32]

This work is industrially sponsored by Kingspan plc., a world leader in high performance insulating materials, and therefore focuses on rigid polyisocyanurate foam insulation, specifically the aging of these foams and the retention of blowing agent over their lifespan. Therefore, the general motivation for this work is to reduce the loss of blowing agent from Kingspan rigid polyisocyanurate foams.

This chapter discusses polyurethanes and polyisocyanurates in depth and the synthesis of foams and what additives are currently utilized in industry to improve the foams produced. Following this, this chapter describes Metal-Organic Frameworks and Metal-Organic

Nanosheets, and their incorporation into polymers. Finally, this chapter will outline the aims and objectives of this work and how the combination of Metal-Organic Materials and polyisocyanurate foams will achieve these goals.

1.2 – Polyurethanes and Polyisocyanurates

1.2.1 – Background

Of the 350 million tonnes of polymers produced in 2018,[41] 18 million tonnes were classed as polyurethanes (PU),[50, 51] making PU the 6th most common polymer in the world.[51] PUs are an unusual polymer group due to the lack of a specific urethane monomer, and the wide diversity of PU available. A significant number of uses for PU have been established since its initial development in 1937, from seat cushions to glues and coatings. [33, 44] PU can be produced in a variety of forms, such as elastomers, coatings, rigid and flexible foams[44] although PU foams are the major product, with rigid foams encompassing about 50% of PU foam production.[44]

1.2.2 – Synthesis of Polyurethanes and Polyisocyanurates

Urethanes (or carbamates) are produced through the reaction between an isocyanate and an alcohol (as shown in *figure 1.2*). If a diisocyanate and a polyol are used in this reaction then a PU is formed.[52]

Typical PU synthesis can be broken down into two methods: "one-shot"[33,53], where all the chemicals are added simultaneously; or via a pre-polymer process that allows for the polymers to grow to around 20,000 gmol^{-1}, until a later point where chain extenders are used to gain higher molecular weights.[45] The one-shot process allows for fast production of the polymer chains, though will produce an excessive amount of heat and requires the reactivity of all components to be similar in order to effectively incorporate them into the polymer chain as desired. The two-step process can allow for better control over the polymer, but is a slower procedure.[45] The method chosen for production will depend on the end application and the materials used.[44]

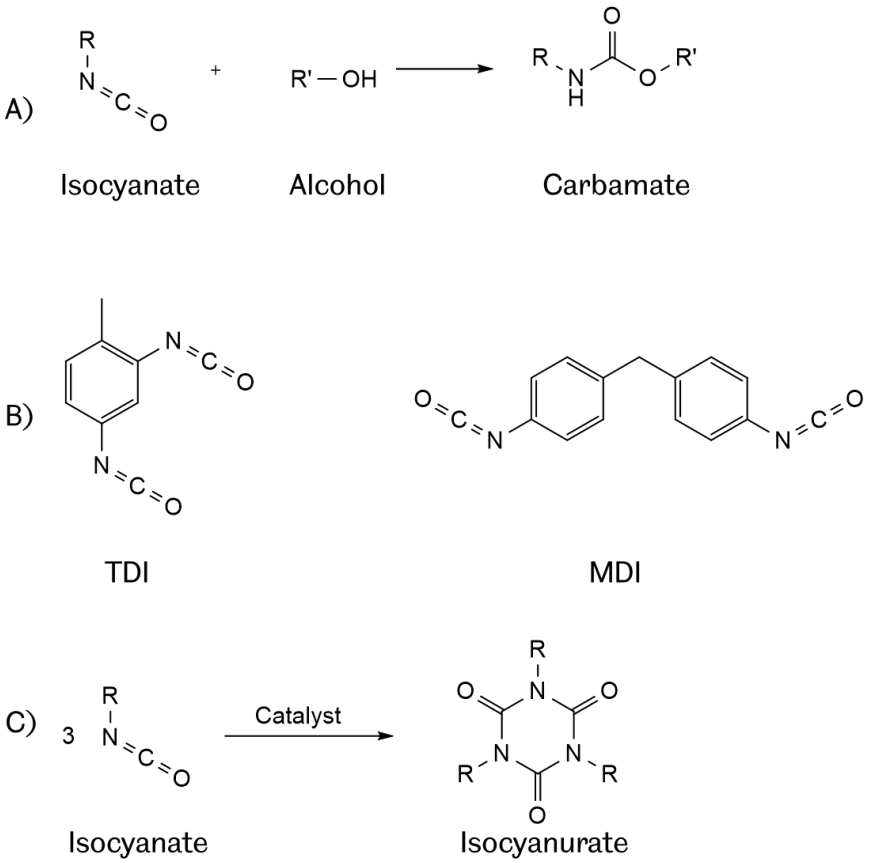

Figure 1.2 A) A generic reaction scheme between an isocyanate and an alcohol to produce a urethane, B) Structures of common isocyanates TDI and MDI, C) Generic reaction scheme for the trimerization of isocyanates into an Isocyanurate[32,33,54]

PU properties can be highly tuned with the choice of alcohols and cyanates. For example, soft PU can be made from long flexible polyols (such as polypropylene glycol [33]), rigid PU from high crosslinking, and hard PU from short chains and high crosslinking.[44,45] Crosslinking of PU can be achieved through a variety of methods, but typically comes from increasing the number of functional groups on the reagents (such as polyols instead of diols, or polyisocyanates instead of diisocyanates).[45] Isocyanates reactivity depends on the chemical structure, but generally, it is found that aromatic isocyanates have a higher rate of reaction, resulting in the two most common diisocyanates used: toluene diisocyanate (TDI) and methylene bis-diphenyl isocyanate (MDI). These diisocyanates have a reactivity of 2 due to their two isocyanate groups (as depicted in figure 1.2).

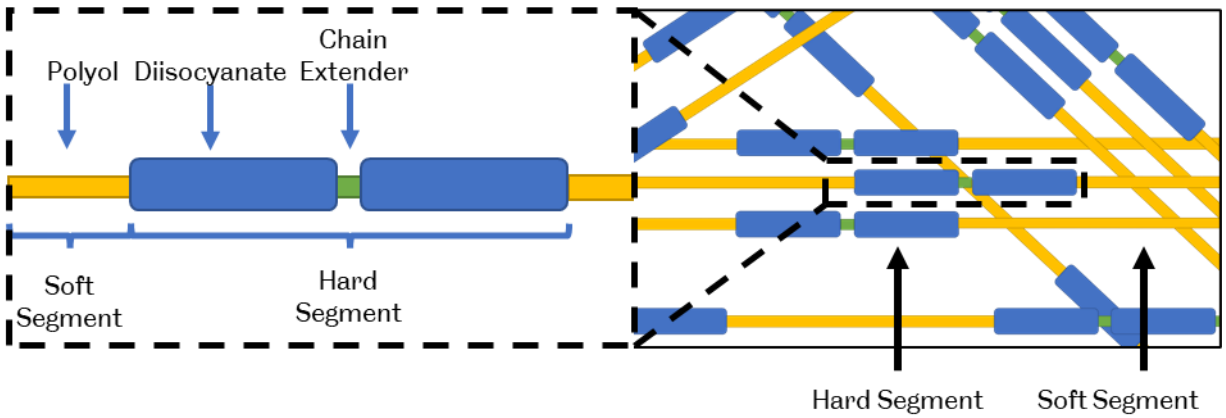

Figure 1.3 An illustration of the hard and soft segments contained within polyurethanes[45]

Polyurethanes consist of hard and soft segment domains within the polymer matrix, demonstrated in figure 1.3.[45] The soft flexible segments (made of the polyol), and hard crystalline segments (made of isocyanate and chain extenders) of the PU can phase separate dependent on what materials and methods are used[52], creating domains that can alter the physical properties of the material dependent on their level of separation.[45] Highly crystalline polyurethanes, therefore containing high amounts of hard segments, result in high thermal stability, resistance to mechanical stress and increased chemical resistance.[33]

Dependent on the polyol used in PU, a wide variety of chemistry and properties can be designed. Reactive properties can arise from the functionality of the hydroxyl group(s) of the polyol, with primary alcohols reacting significantly faster with the isocyanate than secondary or tertiary alcohols.[44] Three main examples of polyols are: polyether polyols (e.g. polyethylene glycol)[54], that are used to increase the PU hydrolytic stability whilst having low cost and viscosities, and produce high quality PU foams;[33] polyester polyols (e.g. caprolactone polyesters), that have high cost and viscosity, but produce PUs with high resistance to cutting and abrasion;[44] and polycarbonate polyols[33], that can give greater oxidative stability and strength, used in many sealants and adhesives.[44] Additionally, the variation in isocyanate in polyurethane synthesis can be expanded through the use of pMDI (where the p suffix denotes an MDI polymer).[32,33,54] pMDI usage can allow for further modification of the desired PU

structure as the functionality of pMDI can be > 2, typically 2.3 – 2.7, compared to MDI's functionality of 2, but also allow for easier manipulation of the isocyanurate as pMDI is liquid at room temperature, being a eutectic mixture of MDI and its higher oligomers, where MDI is a solid.[32,33]

Many different catalysts can be used to promote various reactions within the polyurethane, such as for gelling or trimerization.[54] For promoting the formation of the urethane linkage, the catalysts used work via increasing the bond polarization of the OH or -NCO groups.[44] Very common catalysts include organotins (*e.g.* stannous octoate[55]) and tertiary amines (*e.g.* DABCO [33]). However, these catalysts can cause problems due to their toxicity and typically unpleasant odours.[55]

An isocyanurate link can be generated from trimerization of isocyanates as seen in figure 1.2. Though this reaction does not typically happen under ambient conditions, it requires either heating or specific catalysts (such as trialkylphosphines[33]) to allow the reaction to occur. The primary contrast between urethane and isocyanurate links is that, without the labile hydrogen available, the trimer is much less reactive and has a higher thermal stability.[54] Polymers made from an isocyanurate unit are known as Polyisocyanurates or PIRs, and are typically used for the manufacture of insulating foams due to these higher thermal stabilities, giving better fire retardance, and lower K-values, compared to polyurethanes.[33]

1.2.3 – Polyurethane and Polyisocyanurate Foams

Polymeric foams allow for new properties to be explored and utilized, with typically lower densities, thermal conductivity and rigidity in comparison to bulk polymer structures.[56] The foaming of polymers can be accomplished in a variety of ways, and with PU/PIR there are two major methods: soluble or reactive foaming.[32] These processes correspond with either physical agitation of the polymer matrix with an external force and a source of gas (known as a blowing agent, a gas that expands within the polymer matrix due to the exothermic reaction),

or as a product of the chemical reaction forming the polymer matrix to produce a gas to foam the material.[32]

Commonly, external blowing agents are used to produce foams, where the expansion of a vaporized liquid blowing agent(s) mixed into the PU/PIR mixture occurs due to high temperatures caused by the highly exothermic reaction of trimerization and urethane formation.[33] Additional gas can also be produced during the foaming process in the form of CO_2 as a by-product from isocyanate reactions with water[32] (figure 1.4).

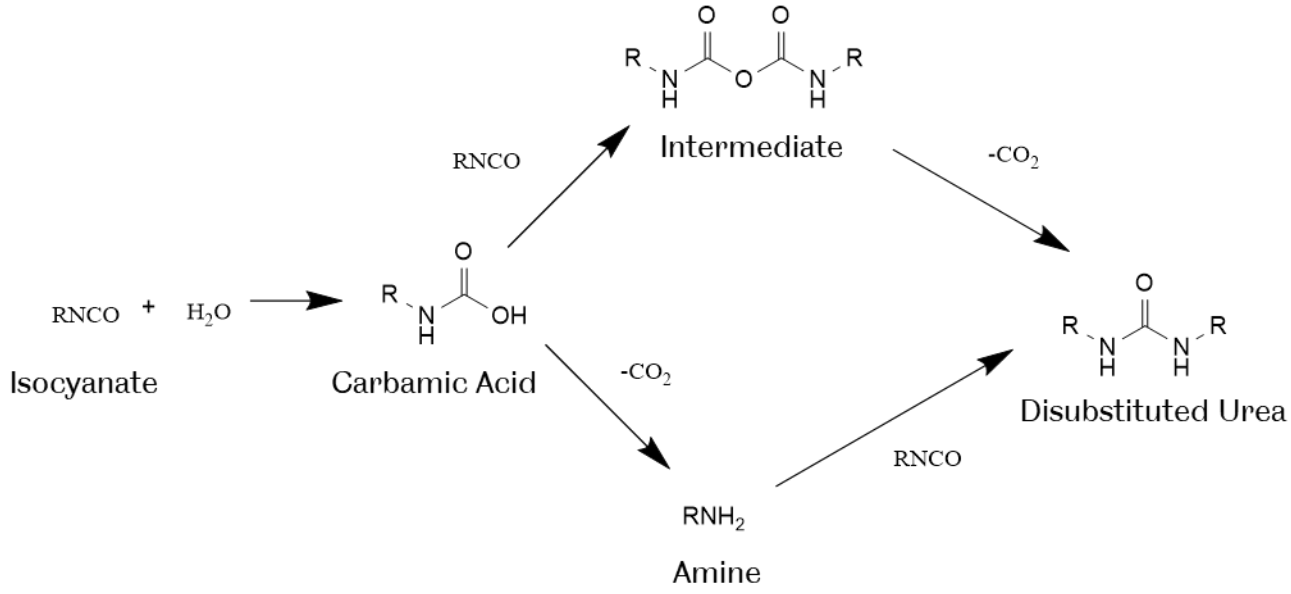

Figure 1.4 Reaction pathway of an isocyanate and water reaction, resulting in the release of CO_2 and, when in presence of additional isocyanate, the production of a urea[54].

An ideal blowing agent for an insulating foam will mix with minimal separation into the reaction mixture as a liquid, with a low boiling point to allow for efficient evaporation during the foaming process, but a high heat capacity to minimise heat transfer once the foam is formed[32,33,54]. Furthermore, an ideal blowing agent will be retained within the foam indefinitely. Though this is not always the case, with loss of blowing agent from the foam arising from any open holes within the foam's cells or diffusion through the polymer membrane. Though, diffusion through the PU/PIR membrane is a complex process involving adsorption, diffusion and desorption.[45]

As a result of legislation being implemented, blowing agents have changed rapidly over the years. Initial blowing agents were chlorofluorocarbons (CFCs) because of their low thermal conductivity, non-combustibility, non-toxicity and ability to mix well with polyurethane precursors[57], but due to the ozone depletion potential of these gases, they have been phased out in favour of hydrocarbons such as isopentane or cyclopentane, and carbon dioxide.[32,54] Pentanes produce several draw backs in their use, namely flammability[57] and higher solubility in PU[58], resulting in increased diffusion across the cell walls. Furthermore, pentanes have roughly 50 % lower insulating performance when compared to CFCs[32]. When carbon dioxide is produced through isocyanate reaction with water as a blowing agent, the reaction can produce significantly higher exotherms, scorching and damaging the foam, alongside increasing the systems viscosity[57].

Foaming relies on three main steps: introduction or production of a gas to the system, expansion of the gas, and stabilization of the bubbles formed.[32] A variety of strategies can be adopted to ensure that the right foam structure is obtained, such as the use of surfactants to stabilize the bubbles/cells formed[33] (with silicone surfactants being very commonly used[32]), or using aromatic isocyanates, as their higher reactivity is needed to produce the network rapidly for stabilization to occur.[50] Foams are typically produced as either rigid or flexible. Rigid foams having their primary use in insulating buildings due to their excellent thermal properties. [32,44,45], and flexible foams in upholstry and the automotive industry.[44] Rigid PIR foams take up a large share of the insulation market[59], specifically in the insulation production due to their high level of closed cells (figure 1.5) that retain blowing agent and lead to low K-values.

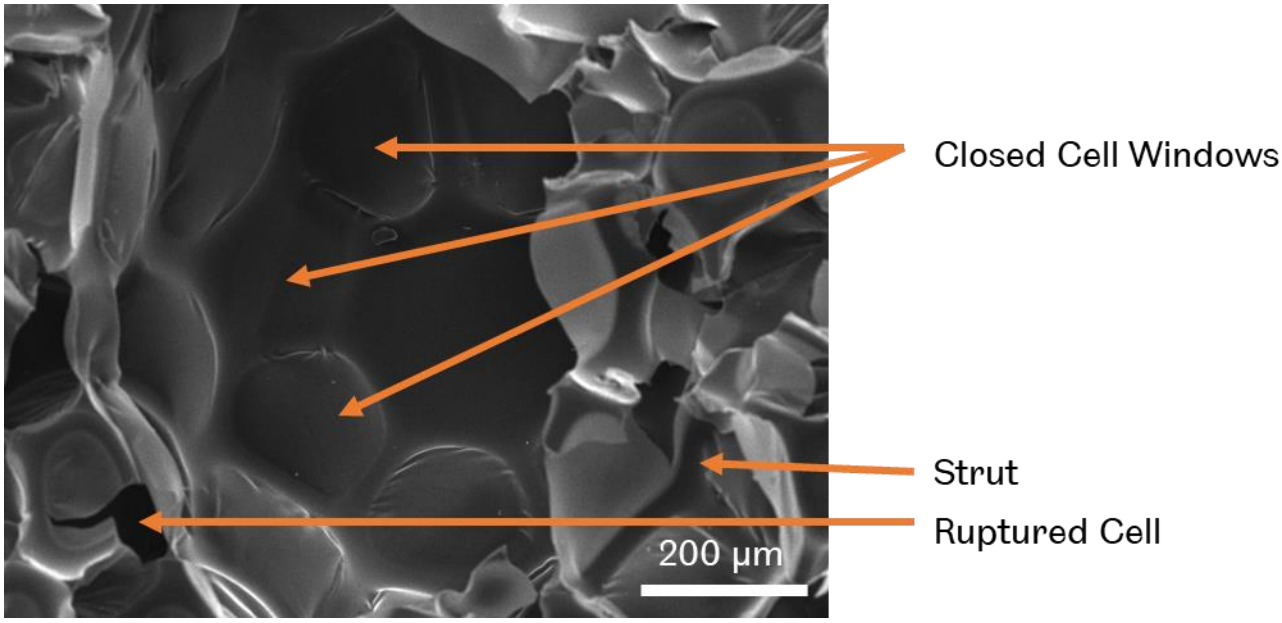

Figure 1.5 SEM image of a PU foam, showing closed cells and a ruptured closed cell

Ambient temperatures can be used to make rigid PIR foams, and they can adhere to a variety of materials.[54] Utilizing shorter high functionality polyols (with a molecular weight of up to around 1000 $gmol^{-1}$), allows for rigid PIR to be produced. The increased number of crosslinks, alongside the trimerization of isocyanates into isocyanurates, causes the polymer chains to have reduced freedom to move, a high glass transition, and the polymer to form a rigid foam.[51] This is important for the synthesis of closed cell foams, so that the windows of each cell remain intact and solid after the blowing process.

Blowing agent is lost from rigid PIR foams over their lifetime, and as a consequence, the foams K-factor will reduce[47–49]. Therefore, blowing agent diffusion has been a focus of study as CFC's were phased out of use[58,60], as modern pentane based blowing agents result in increased risk of loss from the foam due to their decreased vapor pressures[32] and increased solubility in PU[58]. As insulating foams contain a high proportion of closed cells[54], decreasing the foams permeability to blowing agent will retain its thermal properties over the foam's lifetime, as the reduction in loss of the blowing agent gas and uptake of air from the surroundings will maintain the material's K-factor for longer. This can be achieved by increasing the hard segments

content of the foam as the permeability of hard segments is lower for typical blowing agents than soft segments. However, this also alters properties such as processability and cost, making it a sub-optimal choice .[45,61–64] Alternatively, an increased barrier to permeability can be obtained through the use of nanomaterials with high aspect ratios (such as 2D materials), causing a tortuous path for any gases to travel in order to enter/leave any of the foam's cells.[45,52] However, good dispersion is still required for these nanomaterials to be effective in altering the permeability of these foams.[45] Therefore, understanding the types of additives that can be included into PU/PIR will determine design choices for additives for decreasing permeability in the foam.

1.2.4 – Additives in Polyurethanes and Polyisocyanurates

Many different additives can be used with PU/PIR foams as cross linkers, fillers or pigments.[44] A significant proportion of additives for PU/PIR foams are focused on fire retardancy, typically due to their installations within buildings and furniture[65]. Many factors must be considered regarding what additives are used for the PU/PIR made. Primarily, the end application, but also the additives size, shape, load, density and degree of dispersion in the foam itself.[44] A high quality composite is determined by the effective dispersion of the additive in the matrix[52], providing homogeneous properties throughout the polymer matrix, as opposed to agglomerates creating a heterogeneous structure.[66] Dispersion can be influenced by increased mixing of the precursors to ensure better distribution, or through covalently incorporating the additive to ensure favourable interactions.[52] Many additives are inorganic materials, and can include silicones; clays; or simple inorganic clusters.

Silicones are a generic term for siloxane-based polymers that can be flowing oils or solid rubbery products. They can be reactive within the foaming process, reacting with isocyanates via hydroxyl end groups to produce silicone-urethane heteroblock copolymers[33], however are more typically added as a surfactant to stabilize the foaming process, and can alter the closed cell percentage of the final product.[32,33,54] Through the control of the surface tension of the

foaming reaction, bubble size can also be altered for the application, with smaller bubbles typically targeted for rigid insulating foams.[67–69] Though, the prediction of these effects as a function of the silicone structure is not well understood[32], and silicones inclusion into PU/PIR foams is typically limited to 1 % as increased loadings result in diminishing returns, limiting the effects an individual silicone system can have over the foams.[33] Therefore, they are typically used alongside additional additives.

Clays are a cheap and abundant additive that is very frequently added to PU/PIR foams, and can have positive impacts on their flammability[54,65] or mechanical properties[70–72]. Though, in some cases, clays still require modification of surface groups to enhance interaction between the clay additive and the soft/hard segments within the PU/PIR[71]. Clays are typically cell openers for both rigid and flexible foams[73,74], and the increase in viscosity that the addition of clay additives causes can cause issues in processing, as clays can settle out of the foaming mixture due to their size/weight.[33] More recent research has been developed in the use of nanocomposites made from the exfoliation of layered clay structures into highly anisotropic nanoclays[75]. Though the increased anisotropy of these materials can have greater impacts on their properties, they can still significantly increase the viscosity of the foaming mixtures[76].

Many other inorganic types of filler are used to modify the properties of PU/PIR, such as calcium carbonate[32,33,54], molybdenum disulphide[66, 77] and titanium dioxide[33,78]. Though these additives can be cheap and abundant, their use is limited in application, requiring surface modification before foam applications can be achieved.[66] Furthermore, they can settle out of the foaming mixture[32], cause degradation in the strength of foams or increase flammability in some cases.[33]

In conclusion, PUs/PIRs are complex polymers that can be varied through the choice of polyols, isocyanurates, and catalysts. Furthermore, the introduction of blowing agents and surfactants can result in the production of flexible or rigid foams that can be utilized as insulation. These foams then can utilize additives that can lead to a multitude of effects, such as fire retardancy,

improved mechanical strength, and improved retention of blowing agents. Surface chemistry alteration and/or modification of the size to create nanocomposites is becoming necessary for the next generation of PU/PIR composites as cheap and simple additives are modified. Therefore, the use of nanomaterials that are inherently modular in their structures and chemistries would provide an important area of development for the next generation of PU/PIR composites. These nanomaterials could be metal-organic frameworks, and metal-organic nanosheets.

1.3.0 – Metal-Organic Frameworks and Nanosheets

1.3.1 – Background

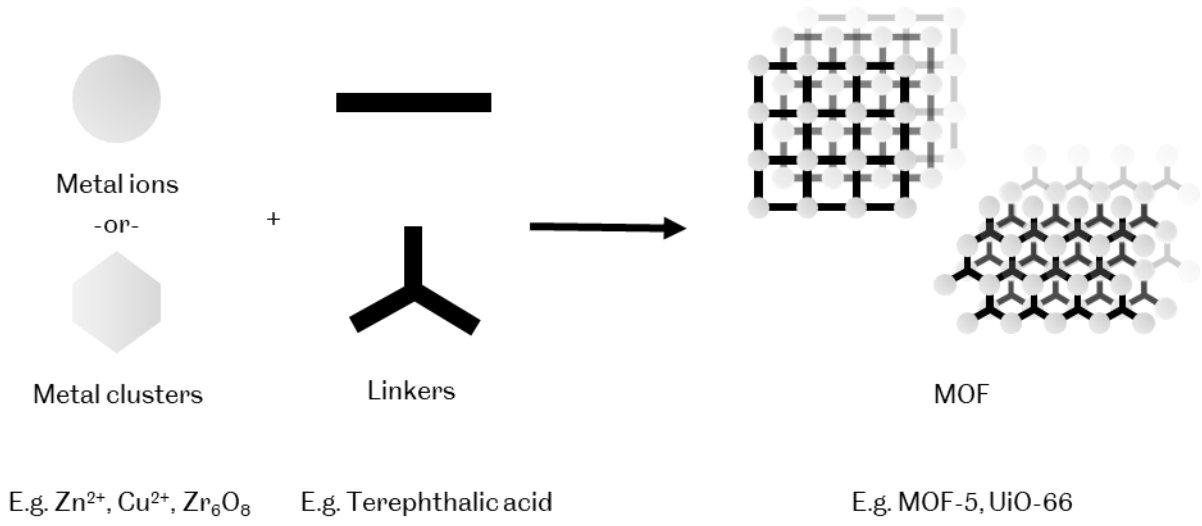

Figure 1.6 Illustrative diagram of modular design of MOFs from metal ions or clusters and linkers

Metal-organic frameworks (MOFs) are co-ordination networks consisting of regularly ordered 3D structures, consisting of organic ligands (figure 1.6) coordinated to metal ions or clusters that contain potential voids.[79–81] MOFs can be synthesized from a variety of metal centres and linkers. For example, linkers can be carboxylate based, N-donor based, and phosphine based, whilst examples of metal centres are Copper, Aluminium, Zinc, Hafnium and Zirconium, with different combinations of linkers and metals resulting in different MOFs.[80,82–86] Furthermore,

dependant on conditions, multiple structures can be synthesized from the same starting materials, for example both ZIF-8 (ball shaped MOFs)[87–89] and ZIF-L (flat leaf shaped MOFs)[90–92] can be synthesized from Zinc and 2-methylimidazole in water.[88] These combinations are also not limited to pure metals or linkers, combinations of different linkers and metals can be contained within a singular MOF synthesized, creating multivariate MOFs.[93–96] This can further be extended to chemical modification of MOF systems, where functional groups can be altered post-synthesis to further diversify the chemistry of MOFs.[97–99] Therefore, this modular approach to the design and synthesis of MOF allows for extremely tuneable materials.[100,101]

Applications of MOFs are wide reaching, with significant study being undertaken on sensing[102–104], catalysis[105–108], gas separation[109–111] and gas storage.[112–114] Many MOFs have been designed with high internal surface areas, large pore sizes, low densities and stable structures.[115] Alongside their chemical structure, the dimensions of MOFs can cause a variety of effects. For example, the properties of a bulk MOF can be significantly different to the nanoparticle in areas such as cellular uptake and porosity.[79]

Whilst a MOF is a 3D structure that can be synthesized in a variety of sizes and shapes, research on the production of 2D MOFs, or metal-organic nanosheets (MONs), has become an increasing trend. MONs are free-standing nanosheets that approach monolayer thicknesses with high aspect ratios, formed of metal ions/clusters and organic ligands as co-ordination networks. MONs offer a material that has vastly different properties from the 3D bulk, and can have varied applications.[101,116] These include, molecular separation[117–120], sensing[121–123] and in electronics[124–126]. If the MOF is designed with strong in-layer bonds (such as co-ordination bonds), but comparatively weaker inter-layer bonds (such as only van der walls forces or hydrogen bonds)[101,127], the layers of the MOF can be pulled apart (known as exfoliation) via a variety of methods to create MONs. This is known as the top-down (figure 1.7) method for creating MONs and can allow for bulk production of nanosheets.

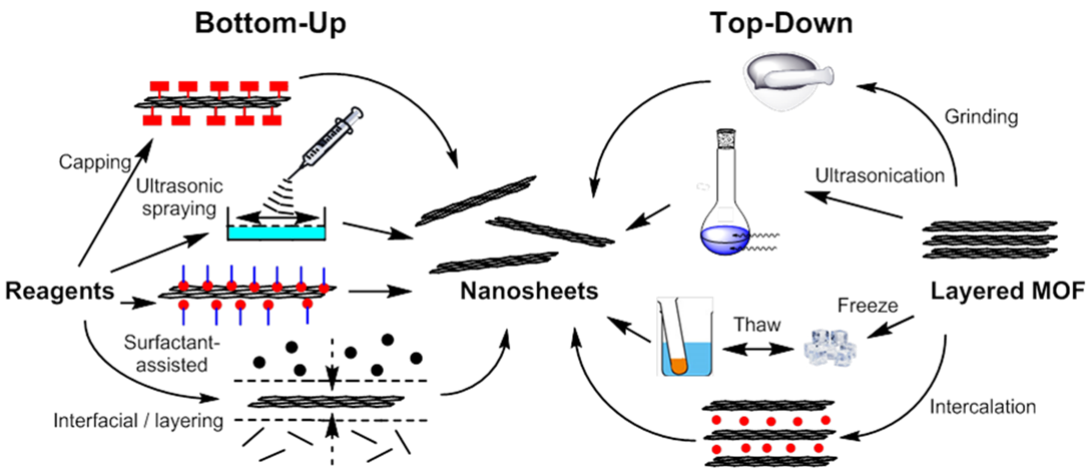

Figure 1.7 Diagram of bottom-up and top-down techniques to produce MONs[101]

Exfoliation of layered MOFs into nanosheets can be achieved in a variety of ways, the most common being using ultrasound energy delivered to a suspension of the MOF through an ultrasonic probe or bath[128]. The energy from ultrasonication produces a variety of effects within a liquid that leads to exfoliation of layered materials. Firstly, the ultrasound waves themselves produce compression and rarefaction cycles, resulting in the creation of microbubbles, or cavities, within the solvent. The rapid collapse of these bubbles can result in high localised temperatures and pressures[129], that if occurring near layered materials, can result in exfoliation. Exfoliation occurs from further microturbulence within the vicinity of the bubble collapse, applying force to the layered material to cause exfoliation[130], or through direct damage to the layered material, causing fragmentation of the structure[131], and therefore exfoliation by extension.

Alternatively, MON's can be synthesised directly from solutions of ligands and metal ions via a bottom-up method which typically uses a capping agent or template to direct synthesis into two-dimensions.[100,101] The bottom-up method can be applied via directing growth along one crystal plane, such as at interfaces (liquid/air or liquid liquid), where growth is restricted at the interface between layers, resulting in enhanced control over the MON thickness. For

example, Rodena *et. al.* utilize a liquid interface between Copper and terephthalic acid linkers to produce CuBDC nanosheets approaching monolayer thicknesses[116].

Alternatively, bottom-up methods could utilize arresting crystallization along a plane through the use of secondary building units that prefer a two-dimensional formation, resulting in the production of nanosheets. For example, the work by Kitagawa *et. al.* utilized the 5,10,15,20-tetrakis(4-carboxyphenyl)porphyrin (TCPP) linker to produce nanosheets of a thickness of ~15 nm without the need for further exfoliation[132].

Finally, restricting the stacking of layers such as with surfactants or ions can result in the production of MONs, where for example Zhao *et. al.* expand on the synthesis of TCPP MONs by utilizing polyvinylpyrrolidone as a surfactant to restrict the growth of the MON, resulting in sub 10 nm MONs[133].

In conclusion, MOFs are extremely tuneable materials that can have their chemistries, sizes and shapes altered through the design of the system. This can be further extended to MONs, with increased anisotropy, they are a new frontier for application. Both MOFs and MONs can be utilized within polymer systems to further expand their applications.

1.3.2 – MOFs/MONs and Polymers

Whilst MOFs and MONs have significant advantages in both design and application as previously discussed, they typically suffer from poor processability[134,135]. With some exceptions, such as MOF glasses[136,137], the brittle powders of MOFs initially were not easily mass produced or combined into singular monoliths for application[138,139]. Though improvements have been developed resulting in some commercialization of MOFs being developed, such as through continuous flow synthesis[140], their high expense and low volumes result in limited market use [141]. The integration of MOFs into polymers has widely been adopted to produce mixed-matrix membranes (MMMs)[105,142,143]. These MMMs combine polymers and MOFs (through simple distribution, or reactions into the polymer membrane) to produce composites that have

higher processability than pure MOFs, with higher selectivity/permeability than pure polymers[111,144].

MOFs can be introduced into a polymer in a variety of ways and at different of stages of polymer synthesis. MMMs are typically produced via the use of a solvent to dissolve a premade polymer and suspend a MOF, then mixing the solutions prior to removal of the solvent to create an MMM[109,145]. This is favoured due to the reduction in viscosity of the polymer and to aid in the dispersion of the MOFs through the polymer matrix, which can then be processed and cured to remove any remaining solvent.[146] These composites allow access to many different polymer architectures and integration within MOFs to produce targeted MMMs for application.[138,146]

For the polymers and MOFs to be combined, design choices to improve the compatibility between the MOF and polymer need to be considered. The MOF and polymer chemistry[147,148], where for example, effectively designed non-covalent interactions can increase adhesion between MOF and polymer[109]. The MOF size/shape[148–150], and polymer or MOF flexibilty[151–153] and loading[145,150,154] can also have significant effects. For example, Armstrong *et. al.* demonstrated that the interaction between the MOF ZIF-8 and electrospun poly(ethylene oxide) can be influenced over the size and shape of the ZIF produced[155]. ZIFs at loadings higher than 33 % demonstrate significant increases in N_2 uptake due to emergent MOF structure at the polymer surface. Additionally, ZIF-8 MOFs that have a diameter larger than the diameter of the spun fibre did not exhibit emergence at the surface, demonstrating the complex interactions between size, shape and surface effects between MOF and polymer.

If the polymer/MOF system is incompatible (for example a highly hydrophobic MOF in a highly hydrophilic polymer[148]), then aggregation[156–158], void formation[148,158] and MOF sedimentation[156] will occur, creating an inferior composite to one with homogenous dispersion of MOF. Additionally, in some cases matching too well can cause polymer surrounding the MOF to rigidify[159–161], resulting in hard regions surrounding the MOF and preventing applications such

as molecular separation from performing optimally. In the context of this work, MOFs have had some introductions into polyurethane already, with a significant amount of research looking at MOFs and polyurethane elastomers. Typically, MOFs (*e.g.* UiO-66[162,163], ZIF-8[164,165], MIL-101[162]) are introduced into PU's for separation applications, improving the selectivity or rejection of undesirables within flow streams[166,167]. For example, PU membranes embedded with UiO-66 or MIL-101 have been utilized by Rodrigues *et. al.* to separate O_2/N_2 and CO_2/N_2[162].

The tunability of nanoscale MOFs makes the ideal candidates to optimise interactions between the MOF and polymer in order to reduce aggregation and encouraging a more homogenous dispersion and so improved performance in applications, such as gas seperation[148,168–170]. Nanosheets offer a good alternative to MOFs for use in MMM as their nanoscale dimensions offer enhanced incorporation into polymers when compared to MOFs[120]. Specifically, the utilization of MONs can provide improved dispersion through polymers[117], and promoted interaction due to their increased surface areas, for example in the Foster group, the inclusion of Zn(TCPP) nanosheets in organic solar cells demonstrated improved crystallinity of the organic polymer in the solar cell and improvement in the efficiency of devices produced[124].

Furthermore, the large aspect ratios of the nanosheets can be used to creates tortuous paths around which molecules must diffuse, an important property in molecular separation and barrier applications.[127,171,172] Building on the extensive work on MOFs for MMM, MON/polymer membranes have had significant success in being applied for a range of molecular separation applications, for example CO_2/N_2 separation (with ZIF-C nanosheets and Pebax)[117] or CO_2/CH_4 separation (with ZIF-8 nanosheets and Matrimid, or Cu(BDC) nanosheets and Polyimide)[118,120].

In conclusion, the addition of MOFs/MONs to polymers presents a unique opportunity to create advanced composites for a myriad of applications but have been used extensively in gas separation. As there is precedence for the incorporation of MOFs into PU to limit the transport

of molecules across the polymer membrane, there is opportunity to utilize MONs to prevent transport of gas through rigid PIR foam.

1.4.0 – Project Context, Aims and Objectives

1.4.1 – Project Context

As previously discussed, with increasing focus on climate change, and the 40 – 50 % of energy used in buildings purely for temperature control [9,44], insulating materials are on the forefront of tackling the issues of climate change. Insulating polymer foams can suffer from the diffusion of their blowing agents out of the material, resulting in lower insulating efficiency. Rigid PIR foams with better blowing agent retention are therefore needed to increase the lifetime of insulated panels. This could be achieved through the use of additives within PIR foams to either prevent, or slow down, the rate of blowing agent diffusion. Whilst research into the diffusion of blowing agent from PU foams has had significant study[58,60] , work investigating prevention of this diffusion between cells is limited, demonstrating the need for research into this area.

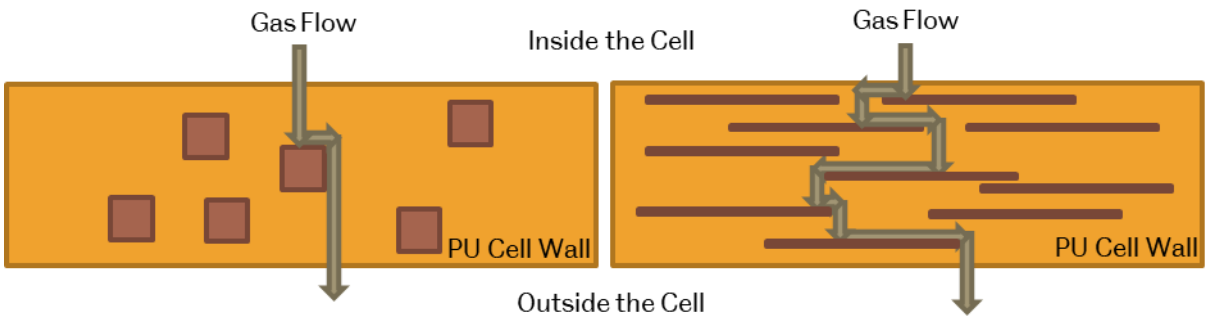

Figure 1.8 Tortuous paths generated using bulky fillers (left) and high aspect ratio fillers (right)

Two-dimensional materials show promise in being the ideal solution to this problem. With high aspect ratios, they can be introduced to the polymer matrix to produce a tortuous path for any diffusing gas (Figure 1.8). However, the interactions between the individual polymer matrixes and the 2D material need to be appropriately designed so that the interfacial adhesion and dispersion of the fillers allow for optimal properties to be reached.

MOFs and MONs present themselves as the ideal targets for understanding what effects additives can have on combatting the loss of blowing agent from rigid PIR foams. Highly tuneable MOFs can be effectively studied for their interactions in a polyisocyanurate matrix, allowing for effects from different metals, linkers, and linker functionalities to be explored to develop the ideal filler material. If the MOFs chosen can be exfoliated, the resulting MONs can then be used with their high aspect ratio to further increase the tortuosity of the path, whilst retaining the interaction seen in the MOF produced. Whilst MOFs and MONs are porous materials, their pore sizes are typically tuned to gases such as H_2[173], N_2[174] or CO_2[175] as described in the previous section, the blowing agents (cyclopentane and isopentane) used within the synthesis of rigid PIR foams are significantly larger. Additionally, by targeting dense MOFs/MONs to produce composites, a tortuous path can be exploited for PIR foam blowing agents.

This research is partially sponsored by Kingspan Insulation ltd, a global leader in high performance insulating materials, so will focus on the development of MOF/MON fillers to be used within a single formula of the company's lines of insulating boards. These are polyisocyanurate based boards used as wall cavity insulation.

1.4.2 – Project Aims and Objectives

The overall aims of the project was to reduce the loss of the blowing agent (isopentane and cyclopentane) from the rigid PIR foams produced by Kingspan for use as insulation. The reduction of the loss of blowing agent was to be achieved through exploring addition of MOFs and MONs within the polymer walls in order to create a tortuous path for the gas to take.

Additionally, this project aimed to modify any MONs produced to understand how they interact with rigid PIR foams, and improve any composites produced. These modifications were through the alteration of functional groups on the surface of MONs either with simple small molecules, or through polymerization of additional polymer chains.

This thesis is structured to test the hypotheses: can MOFs and MONs be used as an additive for rigid PIR foams to reduce the loss of blowing agents and improve long term performance? Therefore, the chapters of this thesis are presented to address key questions in order to test this hypothesis:

1) How can the loss of blowing agent from a Kingspan rigid PIR foam be tested both accurately and repeatably over short time scales? (**Chapter 2**)
2) How do paddle-wheel based copper MOFs and MONs effect the loss of blowing agent during accelerated aging? (**Chapter 3**)
3) How do NH_2-MIL-53 MOFs and MONs effect the loss of blowing agent during accelerated aging? (**Chapter 4**)
4) Can the Cu(ABDC)(DMF) paddle-wheel based MOF be modified to alter the amine functionality of the MOF, and what effect does this have on the MONs? (**Chapter 5**)

The final chapter will draw together insights from across the thesis, conclude to what extent we have answered these questions and address the future potential of MONs as additives in rigid PIR foams.

References

1 X. Li, Y. Zhou, S. Yu, G. Jia, H. Li and W. Li, *Energy*, 2019, **174**, 407–419.

2 S. Chen, G. Zhang, X. Xia, Y. Chen, S. Setunge and L. Shi, *Sustain. Energy Technol. Assessments*, 2021, **45**, 101212.

3 J. Wu, Z. Lian, Z. Zheng and H. Zhang, *Sustain. Cities Soc.*, 2020, **53**, 101893.

4 H. Duan, S. Chen and J. Song, *Energy*, 2022, **245**, 123290.

5 M. Bourdeau, X. qiang Zhai, E. Nefzaoui, X. Guo and P. Chatellier, *Sustain. Cities Soc.*, 2019, **48**, 101533.

6 S. Seyedzadeh, F. P. Rahimian, I. Glesk and M. Roper, *Vis. Eng.*, 2018, **6**, 5.

7 I. G. Dino and C. Meral Akgül, *Renew. Energy*, 2019, **141**, 828–846.

8 D. Ürge-Vorsatz, R. Khosla, R. Bernhardt, Y. C. Chan, D. Vérez, S. Hu and L. F. Cabeza, *Annu. Rev. Environ. Resour.*, 2020, **45**, 227–269.

9 Z. Abdollahnejad, S. Miraldo, F. Pacheco-Torgal and J. B. Aguiar, *Eur. J. Environ. Civ. Eng.*, 2017, **21**, 412–429.

10 N. Bertelsen and B. V. Mathiesen, *Energies*, , DOI:10.3390/en13081894.

11 R. Gross and R. Hanna, *Nat. Energy*, 2019, **4**, 358–364.

12 A. Chapman, K. Itaoka, K. Hirose, F. T. Davidson, K. Nagasawa, A. C. Lloyd, M. E. Webber, Z. Kurban, S. Managi, T. Tamaki, M. C. Lewis, R. E. Hebner and Y. Fujii, *Int. J. Hydrogen Energy*, 2019, **44**, 6371–6382.

13 M. Shatat, D. Tetlow and S. Riffat, *Int. J. Low-Carbon Technol.*, 2015, **10**, 119–130.

14 F. Varriale and P. Jones, *Indoor Built Environ.*, 2016, **25**, 1096–1113.

15 X. C. Scanlon, *United Nations Environment Programme Annual Report 2009*, Nairobi,

2010.

16 J. Rosenow, P. Guertler, S. Sorrell and N. Eyre, *Energy Policy*, 2018, **121**, 542–552.

17 P. Symonds, N. Verschoor, Z. Chalabi, J. Taylor and M. Davies, *J. Urban Heal.*, 2021, **98**, 362–374.

18 S. Kokoni and M. Leach, *Renew. Sustain. Energy Transit.*, 2021, **1**, 100009.

19 A. Hu, S. Levis, G. A. Meehl, W. Han, W. M. Washington, K. W. Oleson, B. J. van Ruijven, M. He and W. G. Strand, *Nat. Clim. Chang.*, 2016, **6**, 290–294.

20 S. Roberts, *Energy Policy*, 2008, **36**, 4482–4486.

21 S. Schiavoni, F. D'Alessandro, F. Bianchi and F. Asdrubali, *Renew. Sustain. Energy Rev.*, 2016, **62**, 988–1011.

22 D. Densley Tingley, A. Hathway and B. Davison, *Build. Environ.*, 2015, **85**, 182–189.

23 I. Siksnelyte-Butkiene, D. Streimikiene, T. Balezentis and V. Skulskis, *Sustainability*, 2021, **13**, 737.

24 T. Dickson and S. Pavía, *Renew. Sustain. Energy Rev.*, 2021, **140**, 110752.

25 W. Villasmil, L. J. Fischer and J. Worlitschek, *Renew. Sustain. Energy Rev.*, 2019, **103**, 71–84.

26 Q. L. Zuo, Y. J. Wang and J. S. Li, *IOP Conf. Ser. Mater. Sci. Eng.*, 2018, **359**, 012041.

27 W. An, J. Sun, K. M. Liew and G. Zhu, *Mater. Des.*, 2016, **99**, 500–508.

28 L. Jiang, H. Xiao, W. An, Y. Zhou and J. Sun, *Energy Build.*, 2014, **82**, 243–249.

29 S. Füchsl, F. Rheude and H. Röder, *Clean. Mater.*, 2022, **5**, 100119.

30 M. S. Al-Homoud, *Build. Environ.*, 2005, **40**, 353–366.

31 J. Yuan, *Sustain.*, 2018, **10**, 2835.

32 P. Bethevas, J. Bicerano, R. van den Bosch, J. Fosnaugh, R. de Genova, M. Brown, F. Casati, C. P. Christenson, P. Clavel and W. Farrissey, *Polymeric Foams: Mechanisms and Materials*, CRC Press LLC, 1st edn., 2004.

33 M. Szycher and P. D, *Szycher's Handbook of Polyurethanes, Second Edition*, CRC Press, 2012, vol. 37.

34 L. Glicksman, M. Schuetz and M. Sinofsky, *Int. J. Heat Mass Transf.*, 1987, **30**, 187–197.

35 F. Hu, S. Wu and Y. Sun, *Adv. Mater.*, 2019, **31**, 1801001.

36 B. G. Rennex, *J. Therm. Insul.*, 1979, **3**, 37–61.

37 P. J. Burns, L. C. Chow and C. L. Tien, *Int. J. Heat Mass Transf.*, 1977, **20**, 919–926.

38 O. Väntsi and T. Kärki, *J. Mater. Cycles Waste Manag.*, 2014, **16**, 62–72.

39 J. L. Sohn, P. P. Kalbar, G. T. Banta and M. Birkved, *J. Clean. Prod.*, 2017, **142**, 3243–3253.

40 A. C. Schmidt, A. A. Jensen, A. U. Clausen, O. Kamstrup and D. Postlethwaite, *Int. J. Life Cycle Assess.*, 2004, **9**, 53–66.

41 T. Hees, F. Zhong, M. Stürzel and R. Mülhaupt, *Macromol. Rapid Commun.*, 2019, 40, 1800608.

42 C. V. Vo, F. Bunge, J. Duffy and L. Hood, *Cell. Polym.*, 2011, **30**, 137–156.

43 S. A. Omer, S. B. Riffat and G. Qiu, *Build. Serv. Eng. Res. Technol.*, 2007, **28**, 275–293.

44 J. O. Akindoyo, M. D. H. Beg, S. Ghazali, M. R. Islam, N. Jeyaratnam and A. R. Yuvaraj, *RSC Adv.*, 2016, 6, 114453–114482.

45 M. Joshi, B. Adak and B. S. Butola, *Prog. Mater. Sci.*, 2018, 97, 230–282.

46 S. Alsoy, *J. Cell. Plast.*, 1999, **35**, 247–271.

47 H. Zhang, W.-Z. Fang, Y.-M. Li and W.-Q. Tao, *Appl. Therm. Eng.*, 2017, **115**, 528–538.

48 U. Berardi and M. Naldi, *Energy Build.*, 2017, **144**, 262–275.

49 M. T. Bomberg, M. K. Kumaran, M. R. Ascough and R. G. Sylvester, *J. Therm. Envel. Build. Sci.*, 1991, **14**, 241–267.

50 Z. S. Petrovic, *Polym. Rev.*, 2008, **48**, 109–155.

51 D. Simón, A. M. Borreguero, A. de Lucas and J. F. Rodríguez, *Waste Manag.*, 2018, 76, 147–171.

52 A. Kausar, *Polym. - Plast. Technol. Eng.*, 2017, 56, 1468–1486.

53 J. Joy, J. Abraham, J. Sunny, J. Mathew and S. C. George, *Polym. Test.*, 2020, **87**, 106429.

54 Kaneyoshi Ashida, *Polyurethane and Related Foams*, CRC Press LLC, 1st edn., 2006, vol. 58.

55 W. Pengjam, B. Saengfak, S. Ekgasit and N. Chantarasiri, *J. Appl. Polym. Sci.*, 2012, **123**, 3520–3526.

56 C. Mougel, T. Garnier, P. Cassagnau and N. Sintes-Zydowicz, *Polymer (Guildf).*, 2019, **164**, 86–117.

57 K. Ashida, *Polyurethane and Related Foams*, CRC Press, 2006.

58 H. Fleurent and S. Thijs, *J. Cell. Plast.*, 1995, **31**, 580–599.

59 V. Dolomanova, C. M. R. Jens, L. R. Jensen, R. Pyrz and A. B. Timmons, *J. Cell. Plast.*, 2011, **47**, 81–93.

60 I. R. Shankland, *J. Cell. Plast.*, 1993, **29**, 114–131.

61 D. K. Chattopadhyay and K. V. S. N. Raju, *Prog. Polym. Sci.*, 2007, 32, 352–418.

62 A. P. Isfahani, B. Ghalei, R. Bagheri, Y. Kinoshita, H. Kitagawa, E. Sivaniah and M. Sadeghi,

J. Memb. Sci., 2016, **513**, 58–66.

63 K. Ulubayram and N. Hasirci, *Polymer (Guildf).*, 1992, **33**, 2084–2088.

64 T. K. Chen, T. S. Shieh and J. Y. Chui, *Macromolecules*, 1998, **31**, 1312–1320.

65 A. Hejna, *Materials (Basel).*, 2021, **14**, 4826.

66 R. Vaithylingam, M. N. M. Ansari and R. A. Shanks, *Polym. - Plast. Technol. Eng.*, 2017, 56, 1528–1541.

67 X. . Zhang, C. . Macosko, H. . Davis, A. . Nikolov and D. . Wasan, *J. Colloid Interface Sci.*, 1999, **215**, 270–279.

68 M. S. Han, S. J. Choi, J. M. Kim, Y. H. Kim, W. N. Kim, H. S. Lee and J. Y. Sung, *Macromol. Res.*, 2009, **17**, 44–50.

69 A. H. Baferani, R. Keshavarz, M. Asadi and A. R. Ohadi, *Adv. Polym. Technol.*, 2018, **37**, 71–83.

70 T. U. Patro, G. Harikrishnan, A. Misra and D. V. Khakhar, in *Polymer Engineering and Science*, Wiley-Blackwell, 2008, vol. 48, pp. 1778–1784.

71 X. Cao, L. James Lee, T. Widya and C. Macosko, *Polymer (Guildf).*, 2005, **46**, 775–783.

72 A. Kausar, *Polym. Plast. Technol. Eng.*, 2018, **57**, 346–369.

73 G. Harikrishnan, T. U. Patro and D. V. Khakhar, *Ind. Eng. Chem. Res.*, 2006, **45**, 7126–7134.

74 J. Zou, Y. Lei, M. Liang and H. Zou, *J. Polym. Res.*, 2015, **22**, 201.

75 Y. H. Kim, S. J. Choi, J. M. Kim, M. S. Han, W. N. Kim and K. T. Bang, *Macromol. Res.*, 2007, **15**, 676–681.

76 T. Widya and C. W. Macosko, *J. Macromol. Sci. Part B*, 2005, **44**, 897–908.

77 H. Ribeiro, J. P. C. Trigueiro, M. C. Lopes, J. J. Pedrotti, C. F. Woellner, W. M. Silva, G. G. Silva and P. M. Ajayan, *J. Appl. Polym. Sci.*, 2018, **135**, 46560.

78 L. He, F. Liu, T. Liu, F. Chen and P. Fang, *Wuhan Univ. J. Nat. Sci.*, 2012, **17**, 377–382.

79 S. Wang, C. M. McGuirk, A. D'Aquino, J. A. Mason and C. A. Mirkin, *Adv. Mater.*, 2018, 30, 1800202.

80 W. Lu, Z. Wei, Z. Y. Gu, T. F. Liu, J. Park, J. Park, J. Tian, M. Zhang, Q. Zhang, T. Gentle, M. Bosch and H. C. Zhou, *Chem. Soc. Rev.*, 2014, **43**, 5561–5593.

81 S. R. Batten, N. R. Champness, X.-M. Chen, J. Garcia-Martinez, S. Kitagawa, L. Öhrström, M. O'Keeffe, M. Paik Suh and J. Reedijk, *Pure Appl. Chem.*, 2013, **85**, 1715–1724.

82 N. Stock and S. Biswas, *Chem. Rev.*, 2012, **112**, 933–969.

83 A. Kirchon, L. Feng, H. F. Drake, E. A. Joseph and H. C. Zhou, *Chem. Soc. Rev.*, 2018, **47**, 8611–8638.

84 M. Ding, X. Cai and H. L. Jiang, *Chem. Sci.*, 2019, **10**, 10209–10230.

85 X. Liu, L. Zhang and J. Wang, *J. Mater.*, 2021, **7**, 440–459.

86 Y. R. Lee, J. Kim and W. S. Ahn, *Korean J. Chem. Eng.*, 2013, **30**, 1667–1680.

87 J. Abdi and H. Abedini, *Chem. Eng. J.*, 2020, **400**, 125862.

88 Y. Lo, C. H. Lam, C. W. Chang, A. C. Yang and D. Y. Kang, *RSC Adv.*, 2016, **6**, 89148–89156.

89 W. Morris, C. J. Stevens, R. E. Taylor, C. Dybowski, O. M. Yaghi and M. A. Garcia-Garibay, *J. Phys. Chem. C*, 2012, **116**, 13307–13312.

90 R. Chen, J. Yao, Q. Gu, S. Smeets, C. Baerlocher, H. Gu, D. Zhu, W. Morris, O. M. Yaghi and H. Wang, *Chem. Commun.*, 2013, **49**, 9500–9502.

91 E. Shamsaei, Z. Qing Tang, F. B. de Souza, E. Hosseini, E. Benhelal, A. Habibnejad

Korayem and W. Duan, *Constr. Build. Mater.*, 2021, **272**, 122015.

92 C. J. Wijaya, S. Ismadji, H. W. Aparamarta and S. Gunawan, *Molecules*, , DOI:10.3390/molecules26154416.

93 H. Deng, C. J. Doonan, H. Furukawa, R. B. Ferreira, J. Towne, C. B. Knobler, B. Wang and O. M. Yaghi, *Science*, 2010, **327**, 846–850.

94 J. Li, Y. Wang, Y. Yu and Q. Li, *Chinese Chem. Lett.*, 2018, **29**, 837–841.

95 L. J. Wang, H. Deng, H. Furukawa, F. Gándara, K. E. Cordova, D. Peri and O. M. Yaghi, *Inorg. Chem.*, 2014, **53**, 5881–5883.

96 Z. Ji, T. Li and O. M. Yaghi, *Science*, 2020, **369**, 674–680.

97 S. M. Cohen, *Chem. Rev.*, 2012, **112**, 970–1000.

98 S. Mandal, S. Natarajan, P. Mani and A. Pankajakshan, *Adv. Funct. Mater.*, 2021, 31, 2006291.

99 K. K. Tanabe and S. M. Cohen, *Chem. Soc. Rev.*, 2011, **40**, 498–519.

100 A. Pustovarenko, M. G. Goesten, S. Sachdeva, M. Shan, Z. Amghouz, Y. Belmabkhout, A. Dikhtiarenko, T. Rodenas, D. Keskin, I. K. Voets, B. M. Weckhuysen, M. Eddaoudi, L. C. P. M. de Smet, E. J. R. Sudhölter, F. Kapteijn, B. Seoane and J. Gascon, *Adv. Mater.*, 2018, **30**, 1–8.

101 D. J. Ashworth and J. A. Foster, *J. Mater. Chem. A*, 2018, **6**, 16292–16307.

102 Y. Liu, X.-Y. Xie, C. Cheng, Z.-S. Shao and H.-S. Wang, *J. Mater. Chem. C*, 2019, **7**, 10743–10763.

103 E. A. Dolgopolova, A. M. Rice, C. R. Martin and N. B. Shustova, *Chem. Soc. Rev.*, 2018, **47**, 4710–4728.

104 Z. Wei, W. Zhu, Y. Li, Y. Ma, J. Wang, N. Hu, Y. Suo and J. Wang, *Inorg. Chem.*, 2018, **57**, 8422–8428.

105 A. Kathuria, N. Brouwers, M. Buntinx, T. Harding and R. Auras, *J. Appl. Polym. Sci.*, 2018, **135**, 1–8.

106 J. García-Álvarez, A. Presa Soto, G. A. Carriedo and L. Quirós-Montes, *Green Chem.*, , DOI:10.1039/c9gc02624j.

107 H. C. Lee, M. Antonietti and B. V. K. J. Schmidt, *Polym. Chem.*, 2016, **7**, 7199–7203.

108 Q. Wang and D. Astruc, *Chem. Rev.*, 2020, **120**, 1438–1511.

109 Y. Zhang, X. Feng, S. Yuan, J. Zhou and B. Wang, *Inorg. Chem. Front.*, 2016, **3**, 896–909.

110 Z. Kang, L. Fan and D. Sun, *J. Mater. Chem. A*, 2017, **5**, 10073–10091.

111 E. Adatoz, A. K. Avci and S. Keskin, *Sep. Purif. Technol.*, 2015, **152**, 207–237.

112 W. Fan, X. Zhang, Z. Kang, X. Liu and D. Sun, *Coord. Chem. Rev.*, 2021, **443**, 213968.

113 H. Li, K. Wang, Y. Sun, C. T. Lollar, J. Li and H. C. Zhou, *Mater. Today*, 2018, **21**, 108–121.

114 R. E. Morris and P. S. Wheatley, *Angew. Chemie - Int. Ed.*, 2008, **47**, 4966–4981.

115 R. Lin, B. Villacorta Hernandez, L. Ge and Z. Zhu, *J. Mater. Chem. A*, 2018, 6, 293–312.

116 T. Rodenas, I. Luz, G. Prieto, B. Seoane, H. Miro, A. Corma, F. Kapteijn, F. X. Llabrés I Xamena and J. Gascon, *Nat. Mater.*, 2015, **14**, 48–55.

117 J. Deng, Z. Dai, J. Hou and L. Deng, *Chem. Mater.*, 2020, **32**, 4174–4184.

118 Y. Cheng, X. Wang, C. Jia, Y. Wang, L. Zhai, Q. Wang and D. Zhao, *J. Memb. Sci.*, 2017, **539**, 213–223.

119 Y. Peng, Y. Li, Y. Ban and W. Yang, *Angew. Chemie - Int. Ed.*, 2017, **56**, 9757–9761.

120 T. Rodenas, I. Luz, G. Prieto, B. Seoane, H. Miro, A. Corma, F. Kapteijn, F. X. Llabrés I Xamena and J. Gascon, *Nat. Mater.*, 2015, **14**, 48–55.

121 V. M. V. and G. Nageswaran, *J. Electrochem. Soc.*, 2020, **167**, 136502.

122 M. Zhao, Y. Huang, Y. Peng, Z. Huang, Q. Ma and H. Zhang, *Chem. Soc. Rev.*, 2018, **47**, 6267–6295.

123 Y. Li, Z. Fu and G. Xu, *Coord. Chem. Rev.*, 2019, **388**, 79–106.

124 K. Sasitharan, D. G. Bossanyi, N. Vaenas, A. J. Parnell, J. Clark, A. Iraqi, D. G. Lidzey and J. A. Foster, *J. Mater. Chem. A*, 2020, **8**, 6067–6075.

125 X. Ren, G. Liao, Z. Li, H. Qiao, Y. Zhang, X. Yu, B. Wang, H. Tan, L. Shi, X. Qi and H. Zhang, *Coord. Chem. Rev.*, 2021, **435**, 213781.

126 J. Wang, N. Li, Y. Xu and H. Pang, *Chem. - A Eur. J.*, 2020, 26, 6402–6422.

127 K. S. Park, Z. Ni, A. P. Cote, J. Y. Choi, R. Huang, F. J. Uribe-Romo, H. K. Chae, M. O'Keeffe and O. M. Yaghi, *Proc. Natl. Acad. Sci.*, 2006, **103**, 10186–10191.

128 H. Tao, Y. Zhang, Y. Gao, Z. Sun, C. Yan and J. Texter, *Phys. Chem. Chem. Phys.*, 2017, **19**, 921–960.

129 K. S. Suslick, D. A. Hammerton and R. E. Cline, *J. Am. Chem. Soc.*, 1986, **108**, 5641–5642.

130 A. V. Tyurnina, I. Tzanakis, J. Morton, J. Mi, K. Porfyrakis, B. M. Maciejewska, N. Grobert and D. G. Eskin, *Carbon N. Y.*, 2020, **168**, 737–747.

131 A. Lucas, C. Zakri, M. Maugey, M. Pasquali, P. Van Der Schoot and P. Poulin, *J. Phys. Chem. C*, 2009, **113**, 20599–20605.

132 G. Xu, T. Yamada, K. Otsubo, S. Sakaida and H. Kitagawa, *J. Am. Chem. Soc.*, 2012, **134**, 16524–16527.

133 M. Zhao, Y. Wang, Q. Ma, Y. Huang, X. Zhang, J. Ping, Z. Zhang, Q. Lu, Y. Yu, H. Xu, Y. Zhao and H. Zhang, *Adv. Mater.*, 2015, **27**, 7372–7378.

134 P. Cheng, C. Wang, Y. V. Kaneti, M. Eguchi, J. Lin, Y. Yamauchi and J. Na, *Langmuir*, 2020, **36**, 4231–4249.

135 A. J. Young, R. Guillet-Nicolas, E. S. Marshall, F. Kleitz, A. J. Goodhand, L. B. L. Glanville, M. R. Reithofer and J. M. Chin, *Chem. Commun.*, 2019, **55**, 2190–2193.

136 Y. Zhao, S. Y. Lee, N. Becknell, O. M. Yaghi and C. A. Angell, *J. Am. Chem. Soc.*, 2016, **138**, 10818–10821.

137 Y. Wang, H. Jin, Q. Ma, K. Mo, H. Mao, A. Feldhoff, X. Cao, Y. Li, F. Pan and Z. Jiang, *Angew. Chemie*, 2020, **132**, 4395–4399.

138 M. Kalaj, K. C. Bentz, S. Ayala, J. M. Palomba, K. S. Barcus, Y. Katayama and S. M. Cohen, *Chem. Rev.*, , DOI:10.1021/acs.chemrev.9b00575.

139 X. Y. Dong, J. J. Li, Z. Han, P. G. Duan, L. K. Li and S. Q. Zang, *J. Mater. Chem. A*, 2017, **5**, 3464–3474.

140 W. L. Teo, W. Zhou, C. Qian and Y. Zhao, *Mater. Today*, 2021, **47**, 170–186.

141 Z. Chen, M. C. Wasson, R. J. Drout, L. Robison, K. B. Idrees, J. G. Knapp, F. A. Son, X. Zhang, W. Hierse, C. Kühn, S. Marx, B. Hernandez and O. K. Farha, *Faraday Discuss.*, 2021, **225**, 9–69.

142 W. Zheng, R. Ding, K. Yang, Y. Dai, X. Yan and G. He, *Sep. Purif. Technol.*, 2019, **214**, 111–119.

143 S. R. Venna, M. Lartey, T. Li, A. Spore, S. Kumar, H. B. Nulwala, D. R. Luebke, N. L. Rosi and E. Albenze, *J. Mater. Chem. A*, 2015, **3**, 5014–5022.

144 J. Dechnik, J. Gascon, C. J. Doonan, C. Janiak and C. J. Sumby, *Angew. Chemie - Int. Ed.*,

2017, 56, 9292–9310.

145 S. Shahid, K. Nijmeijer, S. Nehache, I. Vankelecom, A. Deratani and D. Quemener, *J. Memb. Sci.*, 2015, **492**, 21–31.

146 T. Kitao, Y. Zhang, S. Kitagawa, B. Wang and T. Uemura, *Chem. Soc. Rev.*, 2017, 46, 3108–3133.

147 M. Kalaj and S. M. Cohen, *Angew. Chemie*, 2020, **132**, 14088–14093.

148 L. Ma, F. Svec, Y. Lv and T. Tan, *Chem. – An Asian J.*, 2019, **14**, 3502–3514.

149 Keskin and Alsoy Altinkaya, *Computation*, 2019, **7**, 36.

150 G. W. Peterson, D. T. Lee, H. F. Barton, T. H. Epps and G. N. Parsons, *Nat. Rev. Mater.*, 2021, **6**, 605–621.

151 R. Semino, J. C. Moreton, N. A. Ramsahye, S. M. Cohen and G. Maurin, *Chem. Sci.*, 2018, **9**, 315–324.

152 R. Semino, N. A. Ramsahye, A. Ghoufi and G. Maurin, *ACS Appl. Mater. Interfaces*, 2016, **8**, 809–819.

153 K. Gao, X. Guo, B. Zheng, J. Wang and L. Wang, *Mater. Today Chem.*, 2021, **20**, 100458.

154 L. Ma, F. Svec, Y. Lv and T. Tan, *J. Mater. Chem. A*, 2019, **7**, 20293–20301.

155 M. Armstrong, C. Balzer, B. Shan and B. Mu, *Langmuir*, 2017, **33**, 9066–9072.

156 Y. W. Chang and B. K. Chang, *J. Taiwan Inst. Chem. Eng.*, 2018, **89**, 224–233.

157 F. Xiang, A. M. Marti and D. P. Hopkinson, *J. Memb. Sci.*, 2018, **556**, 146–153.

158 C. Satheeshkumar, H. J. Yu, H. Park, M. Kim, J. S. Lee and M. Seo, *J. Mater. Chem. A*, 2018, **6**, 21961–21968.

159 X. Ding, X. Li, H. Zhao, R. Wang, R. Zhao, H. Li and Y. Zhang, *Chinese J. Chem. Eng.*, 2018,

26, 501–508.

160 Y. Wang, Y. Ren, H. Wu, X. Wu, H. Yang, L. Yang, X. Wang, Y. Wu, Y. Liu and Z. Jiang, *J. Memb. Sci.*, 2020, **602**, 117970.

161 B. Ghalei, K. Sakurai, Y. Kinoshita, K. Wakimoto, A. P. Isfahani, Q. Song, K. Doitomi, S. Furukawa, H. Hirao, H. Kusuda, S. Kitagawa and E. Sivaniah, *Nat. Energy*, , DOI:10.1038/nenergy.2017.86.

162 M. A. Rodrigues, J. de S. Ribeiro, E. de S. Costa, J. L. de Miranda and H. C. Ferraz, *Sep. Purif. Technol.*, 2018, **192**, 491–500.

163 K. Kim, J. Y. Seo, K. Baek, J. Bae and S. Shin, *Polym. Int.*, 2019, pi.5856.

164 E. M. Mahdi and J. C. Tan, *Polymer (Guildf).*, 2016, **97**, 31–43.

165 E. M. Mahdi, A. K. Chaudhuri and J. C. Tan, *Mol. Syst. Des. Eng.*, 2016, **1**, 122–131.

166 J. Li, J. L. Gong, G. M. Zeng, P. Zhang, B. Song, W. C. Cao, H. Y. Liu and S. Y. Huan, *J. Colloid Interface Sci.*, 2018, **527**, 267–279.

167 W. T. Koo, J. S. Jang, S. Qiao, W. Hwang, G. Jha, R. M. Penner and I. D. Kim, *ACS Appl. Mater. Interfaces*, 2018, **10**, 19957–19963.

168 M. S. Attia, A. O. Youssef, M. N. Abou-Omar, E. H. Mohamed, R. Boukherroub, A. Khan, T. Altalhi and M. A. Amin, *Chemosphere*, 2022, **292**, 133369.

169 X. Cai, Z. Xie, D. Li, M. Kassymova, S. Q. Zang and H. L. Jiang, *Coord. Chem. Rev.*, 2020, **417**, 213366.

170 M. A. Aroon, A. F. Ismail, T. Matsuura and M. M. Montazer-Rahmati, *Sep. Purif. Technol.*, 2010, **75**, 229–242.

171 M. van Essen, R. Thür, M. Houben, I. F. J. Vankelecom, Z. Borneman and K. Nijmeijer, *J. Memb. Sci.*, 2021, **635**, 119517.

172 C. Li, C. Wu and B. Zhang, *ACS Sustain. Chem. Eng.*, 2020, **8**, 642–648.

173 R. Thür, N. Van Velthoven, S. Slootmaekers, J. Didden, R. Verbeke, S. Smolders, M. Dickmann, W. Egger, D. De Vos and I. F. J. Vankelecom, *J. Memb. Sci.*, 2019, **576**, 78–87.

174 S. Meshkat, S. Kaliaguine and D. Rodrigue, *Sep. Purif. Technol.*, 2020, **235**, 116150.

175 E. Ahmadi Feijani, A. Tavasoli and H. Mahdavi, *Ind. Eng. Chem. Res.*, 2015, **54**, 12124–12134.

Chapter 2

Development of a robust gas loss analysis method for rigid PIR foams

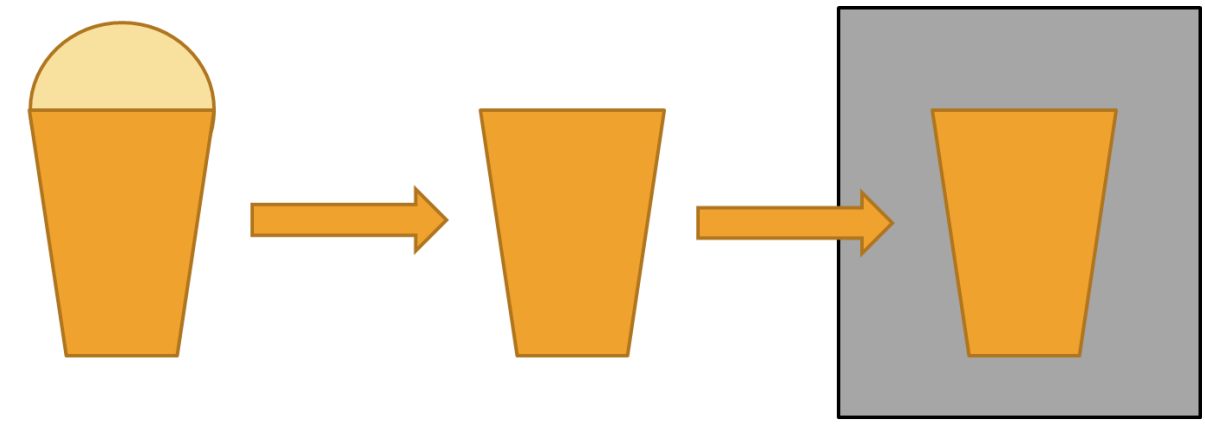

“So, he has no head'

'That’s usually what headless means'

'No head at all?'

'You’re really not getting the whole headless thing, are you?'

'It’s just kind of silly even for us.”

— Valkyrie Cain in Skulduggery Pleasant: Mortal coil, by Derek Landy, an Irish playwright and novelist

2.1 – Introduction and Aims

As discussed in the introduction to this work, the building sector accounts for approximately 25-40 % of total global energy consumption[1–5], where nearly half of the total energy consumed in the UK was used for heating.[6–9] Effectively insulating a building reduces CO_2 emissions caused by heating (or cooling) a building by enabling it to remain at a habitable temperature without losing (or gaining) heat to the outdoors.[10–12]

In polymeric foam insulation, half of the heat transfer is directly from convection of the blowing agent, therefore having a significant impact in the K-factor of the foam insulator[13,14]. In application, the blowing agents for polymer foams have been shown to diffuse out over time, making aging of insulation a barrier to their long term efficiency.[14–17] Therefore, the reduction of gas loss from polymeric foam insulation is an important step in the fight against climate change. In this work, reducing gas loss from Kingspan rigid PIR foam is focused upon, though a singular method first had to be determined to monitor and compare the loss of gas between foams synthesized.

This chapter introduces the synthesis of rigid PIR foams, establishing a method for determining the loss of blowing agent from the foams, and the testing of the composites produced. First, a discussion on design considerations is outlined to justify the experimental decisions made throughout the project. Then, multiple methods to find a rapid screening system for metal-organic frameworks (MOFs) and metal-organic nanosheets (MONs) are investigated to determine the loss of blowing agent from the foams. Finally, the results from tests with inorganic additives were analysed to determine an ideal mass loading for the composite foams.

2.2 – Background/Design considerations

To determine the effectiveness of any material added into the PIR foams, a suitable method of monitoring blowing agent loss needed to be established. Kingspan do not currently have a

standard method for this analysis, and literature into the gas loss from PU/PIR foams explores a variety of methods for analysis dependant on the PU system used[18–22]. This shows not only the necessity to develop an appropriate analysis technique for an individual system, but the novelty of the work undertaken. Considerations for sensitivity of the technique, cost of manufacture, flexibility of synthesis and scalability were at the forefront of the development of any method used.

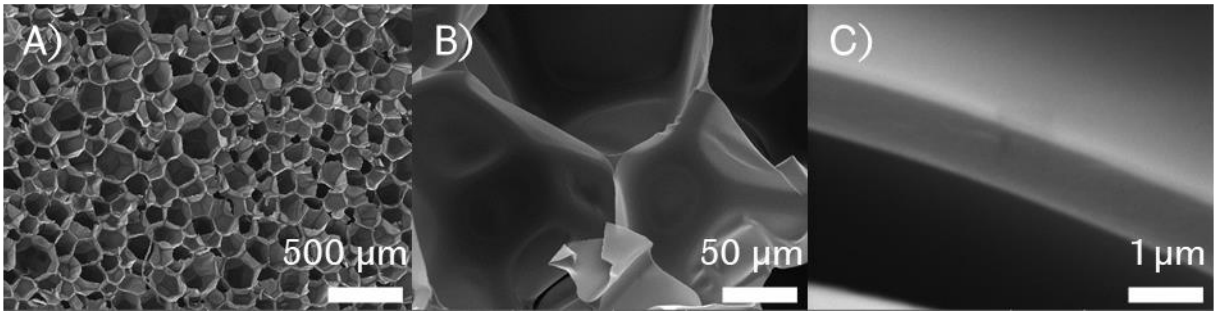

Figure 2.1 SEM images of a cut rigid PIR foam at varying magnifications, A) 100 x, B) 1000 x C) 50,000 x, showing overall structure and cell walls.

Foams are highly complex systems that typically fulfil niche applications dependant on formulation. Rigid PIR foams will contain polyol(s), isocyanate(s), catalyst(s), stabiliser(s), surfactant(s) and numerous other additives discussed previously[23,24,25]. Therefore, to reduce the scope of this work, focus was given primarily to the additives introduced to the foams (*i.e.,* MOFs and MONs), not on the foam formulation itself, and any interactions were taken as a whole between the PIR foam and the additive, rather than individually testing every combination of formulation and additives.

Rigid PIR foams are typically synthesized by pre-mixing a "part A" which contains a polyol, cyclopentane, isopentane, a trimerization catalyst, a surfactant, a flame retardant, and water. A pMDI exclusively constitutes "part B". The reaction was initiated by mixing part B into part A and combined using an overhead stirrer at 3000 rpm for 10 seconds. A 100 g mixture of foam typically rises to over 30 cm (when a 20 cm tall, 5-10 cm diameter tapered cup was used)

before the reaction completes. Polyurethane syntheses are exothermic, and the internal temperatures of the foam was measured to reach temperatures of up to 160 °C before cooling. Figure 2.1 shows three magnifications of a Kingspan rigid PIR foam after synthesis, demonstrating the cellular structure and wall thickness.

For the synthesis of foams, efficient mixing was a crucial step to allow the reagents to combine in the correct ratio and for the creation of nucleation sites for bubbles. Poor mixing can result in poor foams (in this case, open-cells, no rigidity, or no foam at all) being made. Kingspan typically produce small scale batches of foam on the 100 - 500 g scale which, with adequate mixing, are considered to produce material that provides a viable comparison with foam produced through their continuous slab-stock synthesis. Attempts to miniaturize the synthesis further (from 100 g to 10 g) proved difficult as smaller volumes of material meant inadequate mixing took place before the foam began blowing. This resulted in a poor material produced that could not be utilized for analysis.

The physical properties of the composite PIR foams synthesized are a key consideration in designing the method as variations in cell size, wall thickness or open/closed cells will result in significant differences in the rate of blowing agent loss from the foam. In the case of this PIR foam system, an ideal material would have small bubble sizes, with thin cell walls and 100 % closed cells to minimize the conduction of heat through the foam and retain the blowing agent. The foams utilized in this work have an average cell size of 222 ± 27 μm (determined by cell size analysis of scanning electron microscopy (SEM) images), wall thickness ranging in the μm scale (not analysed due to the variability across the system with inadequate testing means), and 85 ± 1 % closed cells.

Additional consideration must also be given to the mechanical properties of the foams, as stability of the final product for installation is an important factor. For generic applications, such as in wall cavities or between loft rafters, 2.4 m x 1.2 m x 25-150 mm slab stock boards of rigid PIR foam boards backed with aluminium sheeting are produced by Kingspan. These

boards are then shipped to retailers/construction sites and manually manipulated and cut when installed as wall insulation. If the addition of MONs were to cause the final product to become unworkable (*e.g.,* too brittle to be manipulated or cut effectively on site), then the foam would not be usable as a product. Additionally, if the addition of MONs were to cause increases in cell size (therefore increasing K-factor) or significant price increases (through the cost of the MONs themselves, through increased cell wall thickness costing more to produce similar volumes of foam) without significant increases in the product's performance, then this would also make the composites unviable as a final product.

While some testing (dynamic and thermal mechanical analysis) has been completed on rigid PIR foams synthesized from Kingspan formulations, little useful information could be derived from the results of the brittle foams at lab scales. Therefore, mechanical testing could not be featured in this work, but no foams or composite foams produced in this work resulted in products that would not be workable in application.

Due to the early development of MONs, synthesis at a g or kg scale is still limited. So, the use of grams of polyurethane with milligrams of MONs, instead of 100's of grams would allow for simplified synthesis and analysis of a target composite MON/PIR foam system before the need for development of scale up of a single MON system. As previously discussed, the miniaturization of the foam synthesis was unsuccessful, therefore, an alternate method for initially testing gas loss from the foams was targeted for development. Ideally, the alternate method would be small scale, quick, and requiring only small amounts of PIR, and therefore MONs, per test.

2.3 – Gas loss methods explored and rejected

This section describes the techniques attempted to produce a small-scale testing route for MOF/MON composites. Initially, PIR/PU membranes are explored as a model for a single cell wall. Following this, small cuts of larger synthesized foams are tested via headspace gas chromatography to monitor gas loss. These techniques demonstrate the decisions made for later testing and the final accelerated aging method chosen for analysis.

2.3.1 – Polyurethane Membrane methods

The first model test system looked at reducing the foam down to a single membrane. Diffusion of gasses are routinely measured across membranes, and are extensive in MON composite literature[26–31], so in initial studies we investigated a polyurethane membrane as a simplified model to probe the effect of additives in the diffusion of blowing agent across the polyurethane foam. The method consisted of a membrane attached to a gas cell (pictured in figure 2.2) containing the blowing agent and the diffusion monitored via FTIR. Initial testing utilized the Kingspan foam formulation prepared at a 0.25, 0.5 and 1 g scale total of part A and part B combined with THF (25 mL) to prevent foaming (by interrupting the surfactant system), whilst still retaining all parts of the formulation and allowing the mixture to be pourable. This mixture was poured into 15 cm petri dishes and allowed to evaporate overnight to form a thin film membrane for the analysis. With increasing mass of polyurethane used, thicker films were produced. The thinner membranes proved too brittle and only the 1 g scale thicker membranes could be mounted successfully to the gas cell.

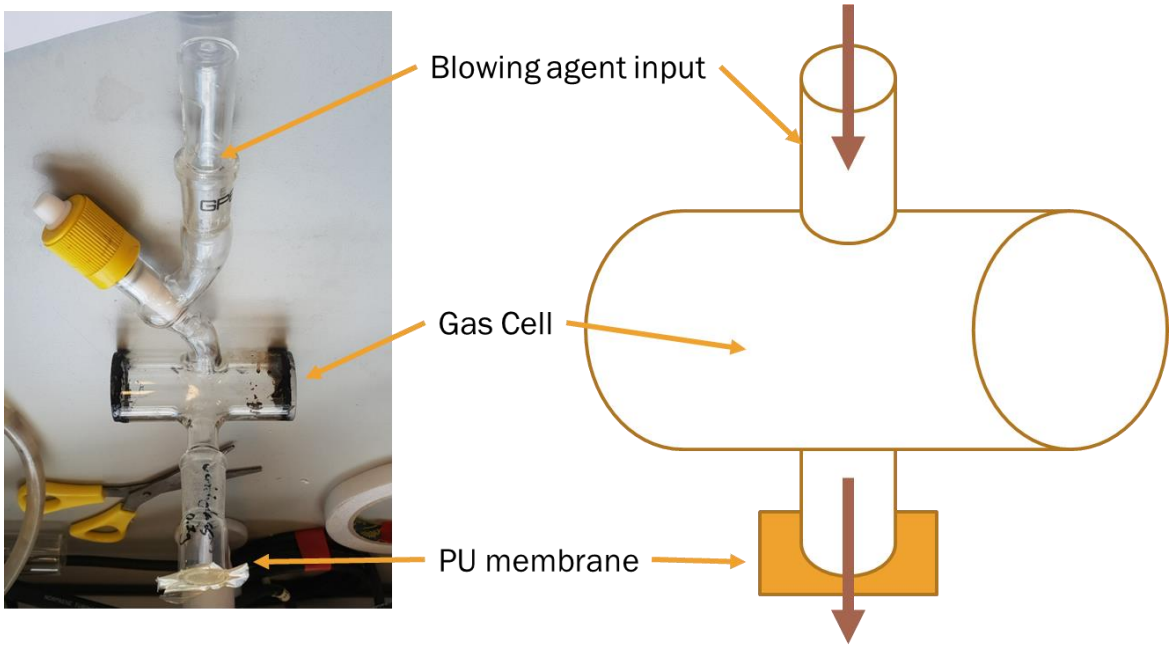

Figure 2.2 Gas cell with PU membrane attached

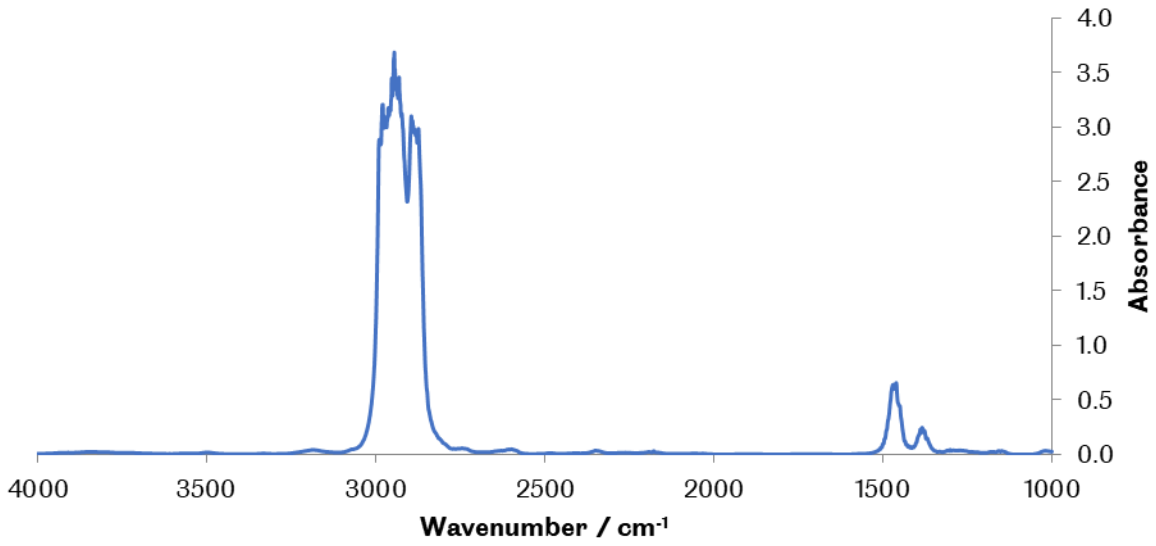

Figure 2.3 FTIR spectra of cyclopentane and isopentane in the gas cell at 500 seconds after blowing agent injection.

Blowing agent was introduced into the cell as a liquid, allowed to fully evaporate where no liquid blowing agent remained in the cell, then the system monitored with FTIR. As can be seen in figure 2.3, the blowing agent shows characteristic absorbance peaks for alkanes. From this,

the peak at 1460 cm^{-1} was monitored and utilized to preform time resolved FTIR, demonstrated in figure 2.4.

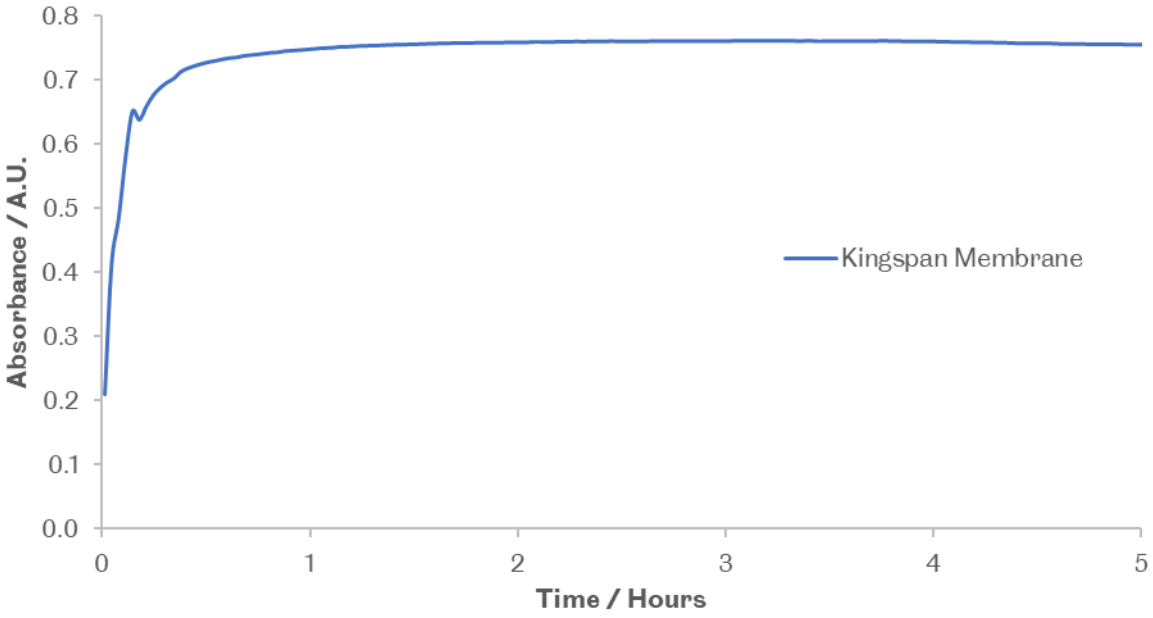

Figure 2.4 Time resolved comparison of the 1460 cm^{-1} absorbance in a gas cell attached to a Kingspan PIR membrane after injection of blowing agent into the gas cell.

Figure 2.4 shows the evolution of the experiment. Initially, the liquid blowing agent was added into the gas cell, defined as the 0 hour. An initial rise was seen as the blowing agent evaporates until it reached a steady concentration at roughly 1 hour, where no visible liquid blowing agent remained. After 5 hours, a steady absorbance was observed by FTIR indicating minimal diffusion through the membrane. This can be attributed to the thickness of the PU membrane not allowing diffusion over a reasonable time-scale. As this technique was to be utilized as a quick sifting method for identifying promising additives, any day to multi-day analysis would be unacceptable, as the equipment could only measure a single sample at a time and was shared across research groups. Therefore, the use of the Kingspan polyurethane was halted.

To simplify the model further, a soluble, non-crosslinked polyurethane elastomer was purchased. This alternative offered several potential benefits, from further simplifying the system (by removing possible additives), to having a more consistent polymer architecture

between batches, and finally being elastic enough to be cast into thinner films than previously made. Therefore, a polyether-polyester polyurethane was purchased from Sigma-Aldrich, dissolved in THF, and cast into petri dishes to form thin films as previously described. These new films were then tested in the gas-cell set up for diffusion of the blowing agent.

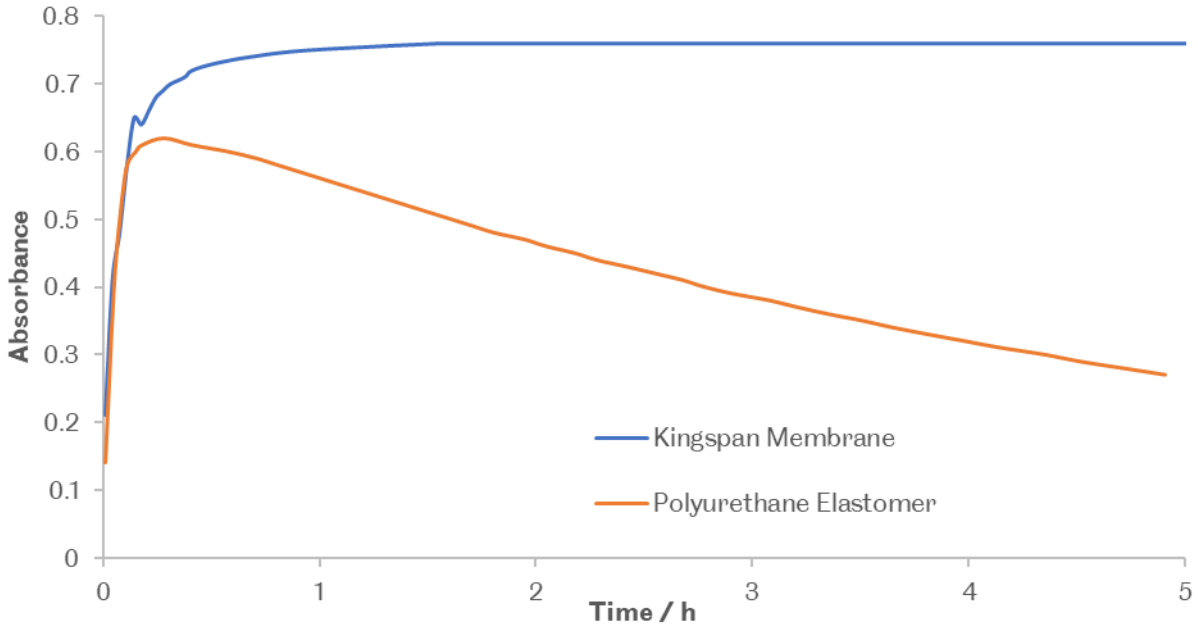

Figure 2.5 Time resolved comparison of the 1460 cm^{-1} absorbance of the gas cell attached to a Kingspan PIR membrane vs. a dissolvable PU model after injection of blowing agent into the gas cell

Initial testing of the polyurethane elastomer showed promise, as seen in figure 2.5 where the loss of gas through the thin film could be measured over the course of hours, a significant improvement over the previous membranes tested.

To establish the reproducibility of the method with the equipment available, repeated tests were performed. Multiple membranes utilizing the same mass of PU elastomer were dissolved in THF before being poured into a petri dish and allowed to evaporate, creating repetitions of membranes of the same thickness. These repeats were labelled A through S and individually measured for their rate of gas loss. Blowing agent was added to the chamber for 1 h before the FTIR monitoring was started, to allow the blowing agent to fully evaporate and saturate the

membrane. The absorbance of the peak at 1 hour was set to 100% after this time and the decrease in intensity was monitored. The result of four repeats over 12 hours are shown in figure 2.6.

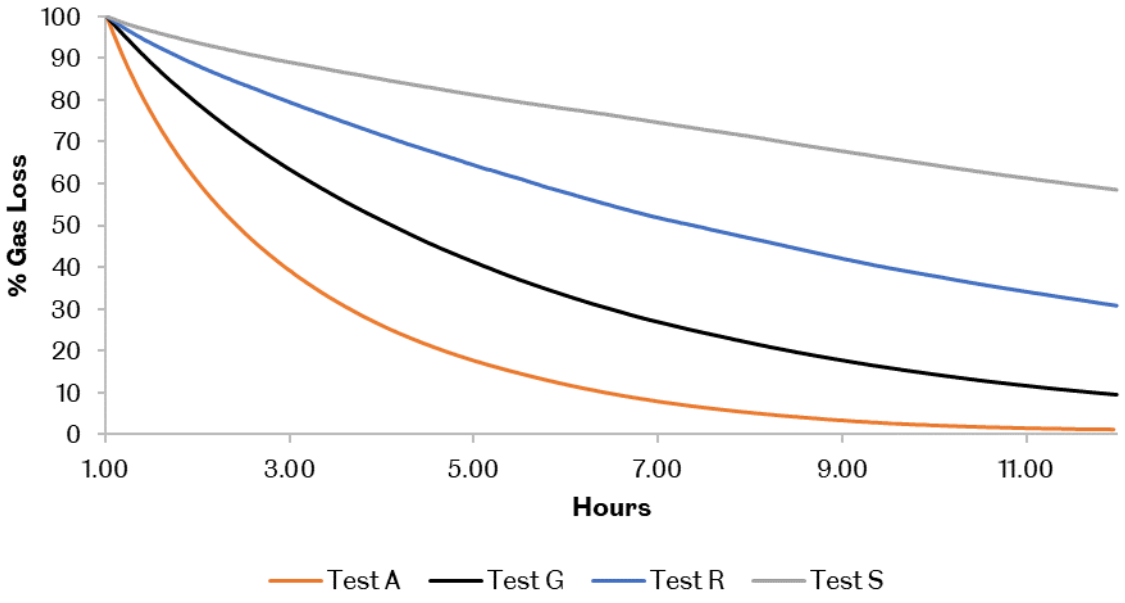

Figure 2.6 Normalized time resolved comparisons of the 1460 cm^{-1} absorbance of the gas cell attached to a dissolvable PU model after injection of blowing agent into the gas cell

Figure 2.6 shows different rates of gas loss over 12 hours when using four repeats of dissolvable PU membranes. As the reproducibility of rate at which the gas left the chamber the membranes was low, this technique was determined to be unusable and the use of a membrane systems for rapid screening of different additives was not pursued further. Likely this is due to pin-hole formation on poorly formed membranes produced by the solvent-casting method. If more advanced equipment for producing membranes or measuring the gas loss was available, this method could be taken further as a sifting method to produce composite PU/MON membranes for analysis.

2.3.2 – Headspace GC monitoring

An alternative method investigated was to synthesise a bulk foam on a 100 g scale, which were then cut into small cubes of a known volume (a volume between 0.1 and 1 cm^3) and sealed into glass vials with a Teflon lid. These vials were then sampled via a needle taking a sample of the gas inside the headspace of the vial and analysed via headspace gas chromatography to directly measure the concentration of blowing agent in the vial at any given time.

The use of smaller cubes from a single batch allowed for multiple repetitions of the data for analysis from a single foam synthesis, reducing the need for multiple foam syntheses. Multiple gas samples were taken from 3 vials over a period of a week to measure the loss of gas from the foams and used to compare the barrier effects between different MON additions.

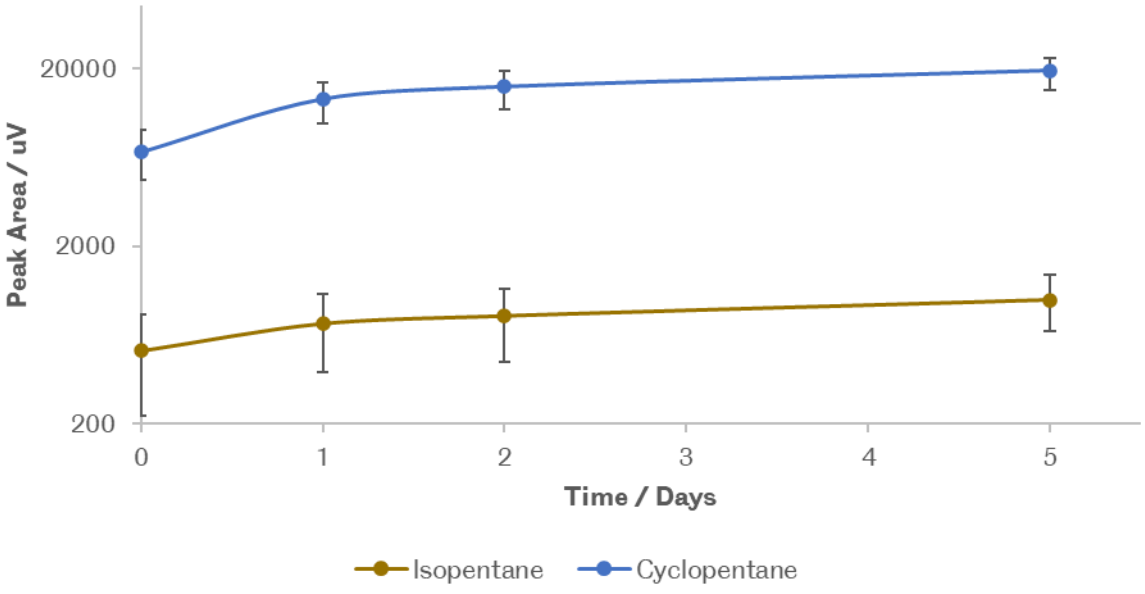

Figure 2.7 Average detection of iso and cyclopentane in the headspace of 3 vials over 5 days of a standard rigid PIR foam

Figure 2.7 shows the increase of the blowing agents (isopentane and cyclopentane) in the sealed vials over 5 days, demonstrating the gas loss from the foam cubes into the headspace above. At the 0 day point the blowing agent is already in the headspace, likely immediately

released from the most outer edges of the foam where cells are damaged from the cutting process. This initial result demonstrated that not only is headspace GC a viable method for detecting both isopentane and cyclopentane, providing opportunity to determine the effects on the individual blowing agents, but also the rate of blowing agent loss over time. The error in the values were determined to be too high, and likely arose from the small amounts of foam being used, creating high surface area variation between each data set. So, a further analysis method was suggested, whereby indirectly measuring the change in mass of the foam cubes over time, the loss of blowing agent from the cells could be inferred.

2.4 – Monitoring mass loss as an effective technique for determining gas loss

As the heavy blowing agent diffused from the foam, a change in mass occurred. By measuring this mass change, the diffusion of blowing agent from the foam could be monitored. However, larger foam cubes would be needed to measure the mass change more accurately with the balances available. Therefore, larger cubes (approximately a volume of 30 cm^3) were initially cut from a single foam. Eight cubes were cut from a single foam synthesis and placed into an oven at 25 °C (for a standard temperature) or 70 °C (temperature utilized by Kingspan in their accelerated aging tests for changes in thermal conductivity) and their mass recorded repeatedly over multiple hours. As the foam cubes would vary in weight due to being hand cut, in figure 2.8 the initial mass is set at 0 % and the reduction of the mass over time is represented as an increase in percentage. The 0 point is not included on the graph as the natural logarithm used for the line of best fit cannot utilize a zero point for its calculation, and so is omitted. The loss of mass is the inferred to be the loss of blowing agent.

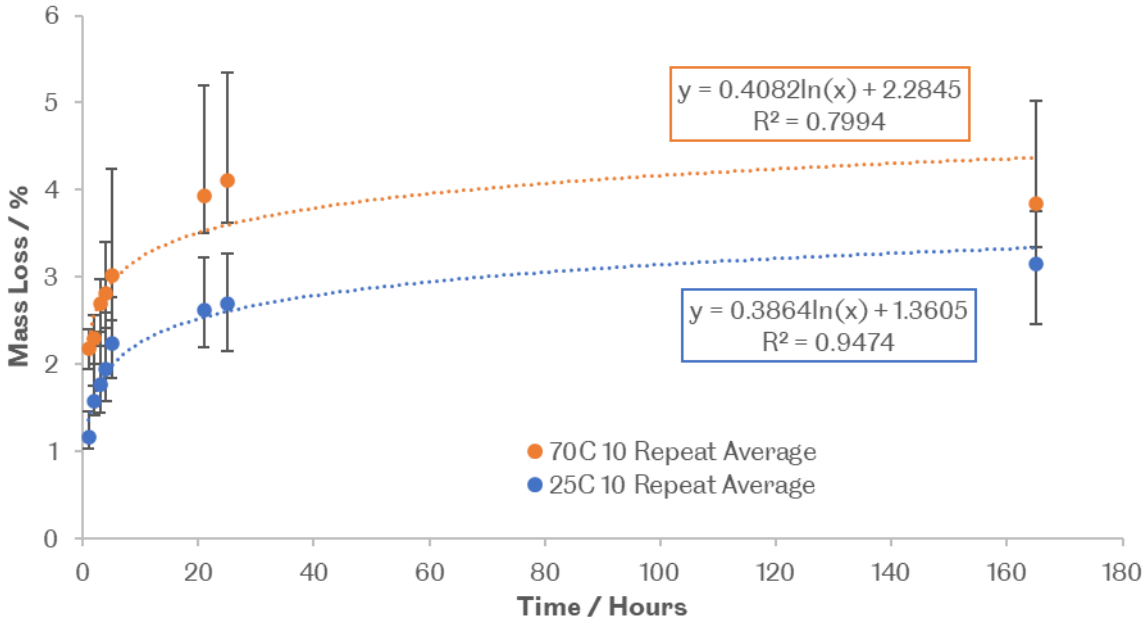

Figure 2.8 Average percentage mass loss from 8 cube cut foams at either 25 or 70 °C of a standard rigid PIR foam

Figure 2.8 shows the mass loss of eight foam cubes placed in an oven at 25 °C or 70 °C for 165 hours. For each temperature a logarithmic decay was observed. The 70 °C sample showed an accelerated mass loss, reaching 3.84 ± 0.52 %, in comparison to the 25 °C data which reached 3.15 ± 0.44 %. The logarithmic decay is expected, as the foam begins with a high loading of blowing agent in the cells which diffuses out, and as the concentration of blowing agent decreases, so does the rate of change. Additionally, the higher temperature samples plateauing with a greater mass loss was also expected, as the rate of diffusion was increased by the increase in temperature. As 5.4 % by weight of the foam charged is blowing agent, this could initially be inferred as the maximum mass loss from the foam through diffusion out of the cells if no air diffused back into the system. However, there were multiple possible volatile constituents within the foam (*e.g.*, blowing agent, water, catalysts, *etc.*), and gasses in the air (Oxygen, Nitrogen, and other traces) that has diffused into the foam. Therefore, this work

focuses on any specific changes from the base Kingspan foam to composite foams produced, rather than direct interpretation of specific amounts of gas lost.

To further develop this promising method, 3 repeats of a foam were produced and measured over the course of 28 days. Figure 2.8 shows significant overlap in error bars in the data points, meaning technique demonstrated low reproducibility and needed to be improved to compare between different samples. Therefore, to reduce this variability further, the method was refined to use an increased mass of foam.

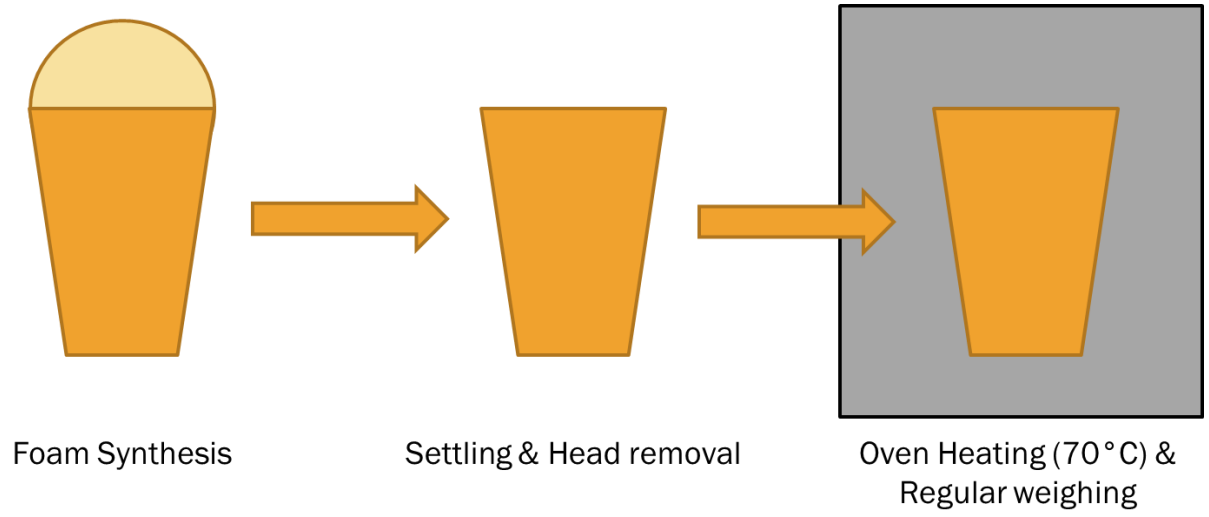

Figure 2.9 A graphical representation of the steps from foam synthesis to accelerated aging

Figure 2.9 illustrates the final process which was developed. A 100 g foam was synthesized in a 1 L Kingspan cup. The head (any foam that has risen beyond the rim of the cup) is then removed down to the top of the synthesis cup. Foams are kept inside the cup for aging and analysis and the foam is adhered well around the inside of the cup after foaming is completed. Although some mass variation was observed (typically between 55-60 g foam remaining with the cup), a single regular surface was exposed from which gasses could escape. This allowed for a significantly more standardised analysis to be undertaken.

To allow for further regularity across the samples, each foam was synthesized, allowed to settle (from any temperature or reactive effects) for 24 hours, then cut using a foam saw, and

allowed to settle for a further 24 hours. These cut foam cups are then placed either into a cupboard at room temperature (to remove any possible sun bleaching effects) or a closed oven and weighed daily over the course of 28 days at a minimum. Utilizing room temperature over a 25 °C oven was chosen to attempt to give further replication of the foam when used in application, and limited oven space was prioritized for high temperature experiments. Variation in weighing times across days is taken as a necessary error due to the length of time required to gain insightful data, and therefore the trends of the data were considered for analysis over individual data points. Though, comparison of the final mass is utilized for representation of effects additives have on gas loss.

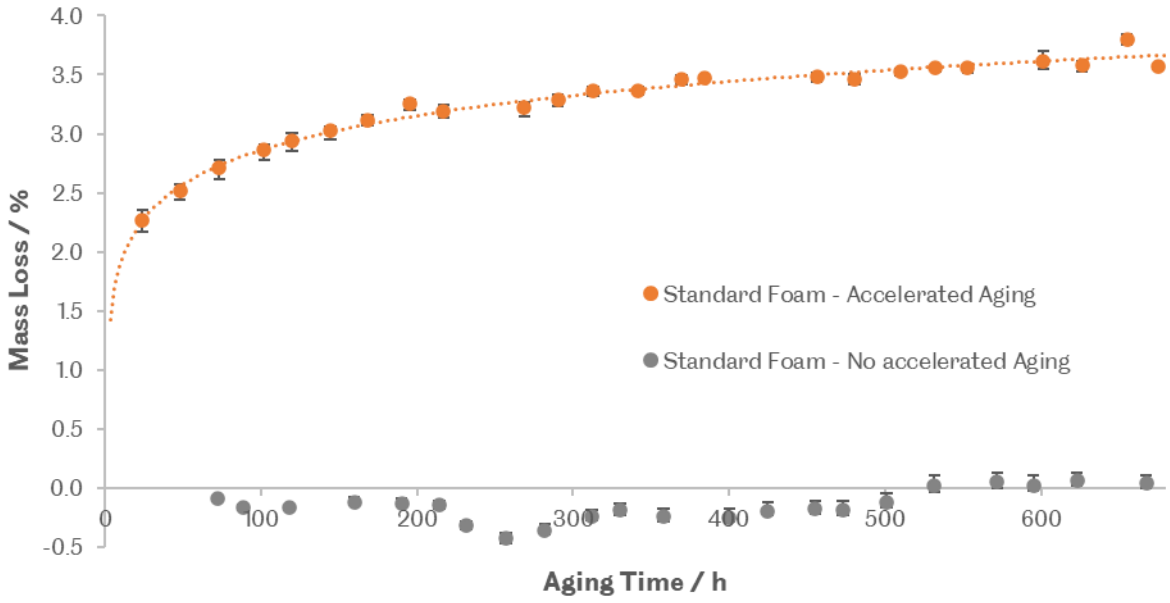

Figure 2.10 Mass loss from rigid PIR foams over time when heated at 70 °C in an oven (accelerated aging) or left under ambient conditions (no accelerated aging)

Figure 2.10 shows how the average % mass loss of three cups either exposed to a room temperature environment or placed into an oven at 70 °C. The room temperature environment foam shows slight increase in mass over the measured time, whilst the foam placed into an oven demonstrates the logarithmic loss of mass as seen previously. The room temperature foam demonstrates the need for heating as the increase in mass (likely due to moisture

adsorption) results in no regular mass loss being observed over the 1000 hours measured. Additionally, the 70 °C foam showed a higher reproducibility in the data over the previous cube cut method, this was expected as with a more accurate method of shaping the foam allows for less deviation across samples. Whilst the increased time to reach a plateau was expected, the rate at which it is reached was initially expected to take much longer due to the significant decrease in exposed surface area. It is possible that the paper cup provides a poor seal between the cup and the foam, leading to gas loss through the edges and making the expected surface area much higher than initially proposed. However, as the reproducibility of the measurement is significantly improved, this was not determined to be an issue with the technique as it would be replicated across all samples.

In conclusion, despite the difficult miniaturization of the foam synthesis, and requirement for an accurate and reproducible analysis, a robust method for monitoring the rate of blowing agent loss has been determined.

While this method takes longer and requires more material than would be desirable, it provides reliable data through a method that is not labour intensive. With the oven available to this researcher, two sets (two batches of three foams) can be analysed in tandem, allowing for research into several different additives to be undertaken simultaneously. This method does have the drawback of scale, as with a 100 g batch of foam, up to 1 g of additive may be needed to create meaningful barrier effects, therefore requiring the synthesis of multi-gram scale MONs. Therefore, some development in the minimum loading of materials into the foams is necessary to reduce this synthesis requirement. Furthermore, to remove the need for unnecessary synthesis of MONs, parent MOFs will need to be tested in the first instance to determine any improvements on the barrier properties which can be enhanced by the increase in anisotropy from MOF to MON.

Finally, due to the complex relationship between the two gasses used for the blowing agent, rate of heating of the thermally insulating foam, multiple additives in the composite, and variance in foam mass, no further modelling of the gas loss behaviour was considered.

2.5 – Evaluation of inorganic layered materials for use as additives in rigid PIR foams

To further test the method developed, and establish good practise for this technique, two layered materials were purchased as model additives to introduce into the foams: MoS_2 and Graphite. Both these materials have been used in gas barrier applications[32,33], foam applications[34,35], and can be exfoliated into nanosheets[36,37], making them the ideal initial testing materials.

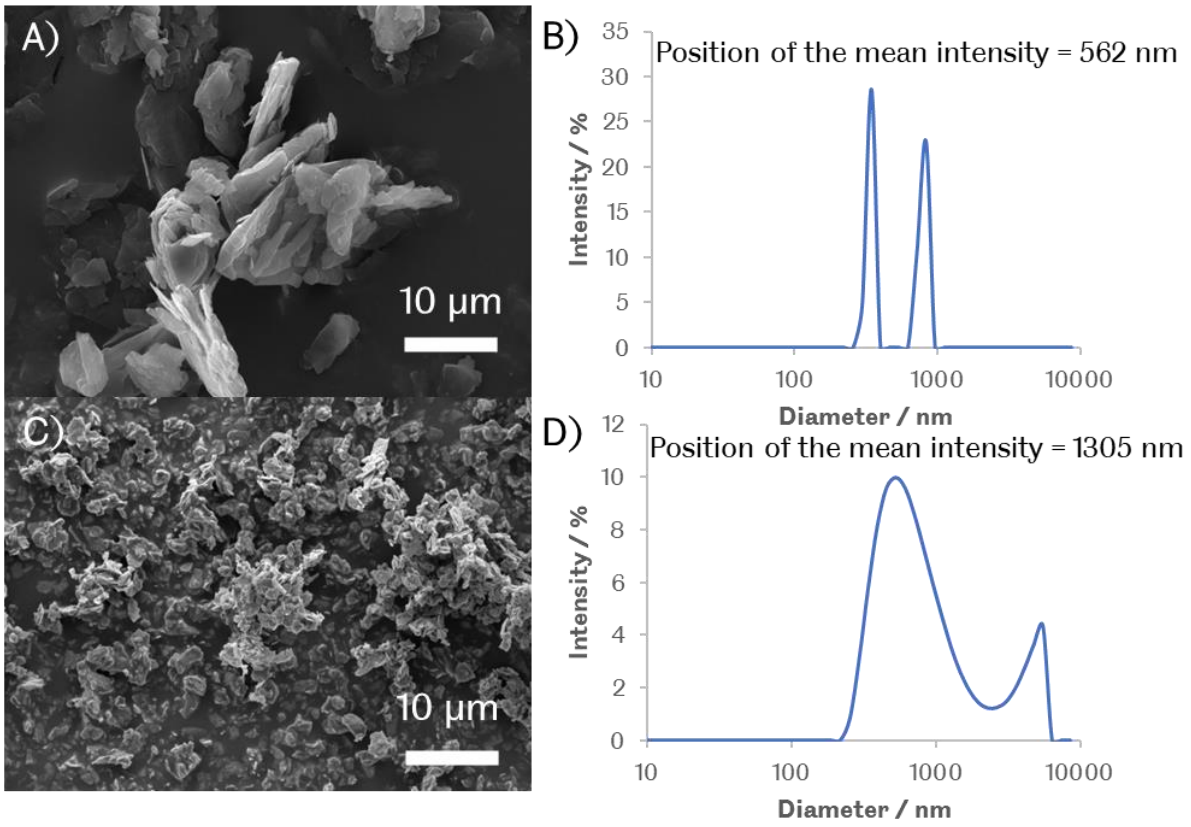

Figure 2.11 A) SEM image of Graphite, B) DLS analysis of graphite in acetonitrile after 60 seconds of sonication at 37 kHz, C) SEM image of MoS_2, D) DLS analysis of MoS_2 in acetonitrile after 60 seconds of sonication at 37 kHz. The position of the mean intensity is quoted for all datapoints within the dataset.

The MoS_2 (particulate size of < 2 μm) and graphite (unspecified size) were purchased and used in composites without any further alteration. As observed in figure 2.11, the size of the particulates used varied depending on the state, dispersion and analysis method used to obtain sizing. In this work, SEM imaging of particulates is used primarily for illustrative purposes and to comment on the structures obtained, whilst the sizes of the material used will be determined by DLS measurement after sonication (37 kHz, 60 seconds to break up aggregates) in appropriate solvents. Due to limitations in dispersion of the additive in solvent, the DLS sizing data is not reflective of the true size. However, as an indicative measurement of size, it is important to utilize this data to compare like for like systems and determine where size effects may be causing differences in the mass loss of the foam and is utilized for comparison for future additives in this work.

Composite foams were synthesized utilizing a percentage addition of the additive that related to the total mass of part A and part B, for example, a 5 % composite would consist of 5 g of additive, with 95 % total part A and part B scaled appropriately. The additive would be added to part A during the mixing process, then combined with part B as previously described for synthesis of a standard rigid PIR foam.

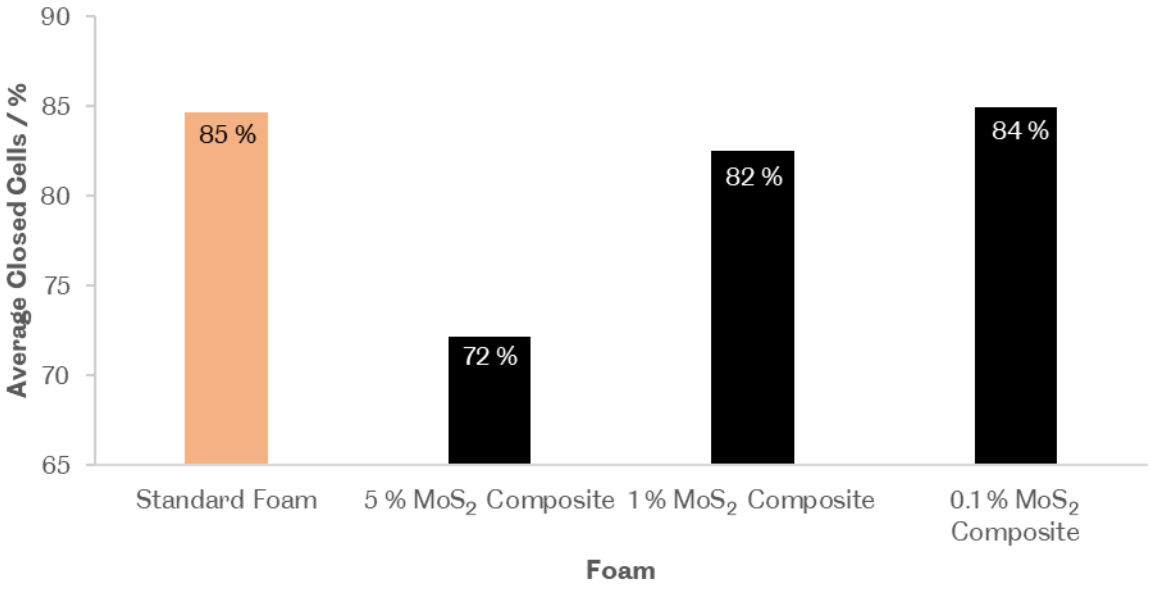

Figure 2.12 Comparison of closed cell content as determined via helium pycnometry of composite foams with different percentage additives of MoS_2 and graphite.

Helium pycnometry analysis was utilized to establish the percentage of closed cells of the foams produced. Additives into PIR foam can act as cell openers[38] and a higher percentage of open cells results in an easier pathway for the blowing agent to leave, reducing the lifetime efficiency of the foam. Therefore, three basic Kingspan rigid PIR foams were used as a standard for closed cell content, those that were used for the 70 °C accelerated aging, which produced a value 85 ± 1 %, a highly closed cell foam.

As seen in figure 2.12 higher loadings of MoS_2 into the foam resulted in significant loss of the closed cell structure, with a MoS_2 composite of 5 % wt/wt reducing the closed cell content to 72 %. Solid particle defoaming is likely the reason for the cell opening to occur. Whilst the addition of solid particles to foams can increase their viscosity and structural stability, thereby reducing drainage rate and oscillation of cell walls, the hydrophobic[39–41] system was quoted to be 2 µm in size. The bulky hydrophobic particulates interrupt the cell walls during formation, spanning across a wall due to their size, and causing dewetting of the particulate and liquid to flow away from it. This overall causes localized thinning of the cell wall, and eventually, rupture,

creating open cells. With increasing additive loading, the number of sites for thinning increases and causes an increased number of cell walls to open.[25]

Overall, with the consideration of the use of MONs and additive costs, utilizing smaller amounts of additive was ideal. Therefore 0.1 % by weight loadings were targeted, a graphite and a MoS_2 foam accelerated aging study was undertaken to demonstrate the analysis technique and determine if either additive is a viable material for PU foams.

The reproducibility of the accelerated aging technique, where each set of 3 foams is heated to 70 °C and their weight monitored, is demonstrated in figure 2.13. Each foam was prepared as previously described, with each producing highly closed cells (graphite at 84 ± 3 %, MoS_2 at 86 ± 1 %).

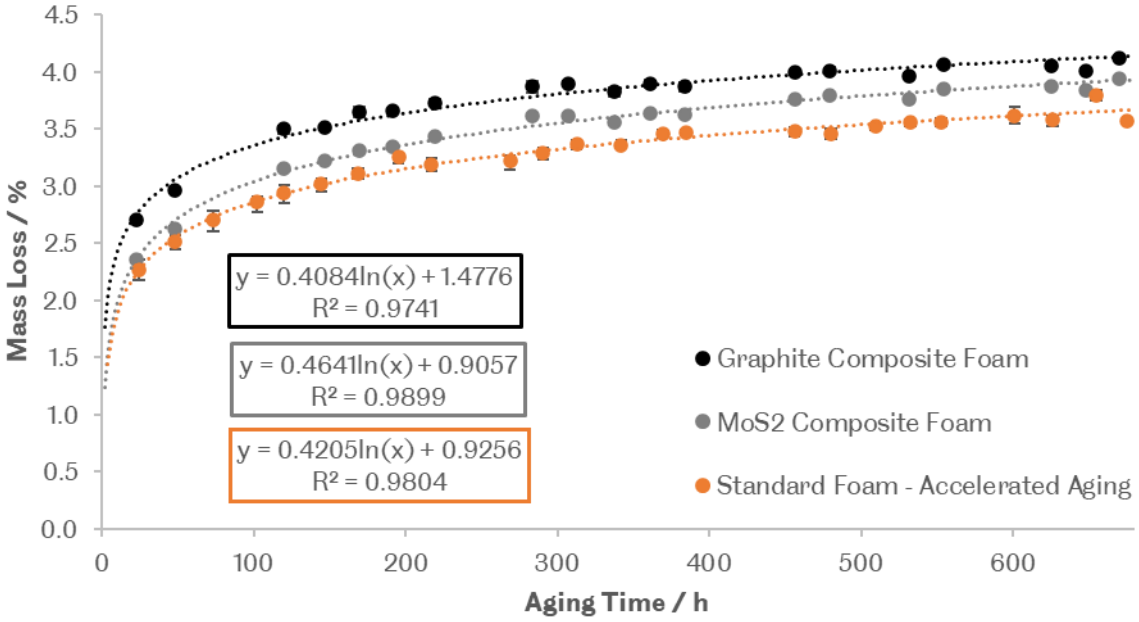

Figure 2.13 Mass loss from rigid PIR foams and composite (graphite or MoS_2) PIR foams over time when heated at 70 °C in an oven.

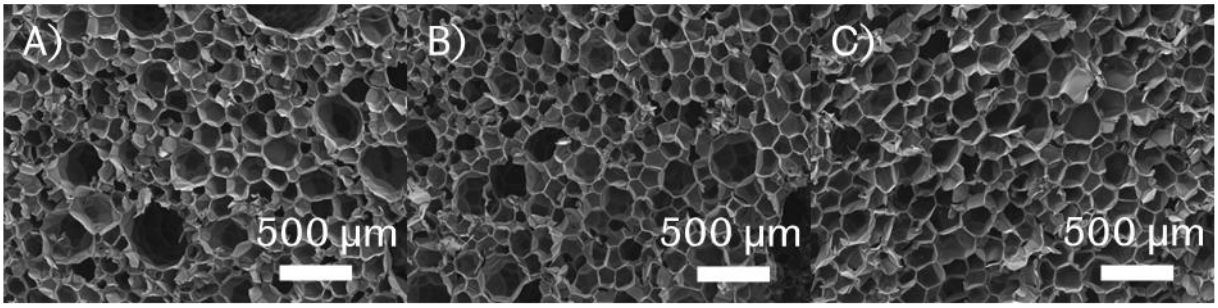

Standard Foam	MoS_2 Composite Foam	Graphite Composite Foam
Closed cell % = 85 ± 1	Closed cell % = 84 ± 3	Closed cell % = 86 ± 1
Cell Size = 222 ± 27 µm	Cell Size = 234 ± 36 µm	Cell Size = 230 ± 29 µm

Figure 2.14 SEM Images, and corresponding closed cell content and cell size, of rigid PIR foams with additives: A) No additives, B) Graphite, C) MoS_2

Figure 2.13 shows the mass loss of 3 sets of foams: a pure foam, a composite foam containing MoS_2 at 0.1 % loading, and a composite foam containing graphite at a 0.1 % loading. In all cases the logarithmic decay of the mass loss is seen, with both the MoS_2 and graphite foams having a higher mass loss (3.94 ± 0.00 % and 4.12 ± 0.02 % respectively at 28 days) over time than the pure foam (3.58 ± 0.04 % at 28 days). The following figure 2.14 shows SEM images of each composite foam with a calculated cell size and closed cell content for the foam underneath.

Both the profiles of the graphite and MoS_2 composite foams are distinct with no overlap of the error bars and had an increased mass loss over the 28 days when compared to the base foam. This was seen as an ideal result for the reproducibility, clearly demonstrating the difference between individual foams for comparison of their additives.

The increased mass loss over time for the composite foams may be partly attributed to the slight increase in cell size, though the values were within error in both composite foams when compared to the standard foams. Alternatively, effects in creating void space or creating more efficient channels for the blowing agent to travel through the additive more easily than the polymer matrix could be a further explanation for the increased mass loss from the composites[42]. Overall, it can be concluded that this analysis technique is ideal for analysing the

barrier properties of the composites and allowing for low scale amounts of additive to be introduced.

Finally, other analysis methods to gain further insight into these composites were considered. Foam was placed into a Micro computerised tomography (μ-CT) scanner to evaluate the structure of the foams produced. Analysis of rigid PIR foam produced a three-dimensional replication of the foam structure that can be analysed as a whole or in individual two-dimensional slices, demonstrated in figure 2.15. However, due to the limitations in resolution of the equipment used, detailed analysis of the structures of the foams could not be achieved as cell walls thinner than 1 μm would be missed in analysis. This method for data analysis was not explored further, but with higher resolution equipment, could be utilized for analysis of composites made in future.

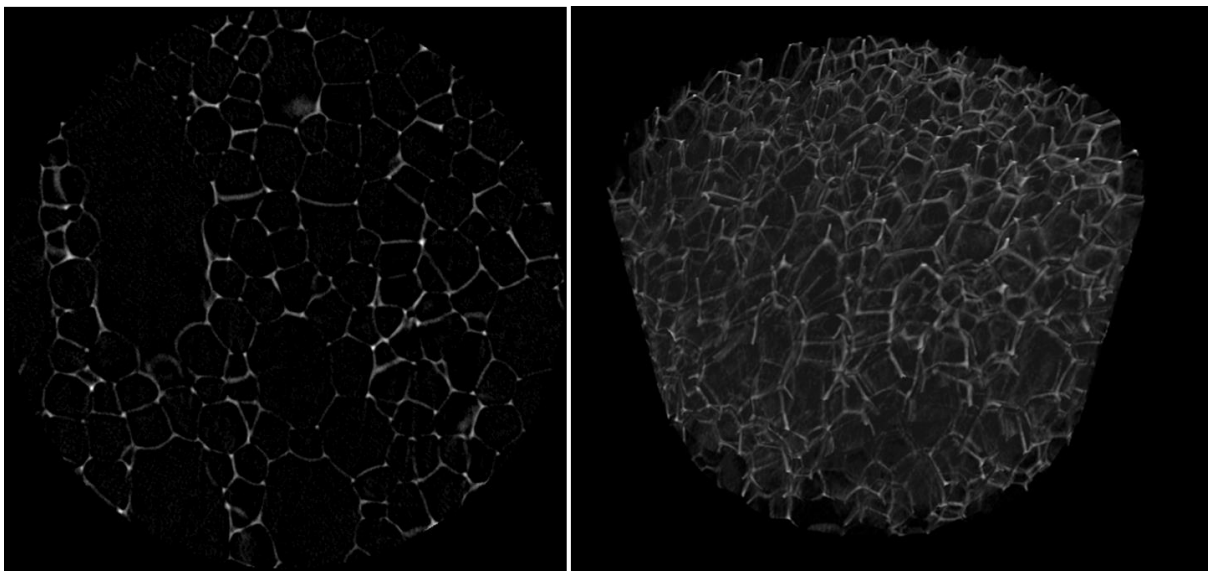

Figure 2.15 A μ-CT scan of rigid PIR foam with a single slice (left) and a 3D region (right) rendered using CTaN software after processing to remove noise. Light regions represent cell walls, dark regions represent void space.

In the composite foams, some highly agglomerated particulates can be seen by eye in some of the foam structure but provided little information. Powder X-Ray Diffraction (PXRD) and Scanning Electron Microscopy with Energy Dispersive X-Ray Analysis (SEM-EDX)

measurements were also attempted to determine information on the structures retained in the foam, or information on the distribution of the additives. However, these techniques provided little data on how the structure may have been altered through the polymerization and mixing process, as in PXRD analysis the crystalline peaks from 0.1 % additive are not resolvable above the scattering from the amorphous polymer matrix. SEM-EDX also could not obtain the resolution to determine distribution of additives in the composite.

2.6 – Conclusions and Future Work

In conclusion, an effective method for determining gas lost from a rigid PIR foam has been established. Namely, the change in mass of a large volume of foam was measured whilst under accelerated aging conditions. Furthermore, for the Kingspan PIR foam system, an ideal method for incorporation of additive has also been established. Additives are included at 0.1 % by weight of the total mixture in the Part A mixture prior to Part B addition, creating 0.1 % composites.

The resultant accelerated aging testing by rate of mass loss allowed for effective and repeatable measurement of the composites. Furthermore, the use of only 0.1 % by weight composites resulted in a reasonable scale for the synthesis of MONs for this testing application. The low labour cost for analysis over the 28 days of accelerated aging also allowed for significant synthesis and testing of other possible MOFs that could be added into the PIR foam. Overall, whilst the anticipated requirement for quick analysis was not accomplished, the primary objective of being able to effectively measure the loss of blowing agent from the foam has been achieved.

In future work, the volume of material required could potentially be reduced through the use of static mixers. Static mixers allow for efficient mixing of small volumes of liquids, which at the start of the project had shown to be the initial issue with the development of the quick analysis method. If foams produced through a static mixer are to the same standard as the

larger mixed foams, then this method could be combined with headspace GC and accelerated aging to create an idealised system that could fast produce multiple batches of PIR foam, age them within 28 days, and determine the ratio of blowing agents leaving over time.

2.7 – Experimental

General techniques utilized across multiple chapters can be found in chapter 7. Namely, elemental analysis, Fourier transform infrared spectroscopy, nuclear magnetic resonance, powder x-ray diffraction, liquid assisted exfoliation of MONs, dynamic light scattering, atomic force microscopy, determination of MON sizes, scanning electron microscopy, pycnometry and determination of cell sizes.

2.7.1 – Foam Synthesis and accelerated aging

Rigid PIR foam is synthesized according to Kingspan's formulation. A "part A" is initially mixed using a polyol, cyclopentane, isopentane, a trimerization catalyst, a surfactant, a flame retardant, and water in a 1 L cardboard Kingspan cup. Once blended using an overhead stirrer (3000 rpm, 10 seconds), pMDI , "part B", is added on top of the part A mixture and the blended again (3000 rpm, 10 seconds). The total mass of the mixture is 100 g when all components are charged. For composite foams, the total mass is reduced to accommodate the percentage loading of the additive chosen (*e.g.* a 0.1 % loading will use a total of 99.9 g of foam formulation and 0.1 g of additive). The additive is incorporated into the Part A mixture prior to mixing. Once the foam had risen a Voltcraft K202 Data Logger and Thermometer thermocouple was inserted 2.5 cm from the top of the foam to measure exotherm.

Figure 2.16 Image of overhead stirrer and typical paper Kingspan cup used for foam synthesis

For accelerated aging measurements, after the foam had stopped rising, it was left to cool for 24 hours. The head of the foam (all foam above the lip of the cup) is then removed by cutting with an insulation saw. The decapitated foam is again left to rest for a further 24 hours before a baseline weight was obtained. The foam was then placed into an oven at 70 °C and periodically weighed on a balance with a tolerance of ± 0.001 g over 28 days.

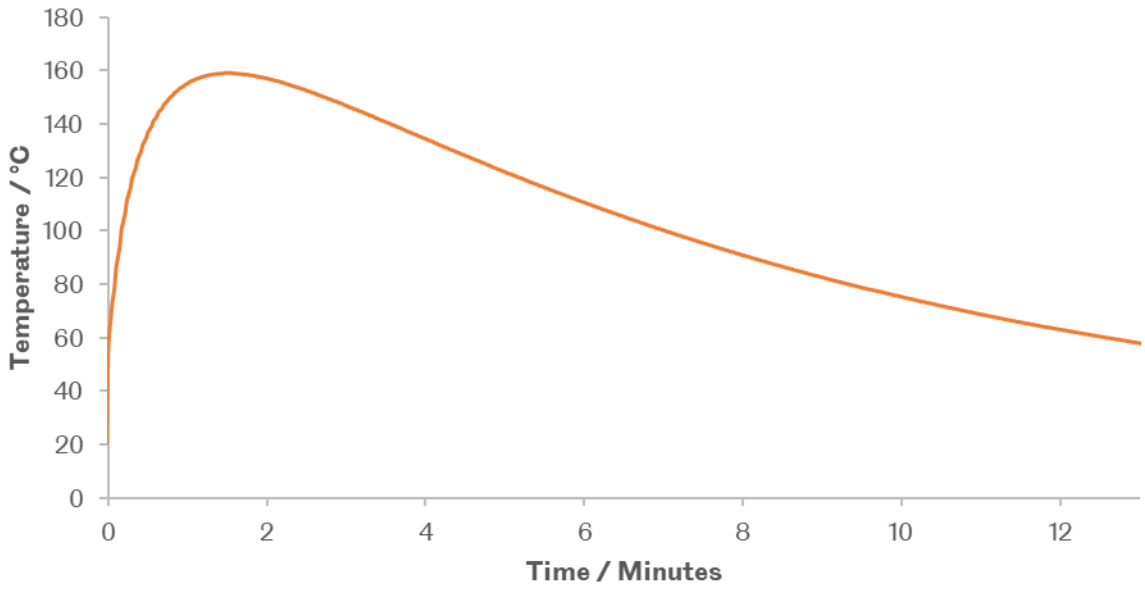

Figure 2.17 Temperature profile of a standard Kingspan PIR foam after mixing. Thermocouple measurement started after the rise of the foam had completed,

Foam	Closed Cell Content / %	Cell Size / nm	Mass loss at 28 Days / %
No Additives	85 ± 1	222 ± 27	3.58 ± 0.04
MoS_2	84 ± 3	234 ± 36	3.94 ± 0.00
Graphite	86 ± 1	230 ± 29	4.12 ± 0.02

Table 2.1 Table of foams synthesized and analysed for accelerated aging experiments, showing closed cell %, cell size and mass loss after 28 days.

2.7.2 – µ-Computerised Tomography Analysis

µ-CT measurements were performed on a Skyscan 1272 desktop high-resolution micro-CT scanner and analysed utilizing CTaN software. Samples of foam were cut into cylinders roughly 5 mm in diameter and 3 cm in height and placed inside the sample holder and sealed for analysis. A camera size of 2016 x 1344, 0.5 Al filter, 2 µm voxel size with 0.4 rotation steps resulting in a 15-minute scan per sample was utilized. In CTaN software a region of interest was selected, and a threshold applied of Low “85” and High “255” to remove noise. Finally, a despeckle function is also applied to remove any final noise.

2.7.3 – Thin film synthesis and analysis

Kingspan formulation thin films were synthesized through blending 0.4 g of Part A (as described in the foam synthesis section) and 0.6 g Part B and allowing to react for 30 seconds, then adding 25 mL of THF and blending the mixture again. The mixture was then poured into a glass petri dish and allowed to evaporate under ambient conditions over 16 hours. The resultant thin film was then peeled off and used for gas cell analysis.

Dissolvable PU thin films were produced using 0.180 g of poly[4,4'-methylenebis(phenyl isocyanate)-alt-1,4-butanediol/di(propylene glycol)/polycaprolactone pellets dissolved in 25 mL of THF and poured into a glass petri dish. The mixture was allowed to evaporate under ambient conditions over 16 hours. The resultant thin film was then peeled off and used for gas cell analysis.

Thin films were then attached to a cut quickfit glass neck via Loctite brand super glue and attached to a custom gas cell with valve controlled liquid input. The gas cell was placed for FTIR analysis and 100 µL of blowing agent was injected into the cell via the valve. The peak at 1460 cm^{-1} was then monitored over a period of time.

2.7.4 – Headspace Gas Chromatography analysis

Foam samples for headspace GC analysis were prepared by cutting previously synthesized rigid PIR foams by hand with a scalpel into small cubes of a known volume (a volume between 0.1 and 1 cm^3) and sealed into glass vials with a Teflon lid. These vials were then sampled via a needle taking a 1 µL sample of the gas inside the headspace of the vial and analysed via headspace gas chromatography to directly measure the concentration of blowing agent in the vial at any given time. Three vials were sampled over 5 days after being left at room temperature. Headspace GC analysis was performed utilizing a Perkin Elmer Autosystem Headspace GC system with nitrogen carrier gas and empty glass capillary column (3 ft x 4 mm I.D. x 0.25 in O.D) at 30 °C. Isopentane and cyclopentane peaks were detected at 2.2 and 3.6

minutes respectively, then were integrated and compared with 0.1 µL standards to determine concentration.

References

1 X. Li, Y. Zhou, S. Yu, G. Jia, H. Li and W. Li, *Energy*, 2019, **174**, 407–419.

2 S. Chen, G. Zhang, X. Xia, Y. Chen, S. Setunge and L. Shi, *Sustain. Energy Technol. Assessments*, 2021, **45**, 101212.

3 J. Wu, Z. Lian, Z. Zheng and H. Zhang, *Sustain. Cities Soc.*, 2020, **53**, 101893.

4 H. Duan, S. Chen and J. Song, *Energy*, 2022, **245**, 123290.

5 M. Bourdeau, X. qiang Zhai, E. Nefzaoui, X. Guo and P. Chatellier, *Sustain. Cities Soc.*, 2019, **48**, 101533.

6 Z. Abdollahnejad, S. Miraldo, F. Pacheco-Torgal and J. B. Aguiar, *Eur. J. Environ. Civ. Eng.*, 2017, **21**, 412–429.

7 N. Bertelsen and B. V. Mathiesen, *Energies*, , DOI:10.3390/en13081894.

8 R. Gross and R. Hanna, *Nat. Energy*, 2019, **4**, 358–364.

9 A. Chapman, K. Itaoka, K. Hirose, F. T. Davidson, K. Nagasawa, A. C. Lloyd, M. E. Webber, Z. Kurban, S. Managi, T. Tamaki, M. C. Lewis, R. E. Hebner and Y. Fujii, *Int. J. Hydrogen Energy*, 2019, **44**, 6371–6382.

10 S. Roberts, *Energy Policy*, 2008, **36**, 4482–4486.

11 S. Schiavoni, F. D'Alessandro, F. Bianchi and F. Asdrubali, *Renew. Sustain. Energy Rev.*, 2016, **62**, 988–1011.

12 D. Densley Tingley, A. Hathway and B. Davison, *Build. Environ.*, 2015, **85**, 182–189.

13 M. S. Al-Homoud, *Build. Environ.*, 2005, **40**, 353–366.

14 S. Alsoy, *J. Cell. Plast.*, 1999, **35**, 247–271.

15 H. Zhang, W.-Z. Fang, Y.-M. Li and W.-Q. Tao, *Appl. Therm. Eng.*, 2017, **115**, 528–538.

16 U. Berardi and M. Naldi, *Energy Build.*, 2017, **144**, 262–275.

17 M. T. Bomberg, M. K. Kumaran, M. R. Ascough and R. G. Sylvester, *J. Therm. Envel. Build. Sci.*, 1991, **14**, 241–267.

18 T. Widya and C. W. Macosko, *J. Macromol. Sci. Part B*, 2005, **44**, 897–908.

19 H. Fleurent and S. Thijs, *J. Cell. Plast.*, 1995, **31**, 580–599.

20 I. R. Shankland, *J. Cell. Plast.*, 1993, **29**, 114–131.

21 G. Biesmans, M. Karremans, D. Randall and S. N. SIngh, *J. Cell. Plast.*, 1998, **34**, 349–359.

22 U. Berardi and J. Madzarevic, *Appl. Therm. Eng.*, 2020, **164**, 114440.

23 M. Szycher and P. D, *Szycher's Handbook of Polyurethanes, Second Edition*, CRC Press, 2012, vol. 37.

24 Kaneyoshi Ashida, *Polyurethane and Related Foams*, CRC Press LLC, 1st edn., 2006, vol. 58.

25 P. Bethevas, J. Bicerano, R. van den Bosch, J. Fosnaugh, R. de Genova, M. Brown, F. Casati, C. P. Christenson, P. Clavel and W. Farrissey, *Polymeric Foams: Mechanisms and Materials*, CRC Press LLC, 1st edn., 2004.

26 Y. Cheng, X. Wang, C. Jia, Y. Wang, L. Zhai, Q. Wang and D. Zhao, *J. Memb. Sci.*, 2017, **539**, 213–223.

27 Y. Peng and W. Yang, *Sci. China Chem.*, 2019, **62**, 1561–1575.

28 G. Liu, J. Tu, C. Wu, Y. Fu, C. Chu, Z. Zhu, X. Wang and M. Yan, *ACS Appl. Mater. Interfaces*, 2021, **13**, 20459–20466.

29 Y. Li, T. Wang and D. Liu, *Chem. – An Asian J.*, 2021, 1–7.

30 M. Gou, W. Zhu, Y. Sun and R. Guo, *Sep. Purif. Technol.*, 2021, **259**, 118107.

31 X. Bi, F. Zhang, S. Zhang, Z. Wang and J. Jin, *ACS Appl. Mater. Interfaces*, , DOI:10.1021/acsami.0c14639.

32 H. Kim, Y. Miura and C. W. MacOsko, *Chem. Mater.*, 2010, **22**, 3441–3450.

33 X. Wang, W. Xing, X. Feng, B. Yu, L. Song, G. H. Yeoh and Y. Hu, *Compos. Sci. Technol.*, 2016, **127**, 142–148.

34 J.-H. Oh, H. R. Lee, S. Umrao, Y. J. Kang and I.-K. Oh, *Carbon N. Y.*, 2019, **147**, 510–518.

35 J. Joy, J. Abraham, J. Sunny, J. Mathew and S. C. George, *Polym. Test.*, 2020, **87**, 106429.

36 A. K. Geim, *Science*, 2009, 324, 1530–1534.

37 W. Wu, J. Xu, X. Tang, P. Xie, X. Liu, J. Xu, H. Zhou, D. Zhang and T. Fan, *Chem. Mater.*, 2018, **30**, 5932–5940.

38 C. Defonseka, *Practical guide to flexible polyurethane foams practical guide to flexible polyurethane foams*, 2013.

39 Y. Song, Z. Jiang, B. Gao, H. Wang, M. Wang, Z. He, X. Cao and F. Pan, *Chem. Eng. Sci.*, 2018, **185**, 231–242.

40 Y. Tang, X. Zhang, P. Choi, Z. Xu and Q. Liu, *Langmuir*, 2018, **34**, 14196–14203.

41 P. Bampoulis, V. J. Teernstra, D. Lohse, H. J. W. Zandvliet and B. Poelsema, *J. Phys. Chem. C*, 2016, **120**, 27079–27084.

42 M. Ahmadi, S. Janakiram, Z. Dai, L. Ansaloni and L. Deng, *Membranes (Basel).*, 2018, **8**, 50.

Chapter 3

Rigid PIR Foams and their composites with Copper paddle-wheel MOFs and MONs

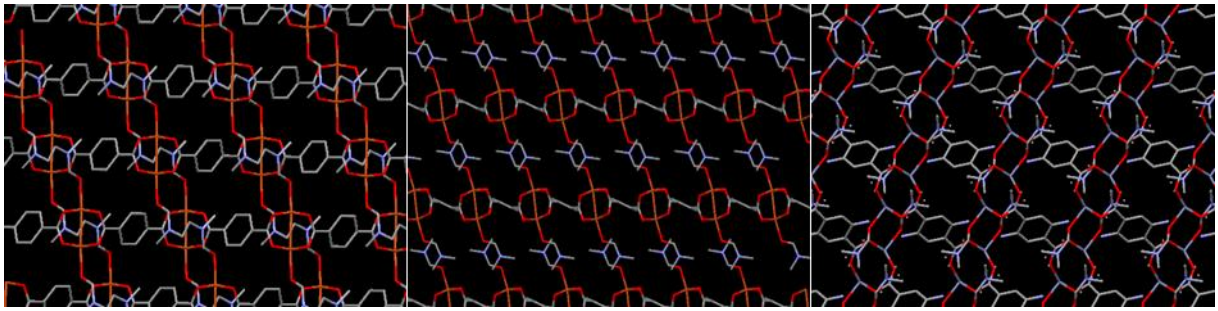

"But there is a limit to thinking about even a small piece of something monumental. You still see the shadow of the whole rearing up behind you, and you become lost in your thoughts in part from the panic of realizing the size of that imagined leviathan."

— The Biologist in Annihilation, by Jeff VanderMeer, an American author, editor, and literary critic.

3.1 – Introduction and Aims

The determination of an effective method for monitoring gas loss from composite rigid PIR foams was established in the previous chapter, allowing for the investigation into effective additives to be undertaken. The aim of the research in this chapter was to reduce the loss of blowing agent from Kingspan's PIR rigid foam through the addition of MOFs and MONs to the system, and evaluate what effects contribute to the reduction of blowing agent loss.

Copper paddle-wheel based MOFs were used to create composites that were tested for their mass loss under accelerated aging conditions. Following this, MONs were also tested to determine if any effects from the increased anisotropy of the MONs could affect the mass loss.

3.2 – Synthesis and analysis of Copper based paddle-wheel MOFs

The Foster group have reported a range of copper paddle-wheel MONs formed utilizing a range of different linkers[1]. These MONs are typically produced through liquid exfoliation of bulk layered MOFs, followed by centrifugation of the solution to remove any remaining unexfoliated bulk MOF and yield a supernatant containing MONs. This method, while being able to produce single layer thickness MONs in some cases, results in relatively low yields of material. As the accelerated aging method developed requires three repeats of a 0.1 % by weight additive (100 mg), bulk MOFs were used rather than exfoliated nanosheets in the first instance. This allowed for more rapid testing of possible systems to investigate the effect of the linkers being used with the copper paddle-wheel system, before establishing a scalable method for the production of MONs for the composite foams.

To create a starting point, three layered MOF systems were chosen: Cu(BDC)(DMF) (where BDC is 1,4-benzenedicarboxylate linker and DMF is the co-ordinated solvent dimethyl formamide), Cu(ABDC)(DMF) (where ABDC is 2-amino-1,4-benzenedicarboxylate) and a new system to the Foster group; Cu_2(BTetC)$(DMF)_2$ (where BTetC is a 1,2,4,5-benzene tetracarboxylate, and referred to as Cu(BTetC)(DMF) throughout the work for brevity).

The simple periodic structure produced between copper and the linkers chosen creates a layered material that can be exfoliated through liquid sonication. As one of the earliest MOF systems used by the group, it presents an ideal starting point as the synthesis, work-up and exfoliation of the system was well studied. Furthermore, copper paddle-wheel MONs use in separation applications of small molecules have been well documented[2–5], indicating possible use as a barrier for the larger pentanes used as the blowing agents.

The synthesis of the MOF can be influenced by a myriad of factors, such as the starting salt or reaction container. A recent study on a closely related system showed that utilizing copper nitrate solvothermally, with no stirring, can allow for the slow synthesis of large MOF crystals, which in turn can be exfoliated into large monolayer nanosheets in low yield[6]. In contrast, the use of copper acetate resulted in the growth of smaller MOF crystals, which could be exfoliated to produce high concentrations of few layer nanosheets with smaller lateral dimensions. As indicated by literature, to retain the closed cell nature of the foam, additives should have a smallest dimension (thickness) less than the cell wall of the foams, or a cell opening effect may occur[7]. Therefore, the synthesis of Cu(BDC)(DMF) and subsequent copper MOFs were undertaken utilizing copper acetate with stirring under heating (110 °C, 16 hours)[8].

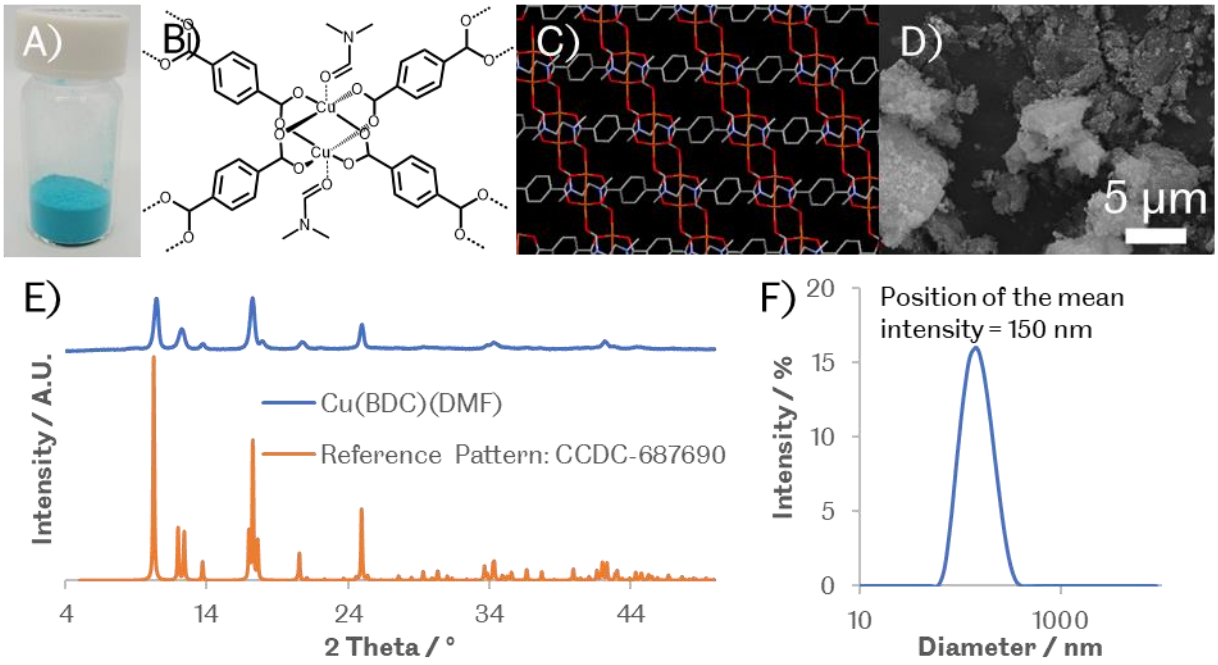

Figure 3.1 showing data for Cu(BDC)(DMF) MOF: A) photograph of MOF as-synthesised B) Chemdraw structure of the paddle-wheel, C) Expanded crystal motif, D) SEM image of the crushed MOF, E) PXRD of the MOF compared to a reference pattern (CCDC-687690)[9], and F) DLS of MOF in acetonitrile after sonication (37 kHz, 60 seconds).

After synthesis of all MOFs PXRD analysis was completed to determine any phase impurities that may exist in the structure, and a digested (where the MOF was broken down via acid/base into free linker and metal ions in solution) sample was created for NMR to determine if any impurities are in the pores of the MOF. Figure 3.1 shows the Cu(BDC)(DMF) synthesized has a PXRD pattern in close accordance with the literature structure, indicating no phase impurities. Furthermore, the NMR analysis (figure 3.11) shows minimal impurities, with some excess of DMF and a negligible amount of acetate still in the MOF structure. This was to be expected with the rapid synthesis of the MOF, and the difficulty of removal of solvents/reagents from the pores post synthesis. SEM imaging showed aggregated particles of the MOF, which DLS measurement in MeCN after dispersion with sonication (37 kHz for 60 seconds) had an average diameter of 150 nm.

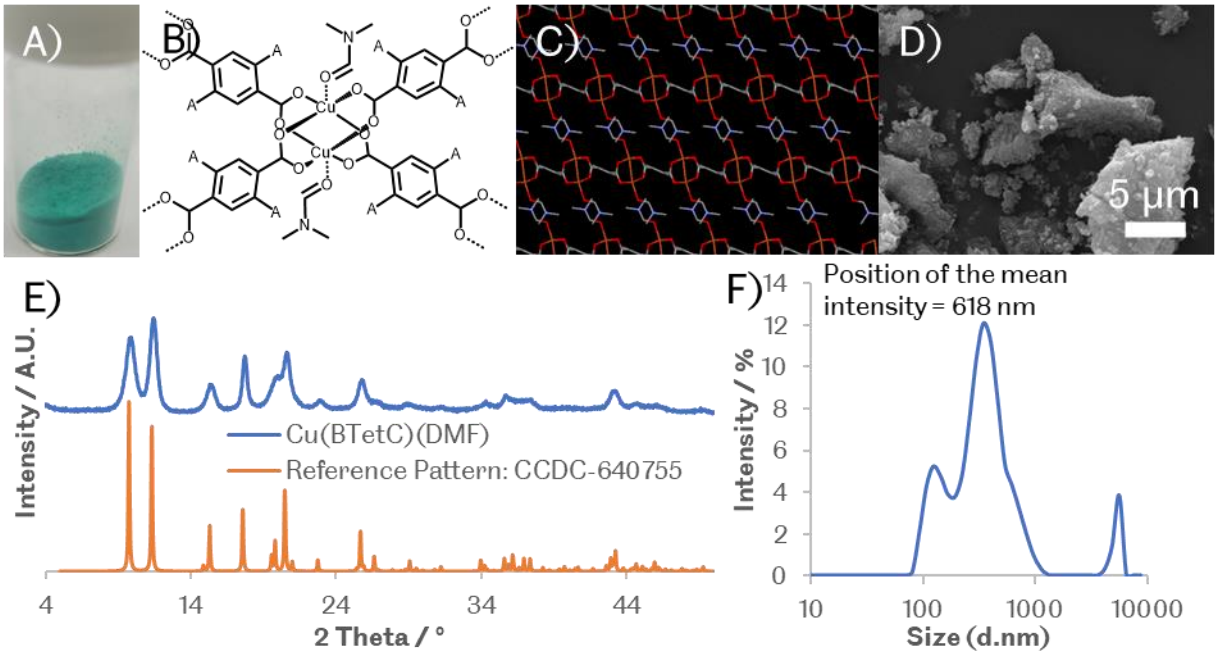

Figure 3.2 showing data for Cu(BTetC)(DMF) MOF: A) photograph of MOF as-synthesised B) Chemdraw structure of the paddle-wheel with additional carboxylic acid groups denoted as "A" for clarity, C) Expanded crystal motif, D) SEM image of the crushed MOF, E) PXRD of the MOF compared to a reference pattern (CCDC-640755)[10], and F) DLS of MOF in acetonitrile after sonication (37 kHz, 60 seconds).

As with the previous MOF, the previously reported Cu(BTetC)(DMF) was synthesised, under the same conditions as Cu(BDC)(DMF) and forms a similar paddle-wheel structure, though with a denser structure in the x and y plane, whilst still being layered in the z plane. The MOFs PXRD pattern showed a good match for the reference compound with no additional peaks. NMR (figure 3.18) showed the expected ratio of DMF to ligand confirming the MOF was formed as previously reported. SEM (figure 3.2) again demonstrated aggregated particles, where DLS measurement provided an average size of 618 nm. This MOF was selected to determine if any effects from a denser structure would create differences in the barrier effectiveness when the composite was synthesized.

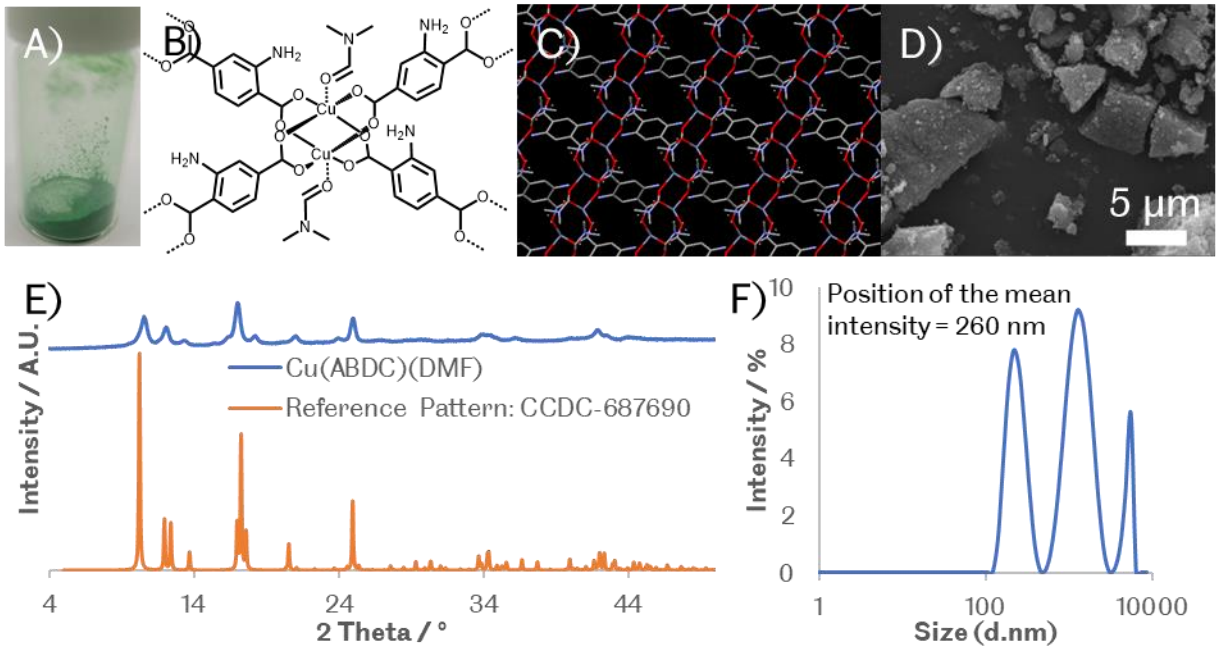

Figure 3.4 showing data for Cu(ABDC)(DMF) MOF: A) photograph of MOF as-synthesised B) Chemdraw structure of the paddle-wheel, C) Expanded crystal motif, D) SEM image of the crushed MOF, E) PXRD of the MOF compared to a reference pattern (CCDC-687690)[9], and F) DLS of MOF in acetonitrile after sonication (37 kHz, 60 seconds).

Cu(ABDC)(DMF) presents an additional alternative to the Cu(BDC)(DMF) system. Again, it is a paddle-wheel system synthesised under the same reaction conditions, but the use of amino-terephthalic acid as the linker introduces amine functionality to the group. Cu(ABDC)(DMF) presents a MOF that can be covalently linked into the polyurethane system, where isocyanate groups can react with the pendent amine to form a urea. Whilst the Cu(BDC)(DMF) and Cu(BTetC)(DMF) MOFs have carboxylic acid groups that could be utilized for covalent attachment at the edges of the MOF, within the crystal structure each carboxylic acid was co-ordinated to a copper centre, making the functionality negligible. The possible reaction between the isocyanate and the amine may allow the MOF to become better integrated into the polyurethane system over the others, avoiding possible void space formation around the MOF due to incompatible surface interactions. Figure 3.4 shows the high purity of the MOF synthesized from the PXRD and NMR analysis provided, where no additional phase impurities

are present in the PXRD pattern, and negligible acetate impurities are present in the NMR spectra (figure 3.25).

Cu(ABDC)(DMF) has been previously utilized for post synthetic functionalization (PSF), where a pre-synthesized MOF's functional groups are utilised to attach alternative groups to alter the MOF/MONs functionality, for example, where a 1,3-propansultone ring was opened onto the amine groups present in Cu(ABDC)(DMF)[8]. This technique allows for the targeting of functionalities that would not be available under a pre-synthetic approach, where the linkers are modified before the MOF was synthesized, as a different structure may be formed. So, Cu(ABDC)(DMF) can be altered to present different functional groups that may be useful to the barrier properties of the composite foam.

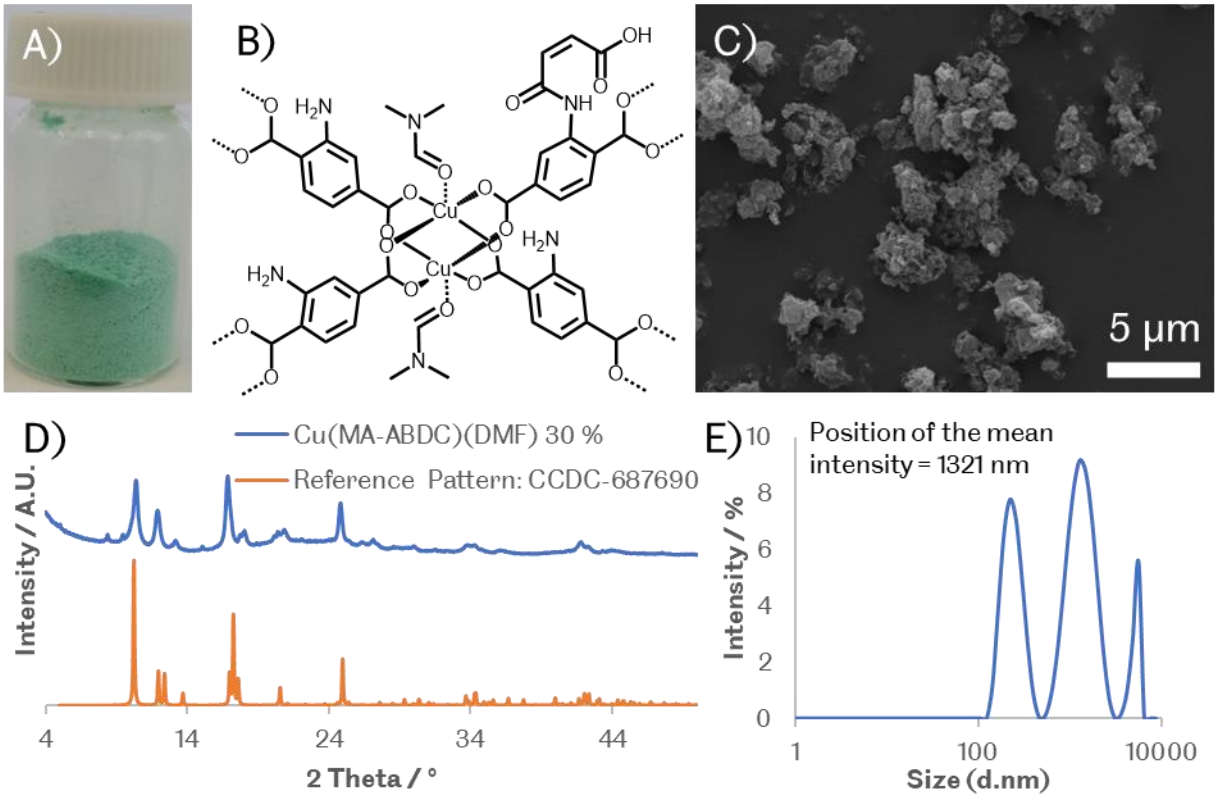

Figure 3.5 showing data for Cu(MA-ABDC)(DMF) MOF: A) photograph of MOF as-synthesised B) Chemdraw structure of the paddle-wheel, C) SEM image of the crushed MOF, D) PXRD of the MOF compared to a reference pattern (CCDC-687690)[9], and E) DLS of MOF in acetonitrile after sonication (37 kHz, 60 seconds).

The details of Cu(MA-ABDC)(DMF)'s synthesis and additional properties can be found in chapter 5, but the purpose of its synthesis was to alter the surface chemistry of the Cu(ABDC)(DMF) system. The Cu(ABDC)(DMF) MOF was reacted with maleic anhydride over 24 hours, ring-opening the maleic anhydride on the amine groups present in ABDC, resulting in a functionalized MOF dubbed Cu(MA-ABDC)(DMF). The introduction of functional groups to the surface can, and in this case, does aid in better exfoliation of the MOF, and in some cases create a more stable material. For addition to the foam, a 31 % functionalization (where 31 % of the ABDC linkers are reacted with maleic anhydride to form an amide) was utilized to provide the highest introduction of carboxylic acid groups to the layers of the MOF without alteration to the structure. These carboxylic acid groups on the surface can react with isocyanates to form amide bonds (through an anhydride intermediate, removing CO_2 to form the amide) to the structure, providing a possible alternative attachment into the PIR system.

As seen in figure 3.5, the powder pattern of Cu(MA-ABDC)(DMF) matches closely with Cu(ABDC)(DMF), with some minor peaks appearing, likely due to desolvation effects during the post-synthetic functionalization step[8]. The NMR spectra shows the functionalization to be 31 %, where the conversion of the ABDC amine to amide pushes the aromatic peaks downfield as they become more deshielded. These amine and amide aromatic peaks are compared to determine the degree of functionalization of the MOF.

3.3 – Synthesis and accelerated aging of Copper based paddle-wheel MOF composite foams

Each Copper based paddle-wheel MOF described in the previous section was used in the synthesis of composite foams. As with the previous composites, 100 mg of each additive (in this case, the MOF) was added to Part A of the foam mixture and blended with Part B to create a 0.1 % composite foam. These foams were analysed for cell size, closed cell percentage and mass loss during accelerated aging.

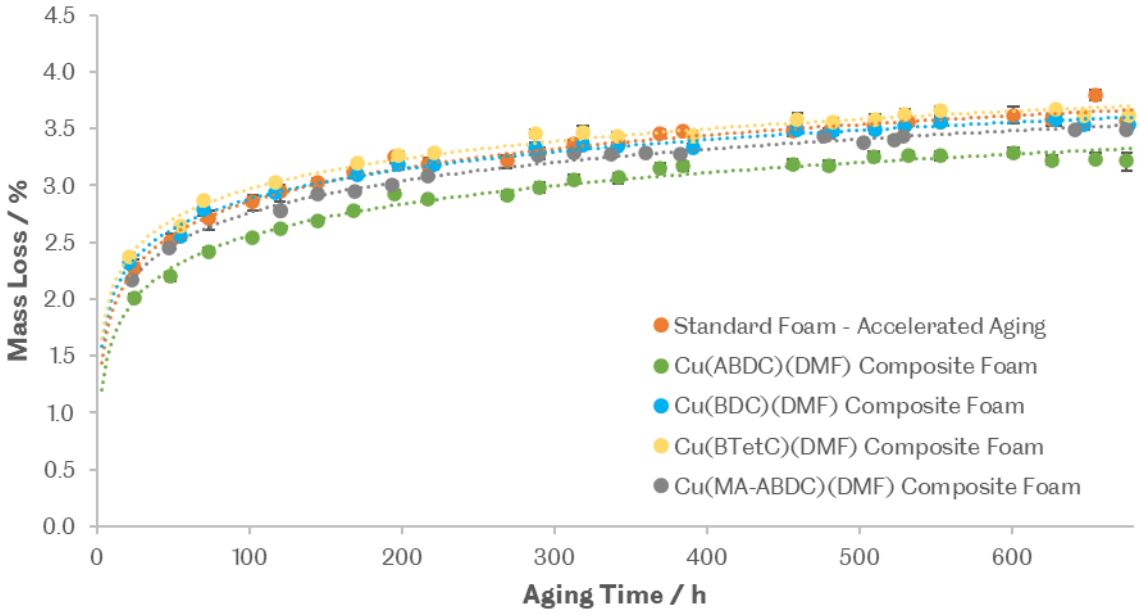

Figure 3.6 Comparison of the mass loss composite rigid PIR foams over time.

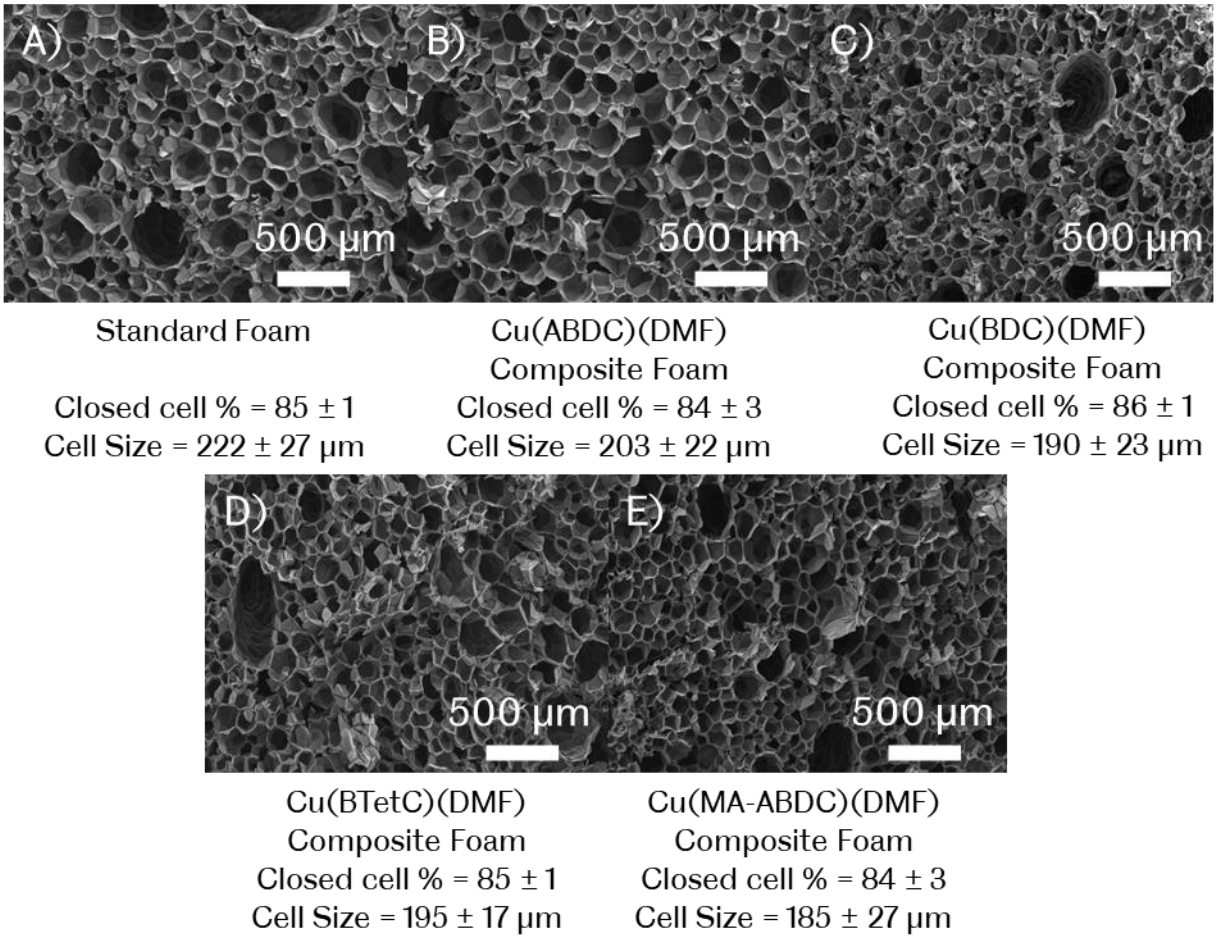

Figure 3.7 SEM Images, and corresponding closed cell content and cell size, of rigid PIR foams with additives : A) No Additive, B) Cu(ABDC)(DMF), C) Cu(BDC)(DMF), D) Cu(BTetC)(DMF), E) Cu(MA-ABDC)(DMF)

Figure 3.6 shows the mass loss of different composite foams containing a Copper based paddle-wheel MOF. Each curve shows the logarithmic decay observed with previous standard and MoS_2/Graphite composites, with the composite mass loss being in the order: Cu(BTetC)(DMF) > standard foam > Cu(BDC)(DMF) > Cu(MA-ABDC)(DMF) > Cu(ABDC)(DMF). Therefore, in this series Cu(BTetC)(DMF) performed as the worst MOF for retention of blowing agent, and Cu(ABDC)(DMF) performed as the best.

To understand the effect that the different MOFs had on the structure of the foam, the average cell size was measured via SEM and the closed cell content measured by pycnometry,

displayed in figure 3.7. The average closed cell content ranged between 84 to 86% the variation was within the experimental error and essentially that of the standard foams. The average cell size dropped from an average of 222 µm for the standard foam to between 196- 183 µm for the foams containing MOFs, although all of these are within experimental error and there was no clear correlation between cell size and performance. These results indicate that the differences in performance can't be explained by macroscopic changes in the cell size or fraction of closed cells.

To determine if particle size also played a factor into the mass retention, the MOFs were analysed via DLS to gain insight into the diameter of the MOFs added to the foam. The size of the MOFs from smallest to largest (determined by DLS) are as follows: Cu(MA-ABDC)(DMF) > Cu(BTetC)(DMF) > Cu(ABDC)(DMF) > Cu(BDC)(DMF). This size hierarchy does not correspond to the mass retention results seen from the composite foams, and therefore also does not explain the changes in performance of the composites.

When considering surface functionality, both Cu(ABDC)(DMF) and Cu(MA-ABDC)(DMF) contain amine groups on their linkers. Cu(MA-ABDC)(DMF) having 31 % less amine groups than Cu(ABDC)(DMF). The addition of amine groups appeared to increase the mass retention of the composite, with a higher amine functionality demonstrating better mass retention.

Overall, the use of MOF-Foam composites shows greater mass retention than the graphite or MoS_2 previously used. Only Cu(BTetC)(DMF) showed a small increase in mass loss when compared to the standard foam, where all other MOFs used increased mass retention. This indicates a possible repulsive effect between the Cu(BTetC)(DMF) system, possibly creating voids[11,12] between cell walls allowing the increase in mass loss.

Cu(ABDC)(DMF) shows the only demonstrably increased barrier effect on the foams, which could be attributed to the amine groups accessible on the surface of the MOF allowing for better incorporation into the polymer network through reactions with the isocyanate groups.

3.4 – Synthesis and accelerated aging of Copper based paddle-wheel MON composite foams

As previously discussed, MONs are highly anisotropic nanosheets of MOFs, typically obtained through top-down exfoliation of a layered MOF to obtain down to single-layered MONs for analysis and application.

Typical exfoliation of the copper MOFs involved mixing 5 mg of MOF in 6 mL of acetonitrile (MeCN) and placing a vial of this mixture into a sonicator bath at 80 kHz for 12 hours. Then the crude MON solution was centrifuged at 1500 rpm for 1 hour to remove larger particulates. To be able to effectively produce, then test, MONs in the PIR foams, the typical exfoliation procedure was scaled-up (200 mg in 240 mL). These bulk exfoliations of MONs were then either centrifuged to remove any bulk unexfoliated material (centrifuged MONs) or left without this centrifugation step to increase yield (uncentrifuged MONs).

Prior discussion highlights the development of this technique to require 100 mg of additive per foam tested, and with this scale of MON production not currently produced by the Foster group, led to the need of the separation of the centrifuged vs uncentrifuged MONs, outlined in figure 3.8.

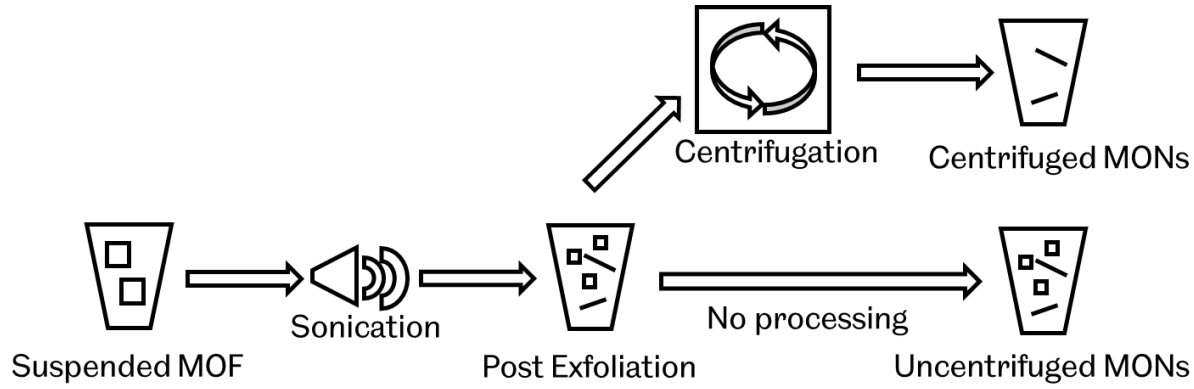

Figure 3.8 Simplified diagram for the production of centrifuged vs. uncentrifuged MONs.

Whilst uncentrifuged MONs would not showcase the ideal scenario with ultrathin materials being added into a composite foam, the significantly increased yields would provide a greater benefit from a cost and waste perspective, whilst allowing some interpretation into the size effects of additives into the composite foams.

Centrifugation resulted in the removal of the larger particulates and so reduced the average size of the additive (table 3.10). Introduction of MONs pre- and post- centrifugation was therefore used to explore the influence of size on mass loss from the foams.

Additionally, both centrifuged and uncentrifuged MONs are dried through additional high centrifugation (12,000 rpm, 30 mins, then removal of any supernatant) and desiccation of the remaining solids prior to being added into the foam. The introduction of solvents into the foam mixture would lead to a failure to produce rigid PIR foams, therefore a dry powder addition was the only viable method to introduce MONs to the system. This may lead to restacking of MON layers or alteration of the MON size from mechanical damage. Therefore, the use of pre and post centrifugation nanosheets will further aid in the interpretation of the size effects on the foams, as if there was no discernible difference between the pre and post centrifuged MONs, then any drying effects can be further investigated to analyse how the MONs behave post drying.

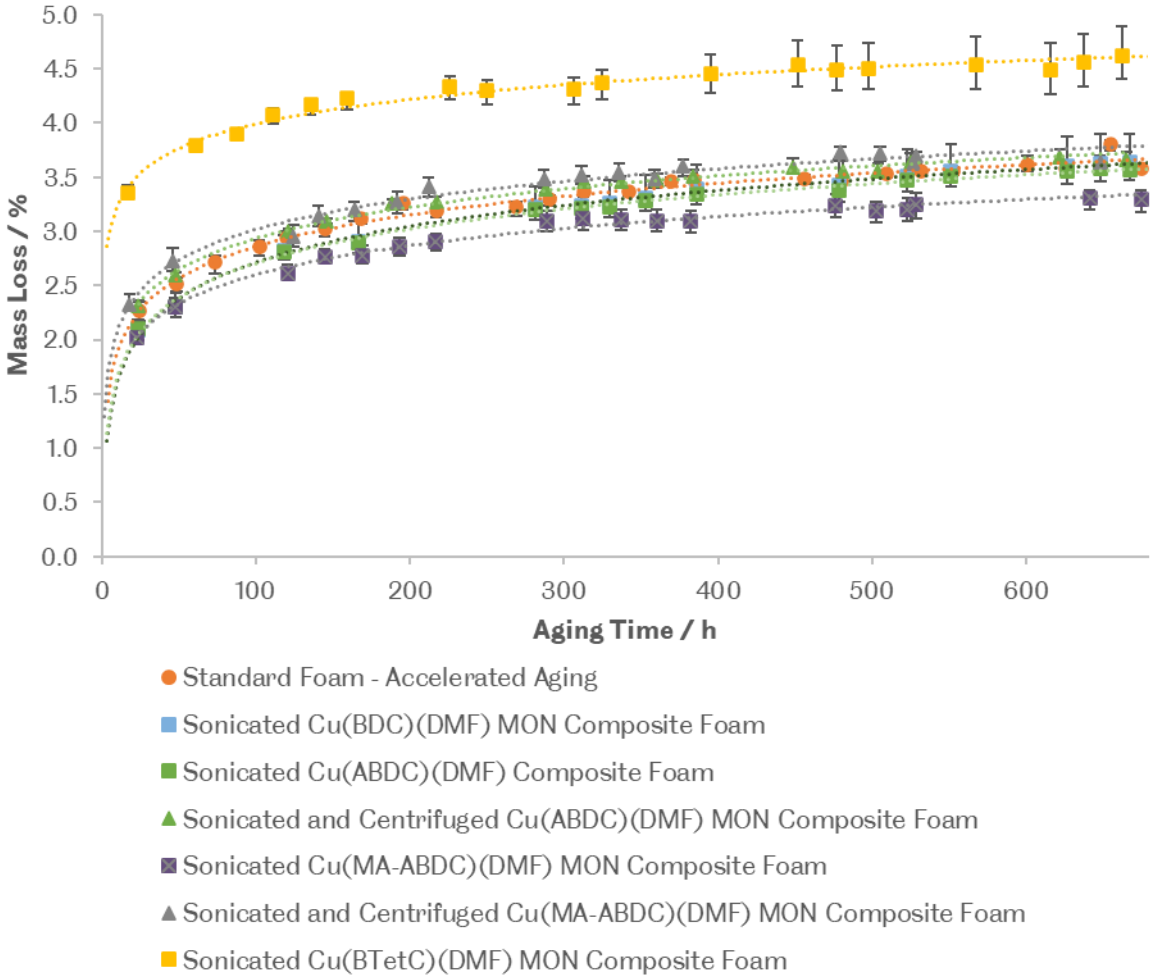

Figure 3.9 Comparison of the mass loss of both centrifuged and uncentrifuged MON composite rigid PIR foams over time.

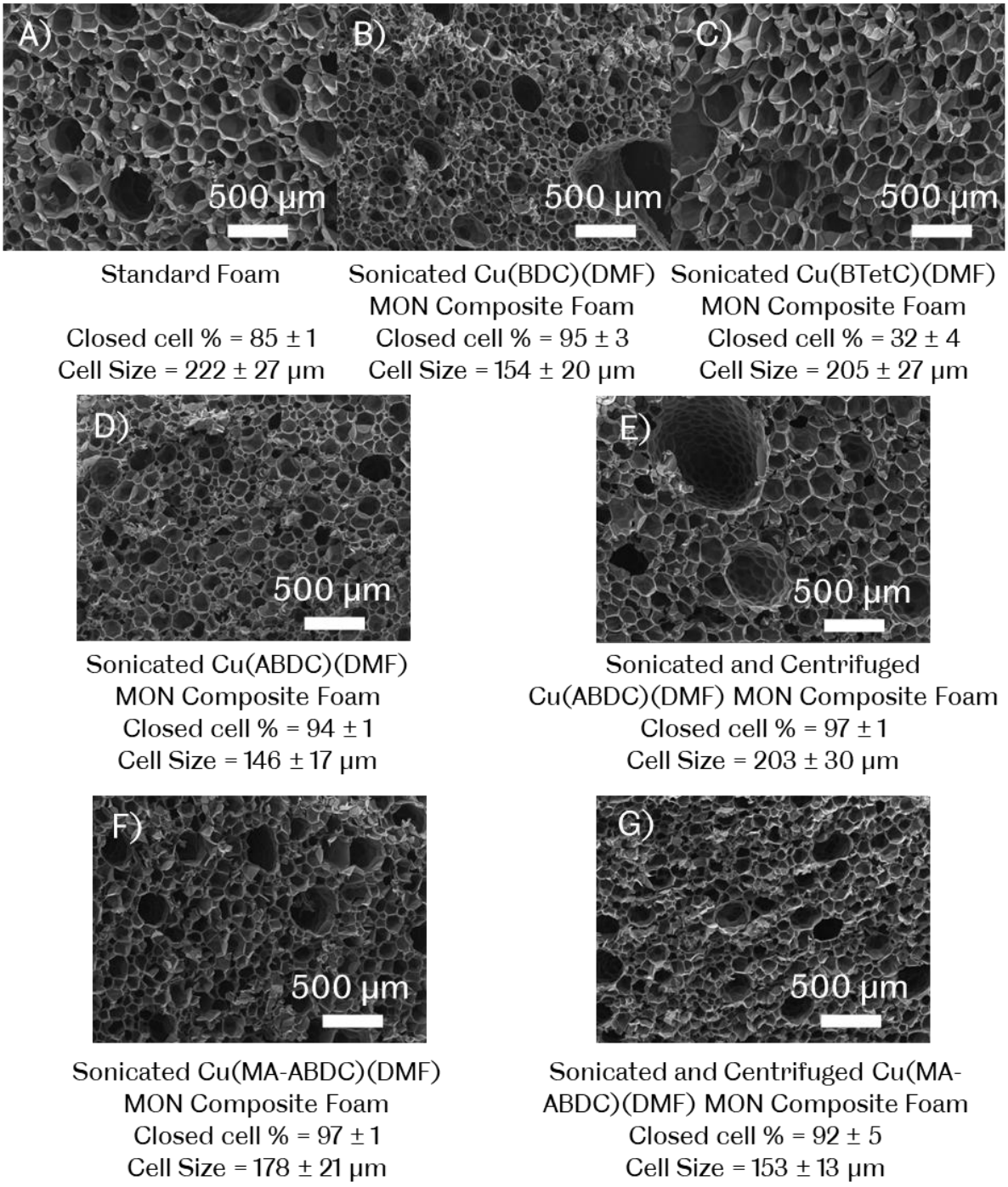

Figure 3.10 SEM Images, and corresponding closed cell content and cell size, of rigid PIR foams with additives: A) No Additive, B) Sonicated Cu(BDC)(DMF) MON Composite Foam, C) Sonicated Cu(BTetC)(DMF) MON Composite Foam, D) Sonicated Cu(ABDC)(DMF) MON Composite Foam, E) Sonicated and Centrifuged Cu(ABDC)(DMF) MON Composite Foam, F) Sonicated Cu(MA-ABDC)(DMF) MON Composite Foam, and G) Sonicated and Centrifuged Cu(MA-ABDC)(DMF) MON Composite Foam.

MON System	DLS position of the mean intensity / nm	DLS PdI	AFM average width / nm	AFM average height / nm
Cu(BDC)(DMF) Uncentrifuged	180	0.143	N/A	N/A
Cu(ABDC)(DMF) Uncentrifuged	581	0.413	N/A	N/A
Cu(ABDC)(DMF) Centrifuged	290	0.386	125 ± 49	22 ± 17
Cu(BTetC)(DMF) Uncentrifuged	693	0.457	N/A	N.A
Cu(MA-ABDC)(DMF) Uncentrifuged	951	0.608	N/A	N/A
Cu(MA-ABDC)(DMF) Centrifuged	552	0.375	60 ± 10	2 ± 1

Table 3.1 Table comparing the size of uncentrifuged, and centrifuged MONs based upon DLS or AFM data. All data for MONs were recorded in their respective exfoliation solvent. AFM data is not presented for uncentrifuged material as particulates would be too large for the technique to measure effectively.

Figure 3.9 shows the mass loss across multiple different composite foams containing either centrifuged or uncentrifuged MONs, with a reference foam also included for comparison. All show typical logarithmic decay as seen in all other results. Centrifuged Cu(ABDC)(DMF) MONs show a slight increase, compared to the standard foam, in the mass loss over the aging period. All other composite foams show a decrease in mass loss over the time period, with the lowest mass loss being attributed to the uncentrifuged Cu(MA-ABDC)(DMF) MONs composite foam. The composite mass loss being in the order: Cu(BTetC)(DMF) uncentrifuged MONs > Cu(ABDC)(DMF) centrifuged MONs > standard foam ≈ all other MON data sets > Cu(MA-ABDC)(DMF) uncentrifuged MONs.

Table 3.1 shows the sizes of MONs measured by DLS and AFM. AFM data was not provided for uncentrifuged MONs due to larger particulates making analysis unviable by AFM. DLS data

shows for both Cu(ABDC)(DMF) and Cu(MA-ABDC)(DMF) the mean intensity of the data was reduced when the MON solution was centrifuged, indicating an overall reduction in particulate size.

The addition of uncentrifuged copper MONs to the PIR foams shows an unexpected trend in figure 3.9, where the Cu(BDC)(DMF) uncentrifuged MONs show a minor improvement on barrier quality over their parent MOFs, but Cu(ABDC)(DMF) and Cu(BTetC)(DMF) shows a poorer quality barrier. Though, Cu(BtTetC)(DMF) uncentrifuged MONs increase can be attributed to the significant reduction in closed cell content due to poor interaction between MON and polymer, as seen with the parent MOF, now increased due to the increased surface area of the MONs. All other MONs demonstrated an increase in closed cell content, indicating a stabilization of the cell walls.

When centrifuged Cu(ABDC)(DMF) MONs were used, the mass loss was further increased compared to both the base MOF and the uncentrifuged material. The lower stability of the Cu(ABDC)(DMF) MOF was attributed to this behaviour, as the amine groups result in a weaker structure that was more rapidly broken down under mild conditions such as in water when compared with Cu(BDC)(DMF) or Cu(BTetC)(DMF)[8,13]. With the increased surface area compared to volume, it was likely the MONs have undergone some degradation and lost their structural integrity, resulting in poorer barrier performance. Therefore, the stability of these MOFs and MONs are in question within the PIR foam.

This comparison can further be shown between Cu(ABDC)(DMF) and Cu(MA-ABDC)(DMF), where the addition of the maleic anhydride to the linker changes the chemistry and stability of the MOF produced, likely allowing Cu(MA-ABDC)(DMF) to better survive the foaming conditions of the composite over Cu(ABDC)(DMF). This may further attribute to the initial determination that the Cu(ABDC)(DMF) MOF performed significantly better than other copper MOFs, the reduction in the overall size of the MOFs due to degradation in the foaming

steps allows for smaller particulates to be added to the foam, allowing Cu(ABDC)(DMF) MOF to provide a better barrier to mass loss.

A similar effect may also cause the decrease of barrier effectiveness of uncentrifuged Cu(MA-ABDC)(DMF) (3.5 % mass loss at 28 days) over centrifuged Cu(MA-ABDC)(DMF) (3.3 % mass loss at 28 days). Whilst the parent MOF has some higher stability over Cu(ABDC)(DMF) in the composite foam, the increase in surface area from uncentrifuged to centrifuged MONs resulted in a higher degree of breakdown in the systems and therefore the demonstrated decrease in barrier properties.

Therefore, Cu(BDC)(DMF) and Cu(BTetC)(DMF) were not further selected for post centrifugation addition, as the stability and interaction of the copper MOFs were brought into question, and the focus was placed on determining a more stable MOF/MON system to utilize.

Additionally, the average cell size (figure 3.10) for the MON systems are lower than any other MOF systems previously used. Therefore, the additives may have acted as nucleation sites and allowed more bubbles to be formed, resulting in a lower cell size to be reached. A lower cell size average would contribute to retention of gas in the foam system, indicating the addition of MONs are creating routes for gas loss not present in the base foam.

Overall, the addition of an uncentrifuged Cu(MA-ABDC)(DMF) MONs provided the best retention of mass of all MONs added, whilst the use of centrifuged Cu(MA-ABDC)(DMF) MONs provided the lowest retention of mass off all MONs added. This was likely due to a mixture of factors, from stability of the MONs in the foam, to effective nucleation of bubbles during foaming and alteration of the closed cell content of the system.

3.5 – Conclusions and Future Work

In conclusion, a variety of copper-based paddle-wheel MOFs and MONs have been synthesized and successfully incorporated at a 0.1 % by weight addition into composite rigid PIR foams. The addition of Copper Paddle-wheel MOFs and MONs can reduce the loss of blowing agent from

rigid PIR foams (3.58 ± 0.04 % at 28 days), with depending on the specific MOF utilized and the centrifugation of the MON used. For MOFs, Cu(ABDC)(DMF) a 0.1 % addition provides the greatest mass retention (3.22 ± 0.09 % at 28 days), where this effect was possibly attributed to the amine functionality of the MOF, or degradation of the MOF size during foaming allowing for an optimally sized additive to be incorporated.

The addition of MONs was separated into two distinct groups, centrifuged and uncentrifuged, where uncentrifuged Cu(MA-ABDC)(DMF)) at 0.1 % addition provides the greatest mass retention (3.29 ± 0.11 % at 28 days). Though, no patterns could be determined between centrifuged and uncentrifuged MONs or functionalities of those used, suggesting further investigation of exfoliation of copper paddle-wheel MONs for addition to rigid PIR composites was needed.

The variation in mass retention between MOFs and MONs demonstrates the complexity of the project, where multiple factors such as the functionality or size of the MOF/MON can affect multiple results such as cell size or closed cell content. Therefore, for future work, investigation of a wider variety of functionalization's, through post-synthetic functionalization of Cu(ABDC)(DMF) could be explored to further determine how functionality effects gas loss. Further exploration into the centrifugation of MONs to target specific sizes could also be utilized to find an ideal size of MON in thickness to add to rigid PIR foam for the optimal integration of the MON into the foam system for gas retention.

3.6 – Experimental

General techniques utilized across multiple chapters can be found in chapter 7. Namely, elemental analysis, Fourier transform infrared spectroscopy, nuclear magnetic resonance, powder x-ray diffraction, liquid assisted exfoliation of MONs, dynamic light scattering, atomic force microscopy, determination of MON sizes, scanning electron microscopy, pycnometry and determination of cell sizes.

3.6.1 – Foam Synthesis

Rigid PIR foam was synthesized according to Kingspan's formulation. A "part A" was initially mixed using a polyol and all additives used in the formulation, in a 1 L cardboard Kingspan cup. Once blended using an overhead stirrer (3000 rpm, 10 seconds), pMDI was added on top of the part A mixture and the blended again (3000 rpm, 10 seconds). The total mass of the mixture was 100 g when all components are charged. For composite foams, the total mass was reduced to accommodate the percentage loading of the additive chosen (*e.g.* a 0.1 % loading will use a total of 99.9 g of foam formulation and 0.1 g of additive). The additive was incorporated into the part A mixture prior to mixing.

For accelerated aging measurements, after the foam had stopped rising, it was left to cool for 24 hours. The head of the foam (all foam above the lip of the cup) was then removed by cutting with an insulation saw. The decapitated foam was again left to rest for a further 24 hours before a baseline weight was obtained. The foam was then placed into an oven at 70 °C and periodically weighed over 28 days.

Foam	Closed Cell Content / %	Cell Size / nm	Mass loss at 28 Days / %
No Additives	85 ± 1	222 ± 27	3.58 ± 0.04
Cu(BDC)(DMF) MOF	88 ± 7	190 ± 23	3.54 ± 0.05
Cu(BDC)(DMF) Uncentrifuged MON	95 ± 3	146 ± 17	3.64 ± 0.23
Cu(BTetC)(DMF) MOF	85 ± 1	195 ± 17	3.62 ± 0.03
Cu(BTetC)(DMF) Uncentrifuged MON	32 ± 4	205 ± 27	4.62 ± 0.25
Cu(ABDC)(DMF) MOF	84 ± 3	203 ± 22	3.22 ± 0.09
Cu(ABDC)(DMF) Uncentrifuged MON	94 ± 1	154 ± 20	3.57 ± 0.06
Cu(ABDC)(DMF) Centrifuged MON	97 ± 1	203 ± 30	3.66 ± 0.07
Cu(MA-ABDC)(DMF) MOF	84 ± 3	185 ± 27	3.50 ± 0.02
Cu(MA-ABDC)(DMF) Uncentrifuged MON	97 ± 1	178 ± 21	3.29 ± 0.11
Cu(MA-ABDC)(DMF) Centrifuged MON	92 ± 5	153 ± 13	3.64 ± 0.08

Table 3.2 Table of foams synthesized and analysed for accelerated aging experiments, showing closed cell content, cell size and mass loss after 28 days.

3.6.2– Synthesis and Exfoliation of Cu(BDC)(DMF)

Copper acetate monohydrate (1.092 g, 5.47 mmol) and terephthalic acid (0.908 g, 5.47 mmol) were separately dissolved in DMF (95 mL). After dissolution, the solutions were combined and stirred at 110 °C under nitrogen from 16 hours. The reaction mixture was centrifuged (12,000 rpm, 10 mins), the supernatant removed, and the solids washed via centrifugation (12,000 rpm, 10 mins) in DMF (3 x 30 mL), then diethyl ether (3 x 30 mL). The sample was dried under desiccation, producing Cu(BDC)(DMF) as a light blue powder. Yield 49.6 % (based on Cu). Elemental analysis: calculated mass for $CuC_{12}H_{12}NO_5$ %: C 43.89; H 3.75; N 4.654 Found mass %: C 43.52; H 3.76; N 4.58. Phase purity confirmed by PXRD (flat plate) comparison (CCDC entry 687690).

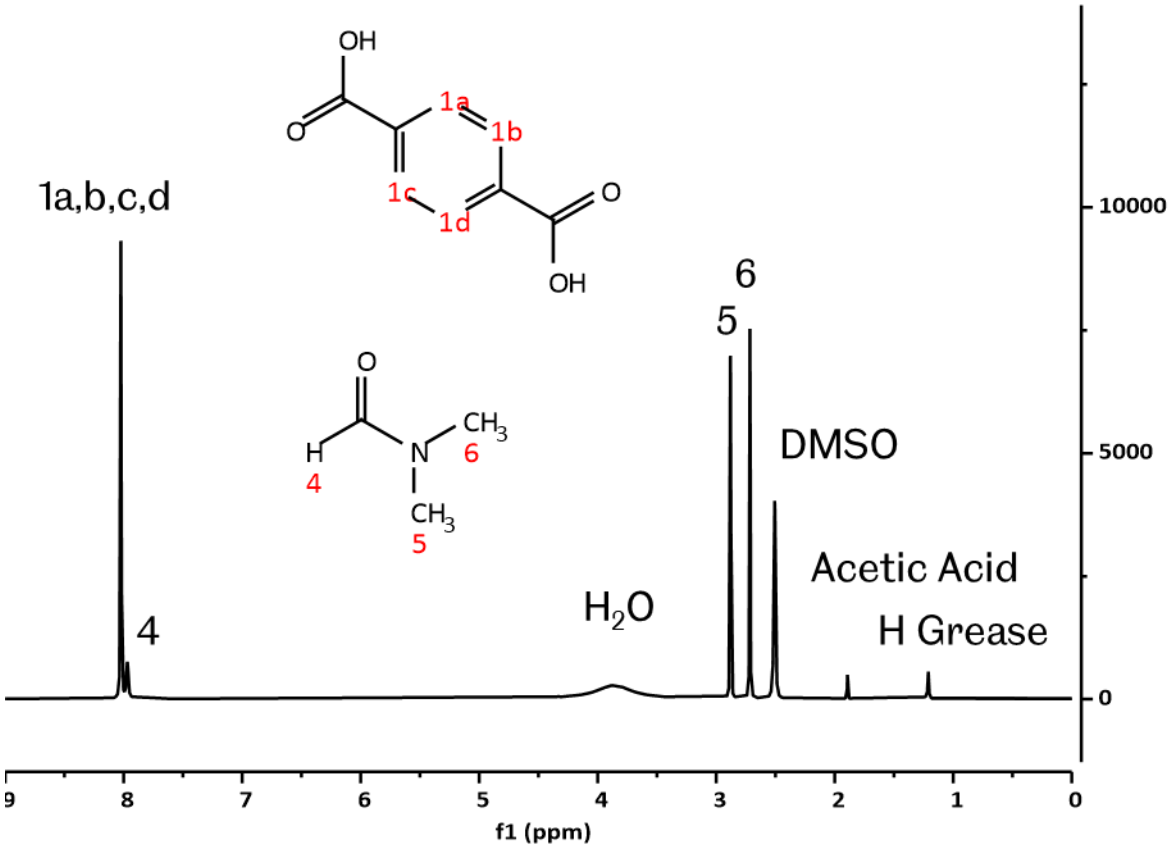

Figure 3.11 ^{1}H NMR spectrum of Cu(BDC)(DMF) digested with DCl/DMSO-d_6 with peaks assigned according to the inset molecular structures. The unassigned peak at 1.90 ppm corresponds to residual acetate.

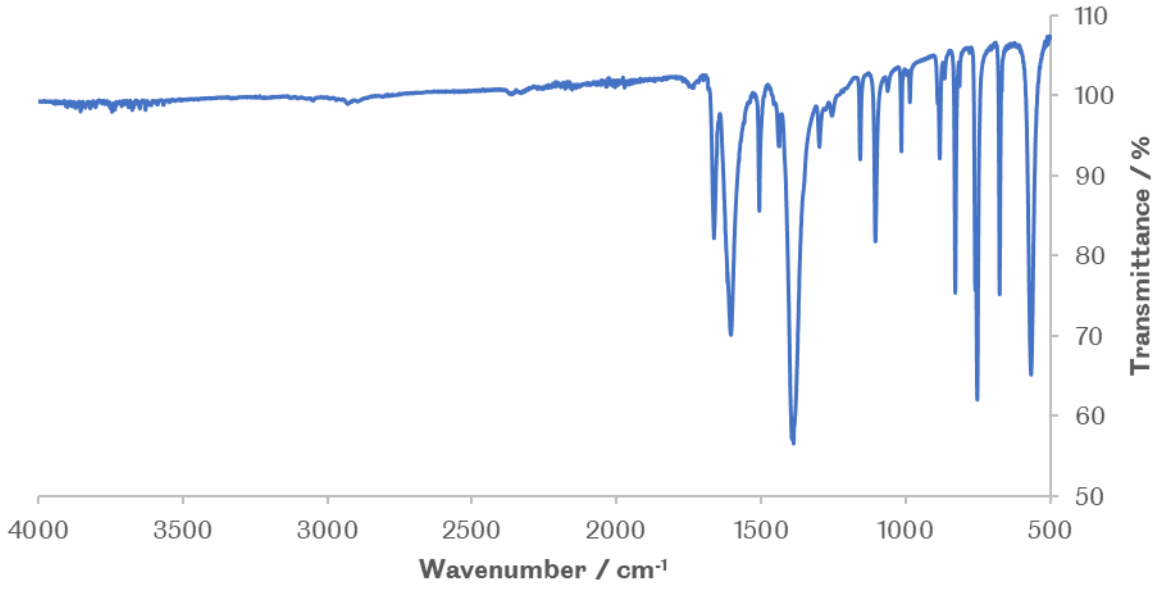

Figure 3.12 ATR FT-IR spectrum of Cu(BDC)(DMF)

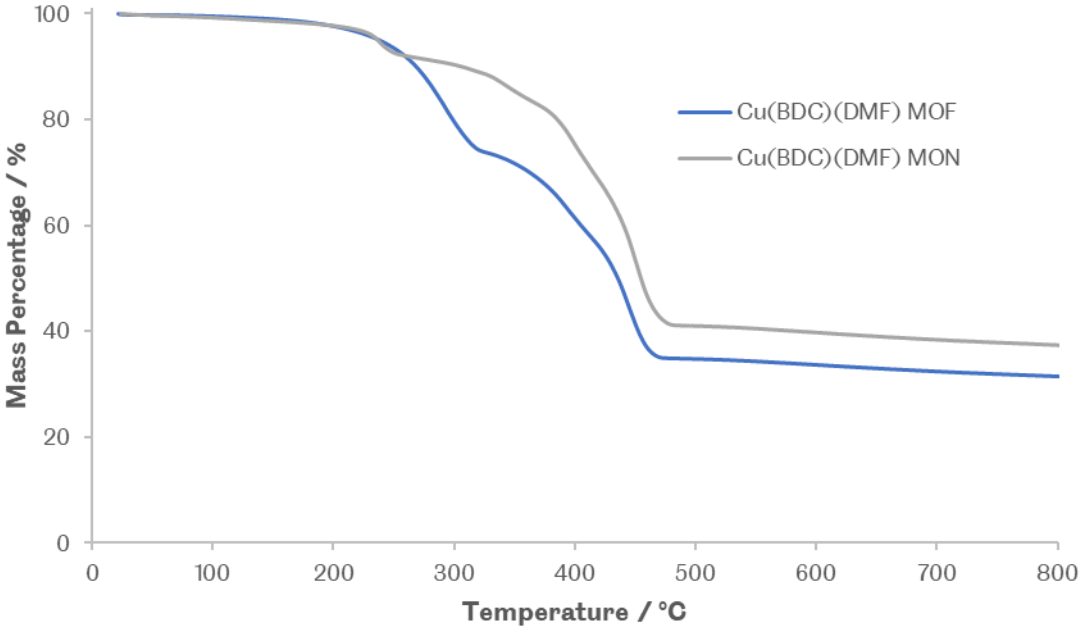

Figure 3.13 TGA plot of Cu(BDC)(DMF)

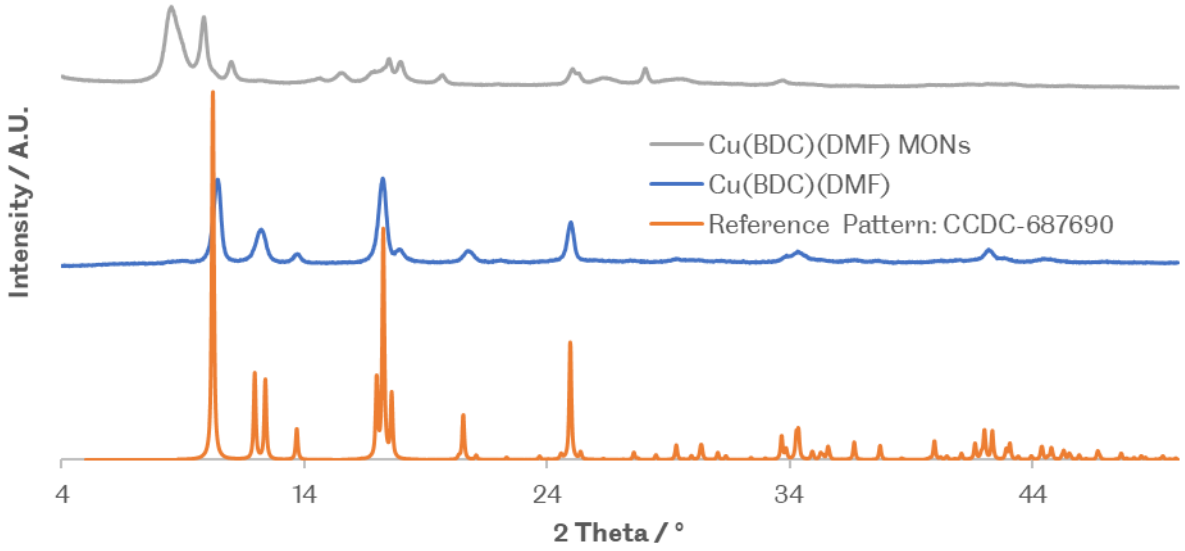

Figure 3.14 PXRD pattern of Cu(BDC)(DMF) pre and post exfoliation compared to a literature standard taken from CCDC[9].

Cu(BDC)(DMF) was exfoliated via liquid assisted ultrasonication as described in the exfoliation method section. A solution of Cu(BDC)(DMF) in acetonitrile (0.83 $mgmL^{-1}$) was used and

sonicated at 80 kHz for 12 hours. Uncentrifuged MON yield: 75.0 % (by mass). The additional peaks seen in the MONs are attributed to the desolvation of the MOF structure causing a phase change during exfoliation in MeCN to a non-layered structure, previously discussed by Ashworth *et. al.*.[14]

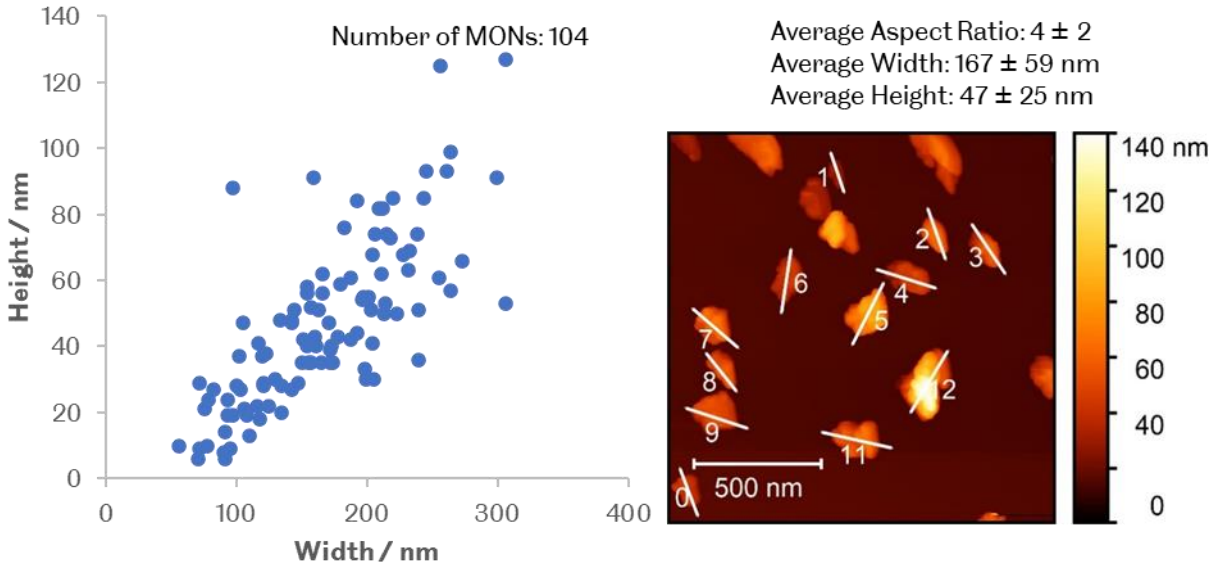

Figure 3.15 Scatter graph and example image of the height and width distribution of Cu(BDC)(DMF) nanosheets

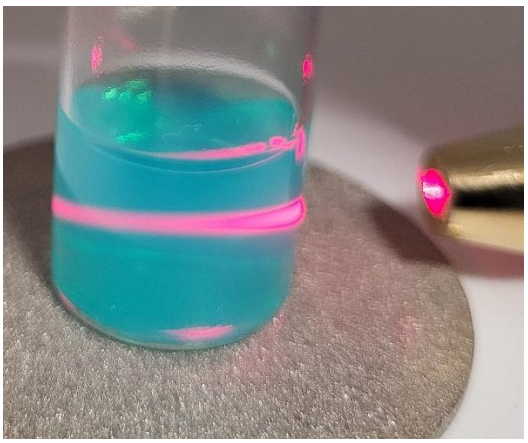

Figure 3.16 Tyndall scattering of Cu(BDC)(DMF) nanosheet suspended in acetonitrile

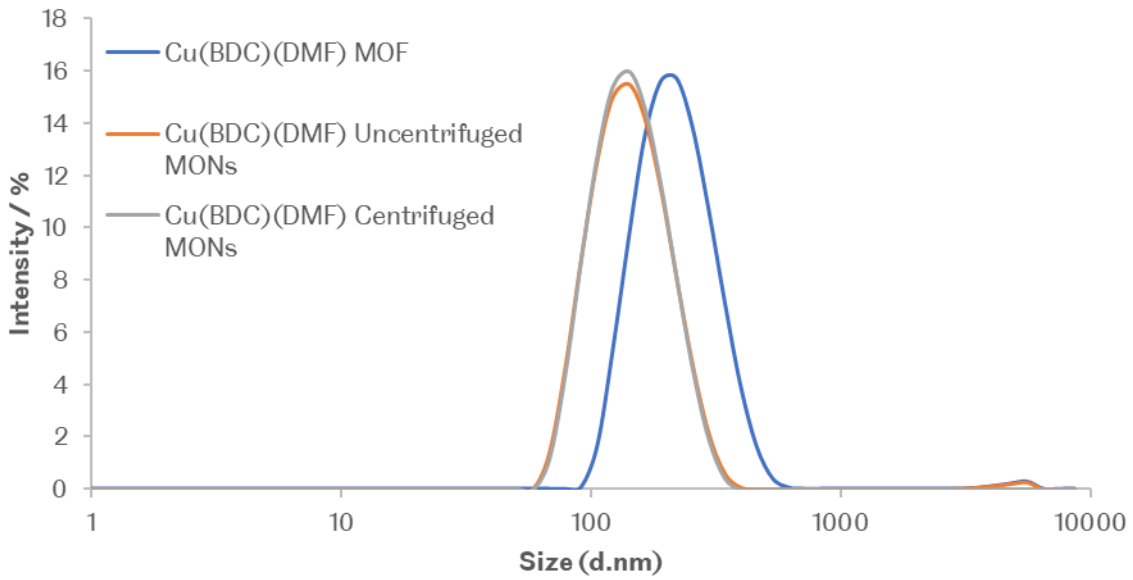

Figure 3.17 DLS analysis of Cu(BDC)(DMF) MOF and MONs when suspended in MeCN

Sample Name	PdI	Position of the mean intensity (d.nm)
Cu(BDC)(DMF) MOF	0.145	258.1
Cu(BDC)(DMF) Uncentrifuged MON	0.143	180.4
Cu(BDC)(DMF) Centrifuged MON	0.128	150.5

Table 3.3 DLS analysis of Cu(BDC)(DMF) MOF and MONs when suspended in MeCN

3.6.3 – Synthesis and Exfoliation of Cu(BTetC)(DMF)

Copper acetate monohydrate (1.222 g, 6.12 mmol) and 1, 2, 4, 5-Benzenetetracarboxylic acid (0.778 g, 3.06 mmol) were separately dissolved in DMF (95 mL). After dissolution, the solutions were combined and stirred at 110 °C under nitrogen from 16 hours. The reaction mixture was centrifuged (12,000 rpm, 10 mins), the supernatant removed, and the solids washed via centrifugation (12,000 rpm, 10 mins) in DMF (3 x 30 mL), then diethyl ether (3 x 30 mL). The sample was dried under desiccation, producing Cu(BTetC)(DMF) as a light teal powder. Yield 58.9 % (based on Cu). Elemental analysis: calculated mass for $CuC_8H_9NO_5$ %: C 36.88; H 3.17; N 5.20; Found mass %: C 36.48; H 3.49; N 5.55. Phase purity confirmed by PXRD (flat plate) comparison (CCDC entry 640755).

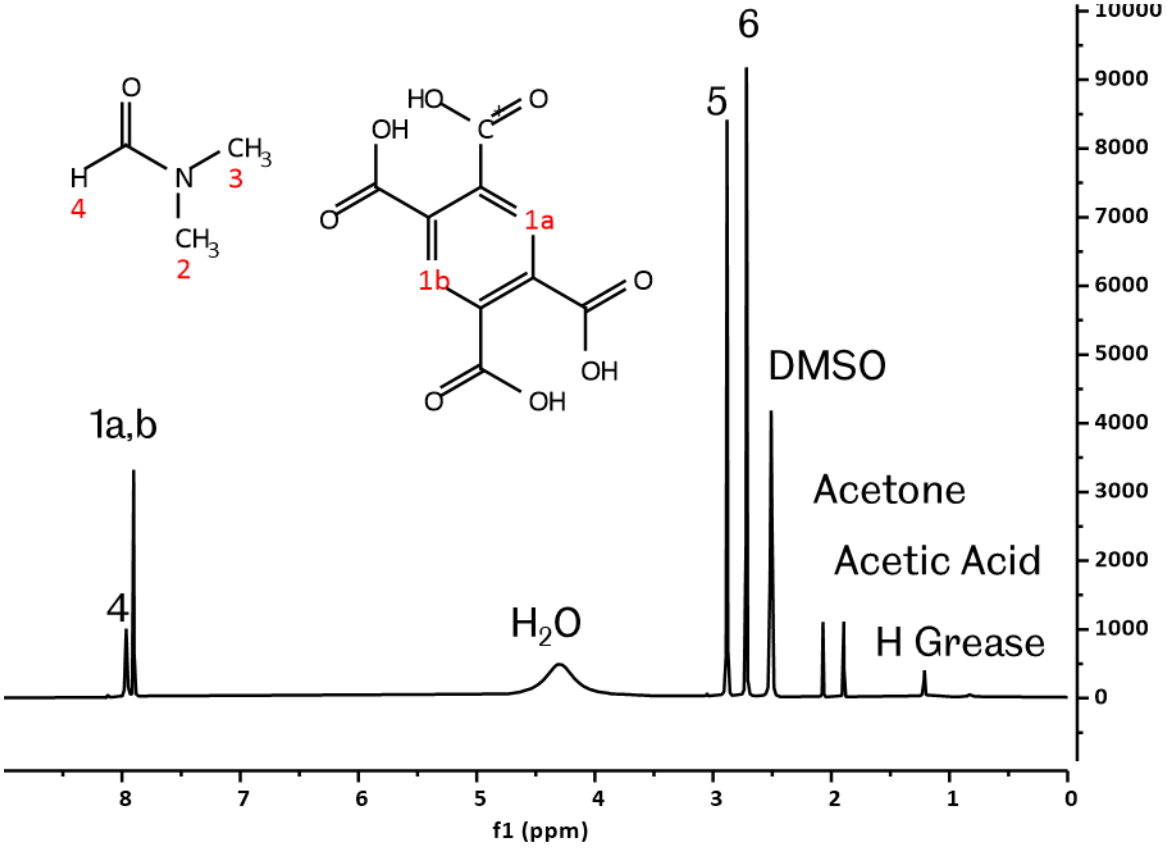

Figure 3.18 ^{1}H NMR spectrum of Cu(BTetC)(DMF) digested with DCl/DMSO-d_6 with peaks assigned according to the inset molecular structures.

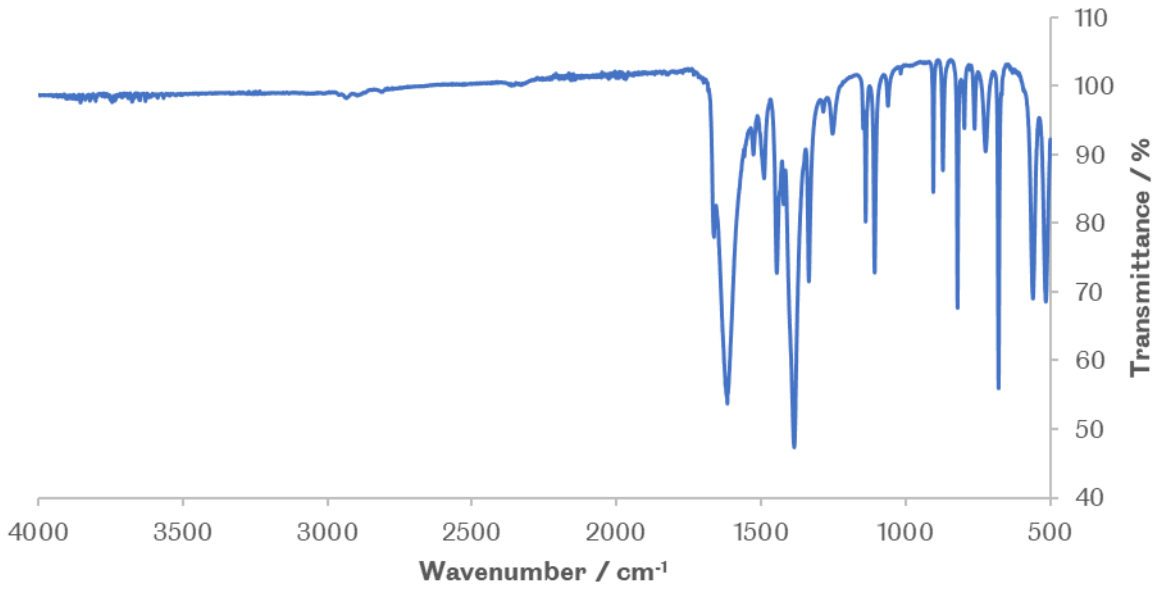

Figure 3.19 ATR FT-IR spectrum of Cu(BTetC)(DMF)

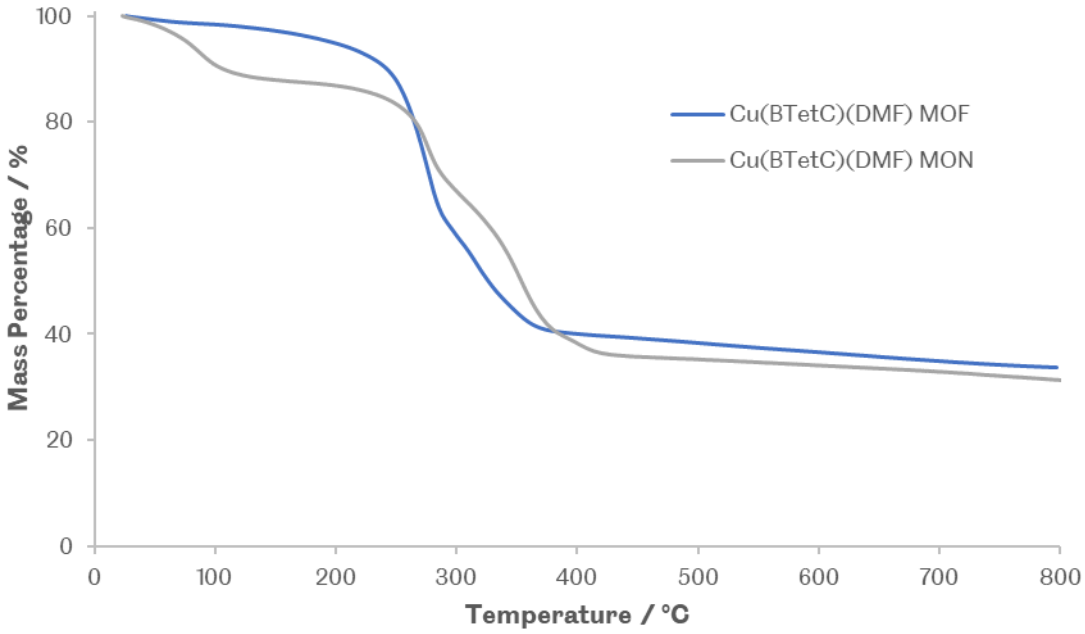

Figure 3.20 TGA plot of Cu(BTetC)(DMF)

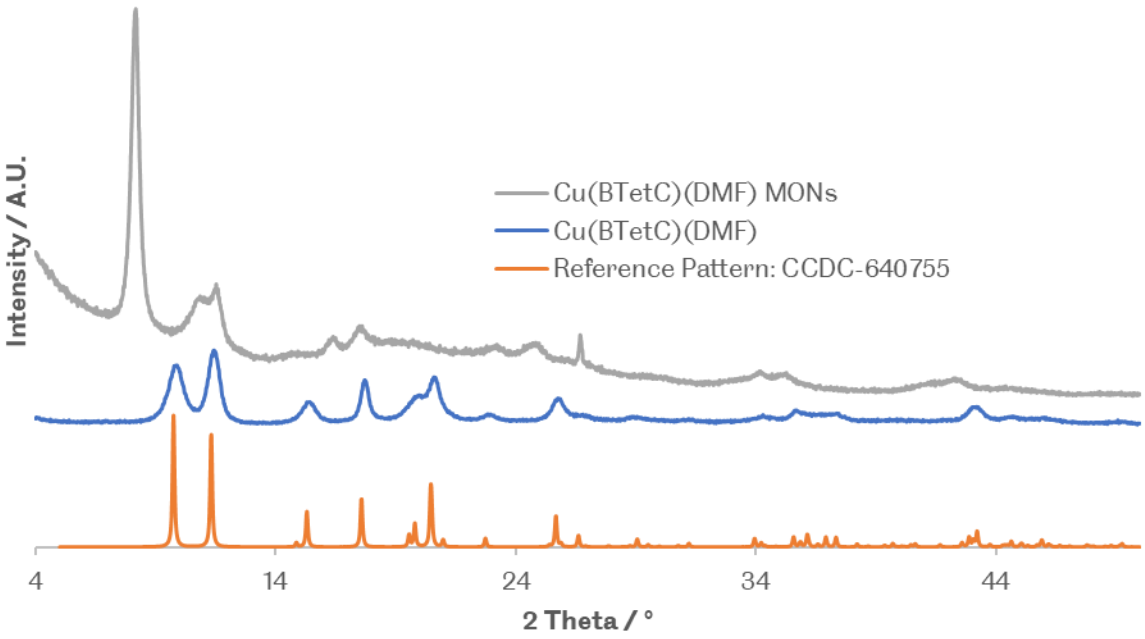

Figure 3.21 PXRD pattern of Cu(BTetC)(DMF) pre and post exfoliation compared to a literature standard taken from CCDC[10].

Cu(BTetC)(DMF) was exfoliated via liquid assisted ultrasonication as described in the exfoliation method section. A solution of Cu(BTetC)(DMF) in acetonitrile (0.83 $mgmL^{-1}$) was used and sonicated at 80 kHz for 12 hours. Uncentrifuged MON yield: 83.7 % (by mass). The additional peaks seen in the MONs are also attributed to the desolvation of the MOF structure similar to those seen in Cu(BDC)(DMF).

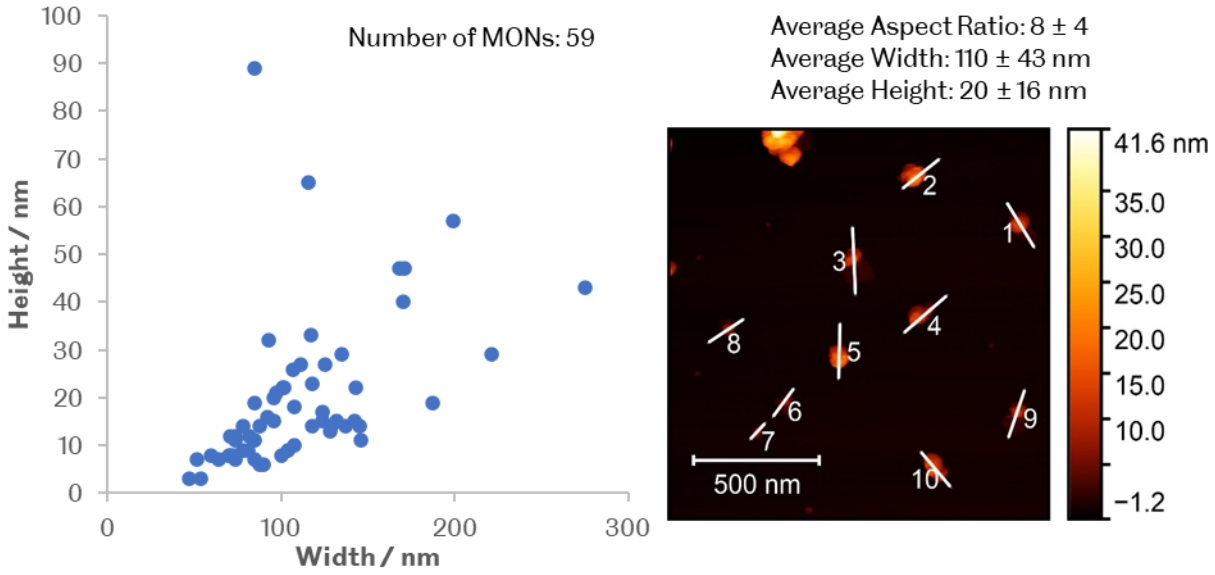

Figure 3.22 Scatter graph and example image of the height and width distribution of Cu(BTetC)(DMF) nanosheets.

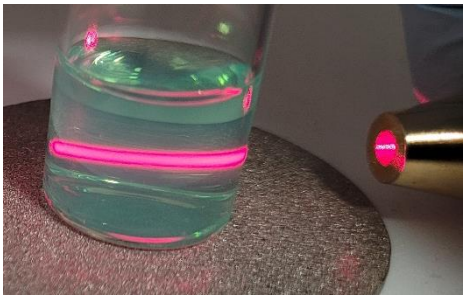

Figure 3.23 Tyndall scattering of Cu(BTetC)(DMF) nanosheet suspended in acetonitrile.

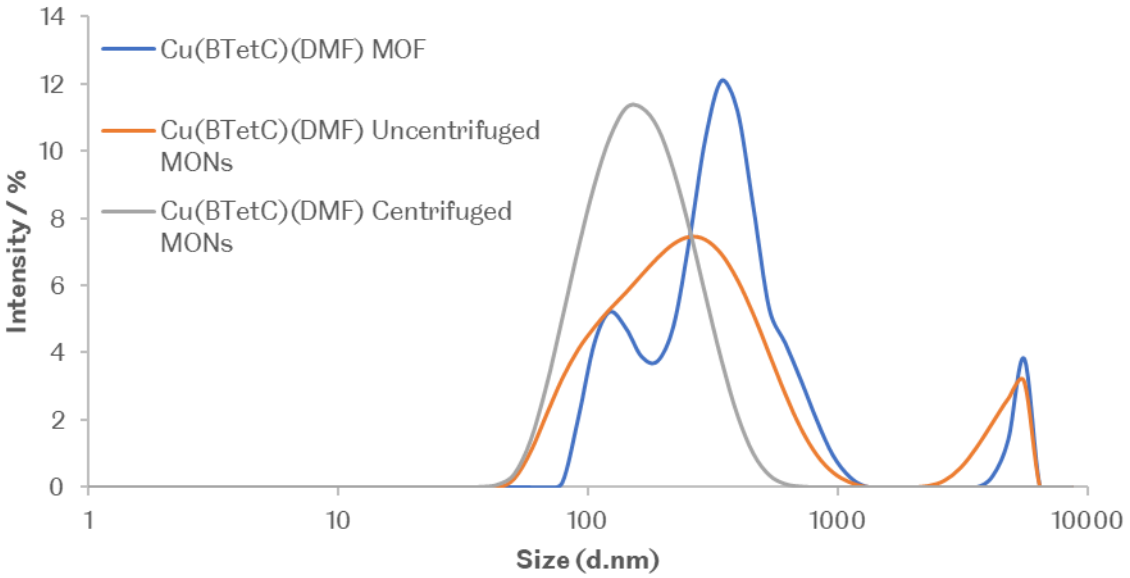

Figure 3.24 DLS analysis of Cu(BTetC)(DMF) MOF and MONs when suspended in MeCN

Sample Name	PdI	Position of the mean intensity (d.nm)
Cu(BTetC)(DMF) MOF	0.606	618.1
Cu(BTetC)(DMF) Uncentrifuged MONs	0.457	693.2
Cu(BTetC)(DMF) Centrifuged MONs	0.169	176.5

Table 3.4 DLS analysis of Cu(BTetC)(DMF) MOF and MONs when suspended in MeCN

3.6.4 – Synthesis and Exfoliation of Cu(ABDC)(DMF)

Copper acetate monohydrate (1.048 g, 5.25 mmol) and aminoterephthalic acid (0.952 g, 5.25 mmol) were separately dissolved in DMF (95 mL). After dissolution, the solutions were combined and stirred at 110 °C under nitrogen from 16 hours. The reaction mixture was centrifuged (12,000 rpm, 10 mins), the supernatant removed, and the solids washed via centrifugation (12,000 rpm, 10 mins) in DMF (3 x 30 mL), then diethyl ether (3 x 30 mL). The sample was dried under desiccation, producing Cu(ABDC)(DMF) as a green powder. Yield: 84.4 % (based on Cu). Elemental analysis: calculated mass for $CuC_{11}H_{13}N_2O_5$ %: C 41.85; H 3.89; N 8.63; Found mass %: C 41.43; H 3.97; N 8.58. Phase purity confirmed by PXRD (flat plate) comparison (CCDC entry 687690).

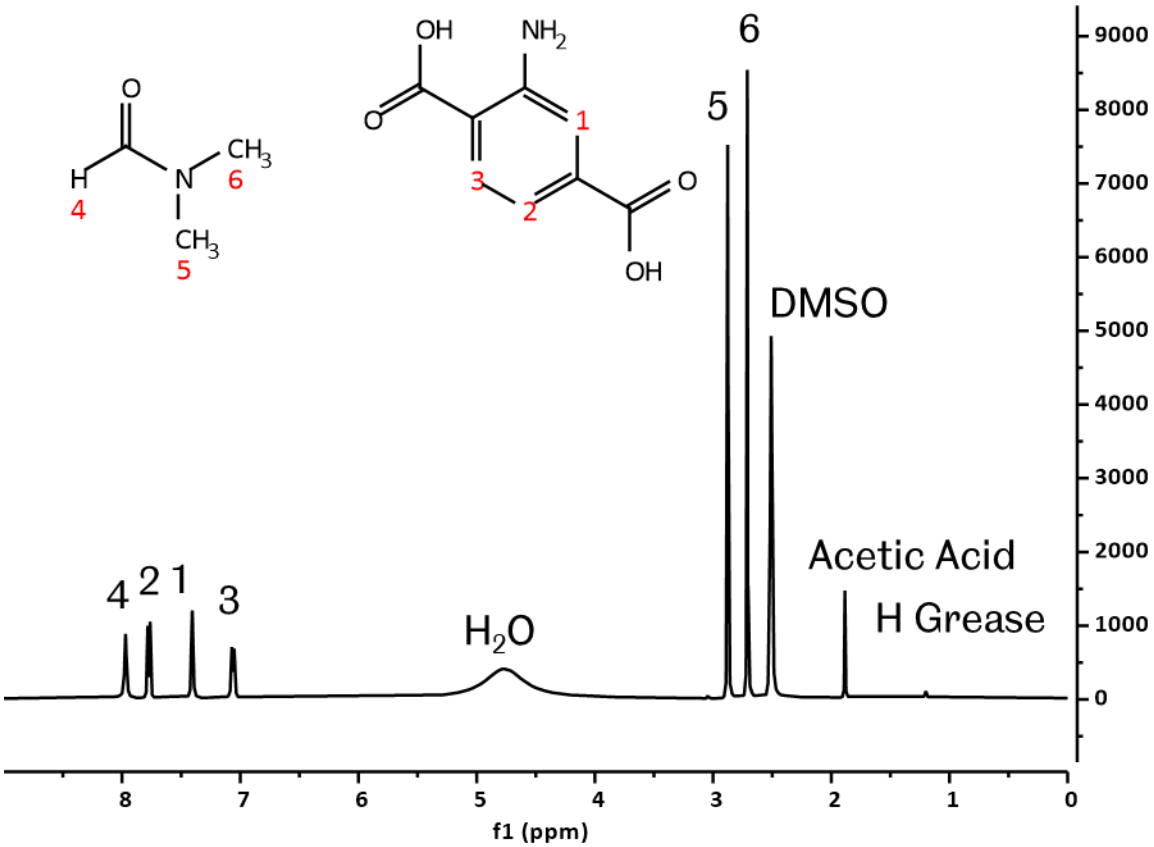

Figure 3.25 ^{1}H NMR spectrum of Cu(ABDC)(DMF) digested with DCl/DMSO-d_6 with peaks assigned according to the inset molecular structures. The unassigned peak at 1.90 ppm corresponds to residual acetate.

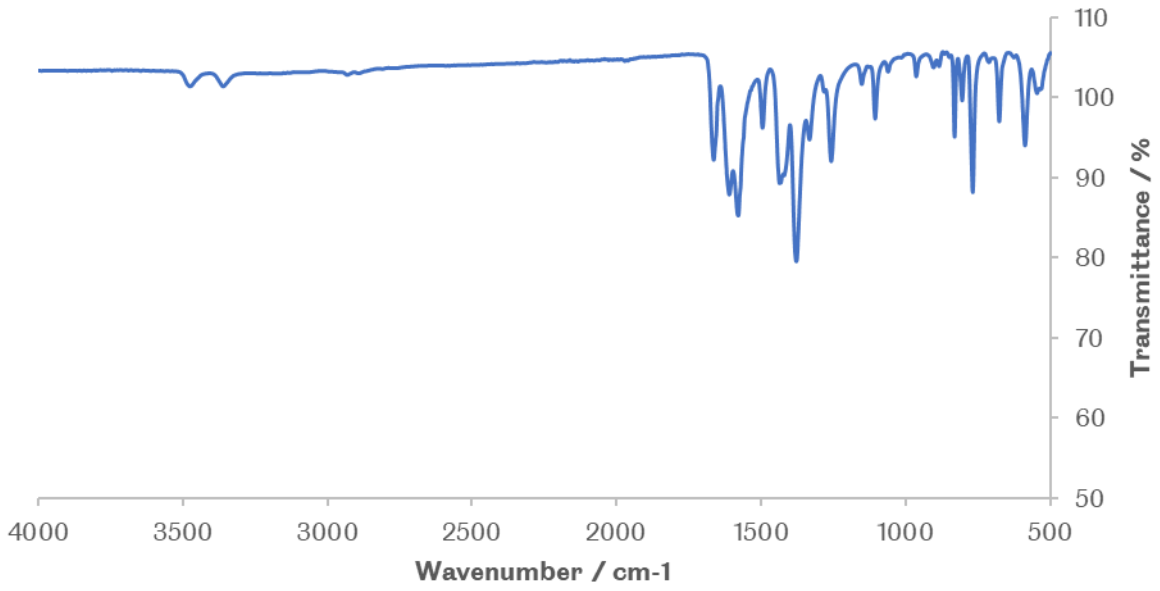

Figure 3.26 ATR FT-IR spectrum of Cu(ABDC)(DMF)

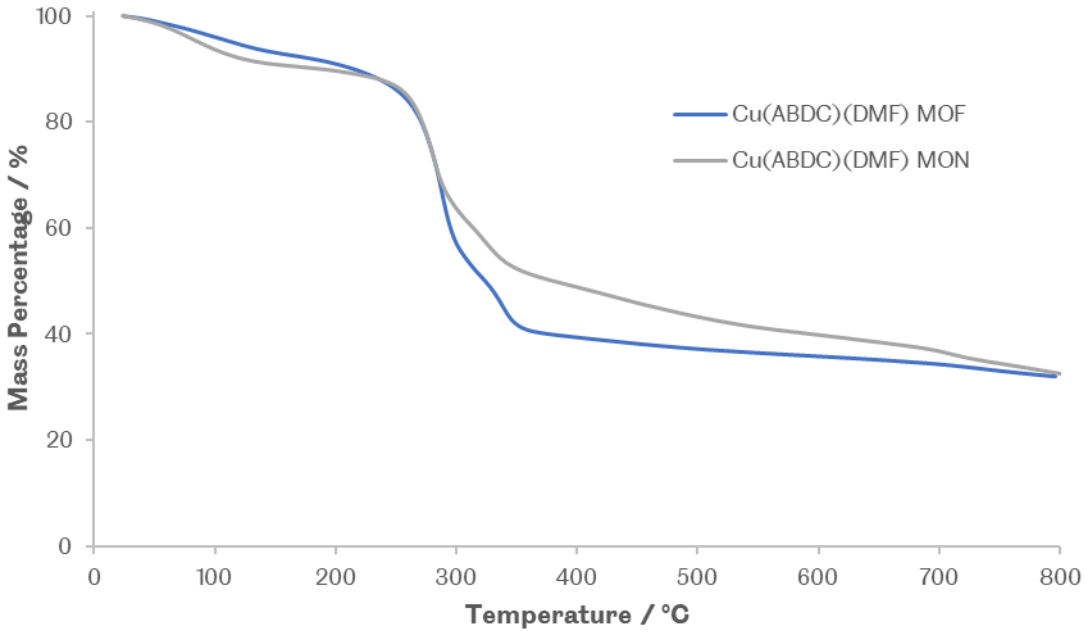

Figure 3.27 TGA plot of Cu(ABDC)(DMF)

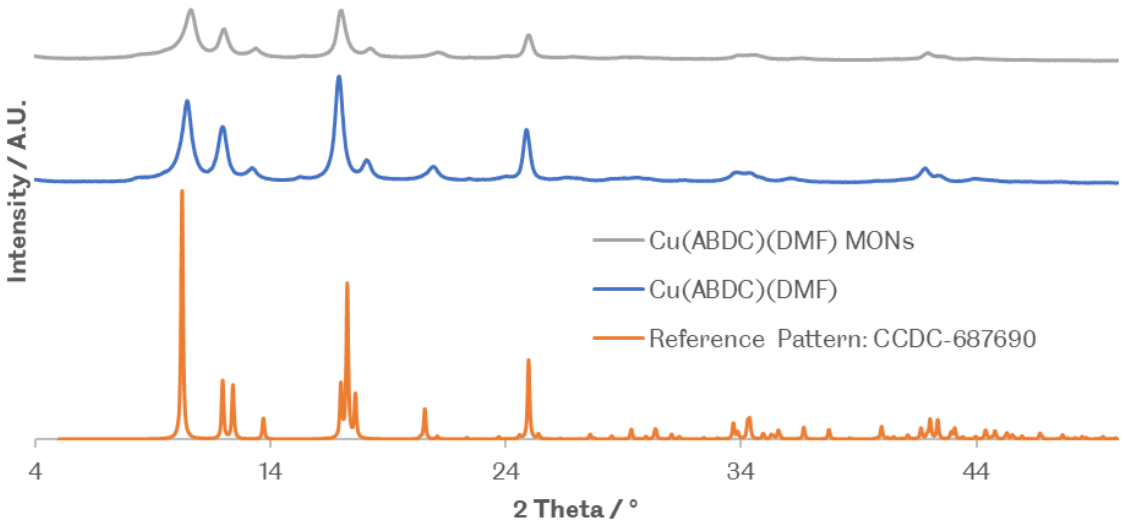

Figure 3.28 PXRD pattern of Cu(ABDC)(DMF) pre and post exfoliation compared to a literature standard taken from CCDC[9].

Cu(ABDC)(DMF) was exfoliated via liquid assisted ultrasonication as described in the exfoliation method section. A solution of Cu(ABDC)(DMF) in acetonitrile (0.83 mgmL^{-1}) was used and sonicated at 80 kHz for 12 hours. Uncentrifuged MON yield: 80.0 % (by mass). Centrifuged MON yield: 64.8 % (by mass).

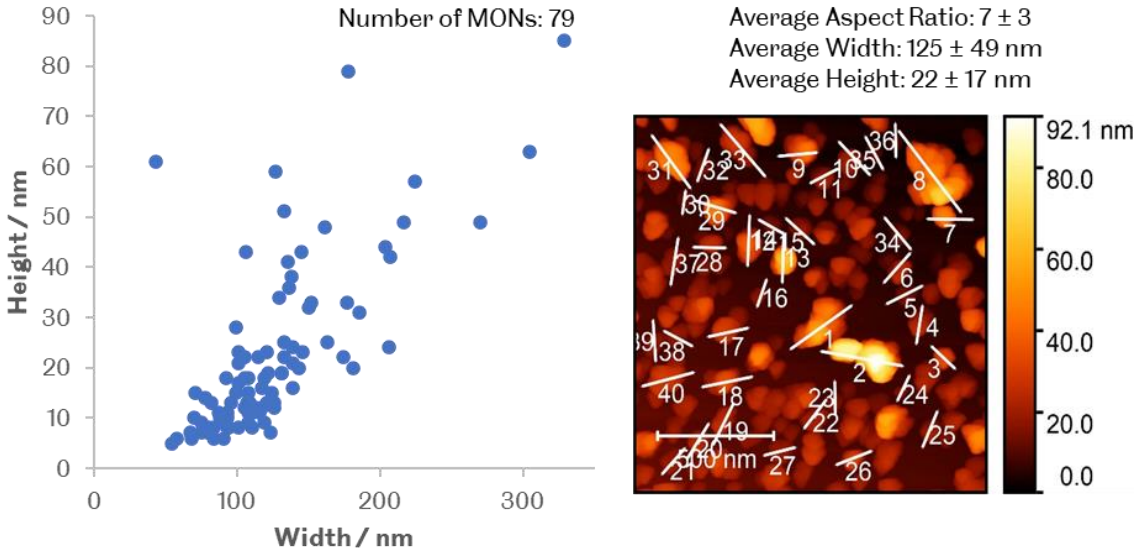

Figure 3.29 Scatter graph and example image of the height and width distribution of Cu(ABDC)(DMF) nanosheets

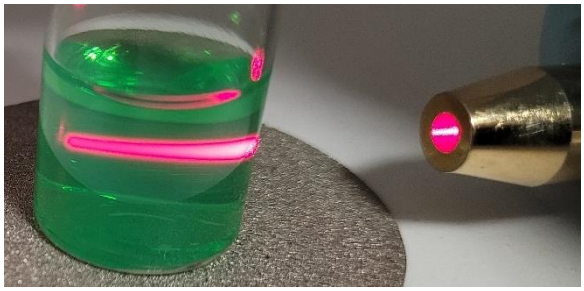

Figure 3.30 Tyndall scattering of Cu(ABDC)(DMF) nanosheet suspended in acetonitrile

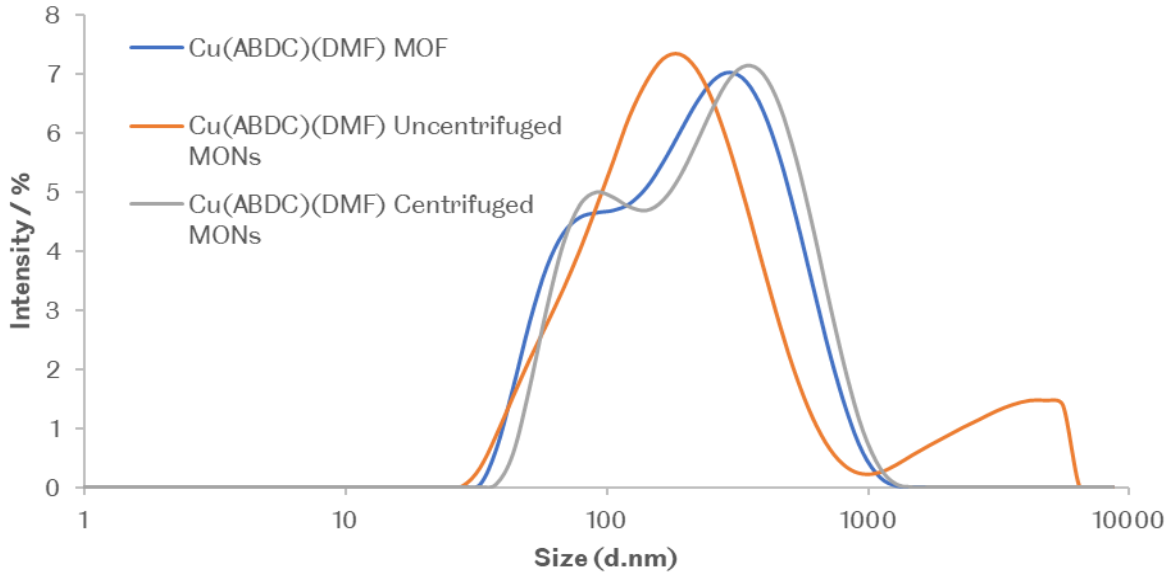

Figure 3.31. DLS analysis of Cu(ABDC)(DMF) MOF and MONs when suspended in MeCN

Sample Name	PdI	Position of the mean intensity (d.nm)
Cu(ABDC)(DMF) MOF	0.377	260.3
Cu(ABDC)(DMF) Uncentrifuged MONs	0.413	580.7
Cu(ABDC)(DMF) Centrifuged MONs	0.386	289.5

Table 3.5. DLS analysis of Cu(ABDC)(DMF) MOF and MONs when suspended in MeCN

3.6.5 – Synthesis and Exfoliation of Cu(MA-ABDC)(DMF)

The synthesis, exfoliation, and further data of Cu(MA-ABDC)(DMF) is described in chapter 5.

References

1 D. J. Ashworth and J. A. Foster, *J. Mater. Chem. A*, 2018, **6**, 16292–16307.

2 Y. Cheng, X. Wang, C. Jia, Y. Wang, L. Zhai, Q. Wang and D. Zhao, *J. Memb. Sci.*, 2017, **539**, 213–223.

3 M. T. Kallo and M. J. Lennox, *Langmuir*, , DOI:10.1021/acs.langmuir.0c02434.

4 R. Dai, X. Zhang, M. Liu, Z. Wu and Z. Wang, *J. Memb. Sci.*, 2019, **573**, 46–54.

5 S. Wang, T. Wang, H. Zheng, F. Fan, Z. Gu, W. He, B. Zhang, L. Shao, H. Chen, Y. Li, X. Zhang, L. Zhang, Y. Fu and W. Qi, *Microporous Mesoporous Mater.*, 2020, **303**, 110254.

6 J. Nicks, University of Sheffield, 2021.

7 M. Szycher and P. D, *Szycher's Handbook of Polyurethanes, Second Edition*, CRC Press, 2012, vol. 37.

8 J. Nicks, J. Zhang and J. A. Foster, *Chem. Commun.*, 2019, **55**, 8788–8791.

9 C. G. Carson, K. Hardcastle, J. Schwartz, X. Liu, C. Hoffmann, R. A. Gerhardt and R. Tannenbaum, *Eur. J. Inorg. Chem.*, 2009, 2338–2343.

10 H. K. Zhao, B. Ding, E. C. Yang, X. G. Wang and X. J. Zhao, *Zeitschrift fur Anorg. und Allg. Chemie*, 2007, **633**, 1735–1738.

11 S. Shahid, K. Nijmeijer, S. Nehache, I. Vankelecom, A. Deratani and D. Quemener, *J. Memb. Sci.*, 2015, **492**, 21–31.

12 H. Li, L. Tuo, K. Yang, H. K. Jeong, Y. Dai, G. He and W. Zhao, *J. Memb. Sci.*, 2016, **511**, 130–142.

13 L. Ji, J. Wang, K. Wu and N. Yang, *Adv. Funct. Mater.*, 2018, **28**, 1706961.

14 D. J. Ashworth, T. M. Roseveare, A. Schneemann, M. Flint, I. Dominguez Bernáldes, P. Vervoorts, R. A. Fischer, L. Brammer and J. A. Foster, *Inorg. Chem.*, 2019, **58**, 10837–10845.

Chapter 4

Rigid PIR Foams and their composites with NH_2-MIL-53 MOFs and MONs

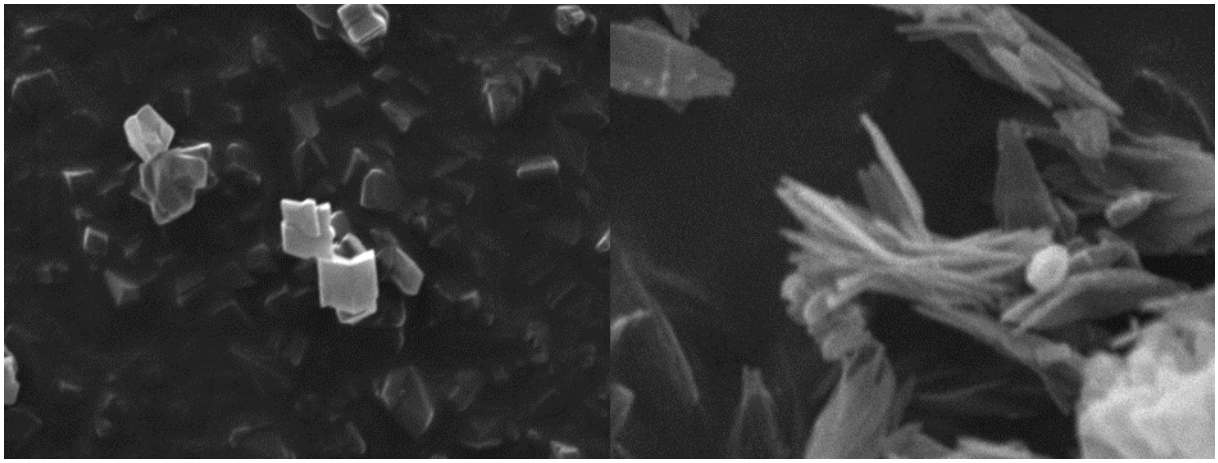

"But I've never seen the Icarus story as a lesson about the limitations of humans. I see it as a lesson about the limitations of wax as an adhesive."

— What If?: Serious Scientific Answers to Absurd Hypothetical Questions, by Randall Munroe, an American cartoonist, author, and engineer.

4.1 – Introduction and Aims

Additions of copper paddle-wheel MOFs and MONs to rigid PIR foam have demonstrated reduction in gas loss in the previous chapter, therefore alternative MOF/MON structures were investigated to be added to rigid PIR foams. The aim of the work described in this chapter was to reduce the loss of blowing agent from PIR rigid foam and evaluate what structural effects contribute to the reduction of blowing agent loss.

A number of factors were considered to determine an alternative system to utilize over the typical copper paddle-wheel MOFs and MONs. These factors were: cost, access to equipment, ease of synthesis, yield, and stability. As expensive or synthetically intensive linkers would create too high of additional costs for the production of composite foams, MOFs such as Zn(TCPP)[1] were discounted. Furthermore, requiring any specific high-pressure equipment or a multi-day high temperature synthesis would also discount any MOFs from being incorporated into the composite foam. Low yields would require multiple syntheses which was also unacceptable from both a waste and cost perspective. Finally, stability in multiple solvents and pH systems was needed to compare against the copper systems and ensure no degradation effects of the MOFs/MONs were being observed in the composite foams. Therefore, the final MOF chosen was NH_2-MIL-53.

This chapter builds on the previous work by exploring Aluminium based MOFs to make composites that were tested for their mass loss under accelerated aging conditions. The MOF was both synthesized unmodulated and modulated to determine what effect shape has on gas loss. From this, a procedure for obtaining MONs from the modulated MOF was developed, then the MONs were tested in the composite to determine whether anisotropy of the MONs could affect the mass loss from the system.

4.2 – Synthesis, modulation, and analysis of the NH_2-MIL-53 MOF

NH_2-MIL-53 is a variation on the MIL-53 MOF system, recognised for its wine rack structure that allows for a 'breathing' effect within the MOF[2]. The choice of NH_2-MIL-53 over MIL-53 was two-fold, the amine groups could allow for better comparison to Cu(ABDC)(DMF), and the surface could then also be modified further through post-synthetic functionalization (akin to Cu(MA-ABDC)(DMF)) to further demonstrate any surface effects.

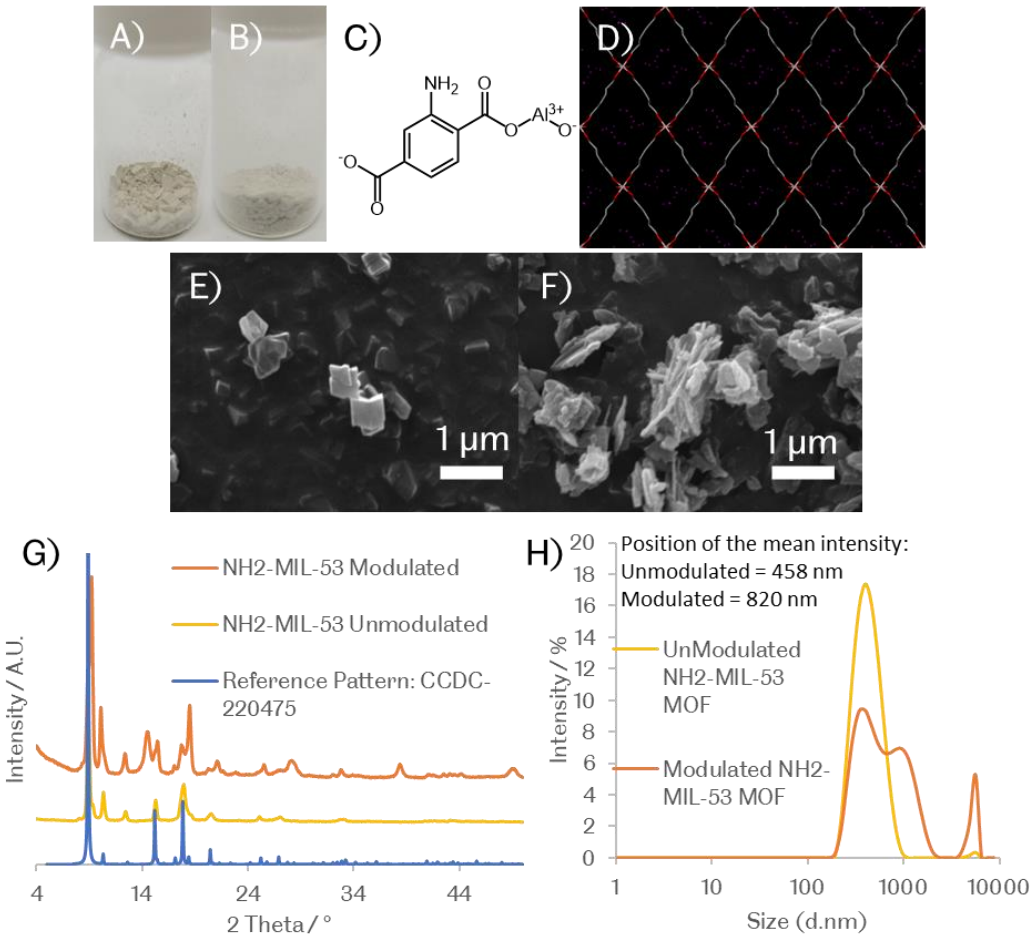

Figure 4.1 showing data for NH_2-MIL-53 MOF: A) photograph of the unmodulated MOF as-synthesised B) photograph of the modulated MOF as synthesized C) Chemdraw structure of NH_2-MIL-53 building unit, D) Expanded crystal motif E) SEM image of the unmodulated MOF, F) SEM image of the modulated MOF, G) PXRD of the unmodulated and modulated MOF compared to a reference pattern (CCDC-220475)[3], and H) DLS of the unmodulated and modulated MOF in acetonitrile after sonication (37 kHz, 60 seconds).

This MOF's selection is significantly different to those previously selected: it does not have the paddle-wheel secondary building unit nor a copper centre and is not a layered MOF that can be exfoliated via ultrasonication. To access nanosheets of NH_2-MIL-53, the MOF must be modulated during synthesis to produce a MOF with a flower-like structure (seen in figure 4.1) that can be turned into MONs via ultrasonication.

The production of both the standard and modulated NH2-MIL-53 is adapted from the work by Jinhuai Liu *et. al.*[2], where the MOF is hydrothermally synthesized at 150°C for 5 hours. In the case of the modulated MOF, urea is added as a modulator during the mixing stage of the reaction and causes the modulated flower-like structure of NH_2-MIL-53 to be obtained.

Both the standard and modulated MOFs produce similar powder patterns (with the modulated demonstrating an additional peak that is also present in the reference paper[2] at 14.6°), but substantially different macro-structures. In figure 4.1 the SEM images (E and F) show the change from the cube like crystals of the unmodulated MOF, to the flower like structure of the modulated MOF. DLS measurement also shows an almost doubling in diameter from 458 to 820 nm of the unmodulated and modulated MOFs respectfully. This variation in a single MOF allows for more in-depth analysis of the effect of structure on the barrier properties in the rigid PIR foam.

4.3 – Synthesis and accelerated aging of NH_2-MIL-53 MOF composite foams

Composite foams containing NH_2-MIL-53 were synthesized as previously described in chapter 3, where a 0.1 % by weight composite is synthesized and then placed in a 70 °C oven for accelerated aging and regular weighing.

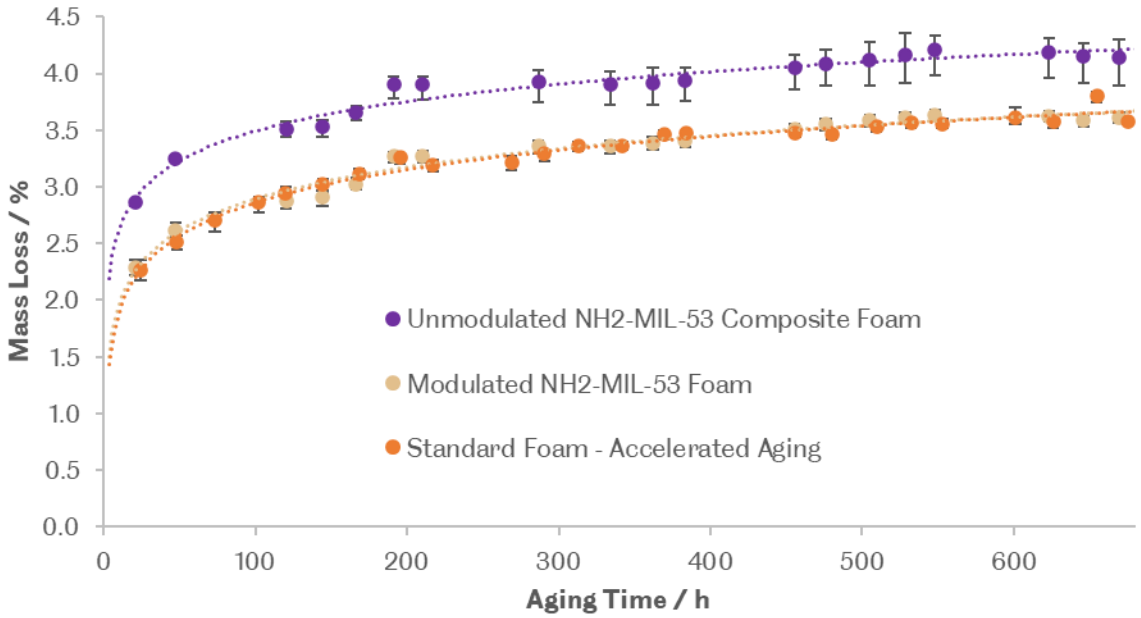

Figure 4.2 Comparison of the mass loss of NH_2-MIL-53 (unmodulated and modulated) composite rigid PIR foams over time compared to a base foam.

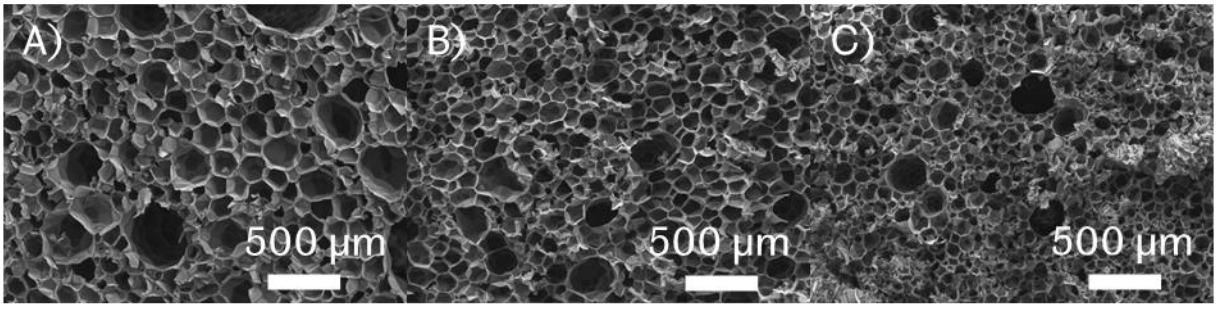

Standard Foam	Unmodulated NH_2-MIL-53 Composite Foam	Modulated NH_2-MIL-53 Composite Foam
Closed cell % = 85 ± 1	Closed cell % = 84 ± 5	Closed cell % = 94 ± 4
Cell Size = 222 ± 27 µm	Cell Size = 179 ± 17 µm	Cell Size = 154 ± 18 µm

Figure 4.3 SEM Images, and corresponding closed cell content and cell size, of rigid PIR foams with additives: A) No Additive, B) Unmodulated NH_2-MIL-53, and C) Modulated NH_2-MIL-53

Figure 4.2 shows two 0.1 % by weight composite foams compared to a standard. One containing an unmodulated NH_2-MIL-53, and one with modulated NH_2-MIL-53. Unmodulated NH_2-MIL-53 demonstrates both a higher mass loss then the standard over time, but also a higher level of variation in data points as the run time reaches 28 days. Modulated NH_2-MIL-53 shows a similar mass loss to the standard foam.

From the accelerated aging data, unmodulated NH_2MIL-53 shows significantly faster mass loss from the foam. Pycnometry analysis (figure 4.3) shows a comparable number of closed cells for unmodulated NH_2-MIL-53 (84 ± 5 %) compared to the base foam (85 ± 1 %). The cell size analysis demonstrates a drop in cell size (179 ± 17 µm) in the foam compared to the standard (222 ± 27 µm), which would typically reduce the loss of blowing agent over time, as smaller cells requires the gas to pass through more cell walls before being released.

In the case of modulated NH_2-MIL-53, the gas loss is comparable with the base foam, indicating that the change in size and shape of the MOF structure has made a significant effect on its behaviour in the foam. Furthermore, the increase in closed cell content (94 ± 4 %) and reduction in cell size (154 ± 18 µm) compared to the base foam (85 ± 1 %, 222 ± 27 µm) may indicate a stabilizing effect on the cell walls during the foaming process. Therefore, this data shows that whilst the modulated system is larger, the increased surface area and alternative shape has made an impact on the mass loss, making not only the size, but shape of the additive important to this study.

Though, for modulated NH_2-MIL-53, both the increase in closed cell content size would typically result in the reduction of mass loss compared to the base foam, which is not evident in the modulated MOF composite. Therefore, it is assumed that the large MOF crystals are also contributing to the transport of gas through the cell walls, causing a higher mass loss over time. As previously stated, the MIL-53 system is a "wine-rack" like structure[2], with long pores that can be accessed through its structure. These pores have been utilized for CO_2 [4–6] capture, and in separation applications of CO_2 and CH_4[7,8]. It is unlikely the blowing agents (iso- and

cyclo- pentane) could be transported through these channels due to their steric bulk compared to the small molecules typically targeted for application of NH_2-MIL-53. So, this route for enhanced gas loss in both systems is unlikely.

Alternatively, formation of void space[9,10] around the MOF in the foam could allow for the transport of gas through the cell walls. However, this explanation would indicate a repulsive effect between the MOF and the PIR, which would lead to drainage away from the MOF and open cell formation due to thinning of the cell walls. This is not evident in either composite system. The modulated MOF that demonstrated a larger size in SEM and DLS analysis (458 to 880 nm respectively) shows a higher closed cell content than the reference foam, and if repulsive effects are occurring, the increase in closed cell content should not occur for larger particulates. Additionally, larger crystals would create larger void spaces, allowing for more efficient transport of gas through the cell wall, which is not evident in the larger modulated MOF. Therefore, the relationship between the MOF and the PIR foam is complex and demonstrates the necessity to study the behaviour of NH_2-MIL-53 MONs for comparison.

4.4 – Development of NH_2-MIL-53 MONs, and their composites with foams

As previously discussed, MONs are highly anisotropic nanosheets of MOFs, typically obtained through top-down exfoliation of a layered MOF to obtain (down to) single-layered MONs for analysis and application. NH_2-MIL-53 is a 3D non-layered MOF system, and therefore under normal conditions, cannot be exfoliated into nanosheets.

Whilst MIL-53 nanosheets have been reported in the literature[11–19], they're typically either flower-like MOFs[2,13–19], their size/shape are not effectively reported[12] or utilize surfactants in their synthesis[11]. Whilst these flower-like MOFs could be utilized for further comparison to understand structural relationships between the MOF and PIR foam, it was determined the lack of control over the structures would not produce meaningful results.

Use of surfactant-based synthesis can control and target MON structures for MOFs that are not layered systems, however, they will contain surfactants either in the pores of the MON or adsorbed to the surface of the MON after synthesis. These were not explored as the alteration of the surfactant system could cause a poor foam to be produced when these MONs are added.

Therefore, the modulated NH_2-MIL-53 system produced was taken forward for testing of MON production. Whilst urea was utilized in the synthesis of these flower-like MOFs, after activation that was developed for this work (overnight reflux in MeOH, overnight reflux in DMF, overnight in an 80 °C vacuum oven) any urea remaining was removed, as is evidenced by the lack of urea peak in the NMR spectra (figure 4.8).

Standard exfoliation utilized by copper-paddlewheel MOFs, 5 mg of MOF in 6 mL of acetonitrile, sonicated at 80 kHz for 12 hours, and centrifuged at 1500 rpm for 1 hour, was applied to the modulated NH_2-MIL-53 system, resulting in no MONs being produced. Likely this was due to poor suspension of the MOF in the solvent, resulting in poor exfoliation of the material, and the gentle exfoliation technique could not liberate nanosheets from the larger flower-like structure.

Therefore, further solvents and sonication routes were tested, resulting in using water as the exfoliation solvent, and 37 kHz for 12 hours with 1500 rpm centrifugation as the exfoliation procedure. The result was MONs that have an average height of 2 ± 1 nm as demonstrated in figure 4.4 and 4.5.

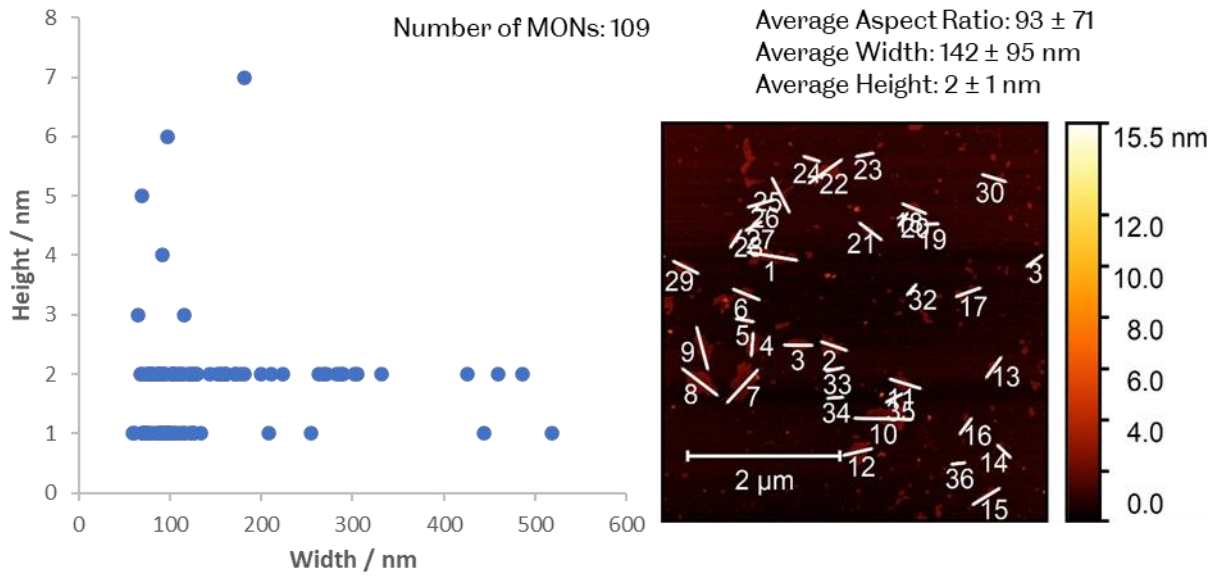

Figure 4.4 Scatter graph and example image of the aspect ratio distribution of Modulated NH_2-MIL-53 nanosheets

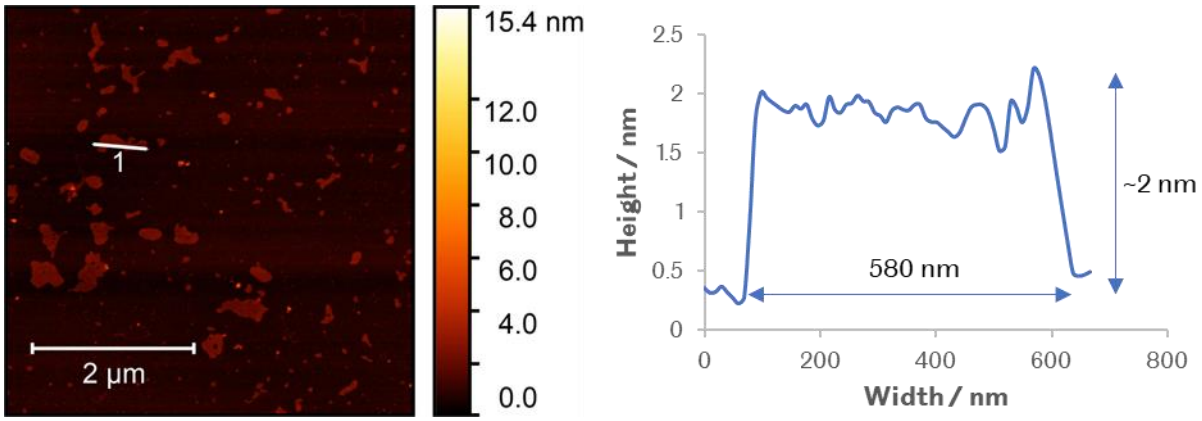

Figure 4.5 Example of a single MON from AFM analysis

When compared to literature analysis, these MONs produced are significantly thinner and have larger aspect ratios. These ultrathin MONs were therefore taken forward for the addition into composite foams. Both centrifuged and uncentrifuged MONs are tested in composite rigid PIR foams similar to those in chapter 3, where a 0.1 % by weight composite was made and placed in a 70 °C oven for accelerated aging and weighing.

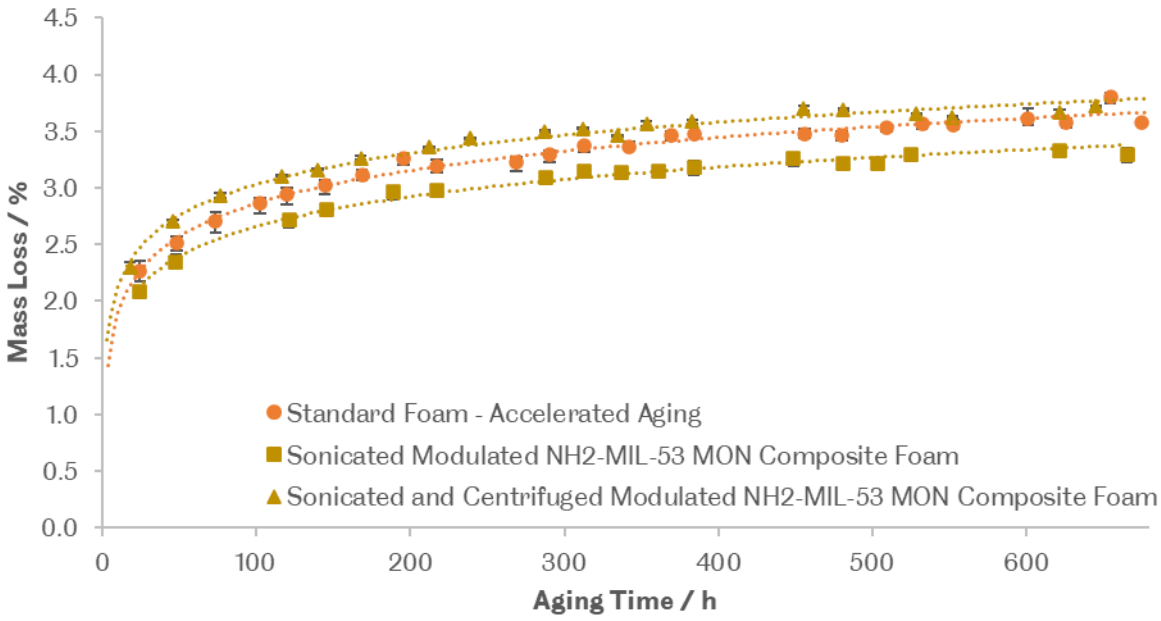

Figure 4.6 Comparison of the mass loss of modulated NH_2-MIL-53 uncentrifuged and centrifuged MON composite rigid PIR foams over time.

Figure 4.6 shows the mass loss of two NH_2-MIL-53 MON composite foams, one uncentrifuged and one centrifuged, compared to a standard foam. The uncentrifuged MON composite showed a lower mass loss (3.30 ± 0.06 at 28 days) over the time tested than the base foam (3.58 ± 0.04 at 28 days), with the centrifuged MON showing an increase in mass loss (3.80 ± 0.01 at 28 days).

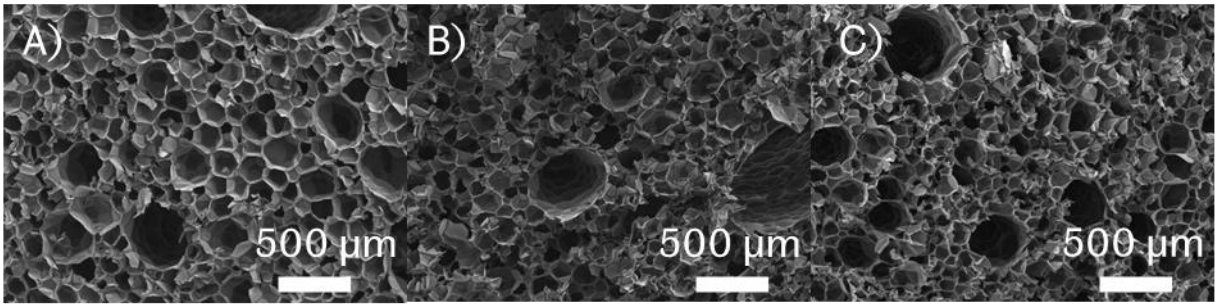

Standard Foam	Sonicated NH_2-MIL-53 MON Composite Foam	Sonicated and Centrifuged NH_2-MIL-53 MON Composite Foam
Closed cell % = 85 ± 1 Cell Size = 222 ± 27 µm	Closed cell % = 86 ± 2 Cell Size = 188 ± 32 µm	Closed cell % = 95 ± 4 Cell Size = 178 ± 24 µm

Figure 4.7 SEM Images, and corresponding closed cell content and cell size, of rigid PIR foams with additives: A) No Additive, B) Sonicated NH_2-MIL-53 MON Composite Foam, and C) Sonicated and Centrifuged NH_2-MIL-53 MON Composite Foam

Figure 4.7 shows the closed cell content and cell size for both modulated and unmodulated MON composites compared to the base foam. For the uncentrifuged MON composite, the closed cell content (86 ± 2 %) was within experimental error of the base foam (85 ± 1 %), and the cell size (188 ± 32 µm) smaller than the base foam (222 ± 27 µm). For the centrifuged MON composite, the closed cell content (95 ± 4 %) was larger than the base foam (85 ± 1 %), and the cell size (178 ± 24 µm) smaller than the base foam (222 ± 27 µm).

MON System	DLS position of the mean intensity / nm	DLS PdI	AFM average width / nm	AFM average height / nm
Modulated NH_2-MIL-53 Uncentrifuged	868	0.253	N/A	N/A
Modulated NH_2-MIL-53 Centrifuged	693	0.457	142 ± 95	2 ± 1

Table 4.1 Table comparing the size of uncentrifuged, and centrifuged MONs based upon DLS or AFM data. All MON data is recorded in water. AFM data is not presented for uncentrifuged material as particulates would be too large for the technique to measure effectively.

Table 4.1 shows the sizes of MONs measured by DLS and AFM. DLS data shows again the position of the mean intensity of the MON is reduced when centrifuged, indicating an overall reduction in particulate size. The AFM data demonstrates that the MONs made from modulated NH_2-MIL-53 are extremely thin with large widths creating highly anisotropic MONs.

The accelerated aging data suggests that whilst the use of NH_2-MIL-53 to make MONs does reduce the mass loss over time compared to the base foam, a similar trend to the copper systems is seen where the uncentrifuged MONs appear to outperform the centrifuged MONs. There are two reasons suggested for this, either the NH_2-MIL-53 MONs are also being degraded similarly to the copper systems seen previously, or the drying of the centrifuged MONs and redistribution into the foam system is causing issues with dispersion within the foam that is not occurring with the uncentrifuged material. Possibly, the centrifuged MONs are forming better aggregates that are not as dispersible when mixed into the Part A mixture when compared with the uncentrifuged material, resulting in poorer barrier quality due to the inefficient dispersion through the foam. This also could apply for the unmodulated MOF composites having a higher mass loss compared to the modulated MOF composites, with larger aggregates allowing for efficient void space between the additive's routes for the

blowing agent to travel through the cell walls of the foam, without disrupting the foams closed cell content.

As described previously, whilst the complex nature of these composites can result in difficult differentiation of effects on the structure, the resultant conclusions that can be taken from the addition of MOF vs MON addition into the foam is that the reduction in size of the additive has made an effect on the mass loss over time, and with the use of dry powders as additives, there is likely an ideal size of additive and route for addition for efficient distribution and incorporation into the foams.

4.5 – Conclusions and Future Work

In conclusion, NH_2-MIL-53 was successfully synthesized in both an unmodulated and modulated form, where the modulated form was then effectively exfoliated into ultrathin (2 ± 1 nm in height) and highly anisotropic (aspect ratio of 93 ± 71) MONs for addition into rigid PIR foams. When added at 0.1 % by weight, the unmodulated MOF caused an increase (4.14 ± 0.22 % at 28 days) in the mass loss from the foams, whilst the modulated MOF was comparable (3.61 ± 0.05 % at 28 days) in mass loss to the base foam (3.58 ± 0.04 % at 28 days). This indicates a complex relationship between the size/structure of the additive and the rigid PIR foam itself.

When exfoliated into MONs, the modulated NH_2-MIL-53 system demonstrated that the centrifuged MONs increase the mass loss (3.80 ± 0.01 % at 28 days) from the foam, whilst the uncentrifuged MONs caused a decrease (3.30 ± 0.06 % at 28 days). A similar pattern to the previous copper paddle-wheel MONs, indicating further study is needed into the effects of size of MONs and distribution and aggregation into the foam systems and how this effects the gas loss from the composites.

In comparison to Cu(ABDC)(DMF) MOF at 28 days (3.22 ± 0.09 % mass loss), the modulated uncentrifuged NH_2-MIL-53 MONs (3.30 ± 0.06 %) performed similarly. Indicating that a

complex relationship between the size, shape and dispersion of the MOFs and MONs into the rigid PIR foam can create similar results concerning gas loss.

As an initial step forward, looking at the dispersion of the MONs in the foam system would highlight the effect of aggregation on mass loss. Therefore, investigation into the distribution of MONs would be an ideal target for future work. A possible route would be to utilize the supernatant of centrifuged MONs and combine them with the polyol to be used in the foam synthesis. The water could then be removed from the mixture under reduced pressure, leaving the MONs dispersed in the polyol, preventing drying and aggregation of the MONs before foaming.

For further testing of MOF systems, or other additives, finding those that can produce a highly stable MOF and be exfoliated into MONs is a challenge. A variety of other MOFs have been tested in this work; UiO-66[20], UiO-67[21], ZIF-8[22], ZIF-L[22], MAMS-1[23], Co-MOF-NS[24], Ni-MOF-NS[25], $Zn_2(Bim)_3$[26] and MIP-202[27] but these either resulted in a cell opening effect; could not be effectively scaled to produce enough material for testing in the foam; or could not be synthesized without phase impurities. However, with advances in MON synthesis, the UiO MOF systems modulated with formic or acetic acid would be an ideal step forward[28]. These MOFs are highly stable and can have a variety of functionalizations from the alteration of the linker used. With the advances from Clare P. Grey *et. al.*[29] and researchers in our own group, these MOFs can now be produced as MONs that would be ideal for the addition into MOFs.

Finally, for further development of the working systems a focus will have to be given to the scalability of MON synthesis. Currently, for the NH_2-MIL-53 system the centrifuged MON yield is 15.7 % by mass of the exfoliated MOF (where the losses come from the 1500 rpm centrifugation step), or for the uncentrifuged MON, the yield is 72.1 % by mass. Which at the current small scale is tolerable, though required 2.4 L of water to be removed from the MONs, at an industry scale would create significant waste. Additionally, the synthesis of modulated NH_2-MIL-53 is currently a batch process requiring an autoclave to heat water to 150 °C, then

washing in both DMF and MeOH before the MOF is produced. Whilst continuous synthesis of some MOFs (such as MOF-5[30]), and porphyrin-based MONs has been attempted, no attempt to continuously produce NH_2-MIL-53 MOFs has been undertaken. Therefore, for continuation of this MOF system, investigation into flow reactions, microwave synthesis and sedimentation techniques would be useful approaches to begin the effective scale up of these MOFs if they are to be used in rigid PIR foams.

4.6 – Experimental

General techniques utilized across multiple chapters can be found in chapter 6 as described in chapter 3.

4.6.1 – Foam Synthesis

Synthesis of foam composites is identical to the procedure outlined in chapter 3 with the use of NH_2-MIL-53 systems in place of copper-paddlewheel MOF/MONs.

Foam	Closed Cell Content / %	Cell Size / nm	Mass loss at 28 Days / %
No Additives	85 ± 1	222 ± 27	3.58 ± 0.04
Unmodulated NH_2-MIL-53 MOF	84 ± 5	179 ± 17	4.14 ± 0.22
Modulated NH_2-MIL-53 MOF	94 ± 4	154 ± 18	3.61 ± 0.05
Modulated NH_2-MIL-53 Uncentrifuged MON	86 ± 2	188 ± 32	3.30 ± 0.06
Modulated NH_2-MIL-53 Centrifuged MON	95 ± 4	178 ± 24	3.80 ± 0.01

Table 4.2 Table of foams synthesized and analysed for accelerated aging experiments, showing closed cell content, cell size and mass loss after 28 days.

4.6.2 – Synthesis and Exfoliation of NH2-MIL-53 (Mod and UnMOD)

Aluminium chloride hexahydrate (0.966 g, 4.00 mmol) and aminoterephthalic acid (0.543 g, 3.00 mmol) are mixed together in water (30 mL) for 30 minutes. For modulated NH_2-MIL-53, urea (0.390 g, 6.50 mmol) was added to the reaction mixture and stirred for an additional 30 minutes. The reaction mixture was then transferred to a Teflon lined autoclave and heated to 150 °C for 5 hours with a heating and cooling rate of 10 °Cmin^{-1}. The yellow solution was then centrifuged (12,000 rpm, 10 mins) to yield a yellow solid. For activation, the product was suspended in DMF (50 mL) with stirring at 110 °C for 16 hours then centrifuged (12,000rpm 10 mins). The off-white product was then suspended in methanol (50 mL) and stirred under reflux for 16 hours. Finally, the product was centrifuged (12,000 rpm 10 mins) and dried under vacuum at 40 °C for 16 hours, resulting in an off-white powder of NH_2-MIL-53. Unmodulated yield: 88.3 % (based on Al), modulated yield: 81.8 % (based on Al). Elemental analysis: calculated mass for unmodulated $AlC_8H_8NO_6$ %: C 39.84; H 3.32; N 5.81; Found mass %: C 43.50; H 3.89; N 6.09. Calculated mass for modulated $AlC_8H_8NO_6$ %: C 39.84; H 3.32; N 5.81; Found mass %: C 30.74; H 3.69; N 5.43. Phase purity confirmed by PXRD (flat plate) comparison (CCDC entry 220475)[3] and comparison to paper by Jinhuai Liu *et. al.*[2]

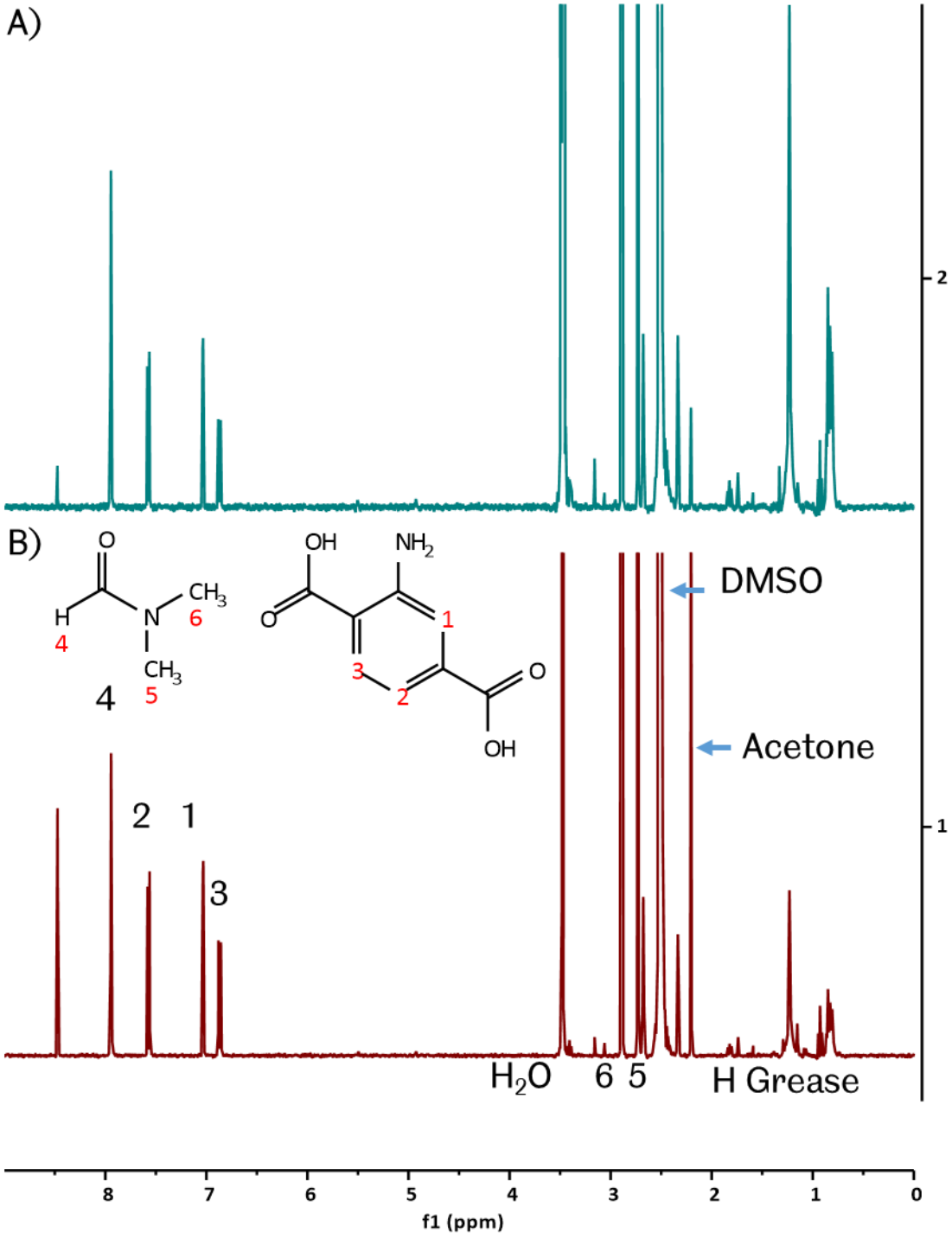

Figure 4.8 ^{1}H NMR spectrum of A) unmodulated and B) modulated digested with NaOD/DMSO-d_6 with peaks assigned according to the inset molecular structures. An additional unassigned peak at 8.5 ppm corresponds to an $AlCl_3.6H_2O$ impurity. Satellite peaks present from DMSO at 2.3 and 2.7 pm.

Due to the high stability of NH_2-MIL-53 NMR data for the system does not encompass a full digestion of the MOF and instead is for basic indication of synthesis.

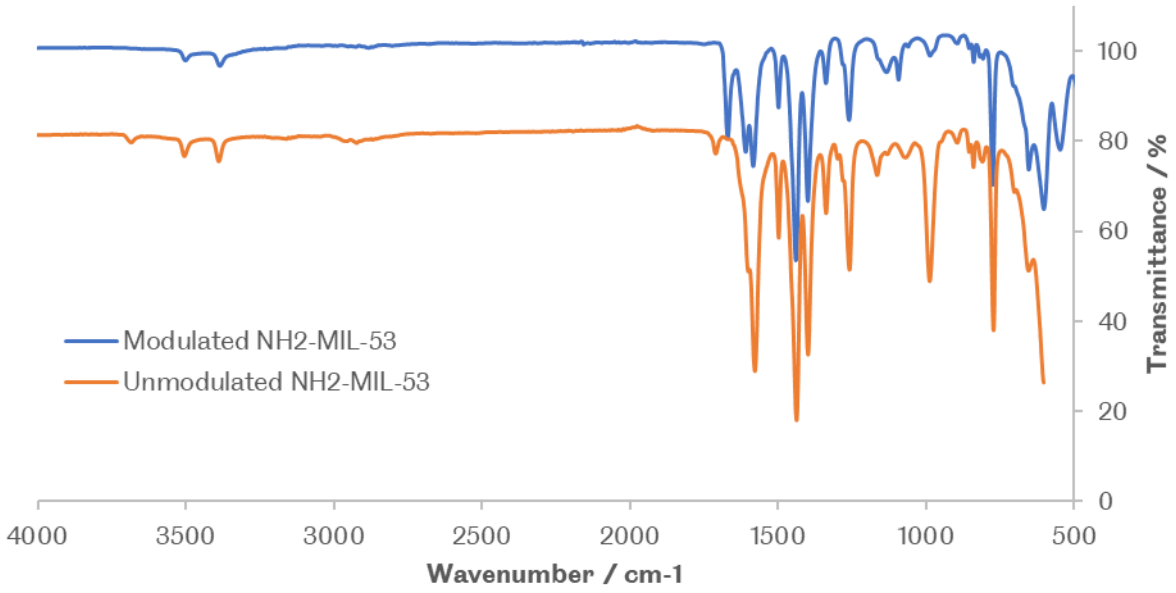

Figure 4.9 ATR FT-IR spectrum of unmodulated and modulated NH_2-MIL-53

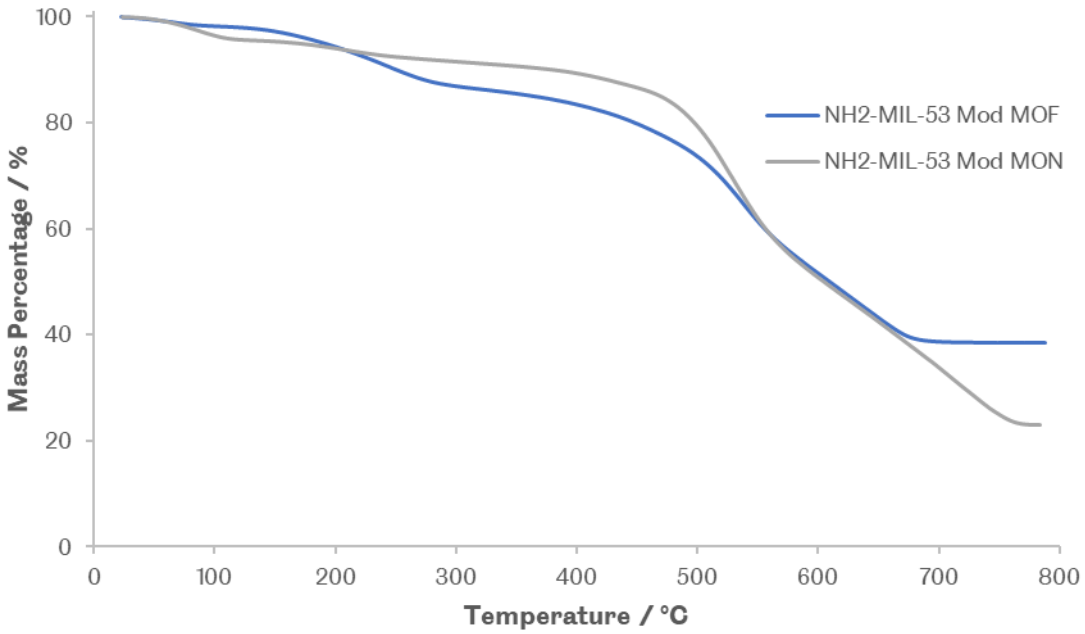

Figure 4.10 TGA plot of modulated NH_2-MIL-53

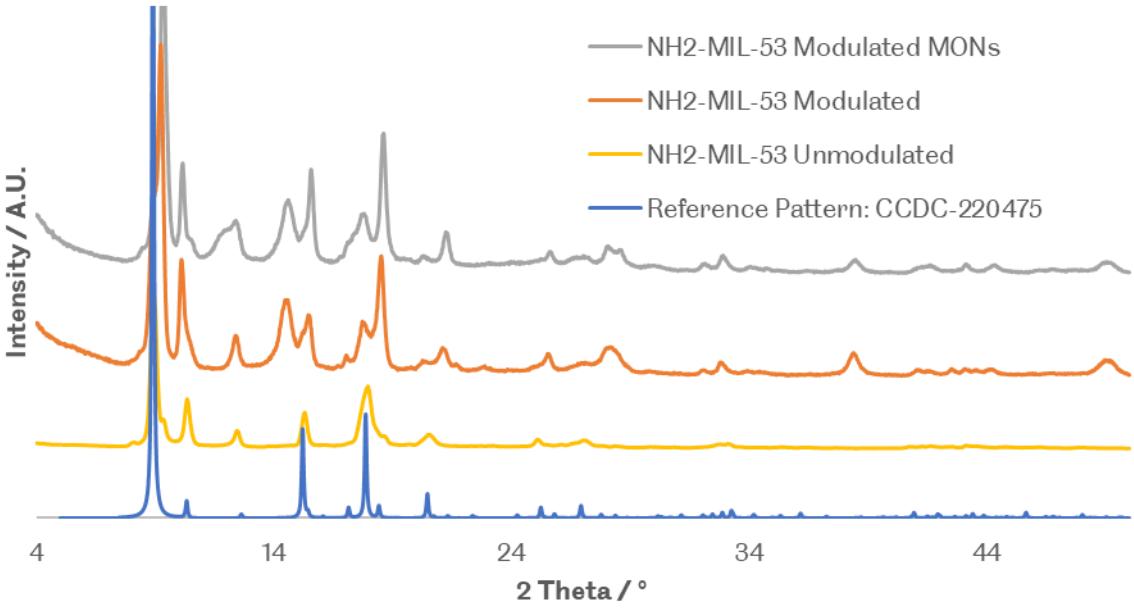

Figure 4.11 PXRD pattern of unmodulated and modulated NH_2-MIL-53 pre and post exfoliation compared to a literature standard taken from CCDC[3].

Modulated NH_2-MIL-53 was exfoliated via liquid assisted ultrasonication as described in the exfoliation method section. A solution of Modulated NH_2-MIL-53 in water (0.83 $mgmL^{-1}$) was used and sonicated at 37 kHz for 12 hours. Uncentrifuged MON yield: 72.1 % (by mass). Centrifuged MON yield: 15.7 % (by mass)..

Figure 4.12 Tyndall scattering of modulated NH_2-MIL-53 nanosheet suspended in water

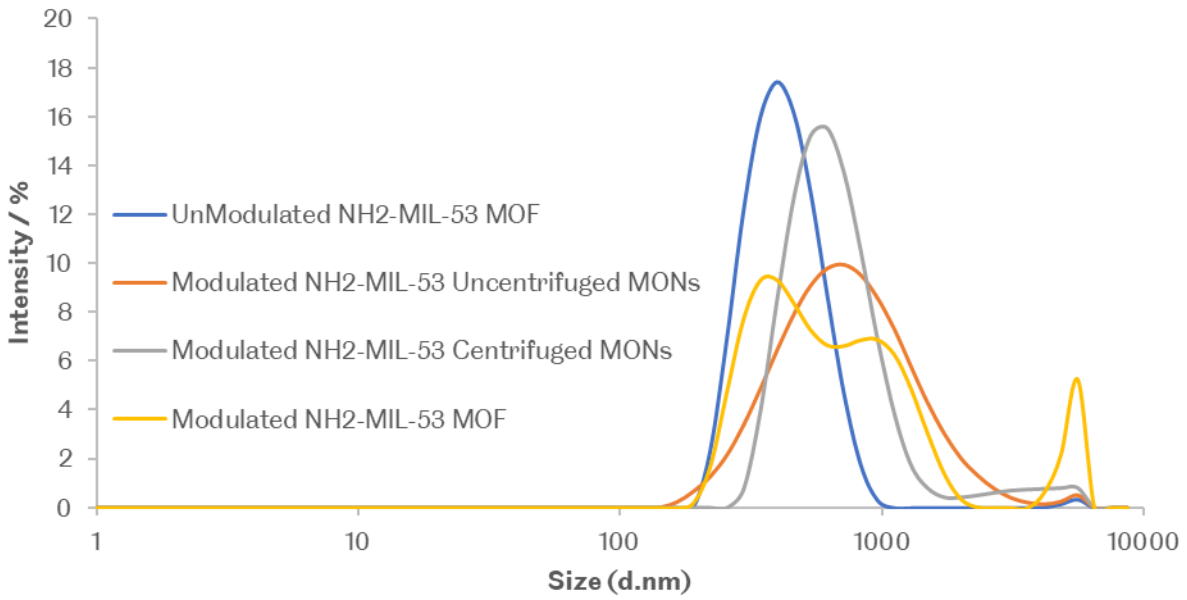

Figure 4.15 DLS analysis of Unmodulated and Modulated NH_2-MIL-53 MOF and MONs when suspended in H_2O.

Sample Name	PdI	Position of the mean intensity (d.nm)
UnModulated NH2-MIL-53 MOF	0.157	457.6
Modulated NH2-MIL-53 MOF	0.598	1031
Modulated NH2-MIL-53 Uncentrifuged MONs	0.253	868
Modulated NH2-MIL-53 Centrifuged MONs	0.187	819.7

Table 4.3 DLS analysis of Unmodulated and Modulated NH_2-MIL-53 MOF and MONs when suspended in H_2O.

References

1 K. Sasitharan, D. G. Bossanyi, N. Vaenas, A. J. Parnell, J. Clark, A. Iraqi, D. G. Lidzey and J. A. Foster, *J. Mater. Chem. A*, 2020, **8**, 6067–6075.

2 Z. Li, D. Zhan, A. Saeed, N. Zhao, J. Wang, W. Xu and J. Liu, *Dalt. Trans.*, 2021, **50**, 8540–8548.

3 T. Loiseau, C. Serre, C. Huguenard, G. Fink, F. Taulelle, M. Henry, T. Bataille and G. Férey, *Chem. - A Eur. J.*, 2004, **10**, 1373–1382.

4 E. Stavitski, E. A. Pidko, S. Couck, T. Remy, E. J. M. Hensen, B. M. Weckhuysen, J. Denayer, J. Gascon and F. Kapteijn, *Langmuir*, 2011, **27**, 3970–3976.

5 M. Mihaylov, K. Chakarova, S. Andonova, N. Drenchev, E. Ivanova, A. Sabetghadam, B. Seoane, J. Gascon, F. Kapteijn and K. Hadjiivanov, *J. Phys. Chem. C*, 2016, **120**, 23584–23595.

6 A. Zárate, R. A. Peralta, P. A. Bayliss, R. Howie, M. Sánchez-Serratos, P. Carmona-Monroy, D. Solis-Ibarra, E. González-Zamora and I. A. Ibarra, *RSC Adv.*, 2016, **6**, 9978–9983.

7 M. Mubashir, Y. F. Yeong, K. K. Lau, T. L. Chew and J. Norwahyu, *Sep. Purif. Technol.*, 2018, **199**, 140–151.

8 M. Loloei, S. Kaliaguine and D. Rodrigue, *Sep. Purif. Technol.*, 2021, **270**, 118786.

9 W. Glassy, *Polym. Eng. Sci.*, 2002, **42**, 1420–1431.

10 W. K. Setiawan and K. Y. Chiang, *Sustain. Environ. Res.*, 2019, **1**, 1–21.

11 A. Pustovarenko, M. G. Goesten, S. Sachdeva, M. Shan, Z. Amghouz, Y. Belmabkhout, A. Dikhtiarenko, T. Rodenas, D. Keskin, I. K. Voets, B. M. Weckhuysen, M. Eddaoudi, L. C. P. M. de Smet, E. J. R. Sudhölter, F. Kapteijn, B. Seoane and J. Gascon, *Adv. Mater.*, 2018,

30, 1–8.

12 X. Guo, Y. Fan, J. Xu, L. Wang and J. Zheng, *Ind. Eng. Chem. Res.*, 2020, **59**, 14825–14833.

13 A. Perea-Cachero, J. Sánchez-Laínez, B. Zornoza, E. Romero-Pascual, C. Téllez and J. Coronas, *Dalt. Trans.*, 2019, **48**, 3392–3403.

14 F. Wu, X. Guo, G. Hao, Y. Hu and W. Jiang, *Nanoscale*, 2019, **11**, 14785–14792.

15 M. Zhao, H. Li, W. Li, J. Li, L. Yi, W. Hu and C. M. Li, *Chem. - A Eur. J.*, 2020, **26**, 17091–17096.

16 B. Yuan, C. Li, L. Guan, K. Li and Y. Lin, *J. Power Sources*, 2020, **451**, 227295.

17 J. Chen, Y. Xu, S. Li, F. Xu and Q. Zhang, *RSC Adv.*, 2021, **11**, 2397–2404.

18 M. Ren, H. Wang, Y. Liu, Q. Ma, W. Jia, M. Liu, H. Wang and Y. Lu, *Anal. Lett.*, 2020, **53**, 2700–2714.

19 Z. Zhao, D. Yang, H. Ren, K. An, Y. Chen, Z. Zhou, W. Wang and Z. Jiang, *Chem. Eng. J.*, , DOI:10.1016/j.cej.2020.125929.

20 M. A. Rodrigues, J. de S. Ribeiro, E. de S. Costa, J. L. de Miranda and H. C. Ferraz, *Sep. Purif. Technol.*, 2018, **192**, 491–500.

21 M. J. Katz, Z. J. Brown, Y. J. Colón, P. W. Siu, K. A. Scheidt, R. Q. Snurr, J. T. Hupp and O. K. Farha, *Chem. Commun.*, 2013, **49**, 9449–9451.

22 Y. Lo, C. H. Lam, C. W. Chang, A. C. Yang and D. Y. Kang, *RSC Adv.*, 2016, **6**, 89148–89156.

23 X. Wang, C. Chi, K. Zhang, Y. Qian, K. M. Gupta, Z. Kang, J. Jiang and D. Zhao, *Nat. Commun.*, 2017, **8**, 14460.

24 W. Chen, B. Han, C. Tian, X. Liu, S. Liang, H. Deng and Z. Lin, *Appl. Catal. B Environ.*, 2019, **244**, 996–1003.

25 X. Huang, *Angew. Chemie Int. Ed.*, , DOI:10.1002/anie.201902588.

26 Y. Peng, Y. Li, Y. Ban and W. Yang, *Angew. Chemie - Int. Ed.*, 2017, **56**, 9757–9761.

27 S. Wang, M. Wahiduzzaman, L. Davis, A. Tissot, W. Shepard, J. Marrot, C. Martineau-Corcos, D. Hamdane, G. Maurin, S. Devautour-Vinot and C. Serre, *Nat. Commun.*, 2018, **9**, 4937.

28 M. J. Cliffe, E. Castillo-Martínez, Y. Wu, J. Lee, A. C. Forse, F. C. N. Firth, P. Z. Moghadam, D. Fairen-Jimenez, M. W. Gaultois, J. A. Hill, O. V. Magdysyuk, B. Slater, A. L. Goodwin and C. P. Grey, *J. Am. Chem. Soc.*, 2017, **139**, 5397–5404.

29 F. C. N. Firth, M. J. Cliffe, D. Vulpe, M. Aragones-Anglada, P. Z. Moghadam, D. Fairen-Jimenez, B. Slater and C. P. Grey, *J. Mater. Chem. A*, 2019, **7**, 7459–7469.

30 C. McKinstry, R. J. Cathcart, E. J. Cussen, A. J. Fletcher, S. V Patwardhan and J. Sefcik, *Chem. Eng. J.*, 2016, **285**, 718–725.

Chapter 5

Functionalization of MOFs for addition to rigid PIR foams

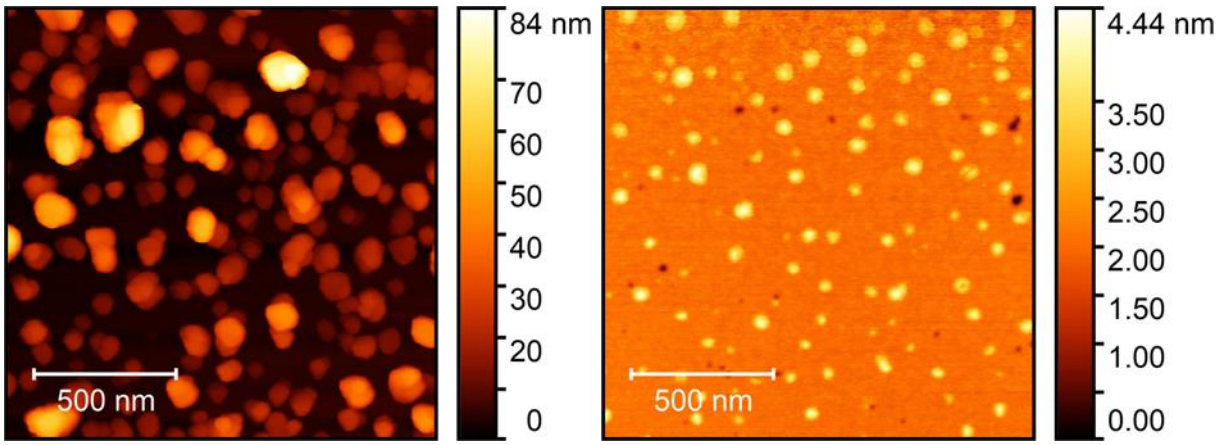

"Still, all I can give is my best. And as Annona would say, should my best prove insufficient, then we will find another way to achieve what's needed."

— Poke in Outer Wilds, by Mobius Digital and Annapurna Interactive, a designer and publisher of exploration games.

5.1 – Context

Post-synthetic functionalization (PSF) has been widely used as a technique to modify the surface properties of metal-organic frameworks (MOFs) to improve their compatibility with polymers[1]. The Foster group, and others, have recently reported the use of covalent PSF to tune the surface properties of metal-organic nanosheets (MONs) to add new sensing and catalytic functionalities[2–4]. In chapter 3 and 4, a wide range of different MONs were investigated as additives for use in enhancing the gas barrier properties of rigid PIR foams. Amongst these results, Cu(MA-ABDC)(DMF), (where ABDC is the 2-aminoterephthalic acid linker, MA is maleic anhydride and DMF is dimethylformamide), a layered amino MOF post-synthetically functionalized with maleic anhydride, showed particular promise. In this chapter, the synthesis and characterisation of Cu(MA-ABDC)(DMF) with different degrees of functionalization is reported along with investigations into its exfoliation. Additionally, as a further step of this work, investigation into the attachment of polymers to the surface of MOFs/MONs is also explored within the latter two sections of this chapter.

5.2 – Introduction and aims

This chapter explores the secondary aim of this project, PSF of MOFs/MONs to enhance the understanding of how the MOFs/MONs behave in rigid PIR foams, and to improve the retention of blowing agent in rigid PIR foam composites. Cu(ABDC)(DMF) MOF was chosen for functionalization due to its amine functionality and previous evidence of functionalization in the Foster group with 1,3-propansultone[2] and conversion of the amine group to an azide for functionalization using click-chemistry[5]. The MOF Cu(ABDC)(DMF) is a previously established layered 3D MOF system that can be exfoliated into MONs through liquid exfoliation in acetonitrile (MeCN). However, no exfoliation conditions were identified which could produce monolayer nanosheets of these systems which limited their use in some applications due to their thickness. The reaction of 1,3-propansultone onto Cu(ABDC)(DMF) MOF prior to

exfoliation reduced the average MON thickness from 25 nm to 1.4 nm^2. Therefore, the use of PSF to alter interactions is also an attractive route to accessing monolayer nanosheets for application.

This chapter was split into three sections, firstly the introduction of maleic anhydride to the surface of Cu(ABDC)(DMF) to produce the Cu(MA-ABDC)(DMF) MOF/MON utilized in rigid PIR composites in chapter 3. The second section describes the attempts to perform ring-opening polymerization onto the surface of Cu(ABDC)(DMF) MOF/MON to produce polymer enhanced materials for incorporation into rigid PIR foams. Finally, the third section describes the introduction of an atom-transfer radical polymerization initiator to the surface of Cu(ABDC)(DMF) MOF/MON, and subsequent attempts at polymerization from the surface.

5.3 – Maleic anhydride functionalized Cu(ABDC)(DMF)

5.3.1 - Introduction

As seen in chapter 3, the Cu(MA-ABDC)(DMF) 31 %, where 31 % of amine groups were functionalized with maleic anhydride, MOF and MON when added to a rigid PIR foam altered the amount of blowing agent lost compared to Cu(ABDC)(DMF). The uncentrifuged MONs of Cu(ABDC)(DMF) showed a greater mass loss than the uncentrifuged MONs of Cu(MA-ABDC)(DMF) 31 % (3.57 ± 0.06 % vs. 3.29 ± 0.11 % mass loss after 28 days respectfully). As discussed in chapter 3, this outcome was likely to be due to a mixture of factors, such as the stability of the MOF/MON and its dispersion/interaction within the PIR foam system. Details for the synthesis of this system and optimisation of the nanosheets were not discussed in Chapter 3, and are instead outlined in the first section of this chapter.

The hypothesis for this PSF was that the replacement of amine groups with carboxylic acid groups (through a reaction with maleic anhydride) on the surface of the Cu(ABDC)(DMF) MOF will allow access to thinner nanosheets through repulsion between layers, and therefore, when

added to rigid PIR foams, will change the amount of gas retained through enhanced tortuous paths in a composite rigid PIR foam after accelerated aging for 28 days.

5.3.2 – Synthesis of Cu(MA-ABDC)(DMF)

Cu(ABDC)(DMF) was synthesised according to methods previously developed within the Foster group[2]. Namely, copper acetate monohydrate and aminoterephthalic acid were dissolved in DMF. The mixture was stirred at 110 °C for 16 hours and washed via centrifugation with fresh DMF and diethyl ether. The resultant green material was dried under vacuum, yielding Cu(ABDC)(DMF).

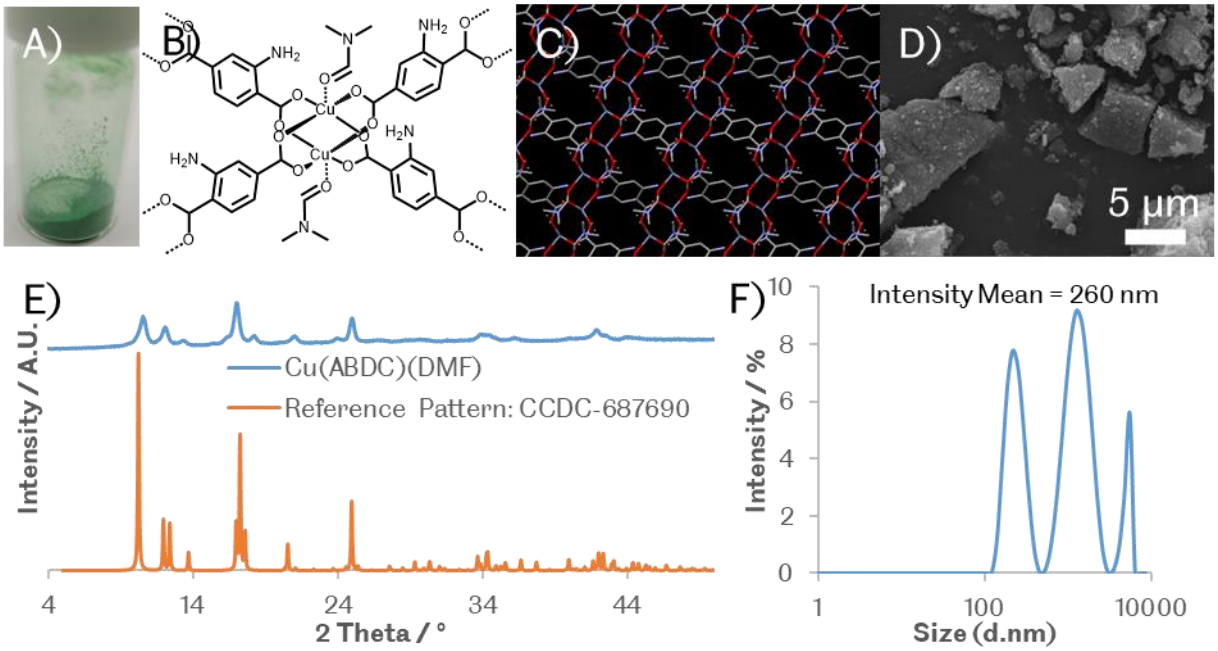

Figure 5.1. showing data for Cu(ABDC)(DMF) MOF: A) photograph of MOF as-synthesised B) Chemdraw structure of the paddle-wheel, C) Expanded crystal motif, D) SEM image of the crushed MOF, E) PXRD of the MOF compared to a reference pattern (CCDC-687690)[6], and F) DLS of MOF in acetonitrile after sonication (37 kHz, 60 seconds).

Figure 5.1. shows data for the characterization of Cu(ABDC)(DMF) MOF. The PXRD pattern was compared with the calculated powder pattern and showed a close match, with some broadening of the peaks due to the small crystallite size. NMR showed the presence of DMF

(at a ratio of 1:1 to ABDC linker) and acetic acid (at a ratio of 0.16:1 to ABDC linker). A formula of $CuC_{11}H_{13}N_2O_5$ was determined from CHN analysis. Therefore, this MOF was utilized for functionalization with maleic anhydride.

Cu(MA-ABDC)(DMF) was synthesized via the suspension of Cu(ABDC)(DMF) and maleic anhydride in chloroform and heated to 55 °C. The reaction was monitored via NMR spectroscopy until the target functionalization was achieved. The resultant green solid was washed repeatedly with chloroform then dried under vacuum. The MOF was analysed via NMR to determine its functionalization before being used for further testing. Herein, each system is refered to as Cu(MA-ABDC)(DMF) XX %, where XX represents the functionalization of the system. For example, a 31 % functionalized MOF will be reffered to as Cu(MA-ABDC)(DMF) 31 %.

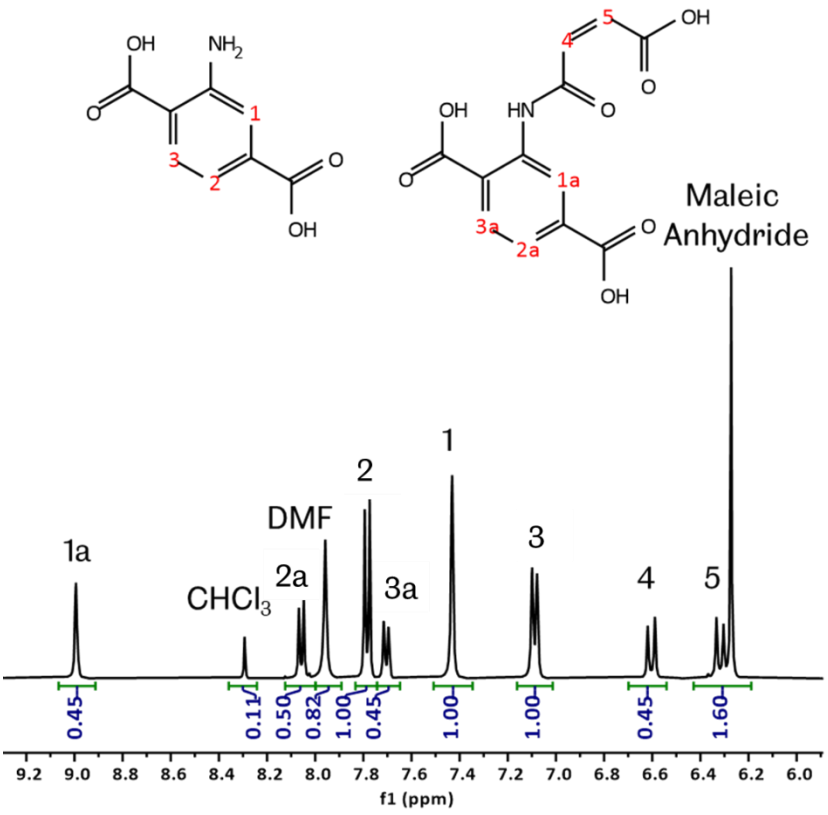

Figure 5.2 ^{1}H NMR spectra of Cu(MA-ABDC)(DMF) 31 % MOF digested with $CDCl_3$/DCl. Residual $CHCl_3$, DMF and Maleic anhydride remain in the pores.

Figure 5.2 shows an NMR spectra demonstrating the functionalization of Cu(MA-ABDC)(DMF), where the aromatic peaks are highlighted. The aminoterephthalic acid aromatic peaks were deshielded after the amine was converted to an amide, moving all peaks downfield. The degree of functionalization was determined by comparing the ratio between the remaining aminoterephthalic acid peaks (i.e. 1, 2 and 3) and the new amide shifted peaks (i.e. 1a, 2a and 3a). NMR analysis showed some MA (at a ratio of 0.19:1 to linker) remained in the pores alongside small amounts of residual solvents ($CHCl_3$, DMF). Material was taken forward for further analysis as exfoliation will increase the surface area of the MOFs as they become MONs, and more of these inclusions will be removed.

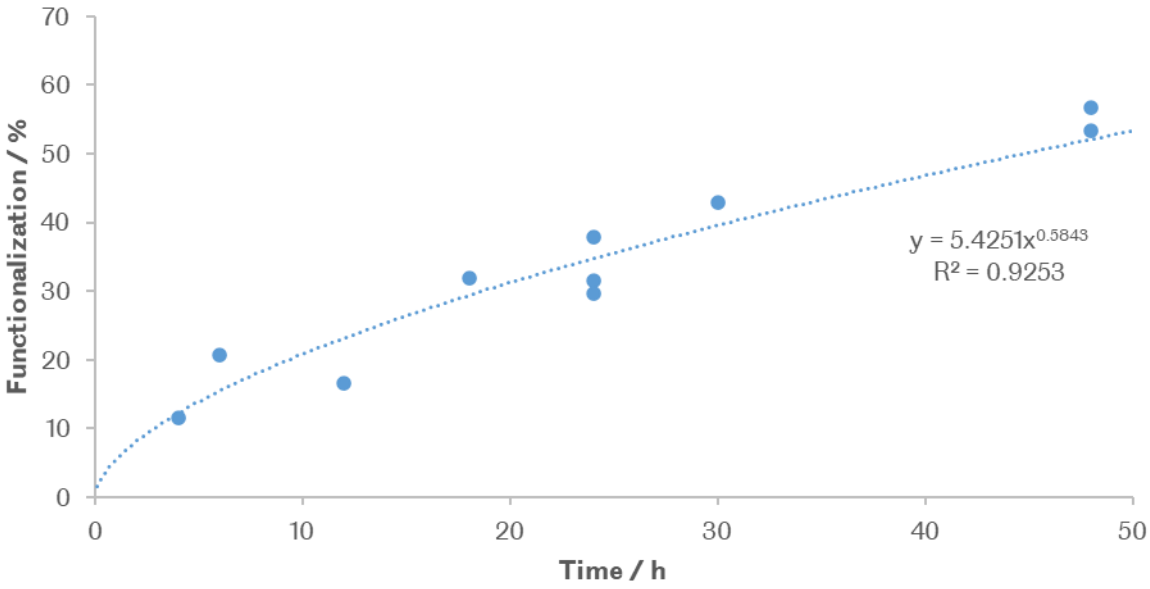

Figure 5.3 Scatter graph of 10 functionalizations of Cu(MA-ABDC)(DMF) MOF produced from differing reaction times.

Figure 5.3 demonstrates the increasing functionalization of Cu(MA-ABDC)(DMF) with time, with increasing time yielding increased functionalization. A maximum of 57 % functionalization was reached in any instance, where further reaction times up to 268 hours did not increase functionalization. The data suggests that the rate of functionalization slows over time, likely due to steric effects, limiting diffusion through the MOF. The highest functionalization achieved

was 57 %, likely further due to the increased steric bulk within the pores of the MOF preventing any further reaction from occurring and limiting the maximum functionality of the system. A similar effect was demonstrated with 1,3-propansultone on Cu(ABDC)(DMF)[2] where a maximum of 25 % functionalization was achieved due to the lack of void space. It was suggested that per paddle-wheel secondary building unit two of the amine groups were functionalized, resulting in 50 % functionalization of the system, with the further 7 % attributed to surface functionalization of the MOF.

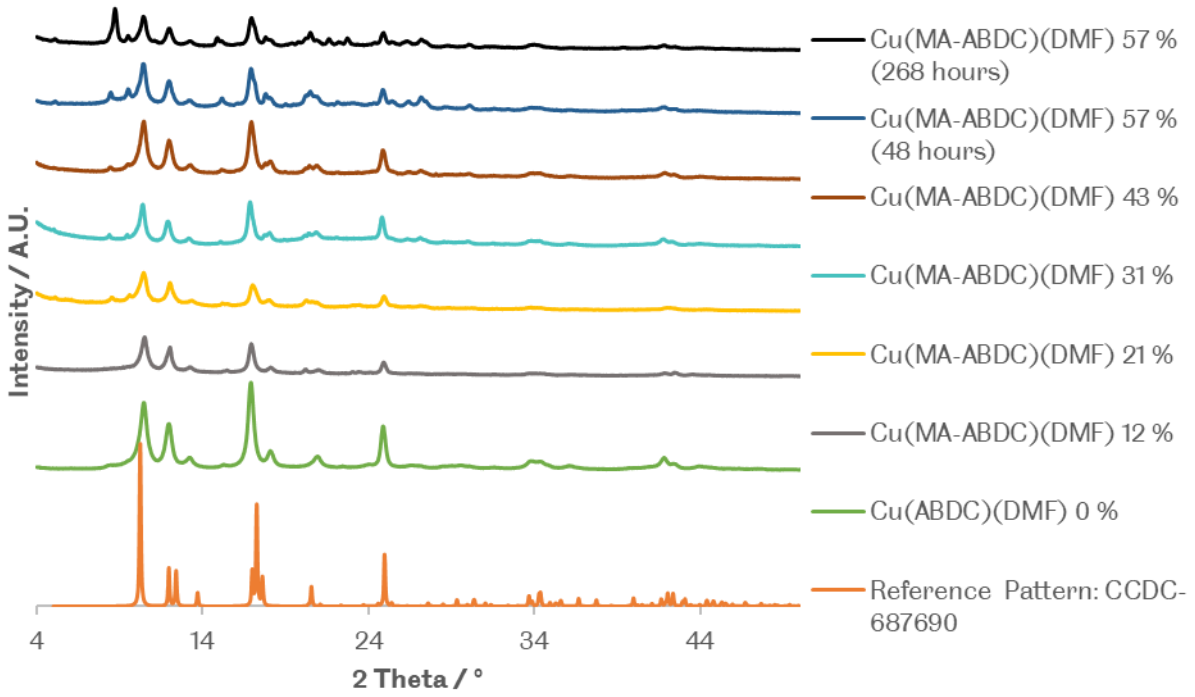

Figure 5.4 PXRD patterns of Cu(MA-ABDC)(DMF) MOF at varying functionalizations compared to a literature standard[6] and the parent Cu(ABDC)(DMF).

Figure 5.4 shows the PXRD patterns of select Cu(MA-ABDC)(DMF) MOFs when compared to a pattern calculated from a single crystal structure reported in the Cambridge structural database and the parent Cu(ABDC)(DMF) MOF. At 12 % functionalization the PXRD pattern matches closely to the reference pattern. At 21 %, 31 % and 43 % functionalization some low intensity additional peaks appear, specifically at 5.1, 8.8 and 9.9 °. At 57 % functionalization (48 hours), the powder pattern contained significantly larger additional peaks throughout the

pattern, that increase when the reaction time is extended to 268 hours. It was suggested that a desolvation effect could be occurring, similarly to Cu(BDC)(DMF) and Cu(BTetC)(DMF) when exfoliated. The DMF content in the MOFs produced does decrease with increased functionalization, for example at 0 % functionalization the DMF ratio is 1:1 linker to DMF, whilst at 12 % the DMF ratio is 1:0.42, and at 31 % functionalization is 1:0.36. However, at 57 % functionalization (48 hours) the DMF ratio is 1:0.27, and at 57 % functionalization (268 hours) it is 1:0.26. Therefore, it was not suggested the loss of DMF solvent from the MOF was the cause of the additional peaks.

A further suggested explanation for the additional peaks increasing intensity with time was due to PSF introducing non-coordinated carboxylic acid groups which have the potential to bind to the copper ions in the system and causing a rearrangement/degradation. This has been demonstrated on alternate MOF systems where incorporating carboxylic acid functionalities can lead to some degradation/structural re-arrangement of a MOF system[7]. This suggestion correlates to the increased intensity of the new peaks from 57 % functionalization at 48 hours and 268 hours. As the longer residence time could have allowed for degradation and re-arrangement of the MOF system to occur. Further study into determining the structural re-arrangement was deemed outside the scope of this work and not appropriate for the addition to rigid PIR foams and therefore was not investigated further.

Therefore, for the purposes of this work, Cu(MA-ABDC)(DMF) was functionalized to 32 % at a maximum (specifically, 12 %, 21 % and 31 %) to avoid significant alteration occurring in the system. These selected functionalizations were then investigated for their potential to produce MONs.

5.4 – Exfoliation of Cu(MA-ABDC)(DMF)

As previously established in the Foster group, Cu(ABDC)(DMF) was most effectively exfoliated by ultrasonication in MeCN. Specifically, 5 mg of MOF was suspended in 6 mL of MeCN in a

glass vial, which was then placed into an ultrasonicator bath at 80 kHz for 12 hours. The resultant suspension was centrifuged at 1500 rpm for 1 hour and the supernatant was removed, AFM analysis (figure 5.5) of the supernatant showed it contained a colloidal suspension of MONs with height in the region of 10's of nanometres and widths in the 100's of nanometres.

For the exfoliation of Cu(MA-ABDC)(DMF), alternative solvents were investigated for their performance for exfoliation. Non-polar solvents such as diethyl ether cause no exfoliation as the MOF was poorly suspended within the solvent, and water was also not used as a solvent due to degradation of the MOF system resulting in no usable MONs. MeCN also caused poor exfoliation of the MOF, resulting in sedimentation as the particulates were not colloidally suspended. The most effective solvent for exfoliation of Cu(MA-ABDC)(DMF) was determined to be ethanol as it produced colloidally stable solutions that could be analysed via AFM as seen in figure 5.5.

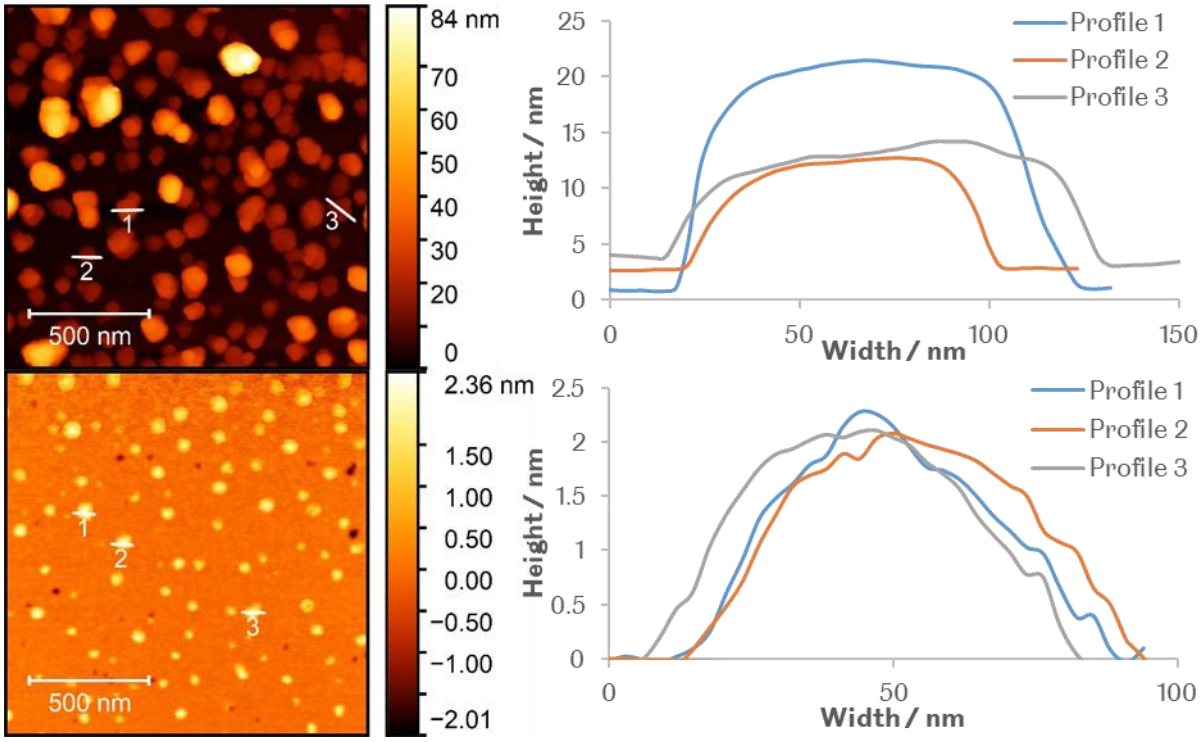

Figure 5.5 Sample AFM images, and respective sample height profiles, of A) Cu(ABDC)(DMF) and B) Cu(MA-ABDC)(DMF) 31 % MON in MeCN and EtOH respectively.

For Cu(ABDC)(DMF) MONs and Cu(MA-ABDC)(DMF) MONs, no direct comparison could be made in like-for-like solvents. As Cu(ABDC)(DMF) MONs do not effectively exfoliate or suspend in EtOH, and Cu(MA-ABDC)(DMF) MONs poorly suspend in MeCN, resulting in large aggregates that cannot be effectively analysed via AFM. Whilst this demonstrates the importance of surface functionality for exfoliation of MOFs, it means direct comparison is limited. Therefore Cu(ABDC)(DMF) data was not included in graphs in figures 5.6 and 5.7, but the data from Cu(ABDC)(DMF) MONs in acetonitrile were included for general comparison.

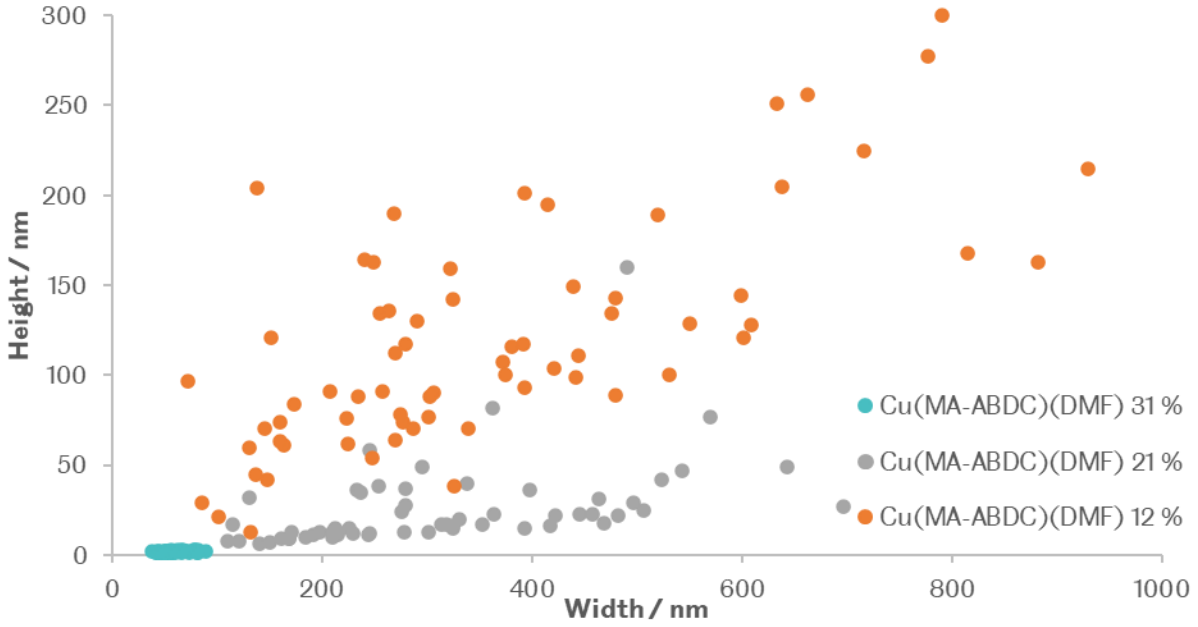

Figure 5.6 Scatter graph of Cu(ABDC)(DMF) and Cu(MA-ABDC)(DMF) 12, 21 and 31 % MON heights and widths in MeCN after AFM analysis.

MON	Average Aspect Ratio	Average Width / nm	Average Height / nm	Total Datapoints
Cu(ABDC)(DMF) (In MeCN)	7 ± 3	125 ± 49	22 ± 17	79
Cu(MA-ABDC)(DMF) 12 %	3 ± 2	375 ± 209	129 ± 82	70
Cu(MA-ABDC)(DMF) 21 %	16 ± 6	319 ± 148	26 ± 24	59
Cu(MA-ABDC)(DMF) 31 %	36 ± 14	60 ± 11	2 ± 1	70

Table 5.1 AFM analysis data of Cu(ABDC)(DMF) and Cu(MA-ABDC)(DMF) 12, 21 and 31 % MON in MeCN and EtOH respectively.

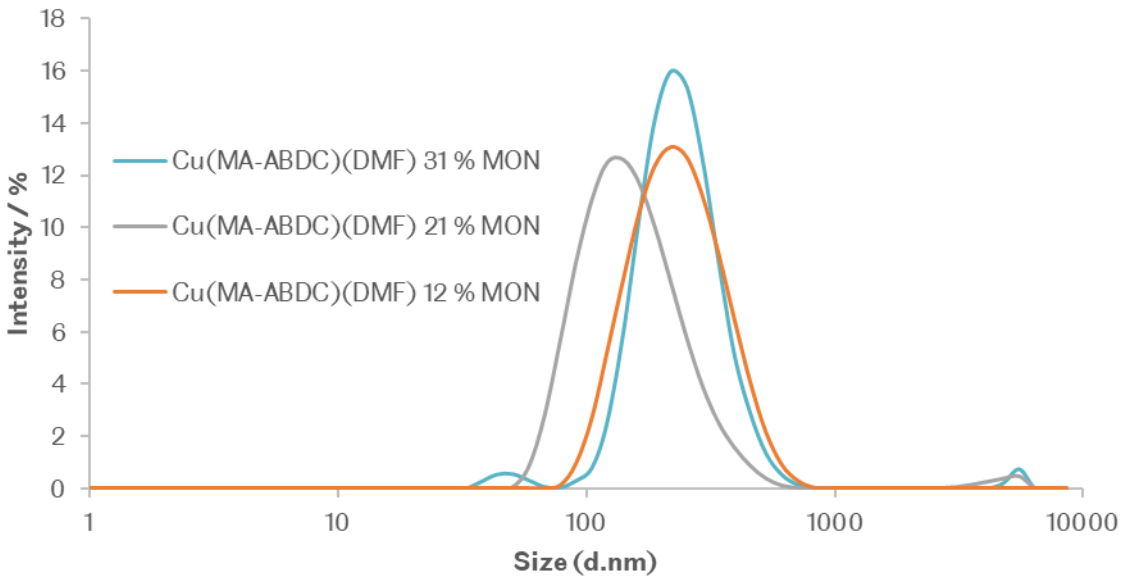

Figure 5.7 DLS analysis of Cu(ABDC)(DMF) and Cu(MA-ABDC)(DMF) MONs in MeCN and EtOH respectively (0.1 mgmL^{-1})

Sample Name	PdI	Position of the mean intensity (d.nm)
Cu(ABDC)(DMF) MON (in MeCN)	0.377	260.3
Cu(MA-ABDC)(DMF) 12 % MON	0.148	251.2
Cu(MA-ABDC)(DMF) 21 % MON	0.184	221.3
Cu(MA-ABDC)(DMF) 31 % MON	0.321	296.5

Table 5.2 DLS analysis of Cu(ABDC)(DMF) and Cu(MA-ABDC)(DMF) MONs in MeCN and EtOH respectively (0.1 mgmL^{-1})

Figure 5.6 and 5.7 shows the comparison of AFM and DLS data from Cu(MA-ABDC)(DMF) 12, 21 and 31 % MONs (5 mg MOF, 6 mL EtOH, 80 kHz 12 hours, 1500 rpm 1 hour) with representation of Cu(ABDC)(DMF) MONs (5 mg MOF, 6 mL MeCN, 80 kHz 12 hours, 1500 rpm 1 hour) included. The AFM data shows that the MONs produced from the Cu(MA-ABDC)(DMF) 12 % and 21 % system in EtOH have larger thicknesses than those from the parent Cu(ABDC)(DMF) in MeCN, though 21 % having a larger aspect ratio. Cu(MA-ABDC)(DMF) 31 %

has a higher aspect ratio and thinner nanosheets than Cu(ABDC)(DMF) in MeCN. The DLS data provides no trend in the position of the mean intensity.

The comparison in the AFM analysis of images demonstrates that Cu(MA-ABDC)(DMF) 31 % exfoliated in EtOH produces an extremely thin MON system, with the average thickness being 2 ± 1 nm. This was a significant improvement over the Cu(ABDC)(DMF) system (22 ± 17 nm in MeCN) and demonstrates the effectiveness of utilizing alternate surface functionality to improve exfoliation of MOFs into MONs. It was suggested that the reduction in MON thickness with increasing functionalization was due to the introduction of carboxylic acids between layers, producing a repulsive effect, making the separation of layers more favourable.

In the DLS dataset, the Cu(MA-ABDC)(DMF) MONs appear to have similar intensity mean values, indicating similarly sized nanoparticles, but no overall trend in size vs. functionality. DLS analysis was utilized to measure the hydrodynamic diameter of particles that are assumed to be homogenous hard spheres. The values produced can be affected by solvent choice, concentration, and the fit-model used to determine size[8]. Furthermore, multiple peaks within the DLS measurements can be indicative of multiple size distributions within a single sample, or an effect of agglomeration within samples[9]. Therefore, for MON systems DLS is at best utilized for comparison of similar systems in the same solvent at the same concentration to obtain trends, over utilizing the data for direct measurement and comparison of size.

The differences between the size trends of Cu(MA-ABDC)(DMF) MONs in AFM and DLS demonstrate the difficulty in accurately determining the size of nanomaterials, and the importance of multiple analytical techniques to determine size. For MONs, it was suggested that owing to possible aggregation and limitations of DLS, the DLS data was not representative of the MONs produced.

Overall, nanosheets produced by Cu(MA-ABDC)(DMF) 31 % in EtOH were smaller than those produce by Cu(ABDC)(DMF) in MeCN when analysed by AFM analysis but show comparable

results through DLS analysis. This demonstrates how changing the surface chemistry of a MOF can lead to effective exfoliation of MONs into alternative solvents. In this case, Cu(MA-ABDC)(DMF) 31 % has been effectively exfoliated into EtOH to produce MONs that have exfoliated at least as effectively as the parent Cu(ABDC)(DMF) MOF in MeCN.

Section 5.5 – Cu(MA-ABDC)(DMF) Intermediate Conclusion

The achievement of ultrathin nanosheets with Cu(MA-ABDC)(DMF) 31 % was an ideal result, as it was another example of how PSF can be used to enhance exfoliation and lead to the formation of monolayer nanosheets. Therefore, following the work of ring opening maleic anhydride onto Cu(ABDC)(DMF), it was suggested that this process could be taken a step further. If ring opening a single small molecule was viable onto the surface of Cu(ABDC)(DMF), then ring-opening polymerization could be utilized to produce polymers covalently attached to the MOF or MON surface. The second section of this chapter describes the attempted ring-opening polymerization onto Cu(ABDC)(DMF) MOFs and MONs.

5.6 – Introduction and aims for polymer functionalized MOFs and MONs

5.6.1 – PolyMOFs and PolyMONs

Linking the ideal properties of MOFs (*e.g.,* gas selectivity[10]) and polymers (*e.g.,* processability[11]) together for application in areas such as gas separation[12,13] is already a rapidly growing area of research. The advantages of combining polymers to MOFs are primarily linked to their applications in gas separation, where the quality of a composite membrane produced from polymers and MOFs are highly dependent on the interaction between the MOF and the polymer. If there is poor interaction then agglomeration and void space formation can occur, reducing the quality of the separation[12], demonstrated in figure 5.8.

This issue can be mitigated by appropriately designing the MOF to better interact with the polymer network[14]. However, this cannot always be achieved whilst retaining certain desirable aspects (such as selectivity or permeability of the MOF network), therefore an alternative

solution can be covalently attaching polymers to the surface of the MOF prior to creating the composite. These materials are known as PolyMOFs, shown in figure 5.8, and can aid in distribution through the polymer matrix and creating an ideal interaction between the MOF and the polymer.

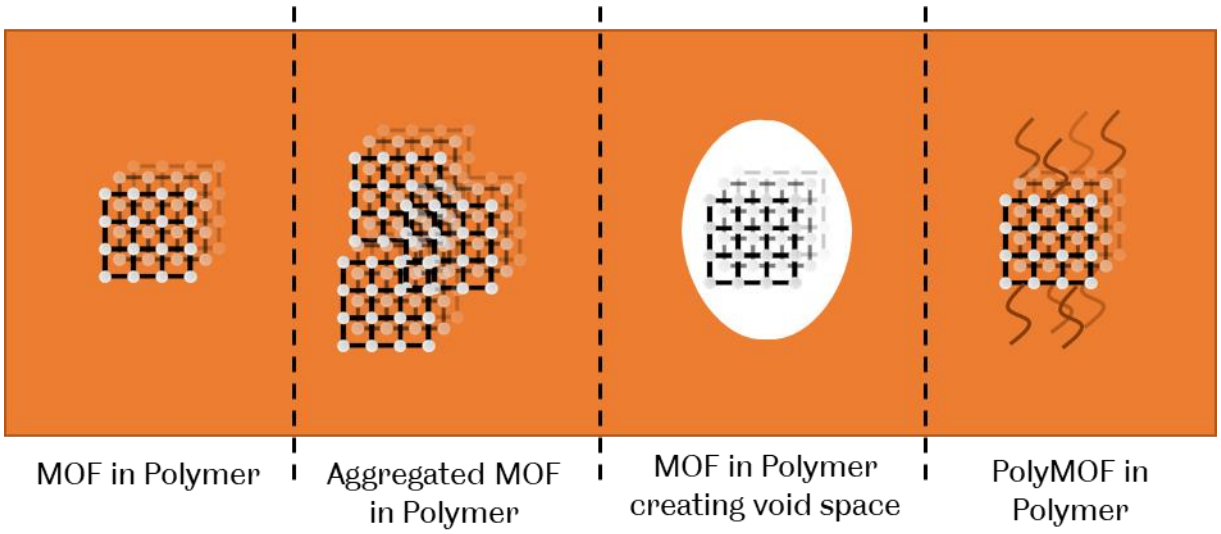

Figure 5.8 Diagram of possible MOF/PolyMOF and polymer interactions

Early PolyMOFs were shown by Prof Seth M. Cohen's group, utilizing polymer chains that contained linkers within the polymer architecture that could then be integrated into a MOF, creating dense MOFs with interwoven polymer chains through their structures[15–17] (described as graft-in PolyMOFs in this work as the polymer is grafted within the MOF structure). Alternative PolyMOFs can utilize polymers covalently attached to the surface MOF through functional groups, instead of within the MOF structure, retaining the MOFs porosity alongside the polymer on the surface[12,18]. For example, the UiO-66 system has been utilized for both attaching pre-made polymers to the surface (graft-to)[19] and modified for the growth of polymers directly from the surface (graft-from)[20].

The following sections describe the attempts to produce the next step of PolyMOFs. As if the same synthetic strategies that produce PolyMOFs are applied to MONs, then subsequently, PolyMONs (shown in figure 5.9) could be produced. These novel materials would gain the

advantage of the high anisotropy of MONs, with the increased dispersibility and processability of polymers. Therefore, the final half of this chapter describes the attempted routes to produce the novel material, PolyMONs.

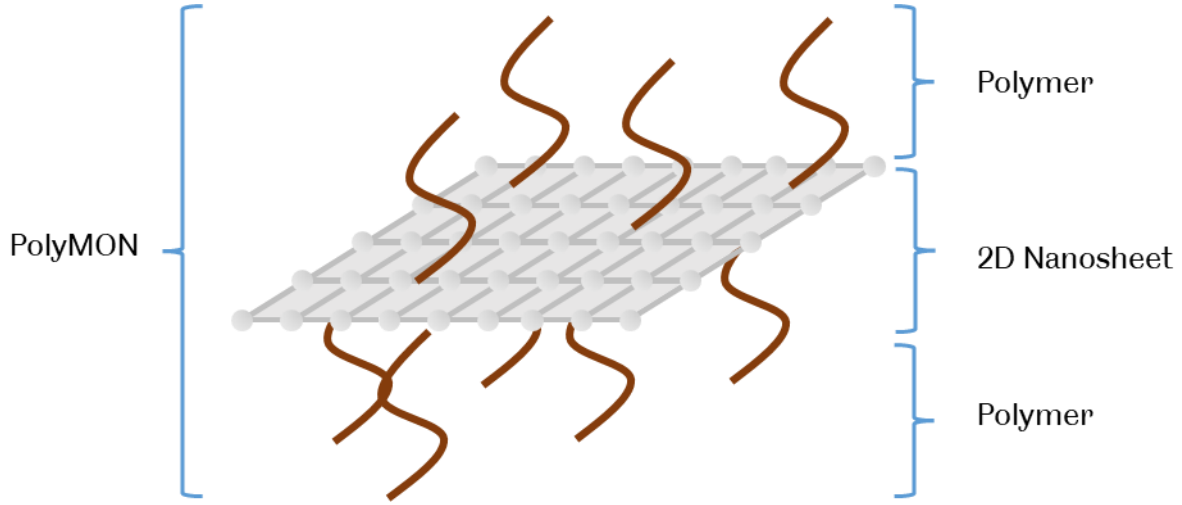

Figure 5.9 Simplified PolyMON diagram

PolyMONs could be prepared similarly to PolyMOFs produced via graft-to (where polymers are grafted to the surface of the MON) or graft-from[21] (where the polymers are grown from the surface of the MON) techniques. Graft-in techniques were not directly considered due to the difficulty of exfoliation of a MOF that has polymers extending between the layers of the MOF structure.

After the success of post-synthetic modification with ring-opening maleic anhydride on Cu(ABDC)(DMF) to create thinner MONs, adding polymers to the surfaces of the MOFs/MONs through ring-opening polymerization could provide new alternative materials for integration into rigid PIR foams.

5.6.2 – Ring-opening polymerization of cyclic esters

Ring-opening polymerization (ROP) utilizes monomers that are constrained in a ring with hetero-atoms that can be polymerized into linear chains through the use of an initiator and catalysts.[22] Typical monomers utilized are lactide, caprolactone or β-butyrolactone. Lactide is

common for the production of poly(lactic acid) (PLA) due to its cheap cost, and 'green' possibilities, where both the monomer can be produced from renewable sources, and the PLA at end of life can be biodegradable.

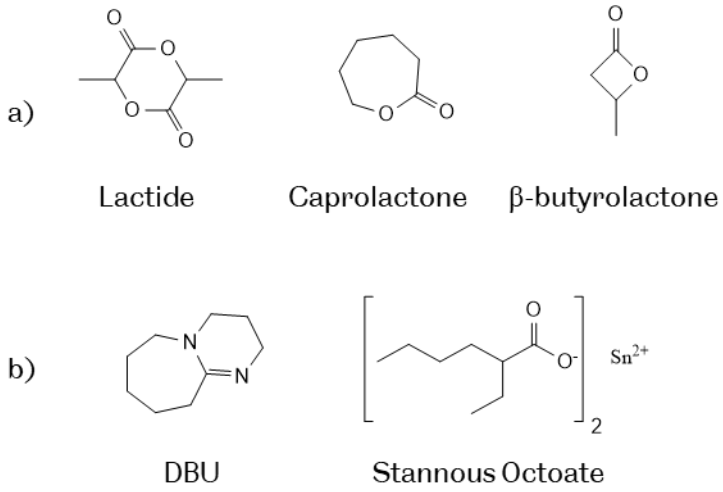

Figure 5.10 Structures of a) cyclic esters commonly used in ring-opening polymerization and b) catalysts used for ring-opening polymerization

Catalysts for ROP are varied, but typically 1,8-Diazabicyclo(5.4.0)undec-7-ene (DBU) or Tin(II) 2-ethylhexanoate (Stannous Octoate) are used due to their cheap cost, ability to produce high molecular weights, and low toxicity. Structures are shown in figure 5.10. DBU catalyses ROP through a nucleophilic attack of the monomer, allowing polymerization to take place in solution where the DBU is removed by a free alcohol or amine[23–25]. Alternatively, stannous octoate catalyses ROP via a co-ordination insertion mechanism, first coordinating to the initiator (alcohol[26] or amine[27]), then to a cyclic ester for polymerization, promoting further polymerization through co-ordination to the free alcohol at the end of the polymer chain in each instance[26].

ROP can be utilized to produce polymer chains from a surface (surface ROP)[28], and was an ideal candidate for PolyMOF/PolyMON synthesis. In the context of PolyMONs, Poly(Lactic Acid) (PLA) was targeted due to its cheap monomer (lactide), the monomers well studied reaction,

and the combination of PLA and Polyurethane was already demonstrated within literature, with PLA being directly used as polyol for PU synthesis in some cases[29–31].

ROP can be undertaken in mild conditions, giving an opportunity for Cu(ABDC)(DMF) to be utilized for these reactions, where the low stability of the MOF prevents harsh polymerization techniques.

5.6.3 – Aims and objectives for PolyMOFs/PolyMONs

In the current literature, there are no specific examples of polymers covalently attached to free standing MONs to produce PolyMONs, and the synthesis of these novel materials would allow for significant modification of MONs for not only the introduction to rigid PIR foams, but allow for a new area of MON, and composite, research to be explored. Additionally, there are no specific examples of ROP being utilized to produce PolyMOFs, making the investigation of the techniques use for both PolyMOF and PolyMON synthesis novel.

The desired aim for this section was to produce polymer functionalized MONs for addition to PIR foams to improved gas retention by further tuning the structure of the MONs to better interact with the rigid PIR foam. This would be attempted through ROP of cyclic esters onto the surface of Cu(ABDC)(DMF) as a graft-from technique, to grow PLA chains directly from the MOF/MON surface.

Work on ROP is described through the chapter, beginning with initial testing of conditions varying time, catalyst, monomer, and MOF to find an optimum system for the growth of polymers from the MOF surface, then attempt the same synthesis on pre-exfoliated MONs. From this, then a small section of alternative attempts with alternative monomers and the NH_2-MIL-53 MOF is described.

5.7 – Attempted routes for ROP onto Cu(ABDC)(DMF)

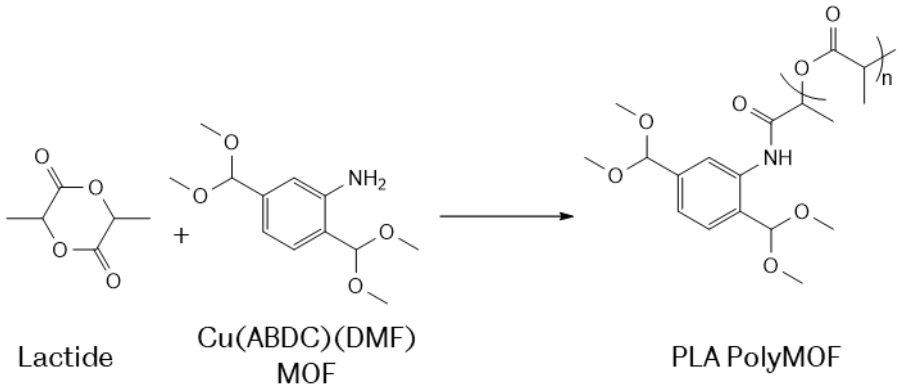

Figure 5.11 PLA polymerization from the ABDC linker of Cu(ABDC)(DMF)

In a standard reaction, Cu(ABDC)(DMF) MOF and monomer were degassed under high vacuum and repeatedly flushed with argon. Dry dichloromethane and catalyst were introduced to the reaction, and the mixture was refluxed until completion. To terminate the reaction, the mixture was exposed to air, and centrifuged at 12,000 rpm for 30 minutes. The supernatant was discarded, and fresh solvent was re-introduced to the solids to remove any remaining monomer or catalyst and wash the material. The solids were centrifuged again, and this process was repeated 5 times. To initially determine if polymerization had occurred, a sample was taken from the reaction mixture during polymerization, dried under reduced pressure, mixed with deuterated solvent, and sonicated at 37 kHz for 30 minutes. No acid digestion was utilized for NMR analysis to prevent possible degradation of any polymer chains produced alongside the MOF structure, instead, sonication was utilized to liberate polymer chains from the structure. Specific variations and results on experimental conditions can be seen in figure 5.29 in the experimental section.

Initial experiments utilized 1,8-Diazabicyclo(5.4.0)undec-7-ene (DBU) as a catalyst with lactide as a monomer for ROP on Cu(ABDC)(DMF) MOF. DBU was chosen as the initial catalyst due to initial availability. NMR observations (figure 5.12) when sampling the reaction mixture showed

peaks for the lactide in solution (peaks 1 and 2), but also demonstrated additional peaks (1a, 2a and 3a), which were attributed to PLA, indicating DBU had catalysed ROP in solution.

After the reaction was stopped and solids were obtained and washed to determine if polymerization had taken place on the MOF surface, the resultant material had a significantly lower mass than the amount of MOF used for initiation. It was determined that the use of DBU as a catalyst caused degradation of the copper MOF systems, which was further demonstrated with increased reaction times (up to 16 hours) produced a yellow solution, indicating digestion of the MOF system.

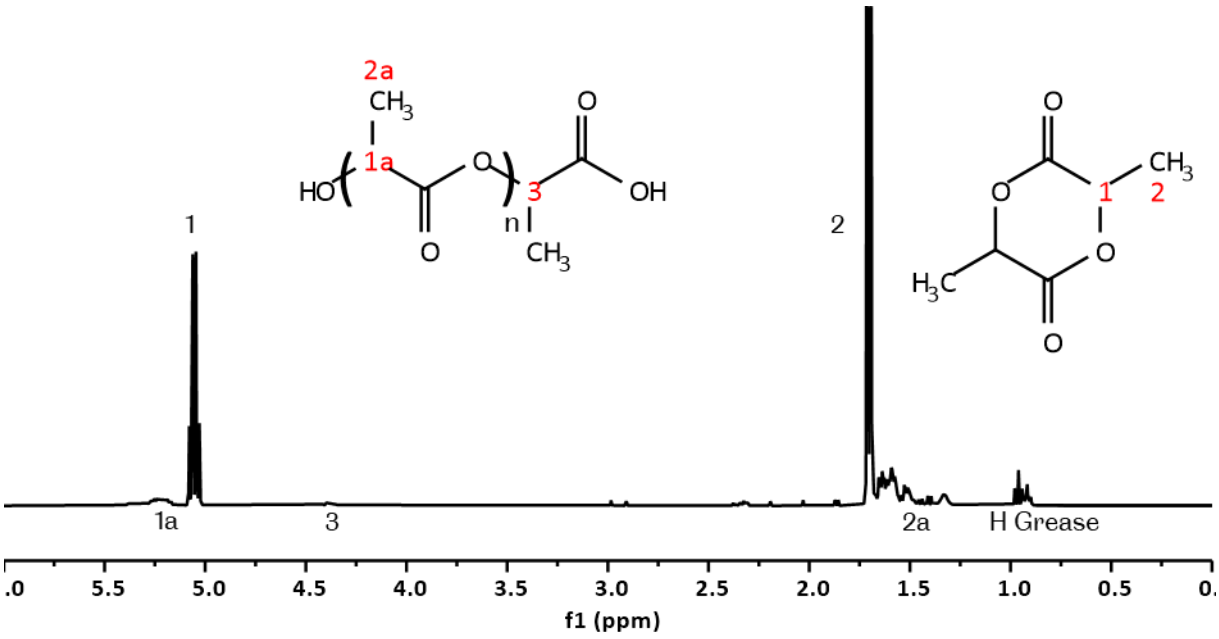

Figure 5.12 ^{1}H NMR spectrum of the initial ROP from Cu(ABDC)(DMF) MOF in $CDCl_3$

Following this result, Stannous Octoate was utilized as an alternative catalyst to DBU. Under similar conditions, with only the catalyst changing, ROP with lactide and Cu(ABDC)(DMF) produced NMR results with similar peaks (1a, 2a and 3a) indicating polymerization. After the final material was washed, no significant reduction in mass was observed.

As no initial degradation of the MOF was observed when utilizing Stannous Octoate as a catalyst, with polymerization being observed in the NMR analysis, the reaction conditions were

taken forward for testing with Cu(ABDC)(DMF) MONs. This was to determine if the MON system would survive under similar conditions and further investigation into the reaction was warranted.

Cu(ABDC)(DMF) MOF was exfoliated in MeCN (5 mg MOF in 6 mL MeCN, 80 kHz, 12 hours. Then centrifuged at 1500 rpm for 1 hour) and dried under reduced pressure. The MONs and monomer were degassed under high vacuum and repeatedly flushed with argon. Dry dichloromethane and stannous octoate were introduced to the reaction, and the mixture was refluxed until completion. To terminate the reaction, the mixture was exposed to air, and centrifuged at 12,000 rpm for 30 minutes. The supernatant was discarded, and fresh solvent was re-introduced to the solids to remove any remaining monomer or catalyst to wash the material. The solids were centrifuged again, and this process was repeated 5 times. This reaction produced similar NMR results (1a, 2a and 3a peaks), with a significant reduction in mass post washing.

Similarly to the MOF system and DBU, the MON system and stannous octoate resulted in degradation. It was suggested that whilst the stannous octoate catalyst did catalyse the initiation and polymerization of PLA, it was still causing some degradation in the MOF, in which was enhanced when utilized with MON due to the increased surface area.

Therefore, the use of DBU and stannous octoate catalysts were not viable for the production of copper paddle-wheel based PolyMONs, as any slight degradation of the MOF system during polymerization will result in significant break down of the copper MON system due to the increased surface area available. Further catalysts were considered, but either were too costly, or likely to cause similar degradation effects, and therefore not explored in this work.

Alternative monomers such as caprolactone and β-butyrolactone (figure 5.10.) were also investigated as monomers to vary possible ring strain on the monomers to encourage initiation. Compared to the Lactide ROP, similar reaction conditions were used, though with

no catalyst. No initiation was observed in NMR analysis under any conditions with any alternative monomer. Therefore, the ROP for Cu(ABDC)(DMF) was discontinued.

As a final investigation, these reactions were also attempted with NH_2-MIL-53 due to the systems higher stability, but no initiation was observed with either DBU or stannous octoate catalyst when combined with any monomer.

5.8 – ROP Intermediate Conclusion

The utilization of ROP with amine-based MOF or MON initiators results in poor initiation and polymerization of the monomer from the surface of the MOF or MON. For Cu(ABDC)(DMF) the catalysts utilized resulted in breakdown of the MOF/MON structure, and at best allowing for free polymerization of liberated linkers from the MOF/MON. For NH_2-MIL-53, no initiation was observed, and when using alternative monomers with increased ring strain, still no initiation occurred. Likely, the amine-based linkers for these MOFs were deactivated from being part of the MOF structure, therefore they can no longer act as initiators for ROP. However, the production of PolyMONs was still a viable route for enhancing the gas retention within rigid PIR foams. Further synthetic possibilities were explored, resulting in the final section of this chapter which describes a further graft-from method; atom-transfer radical polymerization.

5.9 – Atom-Transfer Radical Polymerization Introduction

Atom-transfer radical polymerization (ATRP) is a controlled "living" polymerization pioneered by Krzysztof Matyjaszewski[32–35]. The technique utilizes an initiator containing a halogen group, vinyl/methacrylate monomers and a copper catalyst to perform the reaction.

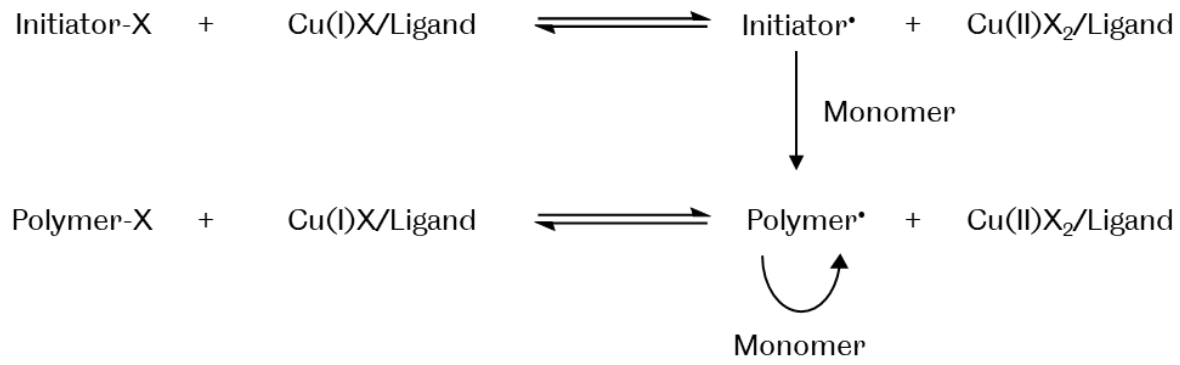

Figure 5.13 Simplified diagram of ATRP

In practise, the reaction proceeds by the reaction scheme detailed in figure 5.13, where initially halogen group from the initiator is removed by the copper catalyst, producing a free radical. This radical is then free to attack a monomer and begin the polymerization process. However, the reaction with the copper catalyst is reversible, and by design, heavily favours the re-introduction of the halogen to the propagating species. The utilization of this method results in very few radical groups being accessible at any point in time, rapidly reducing the speed of the polymerization and creating a controlled reaction. Therefore, a low polydispersity can be accessed, and few termination steps occur. This polymerization method can allow the ability to produce heteroblock copolymers from the polymers produced.

This method has been extensively explored, resulting in alternative catalysts, monomers, and conditions. For this work, the utilization of ATRP from surfaces was the inspiration[32], as ATRP initiators have been attached to surfaces to produce both graft-to and graft-from polymers

ATRP has been used extensively in MOF systems to create PolyMOFs, where α-Bromoisobutyryl bromide is reacted with functional groups available on MOFs to produce an effective ATRP initiator on the surface of the MOF[36–38]. From there a range of polymers can be grown from the surface for a variety of applications.

Currently this technique has not been utilized for Cu(ABDC)(DMF) and has had limited use with NH_2-MIL-53[39]. In this work a multitude of routes were attempted to functionalize both MOF systems.

5.10 – ATRP initiator integration in Cu(ABDC)(DMF) MOF/MON

As an initial step in the production of PolyMONs from ATRP, an appropriate initiator has to first be introduced to the surface of the MOF/MON. As previously described, multiple routes have been explored for alternative MOFs for the attachment of ATRP initiators to their surfaces, which can be applied to Cu(ABDC)(DMF). Therefore, the following section describes the attempted attachment of initiators to Cu(ABDC)(DMF) MOF and MON.

5.10.1 – Post-synthetic attachment of α-Bromoisobutyryl bromide

For Cu(ABDC)(DMF), the initial method for functionalization was a post-synthetic route where α-Bromoisobutyryl bromide (BiBB) was combined with MOF or MON in $CHCl_3$ and triethylamine (TEA) for up to 16 hours. For the copper-based MOFs utilized, in every case a breakdown of the MOF had occurred. NMR analysis showed the functionalization of the amine group on the linker does occur, but due to the production of HBr as a by-product of the reaction, the overall MOF structure is rapidly degraded, resulting in a black solution.

A stable functionalized MOF can be formed (denoted as Cu(Br-BDC)(DMF)) with a functionality of up to 5 %, through short (<1 hour) reaction times and high levels of TEA (10 x molar excess). Additionally multiple washing cycles are required to remove any degraded linkers from the MOF pores. The MOF was analysed via NMR to show the functionality of the Cu(Br-BDC)(DMF) produced (figure 5.14) and the structure was analysed via PXRD analysis when compared to a literature standard and parent Cu(ABDC)(DMF) MOF (figure 5.15), demonstrating a phase-pure functionalized MOF.

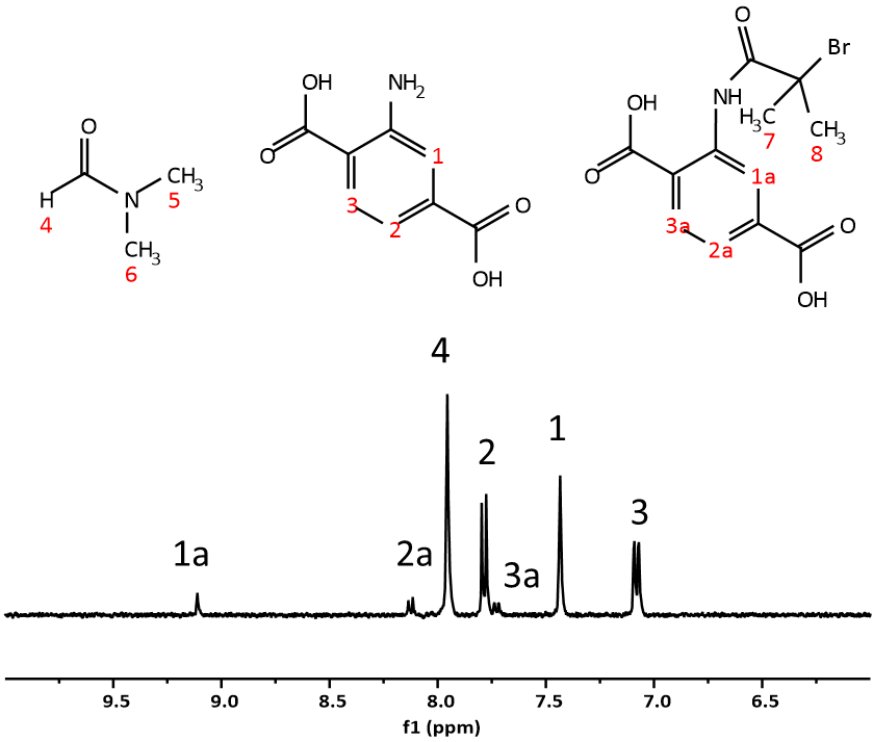

Figure 5.14 NMR of the functionalized Cu(ABDC)(DMF) after reaction with BiBB. Peaks 5 and 6 omitted for clarity.

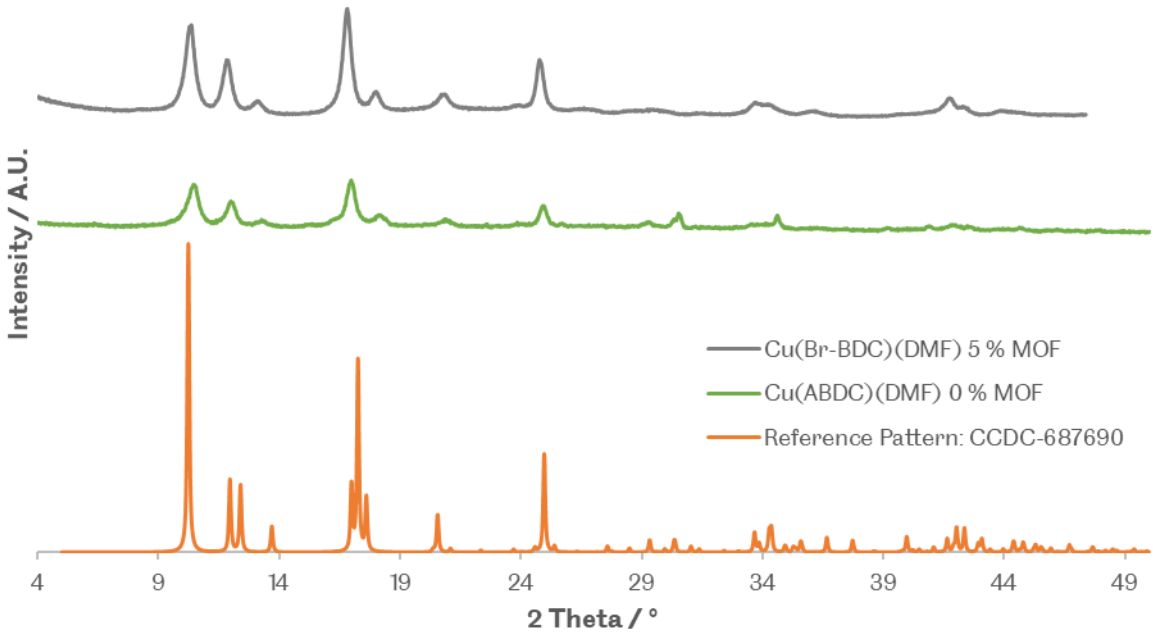

Figure 5.15 PXRD pattern of Cu(Br-BDC)(DMF) MOF compared to a literature standard[6] and the parent Cu(ABDC)(DMF).

The maximum of 5 % functionality for the Cu(Br-BDC)(DMF) system is likely due to rapid surface functionalization of the MOF, with higher functionalities causing digestion of the MOF system instead, releasing the functionalized linkers and reducing the final functionalization of the MOF.

5.10.2 – Pre-synthetic attachment of α-Bromoisobutyryl bromide

An alternative method for functionalization of the MOF was also proposed, a pre-synthetic method. Where the linker would be functionalized initially, then incorporated into the MOF structure[34]. The method was followed as outlined by Hui-Chun Lee *et. al.* where ABDC and α-Bromoisobutyryl bromide are reacted under basic conditions at room temperature for 72 hours in dry THF, then precipitated out in toluene. The linker was washed thrice in fresh toluene and centrifuged at 12,000 rpm for 10 minutes to obtain Br-BDC linker.

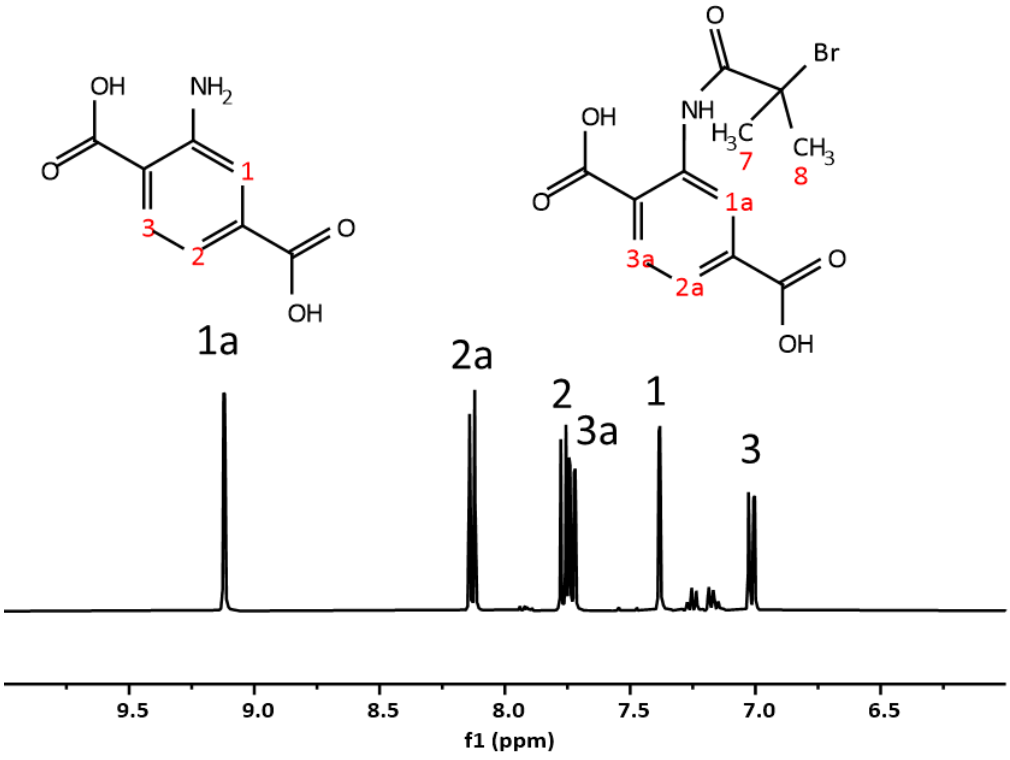

Figure 5.16 ^{1}H NMR spectrum of the Br-BDC linker in DMSO-d_6 with peaks assigned according to the inset molecular structures. A toluene impurity is present at 7.1 and 7.2 ppm.

The resultant Br-BDC linker synthesized produced a mixed system of the original ABDC linker and the new Br-BDC linker at a ratio of 1:1.2 as determined by NMR analysis (figure 5.16). Further separation of this linker mixture was not attempted as introduction of separation steps into the synthesis was deemed to add too much complexity to the synthesis route when considering the aim of producing a scalable and rapidly producible material for the addition to rigid PIR foams. However, when introducing alternative linkers to a system, a mixed linker approach can be used, where two or more linkers are utilized to synthesize a MOF system. Using multiple linkers can aid in retaining a specific MOF structure, and in this instance, utilizing ABDC alongside Br-BDC in the MOF synthesis can target specific Cu(Br-BDC)(DMF) functionalities.

The resultant ABDC/Br-BDC linker mixture was then incorporated into the synthesis of Cu(ABDC)(DMF), where the linkers and copper acetate are dissolved in DMF and heated at 110 °C for 16 hours. The final MOF is washed multiple times with DMF and Diethyl ether using centrifugation (12,000 rpm 10 mins). Different ratio's (5, 12.5, 25 and 50 %, where the percentage denotes the amount of Br-BDC used for synthesis) of the ABDC/Br-BDC linker were incorporated through additional ABDC to the previously synthesized linker mixture. The resultant Cu(Br-BDC)(DMF) MOFs were then analysed by NMR to determine the effective incorporation of the Br-BDC linker, and PXRD to determine the phase purity of the MOF.

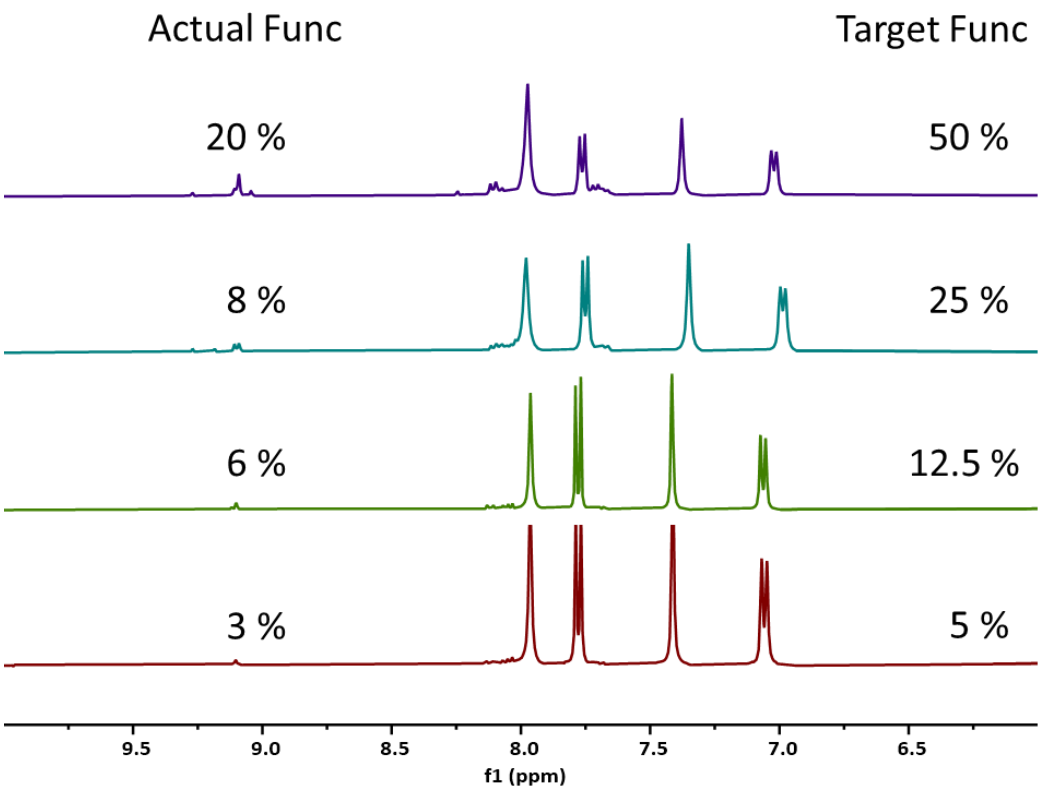

Figure 5.17 ^{1}H NMR spectrum of the Cu(Br-BDC)(DMF) MOFs digested with DCl/DMSO-d_6 where the expected functionalization is labelled on the right-hand side of the spectra, and the calculated functionalization is on the left.

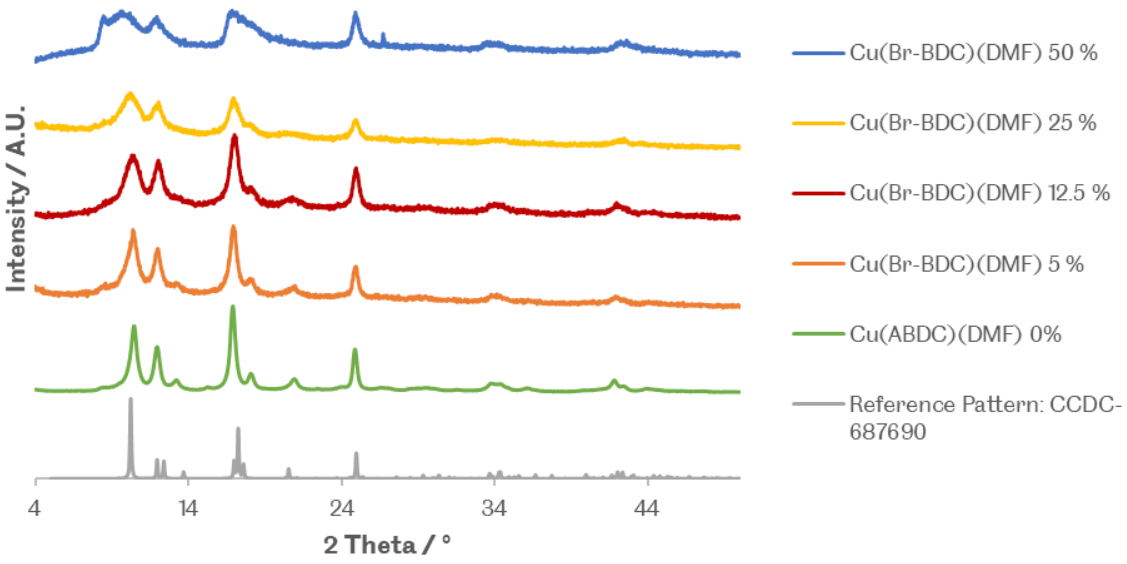

Figure 5.18 PXRD pattern of Cu(Br-BDC)(DMF) MOF at different targeted functionalizations compared to a literature standard[6] and the parent Cu(ABDC)(DMF).

The incorporation of Br-BDC to ABDC linker was determined via the ratios of aromatic peaks in the digested NMR samples of the MOFs. In every case the incorporation of the Br-BDC linker was lower than the amount calculated for synthesis. The expected functionalities were 50, 25, 12.5 and 5 % with actual functionalities of 20, 8, 6, and 3 % respectfully, as determined by NMR analysis (figure 5.17). This is not uncommon for the synthesis of mixed linker systems due to competing factors in both steric and electronic effects where one linker is preferred over another for incorporation into the MOF structure[40]. Furthermore, with higher functionalizations, further peaks indicating impurities were present in the NMR. This indicated during the MOF synthesis there were additional side reactions occurring with the Br-BDC linker utilized.

The PXRD data in figure 5.18 shows that with increasing incorporation of the Br-BDC linker, a change occurs in the MOF structure. As the Cu(Br-BDC)(DMF) system incorporates 20 % (50 % expected) of the Br-BDC linker into the system, the MOF demonstrates significant additional peaks at 8.8 and 18.8 °, likely due to the steric bulk of the size of the Br-BDC linker causing disruption in the packing of the MOF. Due to both the phase impurity and the low incorporation of Br-BDC into the system, alongside the impure synthesis of the linker itself, this route for creating a MOF with an ATRP ready initiator was not continued.

5.10.3 – Post-synthetic attachment of 2-Bromoisobutyric anhydride

A further alternative was the post-synthetic addition of an anhydride, 2-Bromoisobutyric anhydride (BIBA), due to the success in utilizing maleic anhydride to create the Cu(MA-ABDC)(DMF) MOF. Cu(ABDC)(DMF) MOF and BIBA were suspended in $CHCl_3$ with TEA. The mixture was heated at 55 °C for 16 hours before washing $CHCl_3$ and repeated centrifugation (12,000 rpm for 10 mins). The resultant NMR analysis demonstrated a functionality of up to 1 % that could not be increased with increased BIBA additions or increased reaction times. In the case of the MONs, Cu(ABDC)(DMF) was first exfoliated in MeCN (5 mg MOF, 6 mL MeCN, 80 kHz for 12 hours, 1500 rpm for 10 mins, MONs in supernatant). The MON solution then had

MeCN removed under reduced pressure and the MONs were resuspended in $CHCl_3$ for reaction. NMR's for MON reactions were performed straight from reaction solutions due to the low concentration of MONs utilized.

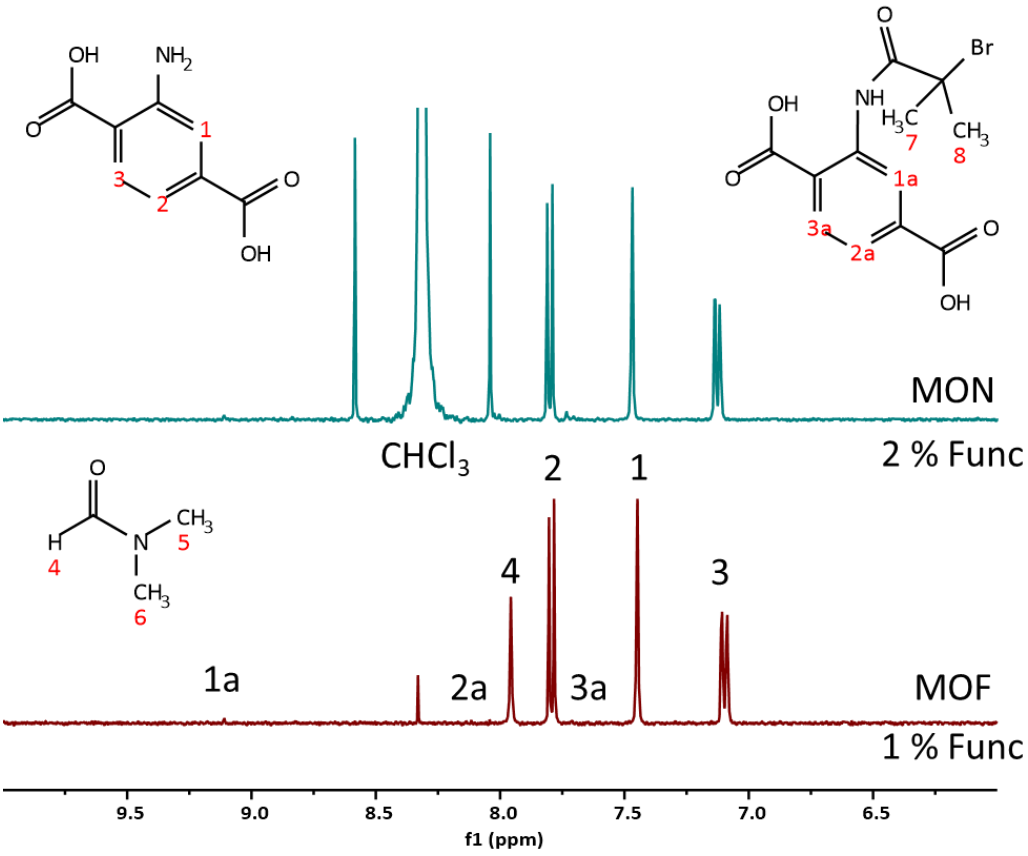

Figure 5.19 ^{1}H NMR spectrum of digested Cu(Br-BDC)(DMF) in DMSO-d_6/DCl, with calculated functionalization labelled. Peaks 5 and 6 omitted for clarity.

The digested NMR (figure 5.19) of the Cu(Br-BDC)(DMF) MOF showed a maximum 1 % functionalization whilst the MON showed a 2 % functionalization. As with the BiBB functionalization, BiBA shows a low functionality after reaction. Likely, the bulky anhydride cannot easily react with the amine groups of Cu(ABDC)(DMF) MOF structure, and the change from the MOF to MON structure allows for more surface area and amine groups to react with, allowing for the slight increase in functionalization. However, with this low functionality and high cost of the BiBA, this route to functionalization was also stopped.

5.11 – Alternative MOFs for initiator attachment

Attempts to produce further ATRP initiator functionalized MOF systems was also investigated to avoid possible degradation from HBr production. MOFs such as UiO-66-NH_2[41] and NH_2-ZIF-7[42] produced by other members of the Foster group were investigated through a reaction of α-Bromoisobutyryl bromide with the corresponding amine MOF as previously performed on Cu(ABDC)(DMF). In each case either inconsistent or no functionalization was observed, and therefore the testing with MOFs provided by other group members was halted. The final MOF tested for ATRP initiator functionalization was NH_2-MIL-53 which has some precedence for ATRP in the literature[39].

Functionalization of NH_2-MIL-53 with α-Bromoisobutyryl bromide was performed by suspending α-Bromoisobutyryl bromide with MOF or MON in $CHCl_3$ and triethylamine (TEA) for up to 16 hours, resulting in functionalization of the MOF and MON.

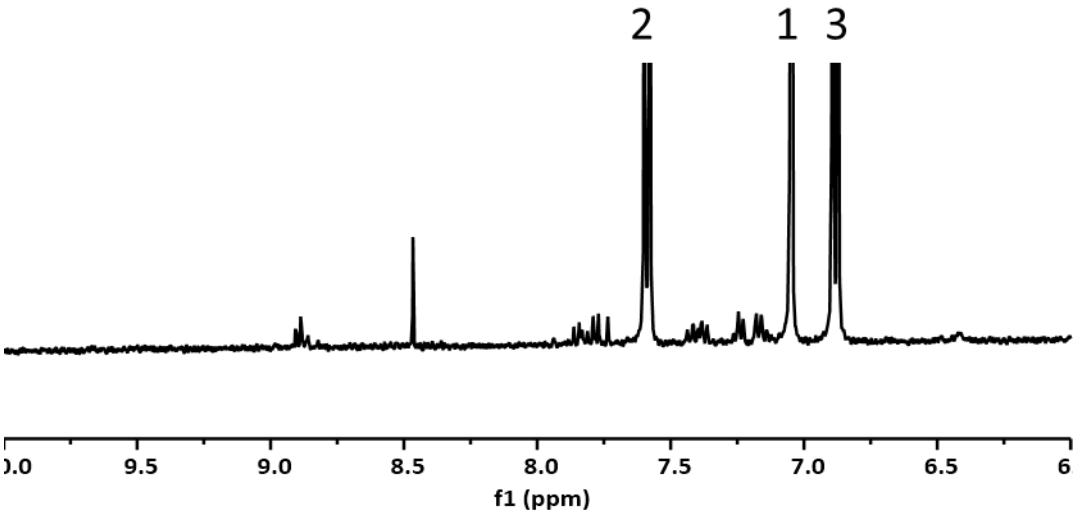

Figure 5.20 NMR of NH_2-MIL-53 MOF and MON after BIBB addition, additional peaks can be seen at 8.9 ppm, 7.7 ppm and between 7.0 and 7.5 ppm.

NMR analysis (figure 5.20) demonstrates some functionalization occurring due to intensity being observed at roughly 8.9 ppm where the 1a amide peak could be assigned. But significant additional impurities were present in the NMR spectra at 8.9 ppm, 7.7 ppm and between 7.0

and 7.5 ppm indicating side reactions were also occurring when utilizing this MOF system. As a result of this investigation, no further ATRP initiator functionalization routes were investigated for further MOFs.

5.12 – Polymerization from initiator functionalized MOFs

To determine if further investigation on the production of ATRP functionalized MONs should be continued to be explored utilizing the Cu(ABDC)(DMF) system, initial tests for polymerization were performed with the 5 % functionalized Cu(Br-ABDC)(DMF) MOF. If the MOF could successfully produce a PolyMOF through he suggested polymerization route, then further investigation into the production of Cu(Br-ABDC)(DMF) MONs would be viable for producing PolyMONs.

Polymerization was attempted by suspending the Cu(Br-ABDC)(DMF) MOF in different solvents (THF, Acetone or Toluene), a copper catalyst (CuBr with PMDETA chelating agent) and a monomer (either styrene or methyl methacrylate). Specific reaction conditions can be found in the experimental section. The resultant analysis by NMR or DSC demonstrated inconsistent results, with polymerization occurring rarely and not reliably when repeated. This indicated the polymerization was not occurring from the MOF/MON system, but from other extraneous variables. Further development of the method included a "sacrificial" initiator, ethyl-bromoisobutryrl bromide (EBiB), where the addition of free initiators has been demonstrated to aid in the ATRP from surfaces[43]. However, inconsistent results were still obtained. A suggested issue was the polymerization was being deactivated in some way due to the Copper MOF system.

An alternate method of ATRP was tested to overcome possible deactivation, utilizing ARGET (Activators ReGenerated by Electron Transfer) ATRP[32]. It was theorized that the CuBr could be reduced by the MOF system, deactivating the copper catalyst from being able to polymerize the reaction. Therefore, in the polymerization reaction a reducing agent (stannous octoate)

was also added, and the copper catalyst exchanged for $CuBr_2$ and PMDETA. However, the initiation and polymerization was again inconsistent, suggesting the MOF system is incompatible with ATRP. Due to time constraints, no further investigation was continued.

5.13 – ATRP PolyMOF/MON Intermediate Conclusion

The synthesis of MOFs and MONs functionalized with ATRP initiators is viable through a variety of different methods, though consideration of the stability of the MOF/MON needs to be considered for the most effective route. For the graft-from polymerization using ATRP on MONs, a significant amount of work is needed to effectively find an optimum system to allow for initiation and polymerization to occur from the surface of the MOF/MON to create PolyMOF/PolyMON.

5.14 – Final Conclusions and future work

In conclusion, post-synthetic functionalization of MOFs can be a powerful tool to target ideal properties for application, such as in the reduction of gas loss from rigid PIR foams, but require targeted MOF selection to obtain ideal results.

Cu(ABDC)(DMF) can be post-synthetically functionalized with maleic anhydride to produce a variety of functionalized Cu(MA-ABDC)(DMF) MOFs, in which the functionality can be determined via NMR analysis. These MOFs can be functionalized up to 57 %, with higher residence times causing changes to the PXRD pattern of the system. When exfoliating the Cu(MA-ABDC)(DMF) MOF, ethanol was the best solvent for exfoliation, and with increasing functionalization, ultrathin nanosheets (2 ± 1 nm in thickness) with large aspect ratio's (36 ± 14) can be produced, as determined by AFM analysis.

When looking to expand ring-opening further with the Cu(ABDC)(DMF) system, ring-opening polymerization was attempted on both the MOF and MON with a variety of catalysts (DBU and stannous octoate) and monomers (lactide, caprolactone and β-butyrolactone), resulting in degradation of the MOF due to its low stability. Utilizing NH_2-MIL-53 as an alternative MOF

system with the same catalysts and monomers results in no initiation or polymerization from the MOF or MON, demonstrating the need for specific MOF structures to effectively introduce polymerization to create a PolyMOF or PolyMON.

Finally, Cu(ABDC)(DMF) can be reacted with α-Bromoisobutyryl bromide to produce Cu(Br-BDC)(DMF). Through PSF the MOF can be functionalized up to 5 % but can result in degradation of the MOF system due to HBr produced as a by-product. When functionalized pre-synthetically, higher functionalities can be achieved, but cause disruption in the packing of the MOF, altering the PXRD pattern. When utilizing the MOF for ATRP, no reliable polymerization takes place, indicating the need for alternative ATRP routes or MOF systems.

Future work for the Cu(MA-ABDC)(DMF) system would be to further understand the phase change behaviour of the system as the functionalization increases past 43 %, and if the system is still layered and could be exfoliated into nanosheets. Finally, for Cu(MA-ABDC)(DMF), alternative anhydrides could be introduced to the MOF system, to investigate what steric effects take place with varied sizes of reagents, and what phase changes occur with specific functional groups introduced to the MOF/MON.

For the proposed ROP PolyMON system would be to utilize alternative MOFs for ROP that both have higher stability (such as UiO MOFs) and better initiation (such as -OH functionality), that can still access nanosheets. Then, significant advances could be made with ROP PolyMONs, investigating the MONs effects such as polymer tacticity, brush density, bush length, polymer choice or copolymerization.

Finally, for ATRP could include further investigation in functionalizing MOF/MON systems, or alternative ATRP methods, such as ICAR (Initiators for Continuous Activator Regeneration) ATRP. From these suggestions, a variety of different metal catalysts, chelating agents, and monomers can be investigated to determine the appropriate systems that can produce PolyMONs.

Whilst not described in this thesis, preliminary work was attempted on alternative production of PolyMONs, and are also routes that could be utilized in future, demonstrated in figure 5.21.

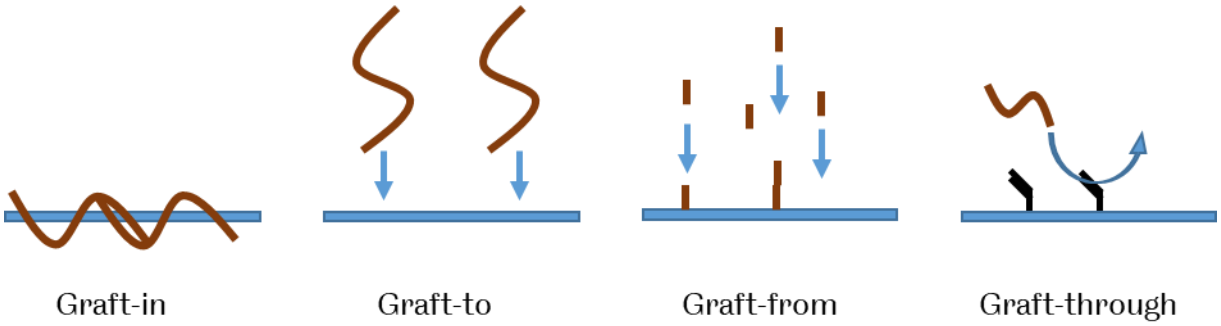

Figure 5.21 Diagrams of different synthetic routes to the synthesis of PolyMONs

Graft-in PolyMONs could be synthesized utilizing Prof Seth M. Cohens work, if the polymer chains could run along the layers of a layered MOF, theoretically creating enhanced stability of the MOF in the x and y-axis with minimal integration along the z-axis, larger and more stable MONs could be produced.

Graft-to polymerization could be a further alternative route to PolyMONs. Possible reactions could be utilized to couple a pre-synthesized polymer's end group to the MON surface, such as an epoxy, or a carboxylic acid utilizing EDC/NHS coupling.

Finally, graft-through polymerization could be an additional route to PolyMONs, where vinyl functionality is introduced to a MON surface (for example through the amine on the MON surface reacting with glycidyl methacrylate) and allowing a free-radical polymerization to take place in solution with the MON, allowing some polymerization to take place on the MON surface and produce a graft-through PolyMON.

Overall, PolyMONs have a significant amount of routes to their synthesis, that with a stable MON system, could allow for a wide variety of structures to be synthesized.

5.15 – Experimental

5.15.1 – Synthesis and Exfoliation of Cu(ABDC)(DMF)

Synthesis and data for Cu(ABDC)(DMF) MOF and MONs can be found in the experimental section of chapter 3.

5.15.2 – Synthesis and Exfoliation of Cu(MA-ABDC)(DMF)

Cu(ABDC)(DMF) (1.000 g, 3.3 mmol) and maleic anhydride (3.220 g, 32.8 mmol) were suspended in chloroform (120 mL). The mixture was stirred at 55 °C under nitrogen and monitored via NMR until the desired functionalization was achieved. The reaction mixture was centrifuged (12,000 rpm, 10 mins), the supernatant removed, and the solids washed via centrifugation (12,000 rpm, 10 mins) in Chloroform (3 x 30 mL). The sample was dried under desiccation, producing Cu(MA-ABDC)(DMF) as a light green powder. Elemental analysis: calculated mass for $CuC_{10}H_7NO_5$ (31 %)%: C 42.87; H 2.75; N 6.07; Found mass %: C 39.26; H 3.305; N 5.64. Elemental analysis: calculated mass for $CuC_9H_6NO_4$ (21 %)%: C 42.08; H 2.81; N 6.29; Found mass %: C 39.75; H 3.68; N 6.73. Elemental analysis: calculated mass for $CuC_8H_6NO_4$ (12 %)%: C 41.37; H 2.85; N 6.48; Found mass %: C 37.28; H 3.43; N 6.1. Phase purity confirmed by PXRD (flat plate) comparison (CCDC entry 687690).

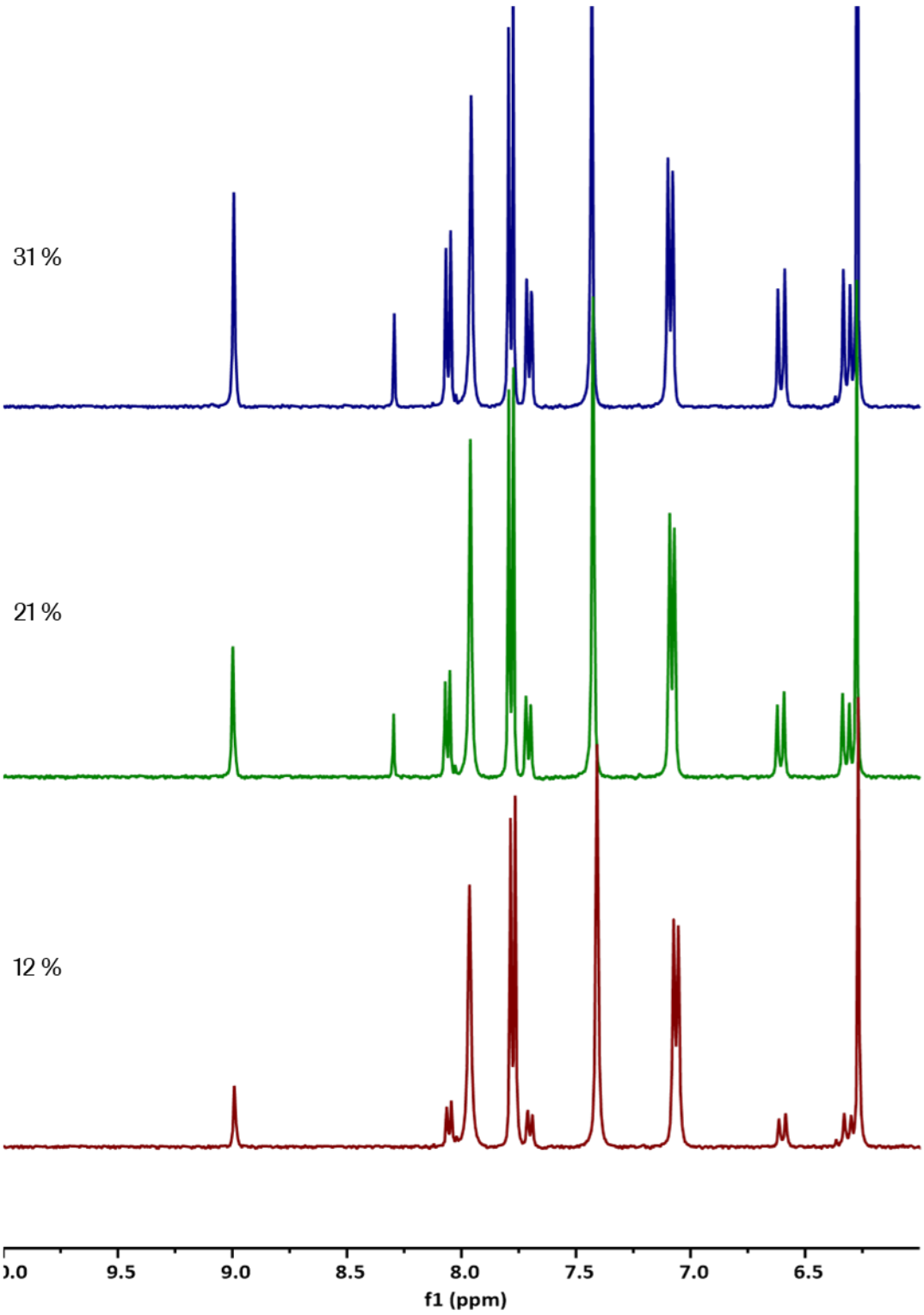

Figure 5.23 ^{1}H NMR spectrum of Cu(MA-ABDC)(DMF) at different functionalizations digested with DCl/DMSO-d_6.The functionality is assigned by the comparison of the amine to amide peaks.

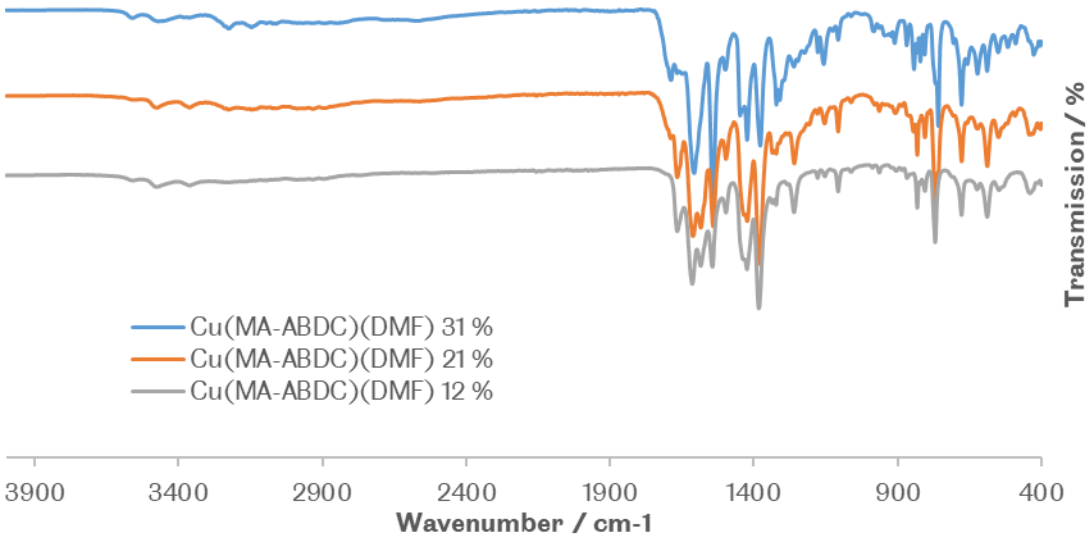

Figure 5.24 ATR FT-IR spectrum of Cu(MA-ABDC)(DMF)

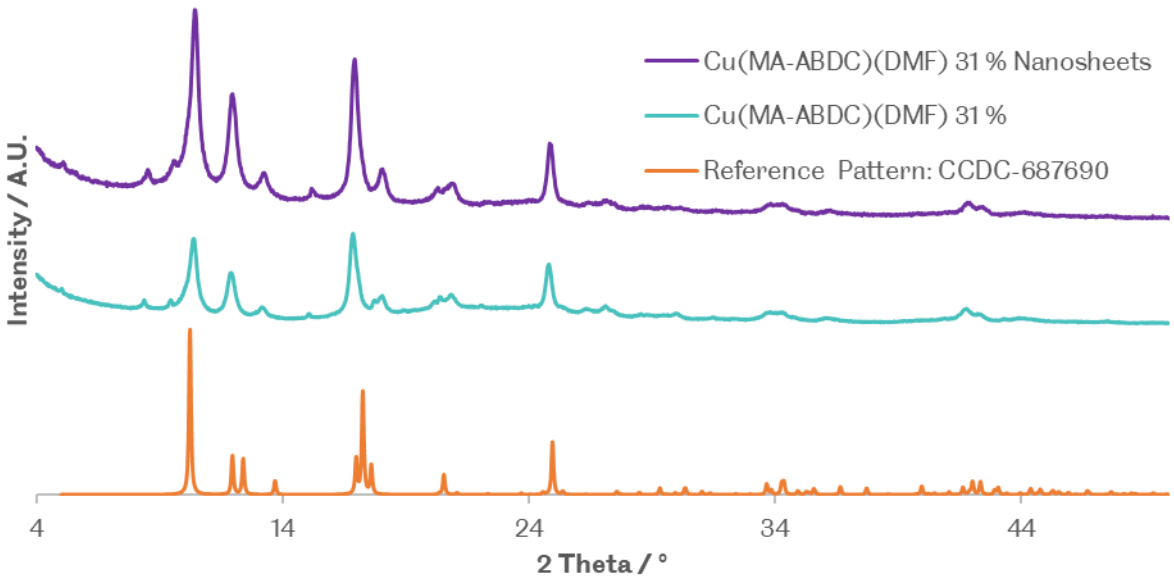

Figure 5.25 PXRD pattern of Cu(MA-ABDC)(DMF) 31 % pre and post exfoliation compared to a literature standard taken from CCDC.

Cu(MA-ABDC)(DMF) was exfoliated via liquid assisted ultrasonication as described in the exfoliation method section. A solution of Cu(MA-ABDC)(DMF) in varying solvents (0.83 $mgmL^{-1}$) was used and sonicated at 80 kHz for 12 hours.

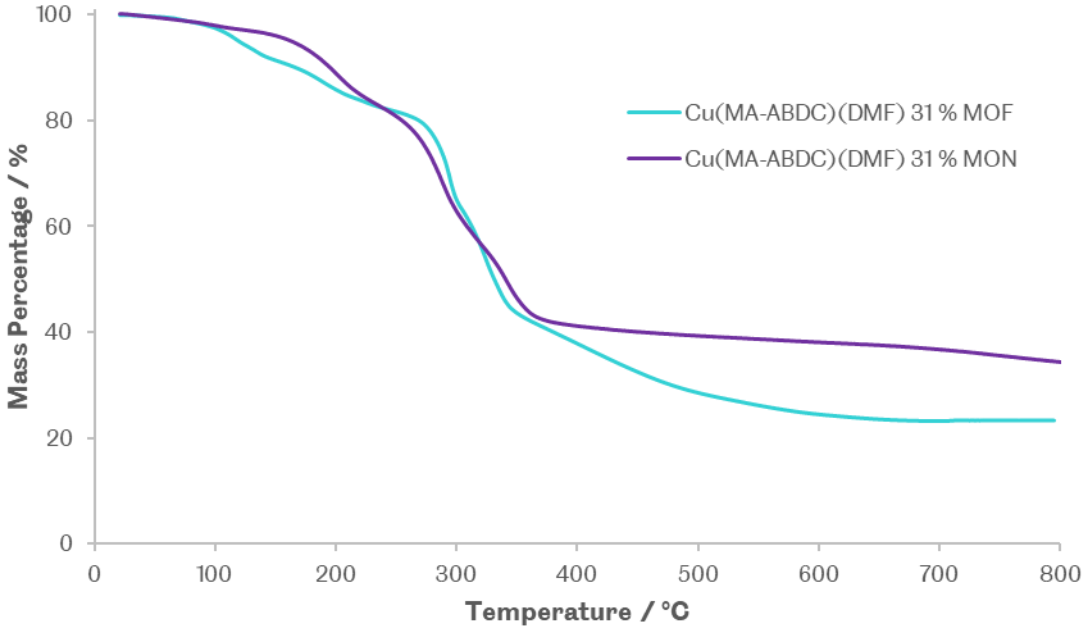

Figure 5.26 TGA analysis of Cu(MA-ABDC)(DMF) 31 % pre and post exfoliation

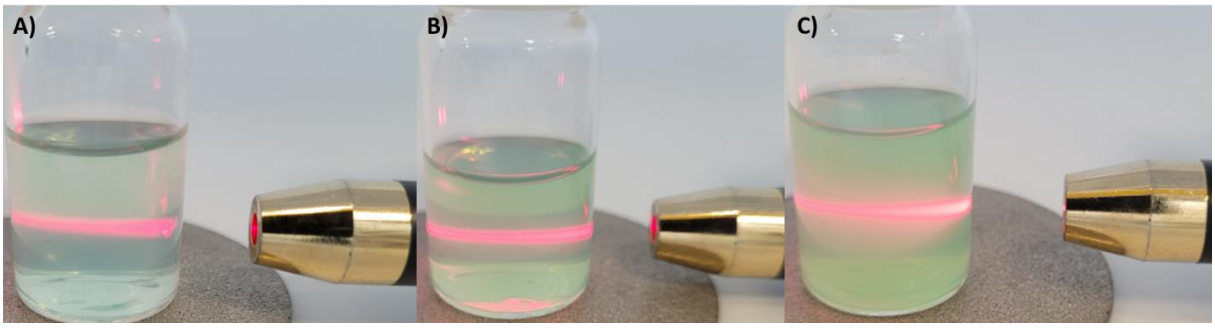

Figure 5.27 Tyndall scattering of Cu(MA-ABDC)(DMF) (A: 31 %, B: 21 %, C: 12 %) nanosheets suspended in EtOH

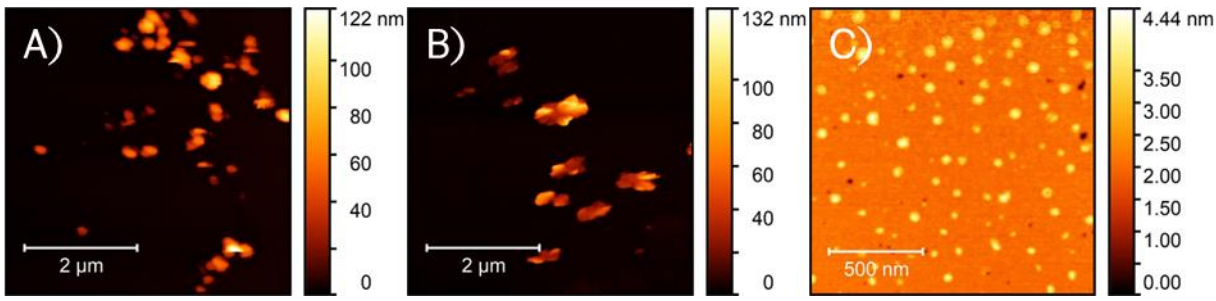

Figure 5.28 Sample AFM images of Cu(MA-ABDC)(DMF) A) 12 %, B) 21 %, C) 31 % MON in EtOH respectively

5.15.3 – Ring-opening Polymerization on Cu(ABDC)(DMF)

MOF/MON (50 mg) and monomer (1 g) were degassed under high vacuum and repeatedly flushed with argon. Dry dichloromethane (125 mL) and catalyst (0.1 mL) are introduced to the reaction, and the mixture was refluxed until completion. To terminate the reaction, the mixture was exposed to air, and centrifuged at 12,000 rpm for 30 minutes. The supernatant was discarded, and fresh solvent was re-introduced to the solids to remove any remaining monomer or catalyst. The solids are centrifuged again, and this process was repeated 5 times. To initially determine if polymerization had occurred, a sample was taken from the reaction mixture during polymerization, dried under reduced pressure, mixed with deuterated solvent, and sonicated at 37 kHz for 30 minutes. No acid digestion was utilized for NMR analysis to prevent possible degradation of any polymer chains produced alongside the MOF structure, instead, sonication was utilized to liberate polymer chains from the structure. Specific variations are detailed in figure 5.29 where polymerization was determined by evidence of 1a, 2a and 3a peaks in in-situ NMR analysis, and degradation observed via either colour change of the reaction solution, or reduction in mass post polymerization.

MOF/MON	Monomer	Catalyst	Reaction Time / h	Polymerization determined by NMR?	Degradation observed?
Cu(ABDC)(DMF) MOF	Lactide	DBU	19	Yes	Yes
Cu(ABDC)(DMF) MOF	Lactide	DBU	3	Yes	Yes
Cu(ABDC)(DMF) MOF	Lactide	Stannous Octoate	3	No	No
Cu(ABDC)(DMF) MOF	Lactide	Stannous Octoate	48	Yes	No
Cu(ABDC)(DMF) MON	Lactide	Stannous Octoate	48	Yes	Yes
Cu(ABDC)(DMF) MOF	Caprolactone	N/A	24	No	No
Cu(ABDC)(DMF) MOF	β-butyrolactone	N/A	24	No	No
NH_2-MIL-53 MOF	Lactide	DBU	24	No	No
NH_2-MIL-53 MOF	Lactide	Stannous Octoate	24	No	No
NH_2-MIL-53 MOF	Caprolactone	DBU	24	No	No
NH_2-MIL-53 MOF	Caprolactone	Stannous Octoate	24	No	No
NH_2-MIL-53 MOF	β-butyrolactone	DBU	24	No	No
NH_2-MIL-53 MOF	β-butyrolactone	Stannous Octoate	24	No	No

Table 5.3 Reaction conditions attempted to produce PolyMOFs or PolyMONs using ROP, and their outcomes.

ROP reactions were performed with assistance from Bradley Westwater of the Dr. Peter Portius group at the University of Sheffield, where reactants and solvents would be provided to Mr. Westwater for synthesis under high vacuum/argon conditions. Upon reaction completion, materials were returned to this researcher for work-up and analysis.

5.15.4 – Post-synthetic attachment of α-Bromoisobutyryl bromide

MOF/MON (50 mg) was suspended in $CHCl_3$ (200 mL) with triethylamine (0.314 mL) with stirring. α-Bromoisobutyryl bromide (0.027 mL) was then added to the mixture and allowed to stir for 1 hour. The resultant Cu(Br-BDC)(DMF) was then centrifuged at 12,000 rpm for 10 mins and washed repeatedly with fresh $CHCl_3$. The resultant green powder was dried under reduced pressure and analysed via NMR to determine functionality.

5.15.5 – Pre-synthetic attachment of α-Bromoisobutyryl bromide

Aminoterepthalic acid (0.5 g) and sodium bicarbonate (0.135 g) are suspended in THF (50 mL) in an ice bath with stirring. α-Bromoisobutyryl bromide (0.198 mL) was added dropwise to the mixture and allowed to stir for 72 hours at ambient temperature. The resultant Br-BDC was precipitated thrice in cold toluene and dried under reduced atmosphere. Purity was determined by NMR and immediately used for MOF synthesis.

MOFs were produced by dissolving Copper acetate monohydrate (1.092 g) and linker mixtures (0.908 g total) separately in DMF (95 mL). After dissolution, the solutions were combined and stirred at 110 °C under nitrogen from 16 hours. The reaction mixture was centrifuged (12,000 rpm, 10 mins), the supernatant removed, and the solids washed via centrifugation (12,000 rpm, 10 mins) in DMF (3 x 30 mL), then diethyl ether (3 x 30 mL). The sample was dried under desiccation, producing Cu(Br-BDC)(DMF) at varying functionalizations.

5.15.6 – Post-synthetic attachment of 2-Bromoisobutyric anhydride

MOF/MON (50 mg) was suspended in $CHCl_3$ (50 mL) with stirring. 2-Bromoisobutyric anhydride (0.334 g) was then added to the mixture and heated at 55 °C for 72 hours. The resultant Cu(Br-BDC)(DMF) was then centrifuged at 12,000 rpm for 10 mins and washed repeatedly with fresh $CHCl_3$. The resultant green powder was dried under reduced pressure and analysed via NMR to determine functionality.

5.15.7 – Polymerization from initiator functionalized MOFs

Cu(Br-BDC)(DMF) MOF (50 mg) was placed in a two neck flask, sealed and degassed thrice with nitrogen. Dry solvent (THF, Acetone or Toluene 5 mL) was then added to create flask A. In a separate flask CuBr (1 mg) and N,N,N′,N″,N″-Pentamethyldiethylene triamine (0.002 µL) were dissolved in dry solvent then added to flask A. Filtered and degassed monomer (styrene or methyl methacrylate 0.1 to 1 mL) was then added to flask A and heated to 70 °C under nitrogen for 2 to 16 hours until the reaction was terminated via exposure to air. The resultant material was centrifuged at 12,000 rpm for 10 mins and washed repeatedly with fresh solvent. The resultant material, if available was analysed via NMR for polymer. Alternative ARGET ATRP reactions are carried out as detailed above but utilizing $CuBr_2$ and a reducing agent (stannous octoate 0.24 µL) is added with the MOF prior to degassing. The resultant green powders were analysed via NMR to determine if polymerization had taken place.

References

1 Y. Zhang, X. Feng, S. Yuan, J. Zhou and B. Wang, *Inorg. Chem. Front.*, 2016, **3**, 896–909.

2 J. Nicks, J. Zhang and J. A. Foster, *Chem. Commun.*, 2019, **55**, 8788–8791.

3 D. J. Ashworth, A. Cooper, M. Trueman, R. W. M. Al-Saedi, S. D. Liam, A. J. Meijer and J. A. Foster, *Chem. - A Eur. J.*, 2018, **24**, 17986–17996.

4 D. J. Ashworth, T. M. Roseveare, A. Schneemann, M. Flint, I. Dominguez Bernáldes, P. Vervoorts, R. A. Fischer, L. Brammer and J. A. Foster, *Inorg. Chem.*, 2019, **58**, 10837–10845.

5 J. Nicks and J. A. Foster, *Nanoscale*, 2022, **14**, 6220–6227.

6 C. G. Carson, K. Hardcastle, J. Schwartz, X. Liu, C. Hoffmann, R. A. Gerhardt and R. Tannenbaum, *Eur. J. Inorg. Chem.*, 2009, 2338–2343.

7 S. J. Garibay, Z. Wang, K. K. Tanabe and S. M. Cohen, *Inorg. Chem.*, 2009, **48**, 7341–7349.

8 P. Hirschle, T. Preiß, F. Auras, A. Pick, J. Völkner, D. Valdepérez, G. Witte, W. J. Parak, J. O. Rädler and S. Wuttke, *CrystEngComm*, 2016, **18**, 4359–4368.

9 T. Zheng, S. Bott and Q. Huo, *ACS Appl. Mater. Interfaces*, 2016, **8**, 21585–21594.

10 R. Lin, B. Villacorta Hernandez, L. Ge and Z. Zhu, *J. Mater. Chem. A*, 2018, 6, 293–312.

11 M. Rezakazemi, A. Ebadi Amooghin, M. M. Montazer-Rahmati, A. F. Ismail and T. Matsuura, *Prog. Polym. Sci.*, 2014, **39**, 817–861.

12 M. Kalaj, K. C. Bentz, S. Ayala, J. M. Palomba, K. S. Barcus, Y. Katayama and S. M. Cohen, *Chem. Rev.*, , DOI:10.1021/acs.chemrev.9b00575.

13 Z. Zhang, H. T. H. Nguyen, S. A. Miller, A. M. Ploskonka, J. B. Decoste and S. M. Cohen, *J. Am. Chem. Soc.*, 2016, **138**, 920–925.

14 A. Kirchon, L. Feng, H. F. Drake, E. A. Joseph and H. C. Zhou, *Chem. Soc. Rev.*, 2018, **47**, 8611–8638.

15 Z. Zhang, H. T. H. Nguyen, S. A. Miller and S. M. Cohen, *Angew. Chemie - Int. Ed.*, 2015, **54**, 6152–6157.

16 S. Ayala, Z. Zhang and S. M. Cohen, *Chem. Commun.*, 2017, **53**, 3058–3061.

17 G. E. M. Schukraft, S. Ayala, B. L. Dick and S. M. Cohen, *Chem. Commun.*, 2017, **53**, 10684–10687.

18 T. Kitao, Y. Zhang, S. Kitagawa, B. Wang and T. Uemura, *Chem. Soc. Rev.*, 2017, 46, 3108–3133.

19 S. Nagata, K. Kokado and K. Sada, *Chem. Commun.*, 2015, **51**, 8614–8617.

20 Y. Li, J. Liu, K. Zhang, L. Lei and Z. Lei, *Ind. Eng. Chem. Res.*, 2018, **57**, 559–567.

21 S. S. Sheiko, B. S. Sumerlin and K. Matyjaszewski, *Prog. Polym. Sci.*, 2008, **33**, 759–785.

22 O. Dechy-Cabaret, B. Martin-Vaca and D. Bourissou, *Chem. Rev.*, 2004, **104**, 6147–6176.

23 N. J. Sherck, H. C. Kim and Y. Y. Won, *Macromolecules*, 2016, **49**, 4699–4713.

24 B. G. G. Lohmeijer, R. C. Pratt, F. Leibfarth, J. W. Logan, D. A. Long, A. P. Dove, F. Nederberg, J. Choi, C. Wade, R. M. Waymouth and J. L. Hedrick, *Macromolecules*, 2006, **39**, 8574–8583.

25 A. Alba, O. T. du Boullay, B. Martin-Vaca and D. Bourissou, *Polym. Chem.*, 2015, **6**, 989–997.

26 D. E. Henton, P. Gruber, J. Lunt and J. Randall, *Nat. Fibers, Biopolym. Biocomposites*, 2005, **48674**, 527–577.

27 A. Kowalski, J. Libiszowski, T. Biela, M. Cypryk, A. Duda and S. Penczek,

Macromolecules, 2005, **38**, 8170–8176.

28 G. Carrot, D. Rutot-Houzé, A. Pottier, P. Degée, J. Hilborn and P. Dubois, *Macromolecules*, 2002, **35**, 8400–8404.

29 K. A. Evans, Z. C. Kennedy, B. W. Arey, J. F. Christ, H. T. Schaef, S. K. Nune and R. L. Erikson, *ACS Appl. Mater. Interfaces*, 2018, **10**, 15112–15121.

30 B. Imre, D. Bedo, A. Domján, P. Schön, G. J. Vancso and B. Pukánszky, *Eur. Polym. J.*, 2013, **49**, 3104–3113.

31 X. Zhou, Y. Li, C. Fang, S. Li, Y. Cheng, W. Lei and X. Meng, *J. Mater. Sci. Technol.*, 2015, **31**, 708–722.

32 K. Matyjaszewski, H. Dong, W. Jakubowski, J. Pietrasik and A. Kusumo, *Langmuir*, 2007, **23**, 4528–4531.

33 K. L. Beers, S. Boo, S. G. Gaynor and K. Matyjaszewski, *Macromolecules*, 1999, **32**, 5772–5776.

34 H. C. Lee, J. Hwang, U. Schilde, M. Antonietti, K. Matyjaszewski and B. V. K. J. Schmidt, *Chem. Mater.*, 2018, **30**, 2983–2994.

35 H. C. Lee, M. Fantin, M. Antonietti, K. Matyjaszewski and B. V. K. J. Schmidt, *Chem. Mater.*, 2017, **29**, 9445–9455.

36 H. Hemmatpour, V. Haddadi-Asl and H. Roghani-Mamaqani, *Polymer (Guildf).*, 2015, **65**, 143–153.

37 S. He, H. Wang, C. Zhang, S. Zhang, Y. Yu, Y. Lee and T. Li, *Chem. Sci.*, 2019, **10**, 1816–1822.

38 H. Liu, H. Zhu and S. Zhu, *Macromol. Mater. Eng.*, 2015, **300**, 191–197.

39 K. Xie, Q. Fu, C. Xu, H. Lu, Q. Zhao, R. Curtain, D. Gu, P. A. Webley and G. G. Qiao, *Energy*

Environ. Sci., 2018, **11**, 544–550.

40 J. Li, Y. Wang, Y. Yu and Q. Li, *Chinese Chem. Lett.*, 2018, **29**, 837–841.

41 Y. Liu, S. Lin, Y. Liu, A. K. Sarkar, J. K. Bediako, H. Y. Kim and Y.-S. Yun, *Small*, 2019, **15**, 1805242.

42 Y. Wang, Y. Ren, H. Wu, X. Wu, H. Yang, L. Yang, X. Wang, Y. Wu, Y. Liu and Z. Jiang, *J. Memb. Sci.*, 2020, **602**, 117970.

43 T. A. von Werne, D. S. Germack, E. C. Hagberg, V. V. Sheares, C. J. Hawker and K. R. Carter, *J. Am. Chem. Soc.*, 2003, **125**, 3831–3838.

Chapter 6
Conclusions and Outlook

Grand Massif, French Alps, 2020

“Don’t adventures ever have an end? I suppose not. Someone else always has to carry on the story.”

— Bilbo Baggins in The Lord of the Rings: The fellowship of the Ring, by J. R. R. Tolkein, an English writer, poet, academic and frequent visitor of the Lickey Hills.

6.1 – Summary of Aims

Insulation has a key role to play in the UK meeting its climate targets, however the performance of current rigid polyisocyanurate foam insulators decreases over time due to the replacement of high heat capacity blowing agents (isopentane and cyclopentane) with air. Additives within insulation could be the key to combatting this issue, where highly anisotropic materials may perform best. Free-standing two-dimensional sheets made from metal ions/clusters and organic linkers known as Metal-Organic Nanosheets (MONs) may be the ideal additives to rigid polyisocyanurate insulation.

This project aimed to reduce the loss of the blowing agent (isopentane and cyclopentane) from the rigid polyisocyanurate (PIR) foams produced by Kingspan for use as insulation. A range of inorganic layered and nanomaterials have been added to PIR foams to act as barrier materials, however, there has been limited success due to poor blending of these inorganic materials within the organic matrix. Here we investigated whether metal-organic frameworks (MOFs) and nanosheets (MONs) could provide better compatibility and create tortuous paths to prolong release of blowing agents from the foams. To further develop this work, novel MOF and MON systems were also to be explored, with alterations of the MOF/MON surfaces to enhance the interaction with rigid PIR foam, and the reduction in gas loss. This chapter looks at the work achieved throughout this thesis and where it may be developed in future.

6.2 – Synthesis and functionalization of Metal-Organic Nanosheets

Copper-based paddle-wheel MOFs were exfoliated into MONs (Cu(BDC)(DMF), Cu(BTetC)(DMF) and Cu(ABDC)(DMF) in **Chapter 3** and Cu(MA-ABDC)(DMF) in **Chapter 5**) and were utilized in the synthesis of composite rigid PIR foams. Whilst Cu(BDC)(DMF) and Cu(ABDC)(DMF) MONs were already known in the literature, this work outlines the first free standing Cu(BTetC)(DMF) and Cu(MA-ABDC)(DMF) MONs produced. The optimization of the unfunctionalized systems was trivial, utilizing known protocols to produce MONs that approach 10s of nanometres in thickness with 100s of nanometres in length. The exploration

of the functionalization of Cu(ABDC)(DMF) into Cu(MA-ABDC)(DMF) resulted in MONs that primarily exhibit monolayer thicknesses with widths of 60 ± 11 nm when exfoliated in ethanol. The increasing functionalization resulted in the reduction of the MON thickness and width, with a 31 % functionalization providing primarily monolayer MONs.

Further functionalisation of MOFs in **Chapter 5** for the aim of producing PolyMONs demonstrated the difficulty of applying reaction conditions ubiquitously to all MOF/MON systems. The specific functionalization of Cu(ABDC)(DMF) utilizing ROP chemistry did not produce polymers from the surface, but did indicate that using alternative MOF systems that could survive the polymerization conditions, could yield in future ROP PolyMONs. Furthermore, with the addition of an ATRP initiator onto the surface of Cu(ABDC)(DMF) to produce Cu(Br-BDC)(DMF), ATRP could become a viable route to PolyMON synthesis utilizing further MOF/MON systems that are compatible with ATRP chemistry.

Chapter 4 expanded the synthesis of MONs to provide a novel freestanding MON of NH_2-MIL-53 through additional exfoliation of a modulated NH_2-MIL-53 MOF. These MONs approached 2 ± 1 nm with 142 ± 95 nm widths that have not been accessed with this system previously. Overall, this work has produced a significant contribution to development of specific nanosheets from MOFs, and approaches to nanosheet synthesis, that can be further utilized for applications outside of this work for other MOF systems.

6.3 – Interactions Between MOFs/MONs and Polyisocyanurate Foams

The interactions between the rigid PIR foam system and MOFs/MONs utilized in this work demonstrate the complexity of the systems involved, but introduction of MONs into rigid PIR foams can reduce the loss of gas from the foam.

Chapter 3 demonstrated that the gas loss from the foams could be significantly reduced when introducing Cu(ABDC)(DMF) MOF or Cu(MA-ABDC)(DMF) uncentrifuged MONs, whilst being increased when introducing Cu(BTetC)(DMF) uncentrifuged MONs. Following into **Chapter**

4, modulated NH_2-MIL-53 uncentrifuged MONs reduced gas loss from the foam, whilst unmodulated NH_2-MIL-53 MOF increased the gas loss.

Reductions in gas loss were likely due to favourable interactions and distributions of the MOFs/MONs through the rigid PIR system. For example, it was suggested the amine functionality of Cu(ABDC)(DMF) MOF allowed for possible covalent linkages within the PIR foam that could allow for better distribution of the MOF and therefore retention of gas within the foam. Following from this, the Cu(MA-ABDC)(DMF) uncentrifuged MONs were suggested to provide an improvement over the parent MOF in gas retention due to the high anisotropy of the MONs and the amine/carboxylic acid functionality that could provide similar covalent linkages in the foam.

In contrast, increases in gas loss from the foams were likely due to unfavourable interactions between the additive and the foam. This was best demonstrated by Cu(BTetC)(DMF) uncentrifuged MONs reducing the closed cell content in the foam, causing a significant increase in gas loss. In contrast, the closed cell content is not reduced for the unmodulated NH_2-MIL-53 MOF composite foam, it was suggested the unfavourable interactions resulted in poor distribution and aggregation of the additives within the cell walls, allowing for possible void space to occur, increasing the loss of gas from the cells.

However, **Chapter 3** discusses the influence on stability of the MOF/MON within the foam as degradation of the MOF/MON can influence the interaction between the MOF/MON and the rigid PIR foam. Specifically, Cu(ABDC)(DMF) MOF provides a greater gas barrier than Cu(ABDC)(DMF) MON, likely due to the breakdown of the MOF/MON during foaming, and the high surface area of the MON resulting in a more efficient breakdown, and therefore poorer overall barrier within the foam. This was the suggested reason for the greater performance of the Cu(MA-ABDC)(DMF) uncentrifuged MONs over the MOF, as the alteration of the linker

could have produced a MON that has a better stability within the foam and allowed the MON to act as a barrier for the blowing agent.

Chapter 4 further outlines a size/shape effect as the modulated NH_2-MIL-53 MOF in the foam performs similarly to the standard foam, whilst the unmodulated NH_2-MIL-53 MOF causes an increased loss of blowing agent. The alteration of the standard cubic MOF to the flower shaper modulated MOF provides both a higher surface area and larger particulates that are added to the foam. Likely the alteration of the structure allows for alternative distribution of the MOF through the foam causing the change in gas loss and behaviour as a gas barrier.

Finally, in all cases the introduction of centrifuge MONs performed worse that uncentrifuged MONs. It was suggested this was due to an inefficient distribution of the dried MONs through the rigid PIR foam that prevented ideal tortuous paths from being created and acting as efficient gas barriers for the composite foams. To further understand how MOFs and MONs behave within the system, further testing of MOF shapes/sizes, MOF /MON functionalities, and alternative methods of distribution within the foam need to be explored.

6.4 – Future Outlook

This work has demonstrated that the loss of blowing agent from rigid PIR foams can be monitored reliably and accurately, additives can be effectively introduced to the foam at 0.1 % by weight, and that MOFs/MONs can be utilized to produce tortuous paths that reduce the loss of blowing agents from the foams over time. This work has achieved its aims to reduce blowing agent loss with MOFs/MONs and has explored the modification of MOFs/MONs to enhance their barrier properties for introduction into rigid PIR foams.

There is a significant amount more work that can be explored following this thesis. The primary point for investigation would be exploring a more effective distribution of MONs within rigid PIR foam to determine if with better distribution, could the MONs provide a better tortuous path. A suggestion would be to introduce a colloidal suspension of MONs to the polyol, and

remove the solvent under reduced pressure, to produce a more effective suspension of MONs in the polyol, prior to foaming. This would remove the drying stage from the production of MON composites and could aid in the distribution of the MONs.

Additional exploration into the miniaturization of the foaming process would allow for a wider variety of MONs to be explored alongside faster screening of composites produced. For example, static mixers could be utilized to miniaturize the synthesis of the foam whilst still effectively mixing the reagents. This could be used with smaller amounts of MONs, allowing access to more structures that could not be explored in this work due to scale-up requirements. Furthermore, this could be combined with headspace GC analysis to effectively seal small volumes of composite foam for aging and detect specific losses of cyclopentane or isopentane from the foam over time.

Alternatively, the exploration of scalability of MONs would be a significant step in further development of this work. Due to the small scale of the MONs produced, analysis of the structures and obtaining reproducible batches that are stable under a range of conditions still provides some challenges. Therefore, either through the synthesis of alternative MOF systems that have high stability and can be modulated for exfoliation (e.g. UiO-66 or MIP-202), or already stable MON systems that have yet to be effectively scaled-up (e.g. Zn(TCPP)) could provide a further insight into the behaviour of MONs within the rigid PIR foams.

For further alternate MOF systems, exploring unique secondary building units or surface functionalities could produce deeper insight into the behaviour of the MOFs in the foams, when then combined with possible modulation to alter the MOF size/shape could provide unique data that is not explored within this work.

From this work specifically, an initial scale-up approach for Cu(ABDC)(DMF) MOF in producing boards of insulation would be an ideal step forward, as the industrial conditions of producing

rigid PIR foam could provide an opportunity to determine more optimal mixing for the composites through high pressure mixing/ enhanced temperatures for reaction.

A myriad of alternative polymerization techniques to produce PolyMON systems can also be studied as only an initial look into the possibilities has been explored in this work. Graft-to polymerization was suggested as the next step as less stable MOFs/MONs would not be subjected polymerization conditions, and instead gentler coupling techniques, such as click reactions could be used. Alternatively, exploring more stable MOFs/MONs could allow for the graft-from techniques initially explored within this work to become viable for synthesis of PolyMONs. Following this, a variety of additional applications could be sought to widen the uses of PolyMONs as tortuous paths, such as gas or water separation, or in the enhancement of polymers through their unique structures.

Overall, this work has met its aims in reducing the loss of blowing agent from rigid PIR foams using MONs, and the exploration of the MOFs in this work has produced novel MONs alongside introducing possible pathways into the synthesis of PolyMONs for the future. Finally, a significant number of possibilities can be built from the foundations of these studies. This work has been my passion for the last four years, I cannot wait to see where it can be taken forward.

Chapter 7

Experimental Methods

"Stop trying. Take long walks. Look at the scenery. Doze off at noon. Don’t even think about flying. And then, pretty soon, you’ll be flying again."

— Ursula in Kiki's Delivery Service, by Studio Ghibli, a Japanese animation studio

7.1 - Introduction

This chapter describes general experimental and analytical techniques used throughout the thesis. Specific techniques and analysis methods will be contained within their respective sections, but to avoid repeated content, this chapter presents a compilation of methods that would otherwise be duplicated.

7.2 – Elemental analysis

Elemental analysis was performed by the microanalytical service at the Department of Chemistry, University of Sheffield using a Vario MICRO Cube in an atmosphere of pure O_2. Results are determined to a tolerance of ± 0.5 % for organometallics.

7.3 – Fourier Transform Infrared Spectroscopy (FT-IR)

FT-IR spectra were recorded using a Perkin Elmer Spectrum 100 FT-IR spectrophotometer, equipped with a SenseIR diamond ATR module. Samples were analysed without further preparation, in reflectance mode between 100 – 600 cm^{-1}, utilizing 12 scans with a spectral resolution of 1 cm^{-1}.

7.4 – Nuclear Magnetic Resonance (NMR)

NMR spectra were recorded at 300 K using a Bruker Advance III HD 400 spectrometer equipped with a standard geometry 5 mm BBFO probe with a single z-gradient at 400 MHz (^1H). MOFs and MONs were digested prior to submission: all copper paddle-wheel based systems used DCL (10 µL) and DMSO-d_6 (0.75 mL), and all NH_2-MIL-53 systems used NaOD (50 µL) and DMSO-d_6 (0.75 mL) with sonication (37kHz, 5 minutes). All samples were filtered through cotton wool prior to submission to remove any undigested particulates.

7.5 – Powder X-Ray Diffraction (PXRD)

PXRD data was collected using Bruker-AXS D8 diffractometer using Cu K_α (λ=1.5418 Å) radiation and a LynxEye position sensitive detector in Bragg Brentano parafocussing geometry using a packed glass capillary or a silicon plate.

7.6 – Liquid Assisted Exfoliation of MONs

Liquid assisted exfoliation of MONs was performed using a Fischerbrand Elmasonic P 30H ultrasonic bath (2.75 L, 380/350W, UNSPSC 42281712) filled with water. The water is thermostatically held at 16 – 20 °C using a steel cooling coil. Initial testing of materials were performed at 6 mL scale in a 10 mL reaction vial suspended in the ultrasonic bath via an overhead stirrer to rotate the samples and avoid "hotspots" to allow for more consistent exfoliations. A nanosheet suspension was then obtained through centrifugation (1500 rpm, 1 hour), with the supernatant separated from the remaining bulk material to yield MONs.

MONs produced at scale for the addition to foam are performed at a 240 mL scale in a 250 mL round bottom flask. Multiple (6-9) exfoliations are performed to yield enough material for addition to the foam.

For un-centrifuged MONs, the solution was sonicated dependant on system requirements and the resultant solution is centrifuged (12,000 rpm, 30 mins) and the supernatant disposed. The remaining material was dried under desiccation for 16 hours before being manually ground with a mortar and pestle for addition to the foams.

For centrifuged MONs, the solution was sonicated dependant on system and the resultant solution was centrifuged (1500 rpm, 1 hour) and the supernatant removed from remaining particulates. The supernatant was then centrifuged (12,000 rpm, 30 mins) and the supernatant disposed. The remaining material was dried under desiccation for 16 hours before being manually ground with a mortar and pestle for addition to the foams.

7.7 – Dynamic light scattering (DLS)

DLS data was obtained using a Malvern Zetasizer Nano series particle analyser, using a He-Ne laser at 633 nm, operating in backscatter mode (173 °). Samples were equilibrated to 298 K for 60 s prior to analysis. 10 measurements were taken per sample, with the position of the mean intensity quoted. MoS_2 and graphite samples were distributed in MeCN with sonication (37 kHz, 60 seconds) prior to analysis. All MOF/MON systems were analysed in the solvent used for exfoliation; namely, MeCN (Cu(BDC)(DMF), Cu(ABDC)(DMF) and Cu(BTetC)(DMF)), EtOH (Cu(MA-ABDC)(DMF)) or water (modulated NH_2-MIL-53)

7.8 – Atomic Force Microscopy (AFM)

AFM images were recorded using a Bruker Multimode 5 Atomic Force Microscope, operating in soft-tapping mode in air under standard ambient conditions. Bruker OTESPA-R3 silicon cantilevers were operated with an amplitude of ~18.7 mV and a resonance frequency of ~236 kHz. Samples were prepared by taking 10 µL drops of MON suspensions (after 1500 rpm centrifugation to remove larger particulates and 10x dilution by volume) onto freshly cleaved mica sheets heated to slightly above the boiling point of the solvent used. These sheets were attached to stainless steel, magnetic Agar scanning probe microscopy disks, and all images process using Gwyddion software.

7.9 – Thermogravimetric Analysis (TGA)

Thermogravimetric analyses (TGA) was measured using a Perkin-Elmer Pyris 1 instrument.

Approximately 10 mg of sample was weighed into a ceramic pan, held under nitrogen flow of 20 cm^3 min^{-1} at 25 °C until a stable mass was recorded, then ramped to 800 °C at 1 °C min^{-1}.

7.10 – Determination of MON sizes

To determine height, width and aspect ratio of MONs, several AFM images were taken of the MONs. The largest dimensions individual MONs are highlighted using Gwyddion software,

ignoring any that are partially offscreen or agglomerations of several nanosheets, and recorded for height and width data to the nearest nanometre. All information is processed, and height, width and aspect ratio are quoted with the standard deviation.

7.11 – Scanning Electron Microscopy (SEM)

SEM imaging was performed using a TESCAN VEGA3 LMU SEM instrument, operating at 15 keV and using the secondary electron detector. Samples were prepared by loading onto a carbon sticky tab on an aluminium stub via grinding (for MOF samples) or placed after cutting with a scalpel (foam samples). These samples are then sputter coated with approximately 20 nm of gold using an Edwards S150B sputter coater before being imaged at a distance of 9mm.

7.12 – Helium Pycnometry

Pycnometry measurements were performed on a Micrometrics AccuPyc II 1340 Gas Pycnometer using 1340 FoamPyc software. Samples of foam were hand cut using a foam saw to roughly 1 $inch^3$, measured using callipers and placed inside the 100 cm^3 sample holder and sealed. Details of the sample volume and mass were entered into the software and a cell fracture test was undertaken with no correction for cut cells. 10 cycles were performed with a fill pressure of 19.5 psig and an equilibration rate of at least 0.1500 psig/min. The closed cell percentage quoted as the average value between the 3 repeated foam syntheses, and standard deviation calculated from these values.

7.13 – Determination of Foam Cell Sizes

Cell size analysis was performed under ISTM standard D3576 – 15, where sections of foams are measured to produce an average cell size analysis. Specifically for this work, a small sample of foam is cut using a scalpel to produce a clean-cut surface. This sample is imaged via SEM, as described above. On each image, three lines are digitally drawn across the width of the image, and cell walls are marked manually. The number of cells between wall marks on one line are

counted and the distance between the first and last mark is measured and used in the equation:

$$t = \frac{n}{w}$$

Where t is the average chord length, n is the number of cells between wall marks and w is the width of a line.

The average cell size of one line is then calculated by the following equation from the ASTM standard D3576-15:

$$d = t(1.623)$$

Where d is the calculated cell size.

A total of 12 lines over 4 images are utilized to create an averaged cell size for each foam system and the standard deviation quoted of the values determined.